



Title image: View into the neutron guide hall west during the construction of the new small angle scattering facility SANS-1 (magenta coloured).

## Annual Report 2009

<b>Directors' Report</b>	<b>4</b>	<b>Reactor</b>	<b>92</b>
Primed for a bright future	7	The operation of the neutron source in 2009	94
The year in pictures	8	Optimization of the Si content in UMo/Al(Si) fuel plates	96
<b>Instruments and Methods</b>	<b>14</b>	Lunar mission and batteries for locomotives - Neutrons for industry	98
New instruments - New opportunities	16	<b>Facts and Figures</b>	<b>100</b>
The neutron resonance spin echo method applied to mode splitting	20	Events: JCNS-workshops, <i>LabCourse</i> and <i>Fortgeschrittenenpraktikum</i>	102
A study of magnetic excitations in $\text{Er}_2\text{PdSi}_3$ using polarised neutron scattering	22	Statistics, meetings, access and much more: The user office of the FRM II and JCNS	104
Effect of macroscopic relaxation on residual stress analysis by diffraction methods	24	Public relations and visitors' service: From cultural heritage to isotopes	106
From prompt gamma activation analysis to prompt gamma activation imaging	26	Publications	108
Geomaterials studied using neutron computed tomography at ANTARES	28	Committees	116
Separating coherent and incoherent scattering: Polarization analysis on protein samples	30	Partner institutions	122
High sensitive analysis of intermetallic layers using a positron beam	32	Staff	124
Positron Age Momentum Correlation (AMOC) measurements on thin $\text{SiO}_2$ layers	34	Imprint	130
Technical developments for instruments	36		
<b>Scientific Highlights</b>	<b>40</b>		
A study of the denaturation of horse heart metmyoglobin by chemical agents using SANS	42		
Study of homogeneous lipid coatings on implant surface materials	44		
Infiltration of a conducting polymer into a mesoporous $\text{TiO}_2$ network	46		
Phospholipid membranes exhibit a flow-like transport mechanism	48		
Globular protein under denaturing conditions	50		
Elastic properties of the interfacial membrane in fluctuating supercritical $\text{CO}_2$ -microemulsions	52		
Nuclear spectroscopy of $^{200}\text{Hg}$ using cold neutron capture	54		
Magnetic structure of a pnictide superconductor determined by single crystal neutron diffraction	56		
In-operando neutron scattering studies of Li-ion batteries	58		
Monoclinic and orthorhombic pyroxene-type $\text{CoGeO}_3$ : Magnetic properties and spin structure	60		
Structures, phase transitions and hydration of $\text{Ba}_4\text{Nb}_2\text{O}_9$ and $\text{Ba}_4\text{Ta}_2\text{O}_9$	62		
Towards lead-free ferroelectrics: A neutron study under real operating conditions	64		
Long-range order in nanodomain FeCo alloys with ternary additions	66		
Anomalous structural behaviour and complex magnetic properties of Co-olivine, $\text{Co}_2\text{SiO}_4$	68		
Search for ferromagnetic quantum criticality using polarized neutron imaging	70		
Skyrmion lattices in metallic and semiconducting $\text{B}_2\text{O}$ transition metal compounds	72		
Spin-excitations of an optimally doped iron arsenide superconductor	74		
Parasitic small moment antiferromagnetism in the hidden order of $\text{URu}_2\text{Si}_2$	76		
Short-ranged spin correlations in the molecular magnet $\{\text{Mo}_{72}\text{Fe}_{30}\}$	78		
Maxon position and linewidth at high pressures in superfluid helium	80		
Magnon damping in spin-ladders	82		
Anisotropy of the superconducting gap in lead investigated by neutron spectroscopy	84		
The life time of elementary excitations in superfluid $^4\text{He}$ studied by resonant spin-echo	86		
Scission gamma-ray measurements at MEPHISTO	88		
Neutron capture cross sections of $^{74}\text{Ge}$ and $^{76}\text{Ge}$	90		

# Directors' Report

1



## Directors' Report: Primed for a bright future

After the initial five years of routine operation, it is worthwhile reviewing some of our achievements and gaining a perspective for the near future. Following the commissioning of the reactor, in May 2005 we started out with a considerable suite of instruments. Today, routine operation comprises four reactor cycles per year of 60 days each at full power of 20 MW, with the operation of 21 instruments, and another nine under construction. In the last year, we have carried out 1030 experiments in total. This could only be achieved due to strong and effective collaboration with partner institutes and universities and the indefatigable efforts and commitment of the scientific and technical staff on site. We would like to express our gratitude to all those who contributed to the success of the project.



The results of our scientific work have been published in prestigious journals. In order to illustrate some of the highlights, we have included short summaries in this annual report. To mention just two: A modern lithium battery and new iron-arsenide based superconductors were investigated at the FRM II. The neutrons from FRM II also made a direct contribution to industry. Last year, 15 tons of silicon were doped via neutron transmutation. Radiopharmaceutical companies such as itm AG (isotopen technologien münchen) have expanded their operations on site and use FRM II and other neutron sources for the production of radioisotopes used in nuclear medicine. MEDAPP, our clinical facility for the direct irradiation of near surface tumors using fast neutrons, performed 216 irradiations of patients in the past year.



Our aim is to maintain a continuous growth in all areas over the coming years. Taking into operation the new guide hall in the east building will enable us to extend the number of simultaneous operating instruments. Of these new initiatives, the biggest project will, without doubt, be the construction of the new ultra-cold neutron source. The collaboration contract in progress with the Federal Ministry of Science and our



partner institutions from the Helmholtz society will provide us with the necessary resources to ensure that profitable scientific use is made of the FRM II. To accommodate the increasing number of staff members and to provide the urgently required work and laboratory space, additional buildings are planned on site. A major step forward in industrial application will be the construction of a molybdenum-99 production facility, an isotope urgently needed for medical diagnostics and treatments. A joint study of IRE (Institut National des Radioéléments) and FRM II, published in June 2009, endorsed the feasibility of such an irradiation facility at our reactor.

Dr. Johann Meier, the Deputy Technical Director, retired at the end of 2009. He studied physics at TUM and served the FRM, and later the FRM II from 1972. He possessed the admirable gift of being able to reconcile both the needs of a safe and sustainable nuclear operation and the often very demanding challenges of the scientists. Considerable thanks are due to Dr. Meier for his long service to science!

For non-scientific readers, a new brochure "Forschung mit Neutronen" was published with the help of Gert von Hassel. Sadly, he passed away on June 14<sup>th</sup>, just days before the work was completed. Gert von Hassel served from 1994 to 2002 as press officer for the FRM II. Indefatigably, he disseminated information about the project through meetings, workshops, presentations, newspapers, television and numerous brochures. We will all remember Gert von Hassel as one of the pioneers of the FRM II.

Last but not least, after seven years of reporting on the FRM II, we have changed both the layout and the focal point of the annual report. Now, more attention is given to scientific results and the highlights achieved from measurements at our institute, although instrumental developments and new methods will still play an important role in our report.

*Klaus Seebach*      *Winfried Petry*      *Ingo Neuhaus*

Klaus Seebach

Winfried Petry

Ingo Neuhaus

# The year in pictures



March 5<sup>th</sup>, 2009: Bayerisches Fernsehen again reports about the neutron source, filming Prof. Dr. Winfried Petry (l.) in the neutron guide hall.



March 2<sup>nd</sup>, 2009: Bayerisches Fernsehen interviews Prof. Winfried Petry (r.) about the controversy surrounding the use of highly enriched uranium at the FRM II.



April 3<sup>rd</sup>, 2009: The Strategierat of the FRM II honours its guest Dr. Rainer Kuch of Technische Universität München (2nd from the right) with a miniature fuel element. The directorate of the neutron source, Dr. Klaus Seebach, Dr. Ingo Neuhaus and Prof. Dr. Winfried Petry (from left) thank Dr. Kuch for his commitment.



February 25<sup>th</sup>, 2009: Meeting of the partners of the Transregio project „From Electronic Correlations to Functionality“ at the FRM II. Dr. Rossitza Pentcheva, Ludwig-Maximilians Universität München, and Prof. Dr. Arno P. Kampf, Universität Augsburg, in the experimental hall.



August 6<sup>th</sup>, 2009: The district administrator of the district of Munich, Johanna Rumschöttel, visits the FRM II with her assistants, having a look into the reactor pool, which is emptied for routine inspections.



July 6<sup>th</sup>, 2009: Prof. Dr. Winfried Petry welcomes the Alumni of the Technische Universität München for a tour of the neutron source.

November 24<sup>th</sup>, 2009: The Bavarian Minister for Science, Dr. Wolfgang Heubisch (m.) visits the FRM II. The FRM II Technical Director, Dr. Ingo Neuhaus (r.), shows the Minister and the President of the Technische Universität München, Prof. Dr. Wolfgang A. Herrmann (l.) the position for the planned molybdenum-99 production in the reactor pool.



July 13<sup>th</sup>, 2009: Congress in honour of the 70<sup>th</sup> birthday of Prof. Dr. Klaus Böning (r.), former project leader of the neutron source planning team, and of Dr. Jürgen Großkreutz (l.), former assistant director at the Bavarian Ministry for Science.



July 14<sup>th</sup>, 2009: Erasmus Mundus MaMA-SELF students performing their Master theses of *Material Science Exploiting Large Scale Facilities* at the FRM II.



June 26<sup>th</sup>, 2009: The steering committee of the Institut Laue-Langevin visiting the neutron source.



August 7<sup>th</sup>, 2009: Dr. Birgit Loeper-Kabasakal, physician for tumour treatment at the FRM II (r.), explains the irradiation facility to physicians and staff of hospitals in Innsbruck and Traunstein.



July 7<sup>th</sup>, 2009: The exterior of the Atomic Egg is restored.



October 1<sup>st</sup>, 2009: Members of the Ministry of Industry and Energy Azerbaijan with the FRM II scientist Dr. Sergey Masalovich (l.) and Dott. Bianca Tonin-Schebesta of the FRM II visitors' service.



October 24<sup>th</sup>, 2009: Happy, that they got one of the 487 places for a guided tour of the FRM II at the open doors. Dr. Aurel Radulescu (l.) takes a group back to the Physics Department (TUM).



September 3<sup>rd</sup>, 2009: Ingrid Lenz-Aktas, candidate of the SPD for the German parliament, gets a look into the reactor pool with the Technical Director of the neutron source, Dr. Ingo Neuhaus.



November 26<sup>th</sup>, 2009: At a press workshop of the Jülich Centre for Neutron Science, Dr. Stefan Mattauch, Dr. Henrich Frielinghaus and Klaus Nusser (from right to left) show journalists the instruments in the neutron guide hall.

July 14<sup>th</sup>, 2009: More than 100 employees and former staff of the neutron source enjoy the summer festival of the FRM II.



December 17<sup>th</sup>, 2009: Dr. Burkhard Schillinger explains the properties of the instrument ANTARES at a live video conference to 60 pupils watching in the Deutsche Museum in Munich.



March 24<sup>th</sup>, 2009: An appealing insight for the Chinese business delegation: The FRM II Administrative Director, Dr. Klaus Seebach (m.), gives the guests a guided tour.

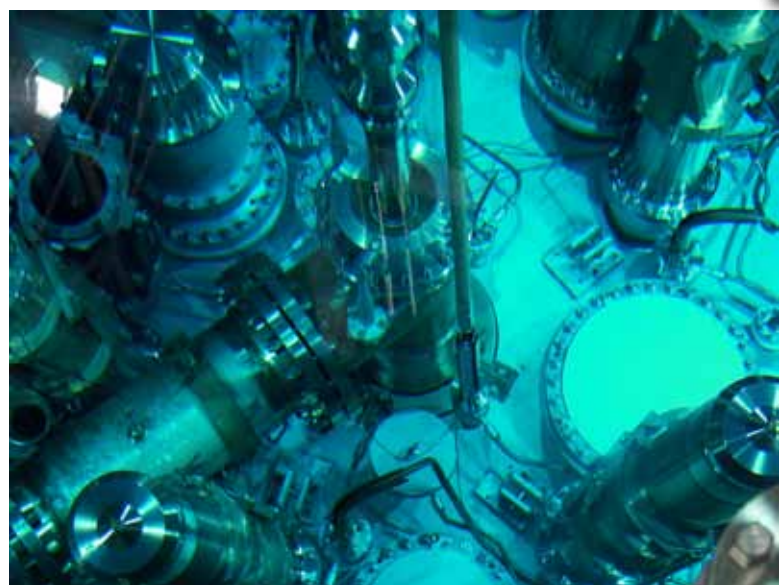


September 28<sup>th</sup>, 2009: A delegation of the French Commissariat à l'énergie atomique and the French embassy get a look inside the neutron source with the Scientific Director Prof. Dr. Winfried Petry (7th from the right).

November 2<sup>nd</sup>, 2009: At a fire service drill the Technical Director Dr. Ingo Neuhaus plays the part of the victim. The plan envisions a cable fire in the reactor hall. The 90 firemen, including firemen of the auxiliary fire brigades and the TUM fire brigade, manage to save the victim and extinguish the fire.



August 19<sup>th</sup>, 2009: A film team of the tv station BR alpha takes a shot of the Atomic Egg.



June 30<sup>th</sup>, 2009: The FRM II announces publicly, that it is able to supply the medically needed radioisotope molybdenum-99. A thimble (white lid in the middle of the bottom of the picture) close to the fuel element can be used for the production.



October 7<sup>th</sup>-9<sup>th</sup>, 2009: Participants of the European Neutron Scattering Association (ENSA), met in Garching. Ensigns indicate the national representatives of the ENSA.



June 14<sup>th</sup>, 2009: Gert von Hassel, former press relations manager of the FRM II died unexpectedly.

An engineer working in the detector tank of the new small angle scattering instrument SANS-1.

# Instruments and Methods

# 2



# New instruments - New opportunities

R. Gilles<sup>1</sup>, A. Ostermann<sup>1</sup>, G. Goerigk<sup>2</sup>, V. Hutanu<sup>1,3</sup>, W. Häußler<sup>1</sup>, S. Mattauch<sup>2</sup>  
R. Georgii<sup>1</sup>, C. Hugenschmidt<sup>1</sup>, P. Link<sup>1</sup>

<sup>1</sup>Technische Universität München, Forschungs-Neutronenquelle Heinz Maier-Leibnitz (FRM II), Garching, Germany

<sup>2</sup>Forschungszentrum Jülich GmbH, Jülich Centre for Neutron Scattering at FRM II, Garching, Germany

<sup>3</sup>RWTH Aachen, Institut für Kristallographie, Aachen, Germany

An impressive vista: Both the experimental and the neutron guide hall are filled to the brim with instruments. Nevertheless, the FRM II suite of instruments increased considerably during 2009. Three instruments (KWS-1, MIRA-2, KWS-3) were commissioned and are now available for experiments. Furthermore a number of major upgrades or extensions such as the CryoPad on POLI-HEiDi or the second arm of RESEDA can be seen. Equally noteworthy are the instruments currently under construction, SANS-1 and BioDiff and the ongoing improvements to the instruments using the positron source NEPOMUC.

## The largest detector tank – SANS-1

Obvious and easily visible of course is the ongoing completion of the small angle scattering instrument SANS-1 built by a collaboration of the Technische Universität München and the

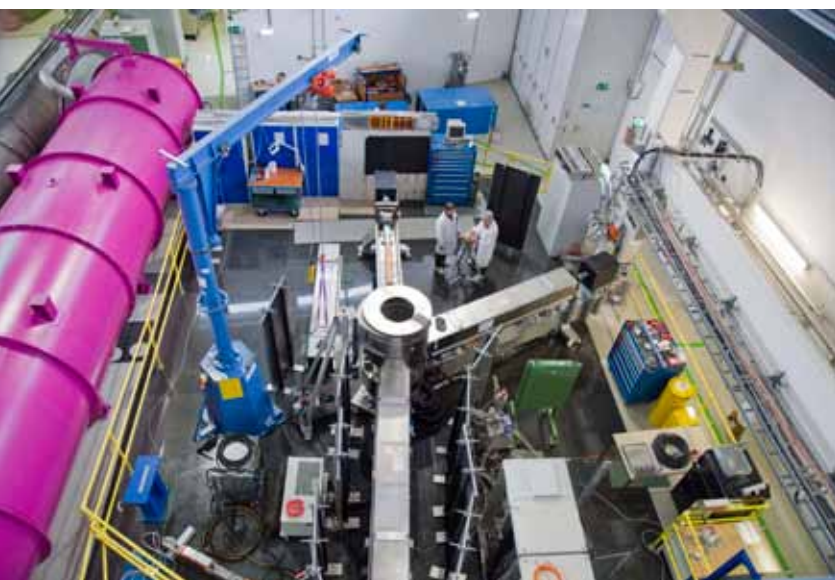


Figure 1: View into the neutron guide hall - on the left side the SANS1 detector chamber; in the centre RESEDA with its second arm under construction.

Geesthachter Neutronenforschungseinrichtung (GeNF) in the neutron guide hall. The installation of the large detector tank allows for sample to detector distances ranging from 1.1 m to 20 m and its internal finalisation marked a mile-stone in this project. The detector, consisting of 128 position sensitive <sup>3</sup>He tubes ( area 100 \* 102 cm<sup>2</sup>), and its electronics have been built and first tests of the electronics undertaken. With the installation of electricity, pressurised air and water completed, the instrument is now ready for the next steps of the commissioning in 2010.

## Small but powerful - BioDiff

Situated in the south-eastern corner of the neutron-guide hall, the first instrument served with neutrons by the neutron guide NL-1, the diffractometer for large unit-cell crystals (for example bio-macromolecules) BioDiff, a joint project of the JCNS and the TUM, is under construction. Having prepared the “dance-floor” and installed the shielding for the monochromator in 2009, the delivery of the main detector and the monochromator will lay the foundations for the first tests with neutrons at the end of 2010.

Using a pyrolytic graphite monochromator (PG002), the diffractometer will be able to operate in the wavelength range 2.4 Å to about 5.6 Å. Higher order wavelength contaminations will be removed by a neutron velocity selector. The main detector of the diffractometer consists of a neutron imaging plate system having a cylindrical geometry to cover a large solid angle. A fast LiF/ZnS scintillator CCD camera is foreseen for additional detection capabilities.

## V-SANS with KWS-3: extending the length scale to the micron

During 2009, the KWS-3 Very Small Angle Neu-

tron Scattering (V-SANS) instrument of the JCNS was commissioned after a major revision of the double-focusing neutron mirror coated with <sup>65</sup>Cu. This resulted in a minimization of the micro-roughness of the mirror, reducing scattering contributions to the background by a factor of 3. Together with the revision of the vacuum system, electronics and software, a completely updated KWS-3 awaits users in 2010. Complementing the pin-hole type instruments, the V-SANS instrument KWS-3 extends the typical accessible length scale of the objects investigated to micron size.

## Commissioning of the Cryopad on POLI-HEiDi.

The Polarisation Investigator (POLI) is a new secondary diffractometer using the focusing monochromator of the single crystal diffractometer HEiDi on the beam port SR9b (hot neutron source). Unique to POLI-HEiDi is that both, the incident beam polarisation and the polarisation analysis use polarised <sup>3</sup>He spin filters. With the commissioning of a new, third generation zero-field polarimeter, Cryopad, built in collaboration with the RWTH Aachen and the ILL Grenoble, spherical neutron polarimetry (SNP) becomes available. After completion of a few further tests, including low temperature sample environment, the SNP on POLI-HEiDi will be available to users in early 2010.

## Second spectrometer-arm for QENS on RESEDA

The upgrade of the Neutron Resonance Spin Echo (NRSE) Spectrometer RESEDA with a second spectrometer arm was completed in 2009, doubling the first spectrometer arm and



Figure 3: POLI-HEiDi with the new CRYOPAD installed.



Figure 2: The new double focussing mirror of KWS 3.

including all parts inside the Mu-metal shielding and the analyzer and detection system. Simultaneous operation with two solid angles of neutron detection for quasi elastic neutron scattering (QENS) is now available.

The ability to use both arms of the secondary spectrometer is particularly suited to a study of diffusion or similar quasi-elastic dynamics in soft matter. The scattering angle can be adjusted up to 100°, in order to study dynamics on small length-scales, making the corresponding correlation times accessible. A typical experiment performed in 2009 was on the temperature dependent dynamics of a polymer melt.

Furthermore a challenging new NRSE technique has been developed at RESEDA in collaboration with a group of scientists from the University of Heidelberg. Employing CASCADE, one of the fastest neutron detectors, the last resonance

flip coil of a standard NRSE setup is no longer needed. The classical spin echo signal is replaced by a time-modulated signal. A demonstrational experiment on a standard sample showed the feasibility and potential of this new technique.

### First neutrons for MARIA

The new neutron reflectometer MARIA (Magnetism Reflectometer with high Incident Angle) is designed to investigate thin magnetic layered structures down to the monolayer scale and lateral structures of nm to  $\mu\text{m}$  sizes. Consequently, the instrument is optimised for a small focused beam and sample sizes of  $1\text{cm}^2$ , and has polarisation analysis as standard.

Besides the reflectometer mode, MARIA will be able to measure, at grazing incidence, small angle scattering (GISANS) mode, with improved resolution in the vertical direction. The latter mode allows lateral structures down to the nm scale to be studied. In December 2009, the instrument was completed up to the sample position and measurements using the first neutrons have confirmed expectations so far. The challenge for 2010 is to characterise the reflectometer fully, starting from the beam profile at different wavelengths and different slit alignments, and ending with the measurement and characterisation of reference samples in the reflectometer and GISANS unpolarised as well as polarised mode.

### MIRA-2, extension of incident neutron wavelength range of MIRA

Commissioning of the MIRA-2 upgrade was completed in 2009. Using a focussing pyrolytic graphite monochromator neutrons with wave-



Figure 4: MARIA - status end of 2009.

length tuneable from  $3.5\text{ \AA}$  to  $6\text{ \AA}$  are extracted from the neutron guide NL-6a. Within 2 h the backend of MIRA can be transferred from the MIRA-1 monochromator (still available for neutrons with wavelength larger than  $8.5\text{ \AA}$ ). The new MIRA-2 setup will be used mainly for cold neutron diffraction and reflectivity measurements with, of course, much higher intensity than the very cold neutron setup MIRA-1.

### Experiments with positrons at NEPOMUC

The positron beam facility NEPOMUC at the FRM II provides the world's highest intensity of a mono-energetic positron beam of  $(9.0 \pm 0.8) \cdot 10^8$  moderated positrons per second for, currently, five different instruments installed on the platform in the FRM II experimental hall (see fig. 6). Outside the biological shield, the beam brilliance is improved by a positron remoderation unit, which is operated with an W(100) single crystal in back-reflexion geometry. The intensity was determined to be  $(5.0 \pm 1.0) \cdot 10^7$  remoderated positrons per second, and the beam diameter amounts to  $< 2\text{ mm}$  (FWHM) in a longitudinal magnetic guide field of 5 mT.

Important features of the instrument for positron lifetime measurements PLEPS (Pulsed Low-Energy Positron System) such as the lateral stability of the beam in the whole energy range (0.2-18 keV) were further improved. PLEPS, which was



Figure 5: View of the MIRA-2 setup.

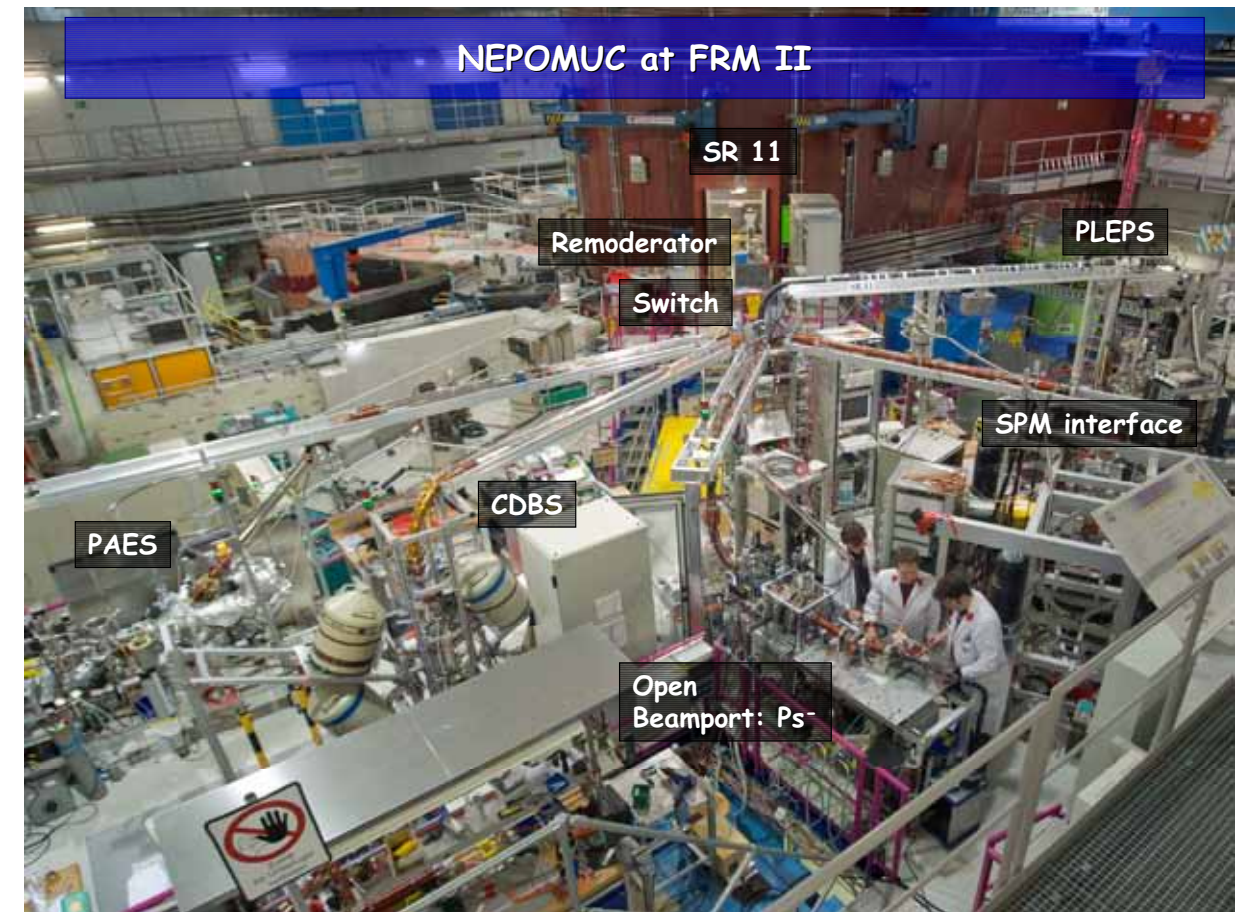


Figure 6: Overview of the positron facility NEPOMUC in the experimental hall of the FRM II.

developed at the Universität der Bundeswehr München, now delivers a pulsed beam with a time resolution of 260 ps, a repetition rate of 50 MHz, and a high peak-to-background ratio of typically  $2 \times 10^4$ . In addition, a first AMOC (Age-Momentum-Correlation) measurement was undertaken, where the lifetime and electron momentum was detected in coincidence.

For the installation of the SPM (Scanning Positron Microscope), an interface was installed with an additional remoderation unit for brightness enhancement. Furthermore, a new pulsing set-up with a chopper and two bunching units were developed and taken into operation.

The CDBS (Coincident Doppler Broadening Spectrometer) now allows temperature dependent measurements down to 80 K, with a lateral resolution below  $300\text{ }\mu\text{m}$ , for defect mapping. The spectrometer is presently being extended by four additional high-purity Ge-detectors.

Within the last reactor cycle, we succeeded in obtaining a PAES (Positron annihilation induced Auger Electron Spectra) in the systems Cu/Pd and Cu/Fe, within exceptional short measurement times ( $< 1\text{ h}$ ). Due to the high positron intensity available at NEPOMUC, PAES with 20 eV

positrons enabled the observation of segregation and alloying at surfaces, and the measurement of Auger transitions with high energy resolution ( $\sim 0.5\text{ eV}$ )

In 2009 the open beam port facility of NEPOMUC was used mainly for the production of the negatively charged positronium ion  $\text{Ps}^-$ . This experiment was carried out in collaboration with the positron group at TUM, the Max-Planck Institute for Nuclear Physics at Heidelberg and the Faculty of Physics of the Ludwig-Maximilians-Universität München. At NEPOMUC, we succeeded in reproducing the value for the  $\text{Ps}^-$  decay rate with a statistical error of 1.1 % within 2 days:  $\Gamma = 2.083(33)\text{ns}^{-1}$ . During the next beam time, the statistics should be further improved by a factor 4, within about 5 days of measurement time, compared to the Heidelberg experiment having had a duration of some 3 months.

# The neutron resonance spin echo method applied to mode splitting

K. Habicht<sup>1</sup>, M. Enderle<sup>2</sup>, B. Fåk<sup>3</sup>, K. Hradil<sup>4</sup>, P. Böni<sup>5</sup>, T. Keller<sup>5,6</sup>

<sup>1</sup>Helmholtz-Zentrum Berlin für Materialien und Energie, Berlin, Germany

<sup>2</sup>Institut Laue-Langevin, Grenoble, France

<sup>3</sup>Commissariat à l'Énergie Atomique, INAC, SPSMS, Grenoble, France

<sup>4</sup>Universität Göttingen, Institut für Physikalische Chemie, Göttingen, Germany

<sup>5</sup>Technische Universität München, Forschungs-Neutronenquelle Heinz Maier-Leibnitz (FRM II), Garching, Germany

<sup>6</sup>Max-Planck-Institut für Festkörperforschung, Stuttgart, Germany

Recent experiments investigating lifetimes of magnon excitations in  $\text{RbMnF}_3$  with neutron resonance spin echo spectroscopy at TRISP, FRM II, provide an excellent testing ground to investigate the potential of the method to determine energy splits with high resolution. We developed an analytical formalism including effects of multiple excitations with different dispersion parameters in the context of neutron resonance spin echo spectroscopy, unresolved with conventional triple axis spectroscopy and compare it to experimental data. Potential future applications are investigations of hybridized phonon or magnon modes, or mixed excitations.

## Correction including instrumental parameters

Neutron resonance spin-echo (NRSE) spectroscopy is a unique experimental tool for measuring the lifetimes of dispersive elementary excitations over extended regions in the Brillouin zone with resolution in the  $\mu\text{eV}$  range. It is of considerable interest to extend the application of the technique one step further, i.e. to resolve modes with a separation in energy which is less than the resolution of standard triple-axis spectrometers (TAS). In the latter case, the spin-echo conditions cannot be satisfied for both modes simultaneously and it is important to understand the consequence for the echo-amplitude. Based on an

extension of Popovici's matrix approach for the TAS resolution function, we have developed the formalism for data correction for NRSE-TAS experiments [1, 2]. We have now generalized our earlier treatment by including instrumental parameters not matching the dispersion properties, allowing the local gradient to have an arbitrary direction in wavevector space and considering scattering from a second mode contributing to the echo amplitude.

## Experiments with $\text{RbMnF}_3$ at TRISP

The case of a second dispersion branch within the background spectrometer resolution has been experimentally realized in NRSE measurements recently performed at TRISP, FRM II, with a particular sample of the simple cubic Heisenberg antiferromagnet  $\text{RbMnF}_3$  consisting of two grains of comparable size. This provides an ideal ground for checking our model against experimental data since the second dispersion surface is identical to the first and its position in  $(Q, E)$ -space is obtained precisely from the experiment, as was the case on the thermal TAS PUMA, FRM II. The spin wave dispersion of magnons in  $\text{RbMnF}_3$  is known in sufficient detail [3]. The relative orientation of the two crystal-lites has been obtained by standard procedures, maximizing the intensity of two Bragg peaks for each of the two grains. Applying an extension of the original UB matrix formalism [4] to inelastic

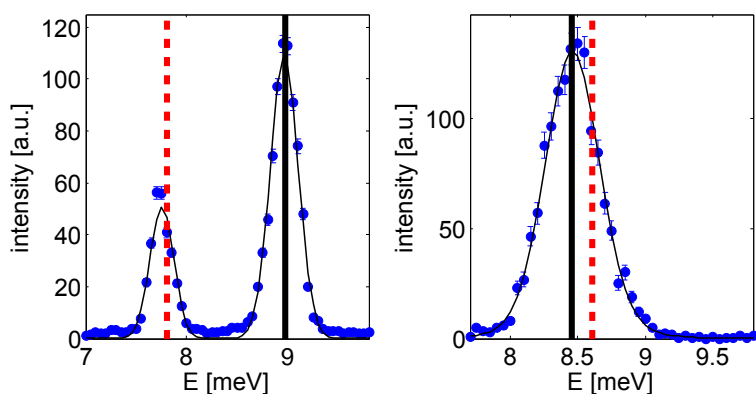


Figure 1: Experimental peak positions (as measured on PUMA) arising from the double dispersion surface compared to calculated peak positions indicated by the vertical lines. The left panel shows data at wave vector  $[0.75 \ 0.75 \ +0.25]$  where a clear separation of the two modes is observed. For the zone boundary magnon at wave vector  $[0.5 \ 0.5 \ -1.0]$  (right panel), the modes are not resolved and the splitting is unnoticeable within standard TAS resolution.

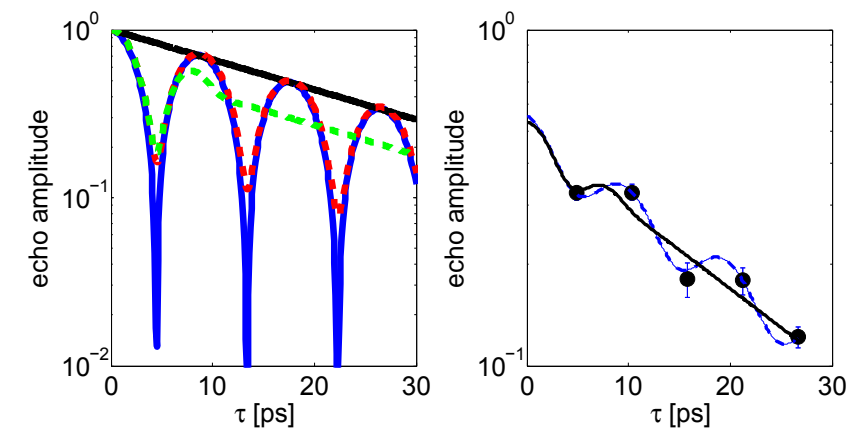


Figure 2: left: Fourier transforms of the scattering function (blue solid) assuming two modes with equal amplitude and  $\Gamma = \Gamma_1 = \Gamma_2 = 27 \mu\text{eV}$ ,  $\Delta E = 0.464 \text{ meV}$ . The red dashed line includes the TAS energy resolution assuming  $\Delta E_{\text{TAS}} = 1.25 \text{ meV}$ . The black solid line shows a single exponential decay corresponding to  $\Gamma$ . Green dashed: The echo amplitude calculated with the full model. Right: Experimental NRSE data from TRISP measured on the zone boundary magnon  $Q = [0.5 \ 0.5 \ -1]$ ,  $E = 8.46 \text{ meV}$  and fit to the simple model (blue). The solid black line is calculated from the full model.

scattering following Lumsden et al. [5], we obtain the peak positions of the inelastic signal in good agreement with experimental data collected on the thermal TAS PUMA in a high collimation configuration (see fig. 1, left, for an example).

The experimental NRSE data for the zone boundary magnon at  $Q = [0.5 \ 0.5 \ -1]$  and  $E = 8.46 \text{ meV}$  has been fit to a simple model. This model is an approximate analytic expression of the echo amplitude in which the line widths are identical, and is given by an exponential decay modulated by a cosine term with period  $T$  inversely proportional to the energy difference and amplitude determined by the intensity ratio of the modes. The energy splitting from the fit to the simple model was found to be  $0.420(19) \text{ meV}$  at a sample temperature  $T_s = 3.18 \text{ K}$  and  $0.414(6) \text{ meV}$  at  $T_s = 7.75 \text{ K}$ . This is in reasonable agreement with the calculated energy split of  $0.464 \text{ meV}$ .

A more involved model requires taking the decaying contribution of the detuned mode into account explicitly. An earlier treatment of the resolution function [1] assumed that the spin-echo conditions are perfectly satisfied and that the TAS resolution ellipsoid coincides with the centre of the dispersion. We have now derived corresponding analytical expressions giving up this restriction and allow for instrumental parameters not satisfying the spin-echo conditions for inelastic, dispersive NSE, as well as two dispersion surfaces with different local gradients in wave-vector-energy space. We express the echo amplitude, using the Larmor phase, as a function of the incident and final wave vectors  $k_i, f$ . Larmor phase, dispersion relation and TAS resolution function are expanded to second order, which allows using a covariance matrix formulation of the resolution problem.

Figure 2 left shows the Fourier transforms of a model scattering function. In figure 2, right, we

show the time dependence of the echo amplitude compared to the simple and full model and find it to be in agreement with the NRSE data within statistical error.

In the specific experiment on  $\text{RbMnF}_3$  magnons, our model allows the identification of those regions in the Brillouin zone where the line-width data is affected by the second grain. This is where the energy separation of the two dispersion surfaces is less than the FWHM of the background TAS resolution, and the depolarization of the second mode not matched to the echo condition is less than 50 % at the smallest experimentally accessible spin echo time used in the data analysis. It is found that a precise measurement of the line width is unaffected by the second grain in most of the Brillouin zone except for small regions close to the zone boundary.

## Investigations of mixed excitations possible

Our analytical formalism permits an investigation of the effects of multiple excitations with different dispersion parameters in the context of NRSE spectroscopy. The significance of this work is to identify conditions which allow one to obtain high-resolution information on the energy splitting of two overlapping dispersive modes which, in general, may differ in their local energy gradient. Potential future applications are investigations of hybridized phonon or magnon modes or mixed excitations. More experimental work is desirable to establish the method when applied to split modes.

[1] K. Habicht et al., J. Appl. Crystallogr., 36, 1307 (2003).

[2] K. Habicht et al., Physica B, 350, E803 (2004).

[3] C. G. Windsor, R. W. Stevenson, Proc. Roy. Soc., 87, 501 (1966).

[4] W. R. Busing, H. A. Levy, Acta Crystallogr. A, 22, 457 (1967).

[5] M. D. Lumsden et al., J. Appl. Crystallogr., 38, 405 (2005).

[6] K. Habicht et al., submitted to J. of Phys.: Conf. Series.

# A study of magnetic excitations in $\text{Er}_2\text{PdSi}_3$ using polarised neutron scattering

F. Tang<sup>1</sup>, M. Frontzek<sup>1</sup>, P. Link<sup>2</sup>, E. Faulhaber<sup>3,4</sup>, A. Schneidewind<sup>3,4</sup>, M. Loewenhaupt<sup>1,4</sup>

<sup>1</sup>Technische Universität Dresden, Institut für Festkörperphysik, Dresden, Germany

<sup>2</sup>Technische Universität München, Forschungs-Neutronenquelle Heinz Maier-Leibnitz (FRM II), Garching, Germany

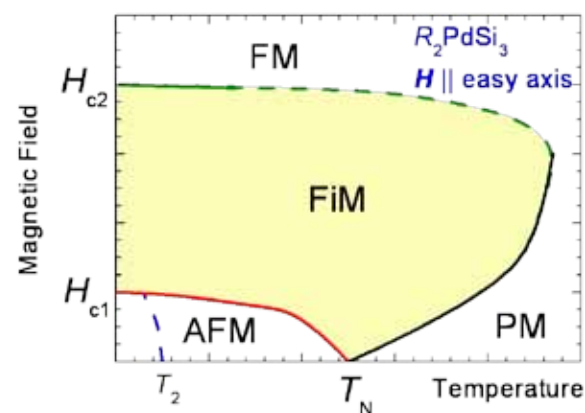
<sup>3</sup>Helmholtz-Zentrum Berlin für Materialien und Energie, Berlin, Germany

<sup>4</sup>Gemeinsame Forschergruppe (PANDA) des HZB und der Technischen Universität Dresden

Inelastic polarised neutron scattering measurements on single crystalline  $\text{Er}_2\text{PdSi}_3$  were performed for the first time on PANDA to identify the nature of magnetic transitions in the compound. Two crystal electric field transitions of energy transfer 3.3 and 3.6 meV had been observed previously, where only one was anticipated. Using the uni-axial polarisation analysis setup, it was determined that both transitions are of the  $J_x$  or  $J_y$  type, suggesting the existence of two  $\text{Er}^{3+}$  sites in the crystal, in agreement with structural studies.

## Large variety of magnetic states

$\text{R}_2\text{PdSi}_3$  (R = rare earth) compounds crystallize in the hexagonal  $\text{AIB}_2$  structure (space group:  $\text{P6}/\text{mmm}$ ) with rare earth atoms on the A positions and Pd and Si atoms on the B positions. The series has been found to exhibit a large variety of magnetic states with rich magnetic properties. This complex magnetic behaviour results from the interplay between the RKKY exchange interaction, magneto-crystalline anisotropy based on crystalline-electric field (CEF) effects and geometric frustration due to the hexagonal crystal structure.



The situation is further complicated by a crystallographic superstructure caused by Pd and Si ordering, featuring a doubled unit cell in the basal plane and octuplicated unit cell along the c direction [2]. The enlarged unit cell implies multiple inequivalent CEF environments for the rare earth ions. Preliminary studies indicate that the crystallographic superstructure is closely related to a generic phase (see fig. 1), with a magnetic structure mimicking the crystallographic superstructure observed in applied magnetic field for most of the compounds in the series 3. The mechanism of the coupling has not yet been determined, however, CEF effects are assumed to play an essential role.

Within the series, the  $\text{Er}_2\text{PdSi}_3$  compound has been found to exhibit a simple CEF excitation spectrum with one dominant, strong transition around 3.5 meV in earlier neutron TOF spectra. The critical field  $H_{c2}$  is found to be relatively small ( $\sim 1.2$  T) for this compound. This allows for inelastic neutron scattering measurements in the FM region, where the CEF level scheme is much simplified, the ground state being the pure state  $|J\rangle$  and only one transition to the  $|J-1\rangle$  state being allowed. However previous neutron spectroscopy on a single crystalline  $\text{Er}_2\text{PdSi}_3$  in magnetic fields up to 12 T performed on the cold triple axis spectrometer PANDA showed, that this strong transition actually consists of two transitions at energy transfers of 3.3 and 3.6 meV

Figure 1: Proposal for a generic phase diagram for  $\text{R}_2\text{PdSi}_3$  when a field is applied along the magnetic easy axis. For details see ref. [3]. The FiM phase has been explicitly confirmed in  $\text{R}_2\text{PdSi}_3$  (R = Tb, Ho, Tm, Er) with neutron diffraction, where a magnetic structure mimicking the crystallographic superstructure has been observed. Note that the phase boundary separating FiM and PM phase does not necessarily start at  $T_N$ .

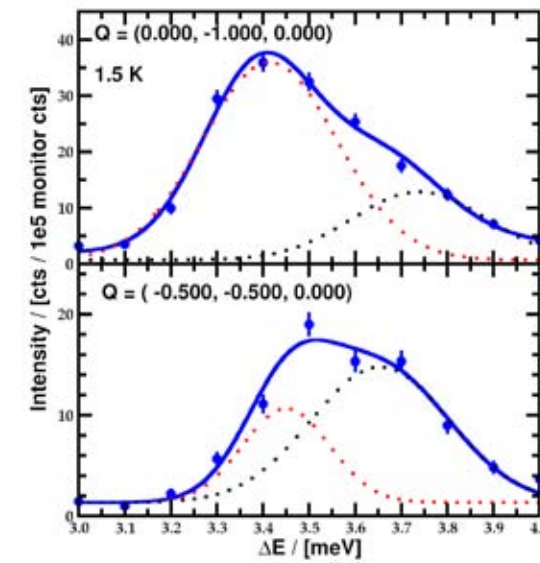


Figure 2: Inelastic scans on  $\text{Er}_2\text{PdSi}_3$  at selected Q points ((0,-1,0): above, (-0.5,-0.5,0): below) measured at zero field and 1.5 K with unpolarized neutrons at PANDA. Blue lines are the total fit with two Gaussian functions to the experimental data. Note the different scale in y axes.

(see fig. 2) [1]. The energy transfers of both transitions increase linearly with increasing magnetic field up to 12 T with an identical slope of  $1 \mu\text{B/g}$ . The questions which arose from this observation concerning the nature of the two transitions and their physical origin.

## Two inequivalent $\text{Er}^{3+}$ sites

Here, we report the first results of inelastic neutron scattering with polarised neutrons on the same single crystal of  $\text{Er}_2\text{PdSi}_3$  using PANDA. The measurements were performed at 10 K, above the Néel temperature  $T_N = 7$  K, to avoid complications from the molecular field in the ordered state. The energy scans at two perpendicular Q positions (0,-1,0) and (1,-0.5,0) showed the transitions at 3.3 and 3.6 meV in the spin flip channel only (see fig. 3). From this, we directly deduce that both transitions are of the  $J_x$  or  $J_y$  type, which suggests that both transitions are from the ground state  $|J\rangle$  to  $|J-1\rangle$ .

As can be seen, the intensity of the 3.3 meV transition at  $Q = (0,-1,0)$  is about twice that at  $Q = (1,-0.5,0)$ , while the intensity of the 3.6 meV transition is almost the same. Defining the (010) direction as the x axis,  $Q = (0,-1,0)$  is then parallel to the x direction and energy scans measured here show only contributions from  $J_y$  type transitions. On the other hand,  $Q = (1,-0.5,0)$  is then parallel to the y direction thus energy scans here

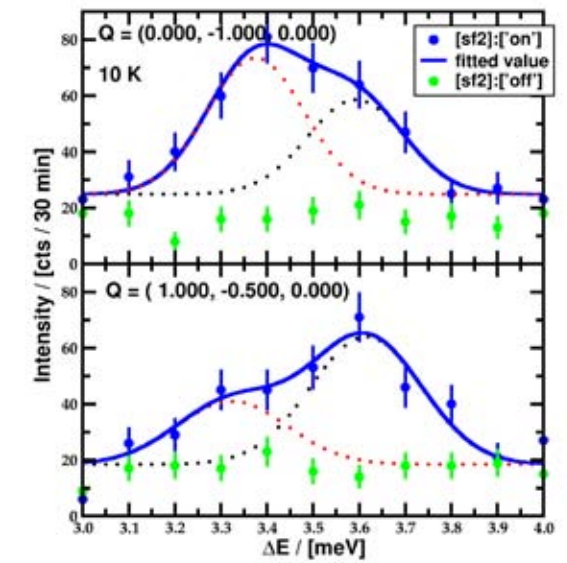


Figure 3: Inelastic scans on  $\text{Er}_2\text{PdSi}_3$  at selected Q points ((0,-1,0): above, (1,-0.5,0): below) measured at zero field and 10 K with polarized neutrons at PANDA. Green circle: non-spin flip channel, blue circle: spin flip channel, blue lines are the total fit with two Gaussian functions to the experimental data.

show  $J_x$  type transitions. Therefore it can be concluded, that the transition at 3.3 meV is mainly of  $J_y$  type while the one at 3.6 meV is a combination of both  $J_x$  and  $J_y$  types. The results can be explained with the existence of two inequivalent  $\text{Er}^{3+}$  sites in the compound and the two transitions are from the two sites respectively. The different composition of  $J_x$  and  $J_y$  type transition in the two transitions hints at different local symmetries. For hexagonal symmetry, there are six equivalent directions in the basal plane and the  $J_x$  and  $J_y$  type transitions should be of equal magnitude. For lower symmetries, i. e. a two fold symmetry, the x and y directions are no longer equivalent, leading to different magnitudes of  $J_x$  and  $J_y$  type transitions. A more detailed analysis is still needed to understand the exact local symmetry. However, it can already be seen that the 3.6 meV transition is from  $\text{Er}^{3+}$  sites with higher symmetry, while the 3.3 meV one is from  $\text{Er}^{3+}$  sites with lower symmetry. This is consistent with the crystallographic superstructure observed in all  $\text{R}_2\text{PdSi}_3$  single crystals, where multiple  $\text{R}^{3+}$  sites are expected.

[1] F. Tang et al, J. Phys.: Conf. Ser. (2009).

[2] J. Dshemuchadse, Diploma Thesis, TU Dresden (2008).

[3] M. Frontzek et al, J. Phys.: Conf. Ser. (2009).

# Effect of macroscopic relaxation on residual stress analysis by diffraction methods

J. Repper<sup>1</sup>, M. Hofmann<sup>1</sup>, C. Krempaszky<sup>2,3</sup>, B. Regener<sup>2,3</sup>, E. Berhuber<sup>4</sup>, W. Petry<sup>1</sup>, E. Werner<sup>3</sup>

<sup>1</sup>Technische Universität München, Forschungs-Neutronenquelle Heinz Maier-Leibnitz (FRM II), Garching, Germany

<sup>2</sup>Technische Universität München, Christian-Doppler-Labor für Werkstoffmechanik von Hochleistungslegierungen, Garching, Germany

<sup>3</sup>Böhler Schmetdetchnik GmbH & CoKG, Kapfenberg, Austria

<sup>4</sup>Technische Universität München, Lehrstuhl für Werkstoffkunde und Werkstoffmechanik, Garching, Germany

One of the basic assumptions of macroscopic residual stress determination by diffraction methods is the identity of the microscopic stress state in the component and the used reference sample, which is often cut from the strained component. Here, the effect of macroscopic relaxation on the microscopic stresses was studied by stepwise machining of a strained IN 718 disc. It turns out that the development of microstresses has to be taken into account in a correct macroscopic stress analysis using neutron diffraction.

## Mixture of macroscopic and microscopic stress

Residual stresses can be distinguished into three types differing in the spatial extension of the stress fields. Microscopic stresses are either volume-averaged over several grains (type II stresses) or localized within a grain (type III stresses). Macroscopic stresses (type I stresses), on the other hand, vary over a length scale which is comparable to the macroscopic dimensions of the component. These stresses are correlated to the service life time of a component. Compressive type I stresses near the surface, for example, can reduce the accumulation of micro-cracks resulting in a gain in life time. In contrast, tensile type I stresses may lead to a reduction of strength and toughness due to spontaneous cracking. Diffraction methods allow the residual stress distribution to be determined non-destructively even deep inside the bulk material. In particular, neutron diffraction allows large penetration depths to be reached. Nevertheless, in diffraction experiments a mixture of macroscopic stresses and microscopic residual stresses (mainly type II stresses) is always detected. In diffraction exper-

iments the macroscopic stresses are determined by comparison of the interference line position of a Bragg reflection of a strained sample and the interference line position of the same Bragg reflection of a macrostress free reference sample. Therefore, one of the basic assumptions in macroscopic residual stress analysis by diffraction methods is the identity of the microscopic stress state in the strained component and in the macrostress free reference sample, otherwise spurious residual stresses will be determined. Hence, the production of the reference sample usually extracted from the strained component, which is assumed to have no influence on the microscopic stress state in the material.

## Plastic deformation

The influence of the macroscopic stress relaxation during the extraction process on the microscopic stress state was investigated at a disc consisting of the high temperature Nickel-base superalloy IN 718 with a thickness of approx.



Figure 1: Photography of the disc after the experiment. The disc radii were reduced stepwise by electrical discharge machining. The results for the discs with radii of 10 and 20 mm are discussed elsewhere.

18.5 mm and an original diameter of approx. 100 mm. The disc was forged at 990 °C with a soaking time of 65 min. The forging procedure results in a high degree of plastic deformation within the sample material. It was cooled down to room temperature by water quenching to ensure high macroscopic residual stress gradients within the disc. This cooling process is expected to suppress the precipitation of additional phases within the matrix phase and the material can be treated as a single phase material. The residual stress state in the centre of the disc was unloaded by a reduction of the diameter of the parent disc (R = 50 mm) by electrical discharge machining to R = 2 mm (fig. 1).

The neutron measurements to determine the residual stress states in the samples were carried out at the materials science neutron diffractometer STRESS-SPEC at the neutron source FRM II [1]. The strains in the three principal directions  $x_1$ ,  $x_2$  and  $x_3$  were measured. The Bragg reflection of the Ni{311} lattice planes of the matrix phase can be found at  $2\theta = 91.3^\circ$  for a wavelength of  $\lambda = 1.556 \text{ \AA}$ . The gauge volume was adapted to  $3 \times 3 \times 3 \text{ mm}^3$  to ensure good counting statistics. Through-thickness scans were performed with eleven measurement points along the centre axis of the disc. The sample with R = 2 mm is free of macroscopic stresses and hence it is used as reference sample.

## Contradiction to mechanical equilibrium

The residual stress distribution of the parent disc (R = 50 mm), determined experimentally using the scattering angles measured for the R = 2 mm sample as reference values, is shown in figure 2. The results are compared to the macroscopic residual stress distributions calculated by a FE-model. There are significant differences between the simulated residual stress distribution and the experimentally determined stresses because of asymmetries and quantitative differences in the stress values. In contrast to the simulated stresses the experimental data show non vanishing axial stresses and thus clearly contradict the mechanical equilibrium; (the axial stresses must vanish in the middle of the disc for negligible free edge effects).

These discrepancies can be explained by disregarding the changed microscopic residual stress

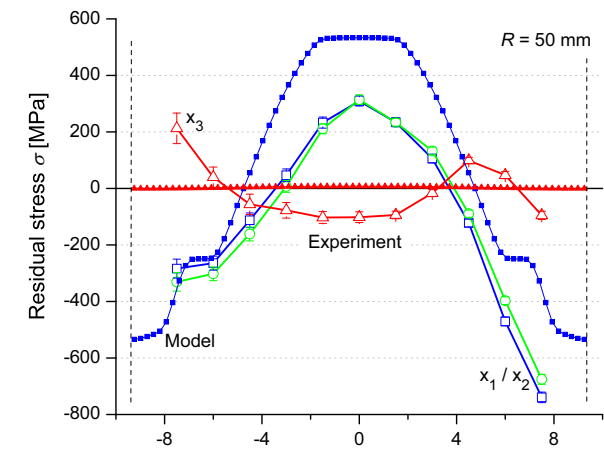


Figure 2: Residual stress distributions in the three principal directions  $x_1$  (squares),  $x_2$  (circles) and  $x_3$  (triangles) across the thickness of the parent disc. The dashed lines on both sides of the graphs mark the upper and bottom surfaces of the disc. The experimental results (open symbols) are compared with the macroscopic stresses calculated by a FE-model simulation (filled symbols).

state resulting from the relaxation of the stresses during the extraction of the sample with R = 2 mm from the uncut disc (R = 50 mm). The cutting process relaxes load large enough to induce local plastic deformation. Then, macroscopic unloading results in an elastic straining (e.g. at the grain boundaries) of grains adjacent to plastically deformed regions. These strains result in microscopic (type II) residual stresses [2, 3, 4]. The level of these stresses varies locally in the material because it is governed by the elastic and/or plastic anisotropy of individual grains. Variations in the degree of pre-deformation of different material regions owing to locally differing quenching conditions also results in non-uniform micro-stress distributions across the thickness of the sample (responsible for the asymmetries in the experimentally determined stress distributions in fig. 2). The grains in highly stressed regions may have already yielded, whereas other regions mainly contain elastically strained grains. In addition, different stress gradients in the initial stress state of the parent disc may transfer larger loads to surrounding material areas during unloading. The microscopic stresses reach stress levels of about +100 MPa, which is approximately 25 % of the maximum initial stress amplitude.

[1] M. Hofmann et al., Neutron News, 18 (4), 27 (2007).

[2] D. Dye et al., Curr. Opin. Solid State Mater. Sci., 5, 31 (2001).

[3] H. J. Stone et al., Acta Mater., 47 (17), 4435 (1999).

[4] B. Clausen et al., Acta Mater., 46 (9), 3087 (1998).

# From prompt gamma activation analysis to prompt gamma activation imaging

L. Canella<sup>1</sup>, P. Kudejova<sup>2</sup>, R. Schulze<sup>3</sup>, A. Türler<sup>4</sup>, J. Jolie<sup>3</sup>

<sup>1</sup>Technische Universität München, Institut für Radiochemie, Garching, Germany

<sup>2</sup>Technische Universität München, Forschungs-Neutronenquelle Heinz Maier-Leibnitz (FRM II), Garching, Germany

<sup>3</sup>Universität zu Köln, Institut für Kernphysik, Köln, Germany

<sup>4</sup>Paul Scherrer Institut, Villigen, Switzerland

We report on a first comprehensive experiment on a piece of the Allende meteorite using both the standard Prompt Gamma-ray Activation Analysis (PGAA) and the novel method Prompt Gamma-ray Activation Imaging (PGAI). With the PGAA setup, the elemental composition of the heterogeneous meteorite sample was determined. Subsequently, the PGAI setup allowed the distribution of elements to be 'visualised' in 2D. As an example, maps of the matrix elements Si, Fe and Mg are presented. The first results obtained are encouraging and useful for a further development and refinement of this technique.

PGAA is a non-destructive radioanalytical technique that employs the neutron capture reaction  $Z^A(n,\gamma)Z^{A+1}$  to determine of the elemental composition in the full volume of various samples. The key feature of the PGAA instrument at the FRM II is a high intensity cold neutron flux (mean energy of 1.83 meV). The maximal thermal equivalent flux amounts to  $\sim 2 \cdot 10^{10}$  n/cm<sup>2</sup>s, obtained by an elliptically tapered focussing neutron guide element for the last 7 m of the neutron guide [1]. This particular design was developed with the gain of producing an intense neutron beam for position-sensitive PGAA (also called Prompt Gamma-ray Activation Imaging (PGAI)), yielding a 2D, or even 3D, information on the element distribution in the



Figure 1: Allende meteorite, 220mg, about 11mm long, 5 mm wide and between 1 - 4 mm thick.

sample volume. PGAI has been combined with a small neutron tomography system (NT), which complements the 3D elemental analysis by providing the information on the internal structure of the sample and thus simplifying the orientation inside the object of interest.

This new setup was developed and tested by a cooperation of the PGAA groups in Budapest and at the FRM II in the framework of the EU project ANCIENT CHARM [2,3,4]. To make a fast, independent test of all the different measurement possibilities at the PGAI instrument, a small piece of the Allende meteorite was subsequently studied by PGAA, NT and PGAI [5].

## Allende meteorite

The Allende meteorite fell in February 1969, close to the Mexican village of Pueblito de Allende and is among the most intensely studied meteorites in history. The structure of the meteorite is very heterogeneous with lots of inclusions (up to mm in size) called "chondrules". According to the official classification, the meteorite belongs to the group of CV3 carbonaceous chondrites.

Figure 1 shows the sample used for this experiment. The large inclusions gave us some chance of already seeing heterogeneity with the present PGAI set up, although only 2D measurements were planned.

## PGAA measurement

This small meteorite was first measured using the standard PGAA setup to obtain an overall composition of its full volume. The results of the analysis are shown in table 1. For comparison, literature values for the composition are also given there. The interesting part is the comparison with the PGAA measurement carried out for the same piece of the Allende meteorite at the

Budapest PGAA station. The results obtained at FRM II are in a good agreement with those obtained in Budapest, e.g. Mg, Si, Mn, Fe, and Ni give the same result within one standard deviation. The differences between our measurement and the values given by Jarosewich [6] and Kallemeyn [7] are due to the heterogeneity of the Allende meteorite. The values in [6,7] give the average concentration over the whole of the Allende meteorite whereas we have measured only a tiny part of it.

## 2D PGAI

For the 2D PGAI, the neutron beam was collimated to obtain a resolution of 2 mm x 2.5 mm at the sample position and the meteorite was scanned in 3 horizontal and 5 vertical steps, giving 15 spectra in total. The scanning grid was prepared based on the neutron radiography (NR) of the meteorite positioned in the neutron beam before the PGAI measurements (fig. 2a).

The 2D charts for the main elements found inside the meteorite - Fe, Si and Mg - are shown in figures 2 b-c. The contour lines define the distribution of the counts for the given element. As can be seen in figures 2 b) - d), the distributions for Fe, Si and Mg are slightly different from one another. However all the elements have the higher amount on the right-hand side of the sample, where the object is thicker (the concentrations were not recalculated to account for sample thickness). For the trace elements (like Al, S, Ti), we expect a higher differentiation in the scanned elemental distribution. However, these elements could not be analysed during this experiment because of insufficient statistics resulting from the short measuring time per position.

## 2D maps for major elements in the sample

By examining a small piece of the Allende meteorite we have successfully shown the progression from the PGAA to the 2D PGAI technique. When using the standard PGAA method, the elemental composition of the bulk sample was determined, the PGAI technique derived 2D maps for the three major elements in the sample. Neutron radiography was used for precise orientation of the measured area. These encouraging results show prospects for further improvement. For the PGAA measurements, a more precise sample analysis, lower radiation background and a reduction in disturbing electronic noise

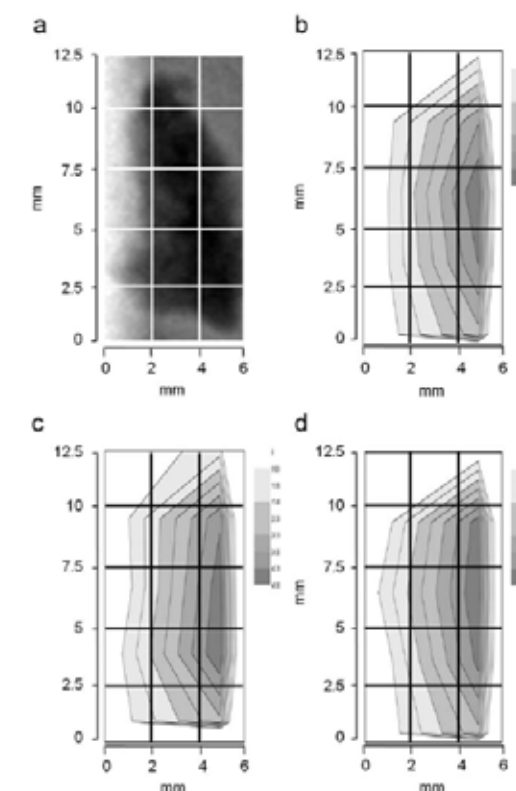


Figure 2: a) radiography of the Allende meteorite in the measured position b) 2D distribution of the main element Fe, c) Si and d) Mg obtained with PGAI technique.

are needed. A better peak-to-background ratio would allow us trace elements to be measured in real time as well as an improved spatial resolution and, finally, the 3D imaging for such small samples, are the challenges for PGAI.

Element	FRM II	Buda <sup>a)</sup>	Jaros.	Kall.
Mg	13.00 ± 0.58	13.20 ± 0.69	14.85	14.80
Al	1.377 ± 0.060	1.406 ± 0.036	1.731	1.760
Si	14.81 ± 0.38	14.68 ± 0.34	16.00	-
Cr	0.357 ± 0.010	0.334 ± 0.008	0.356	0.363
Mn	0.1350 ± 0.0039	0.1396 ± 0.0026	0.1394	0.1450
Fe	23.95 ± 0.46	23.85	23.85	23.70
Co	0.0410 ± 0.0015	0.0391 ± 0.0008	0.01 - 0.02	0.0662
Ni	0.879 ± 0.026	0.868 ± 0.015	0.36 - 0.85	1.33

a) The values are normalised for the Fe concentration given by Jarosewich [5]

Table 1: Comparison between the PGAA values obtained at FRM II and Budapest and literature values on the Allende meteorite obtained by Jarosewich (1990) and Kallemeyn and Wasson (1981). All the values are in %w and errors are in 1-σ standard deviation.

[1] P. Kudejova et al., J. Radioanal. Nucl. Chem., 278, 691 (2008).

[2] ANCIENT CHARM project: <http://ancient-charm.neutron-eu.net/ach>.

[4] T. Belgya et al., J. Radioanal. Nucl. Chem., 278, 713 (2008).

[5] L. Canella et al., Appl. Radiat. Isot., 67, 2070 (2009).

[3] G. Gorini, Il Nuovo Cimento (1), 1 (2007).

[6] E. Jarosewich, Meteoritics, 25, 323 (1990).

[7] G. Kallemeyn et al., Geochim. Cosmochim. Acta, 45, 1217 (1981).

# Geomaterials studied using neutron computed tomography at ANTARES

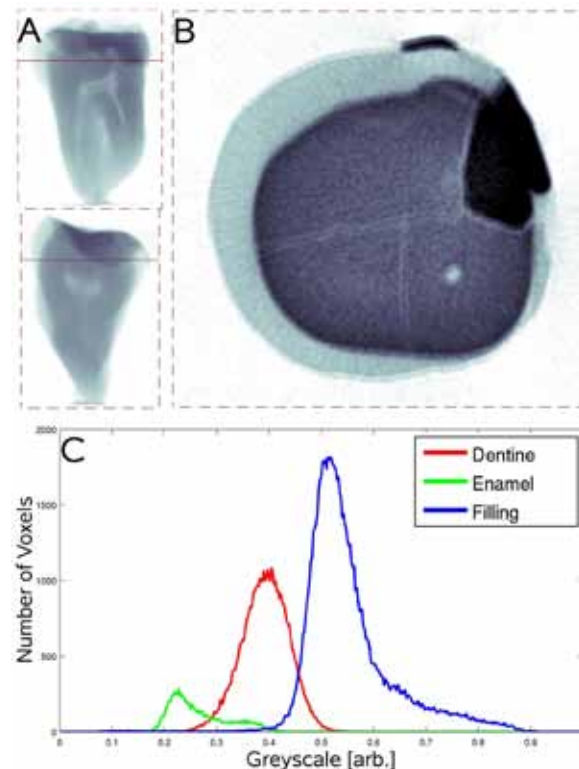
K.-U. Hess<sup>1</sup>, A. Flaws<sup>1</sup>, B. Schillinger<sup>2</sup>, M. Mühlbauer<sup>2</sup>, M. Schulz<sup>2</sup>, E. Calzada<sup>2</sup>, D. B. Dingwell<sup>1</sup>

<sup>1</sup>Ludwig-Maximilians-Universität München, Fakultät für Geowissenschaften, München, Germany

<sup>2</sup>Technische Universität München, Forschungs-Neutronenquelle Heinz Maier-Leibnitz (FRM II), Garching, Germany

Having improved the detector resolution at ANTARES to 20-30  $\mu\text{m}$ , neutron computed tomography has become suitable for geomaterial analysis for the first time. Neutrons are strongly scattered by hydrogen bearing minerals, yielding a phase contrast not available in conventional X-ray computed tomography. In particular, bio-geomaterials such as shells, bones and fossils benefit greatly from such phase contrast. Here, we report on experiments on a human tooth and a synthetic melt containing crystals, which demonstrate the strength of this method.

Detector resolution at the radiography and tomography facility ANTARES has been improved to 20-30  $\mu\text{m}$ , a range which is useful for geo-



material analysis. For the first time geoscientists are able to use neutron computed tomography (NCT) to characterise fine features such as crystals, cracks and pores. Neutrons are strongly scattered by hydrogen bearing minerals, yielding a phase contrast not available in conventional X-ray computed tomography. In particular, bio-geomaterials such as shells, bones and fossils benefit greatly from such phase contrast. The sensitivity of NCT imaging to hydrogen also makes it possible to build 3D maps of the water content in a sample, making it a powerful tool for the study of water diffusion. Water can also be used as a contrast material to highlight the presence of an open crack or pore space, even below the resolution of the method. A software suite has been developed for extended processing, visualisation and quantitative analysis of geomaterial tomography data. It offers a number of new tools including: phase separation by object recognition, 3D anisotropy and surface roughness characterisation.

## Direction and magnitude of an anisotropy

Often the subtle alignment of crystals or sheared bubbles trapped in volcanic glass can tell us a great deal about the dynamic history of a sample. For this reason a number of 3D anisotropy algorithms have been developed as part of the Tomoview software suite. Either by ellipsoid fitting or a full mapping of an object's surface orientation, they provide a histogram of the surface area as a function of spherical angle, which indicates the direction and magnitude of the anisotropy. This new analysis method has already been used

Figure 1: A) Line-integrated side profiles of a human tooth. B) A reconstructed cross section of that same tooth, in which the different layers of enamel (pale); dentine (mid-shade), and filling (dark) are clearly visible to the eye. C) Histograms taken from volumes within each region show that a significant greyscale overlap between the materials exists.

to study rock deformation, by tracking both the volume and orientation of crack planes as they form. The relatively long penetration length of NCT imaging allows us to study large (of the order of several cm) samples, and is particularly useful for studies of brittle deformation, where the sample can be too delicate to remove from the metal jacket in which it was deformed.

## Object recognition

Often the attenuation range of different materials within a sample overlap makes it difficult to isolate a particular phase for rendering or characterisation. This can be true even in cases with relatively good phase contrast, such as bio-geomaterials. In the example below we study the enamel, dentine and a filling inside a human tooth. By eye it is possible to recognise where one material ends and the other begins. However, histograms taken within these regions show there is a significant greyscale overlap between the three materials (see fig. 1).

To threshold the data we must therefore employ a new method, developed as part of the software package, called Object Recognition Thresholding (ORT). This algorithm uses edge detection to find the boundaries of objects from the greyscale gradient [1]. We then create a binary image by defining each volume element (or voxel) containing an edge as 0 and every other voxel as 1. Imagine that we now have a set of disconnected objects. Each formed by connected ones and separated by a thin void of zeroes. Each object can be characterised in terms of its volume; aspect ratio, average greyscale, and orientation. These properties can then be used as

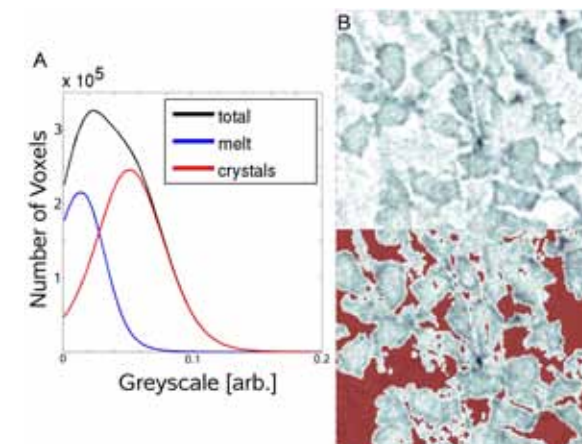


Figure 3: A) The greyscale histogram of this sample shows very strong overlap between the crystal and glass phase. B) However, using object recognition thresholding it is possible to cleanly separate the crystals from the melt.

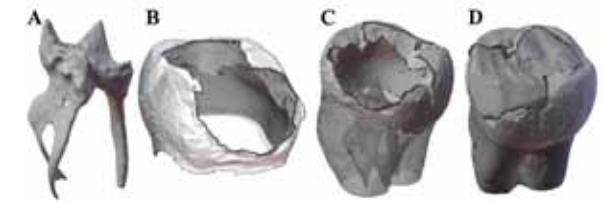


Figure 2: Surface rendering of tooth materials separated using object recognition thresholding A) the pulp cavity; B) enamel, C) dentine – shown here as the translucent surface, and D) the full tooth including the filling at the top.

additional qualifiers to select or exclude objects, and thereby threshold the data. For example, we could choose to select all voxels within the greyscale range 0 to 0.2, and only those belonging to objects with volumes greater than  $10^3$  voxels. In figure 2, we show the pulp cavity, enamel, dentine and filling separated from each other using ORT. This allows us to study the growth features of the different material phases in unprecedented detail.

The above case was chosen as an illustration of a best-case scenario, using the relatively good phase contrast of bio-geomaterials. A far more challenging example of the greyscale overlap, is the study of a synthetic melt containing crystals. The contrast between the two materials is extremely poor. Even to the eye, the crystals are only visible due to the shape of their edges. This is particularly evident when we study the total greyscale histogram shown in figure 3. The overlap is so strong that only one peak is visible. However, using ORT it was possible to cleanly separate the crystals from the melt using their volume, shape, and object-averaged greyscale as qualifiers rather than a greyscale range. The resulting histograms (blue/red) show the extent of the initial greyscale overlap.

## Objects cleanly isolated

Improved detector resolution has allowed us to probe the smaller spatial scales of crystals; cracks, pores, and other structures of interest. Purpose built software allows us to quantitatively study anisotropy within the sample, shedding light on its dynamic history, and has vastly increased the applicable range of NCT analysis by allowing us to cleanly isolate and characterise objects, even in cases with very poor phase contrast.

[1] J. Canny, IEEE TPAMI, 8 (6), 679 (1986).

# Separating coherent and incoherent scattering: Polarization analysis on protein samples

A. M. Gaspar<sup>1,2</sup>, S. Busch<sup>1,2</sup>, M. S. Appavou<sup>1,3</sup>, W. Haeussler<sup>2,4</sup>, R. Georgij<sup>2,4</sup>, Y. Su<sup>3</sup>, W. Doster<sup>1</sup>

<sup>1</sup>Technische Universität München, Physik Department E13, Garching, Germany

<sup>2</sup>Technische Universität München, Forschungs-Neutronenquelle Heinz Maier-Leibnitz (FRM II), Garching, Germany

<sup>3</sup>Forschungszentrum Jülich GmbH, Jülich Centre for Neutron Scattering at FRM II, Garching, Germany

<sup>4</sup>Technische Universität München, Physik Department E21, Garching, Germany

When measuring the total scattering function it is difficult to interpret the results when the coherent and incoherent scattering of the sample are of the same order of magnitude. These terms provide information on different dynamical processes and, therefore, give rise to distinct scattering functions. Polarization analysis provides a means of experimentally separating the coherent and incoherent nuclear scattering functions terms. Experimental results obtained on protein samples over a wide Q-range, from the small-angle to the wide-angle region, demonstrate this information is a prerequisite for interpreting time-of-flight or backscattering experiments.

Static scattering measurements using polarization analysis were performed at two different instruments at the FRM II, DNS and MIRA, in the latter case using two different setups [1]. This allowed one to cover a wide Q-range: going from the small-angle region, where scattering from a protein solution is dominated by the coherent term, to the wide-angle region, usually explored in quasielastic neutron scattering measurements under the assumption that the incoherent term dominates. In these experiments, one separates coherent from incoherent scattering using a polarized incident neutron beam by taking into account that only 1/3 of the spin-incoherent scattering events are without spin flip while all the

Figure 1: Coherent and incoherent scattering intensities obtained for some solutions of protonated proteins in D<sub>2</sub>O: a) Small-angle scattering region  $0.006 < Q < 0.04 \text{ \AA}^{-1}$  (MIRA); b) Intermediate scattering region  $0.04 < Q < 0.4 \text{ \AA}^{-1}$  (MIRA); c) Intermediate to wide-angle scattering region  $0.15 < Q < 2.35 \text{ \AA}^{-1}$  (DNS).

coherent nuclear scattering events are without spin flip [2, 3]. A detailed presentation can be found in our recent publication [1].

## Successful separation

Figure 1 illustrates the successful separation of the coherent and incoherent static structure factors, over the different Q-ranges for some protein

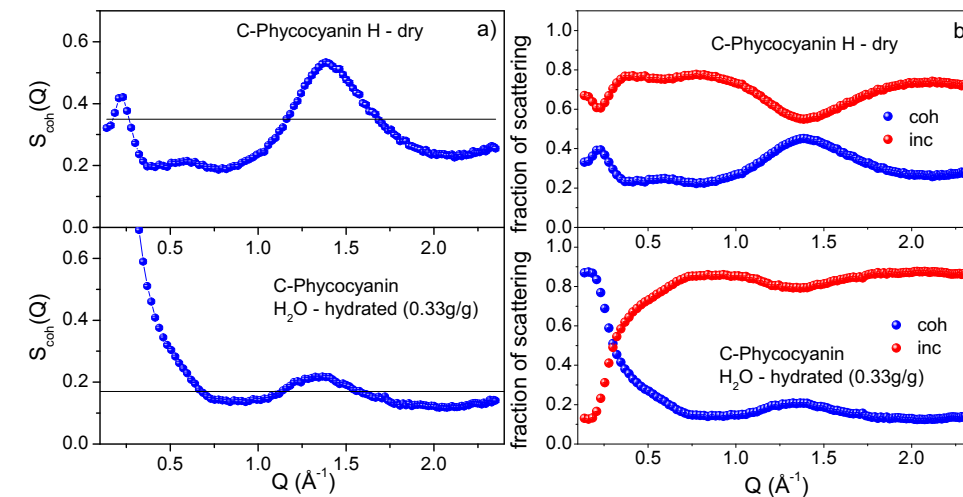
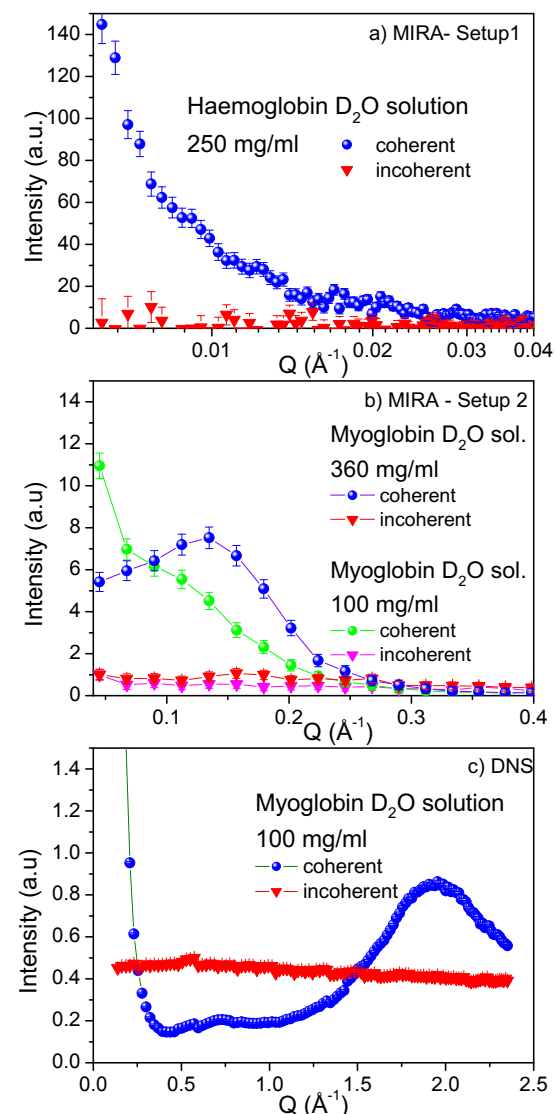


Figure 2: (a) Coherent structure factors and (b) Q-dependent fractions of coherent and incoherent scattering events obtained for per-deuterated C-phycoyanin powders. The straight horizontal lines in (a) represent for each sample the value  $\sigma_{\text{coh}}/\sigma_{\text{tot}}$ .

solutions. As expected, the incoherent term appears as a flat featureless term, while the coherent term changes significantly with Q. It exhibits the expected behavior both in the small angle region (a), where a fast decay with Q is observed, as well as in the intermediate (b) to wide angle (c) regions, where coherent peaks are clearly visible. These results demonstrate the clear predominance of the coherent term in the small-angle scattering region (fig. 1a). For higher Q-values, the decaying coherent intensities become of the same order of magnitude as the incoherent term, with the coherent term falling underneath the incoherent term around  $0.25 - 0.30 \text{ \AA}^{-1}$  (fig. 1b-c). The situation of a clear predominance of the incoherent term is, however, never observed, the two terms playing alternating roles for  $Q > 0.3 \text{ \AA}^{-1}$  due to the oscillations of the structure factor (fig. 1c).

Figure 2 depicts for  $0.15 < Q < 2.35 \text{ \AA}^{-1}$  the results obtained for powders of a per-deuterated protein, such as the ones usually employed in protein hydration water dynamics investigations. The maxima and minima observed in the structure factors (fig. 2a) are consistent with previous results. The amplitude of the oscillations appears reduced for the hydrated powder due to the overall reduction in the coherent scattering power of the sample. Conversely, below  $0.60 \text{ \AA}^{-1}$ , an increase of the coherent scattering is observed due to the H<sub>2</sub>O hydration layer around the protein.

As for the fractions of coherent and incoherent scattering (fig. 2b), two aspects are worth mentioning: First, the incoherent term supersedes the coherent, both for the dry and hydrated powder for  $Q > 0.60 \text{ \AA}^{-1}$ . However the two terms are of the same order of magnitude. In addition, it

should be noted that only about 55 % of the total scattering corresponds to incoherent scattering from the hydrated layer of the protein. Second, for the hydrated sample and for  $Q < 0.60 \text{ \AA}^{-1}$ , the coherent term increasingly dominates the scattering signal, coming above the incoherent term for  $Q < 0.30 \text{ \AA}^{-1}$ . Such a change must, therefore, necessarily be taken into account when interpreting dynamic neutron scattering results collected over this Q-range, especially if Q-dependent effects are under consideration.

## Mixture of coherent and incoherent scattering

Polarization analysis allowed for the successful separation of the coherent and incoherent scattering from different protein samples, over a wide range of Q-values. The results obtained show, for all the samples investigated, that the situation of a clear predominance of the incoherent term, to the extent that the coherent scattering can be neglected, is never observed. Hence, when interpreting results of dynamic neutron scattering experiments one should bear in mind that a mixture of coherent and incoherent scattering is present. Undertaking quasielastic scattering experiments with polarization analysis appears as a natural and promising step forward in these investigations.

[1] A. M. Gaspar et al., *Biochim. Biophys. Acta*, 1804, 76 (2010).

[2] R. M. Moon et al., *Phys. Rev.*, 181, 920 (1969).

[3] O. Schärpf, *Physica B*, 182, 376 (1982).

# High sensitive analysis of intermetallic layers using a positron beam

P. Pikart<sup>1,2</sup>, C. Hugenschmidt<sup>1,2</sup>, K. Schreckenbach<sup>1,2</sup>

<sup>1</sup>Technische Universität München, Physik Department E21, Garching, Germany

<sup>2</sup>Technische Universität München, Forschungs-Neutronenquelle Heinz Maier-Leibnitz (FRM II), Garching, Germany

Positron annihilation spectroscopy is widely used as a non-destructive technique in material science due to its high sensitivity to lattice defects in the volume of the sample. Furthermore, embedded layers and clusters of low concentration can also be detected with positrons. For these studies, the element dependent positron affinity is an essential value for the sensitivity of the measurement. For pure elements, these affinities are known from theoretical calculations, but there are few experimental results reported as yet. In this experiment, the influence of the positron affinity on the sensitivity of this technique is systematically studied.

## Coincident Doppler Broadening (CDB)

When a positron is implanted into a sample, it rapidly thermalizes at a mean implantation depth set by material parameters and the positron energy. After thermalization, the positron can be trapped and annihilates with an electron of the sample. Because the momentum of the thermalized positron is much lower than the mean

momentum of the electrons, the Doppler-Broadening of the annihilation radiation is defined by the momentum distribution of the annihilated electrons. This distribution is therefore characteristic for different elements and defect types. Consequently, by a precise measurement of the Doppler-broadened 511 keV-annihilation line at the CDB-Spektrometer of the NEPOMUC beamline, it is possible to analyze the annihilation site for chemical composition.

## Layers of different elements on aluminium

In the sample volume, regions of higher positron affinity form a potential well and can trap the thermally diffusing positron. Hence, the sensitivity for clusters of a high affinity is greatly enhanced [1]. At the Paul Scherrer Institute in Villigen a systematic study of this effect using layers of different elements of various thickness grown on an aluminium substrate and covered with an aluminium layer of constant thickness were undertaken. This covering layer allows the positrons to be preferentially implanted at the depth of the intermediate layer.

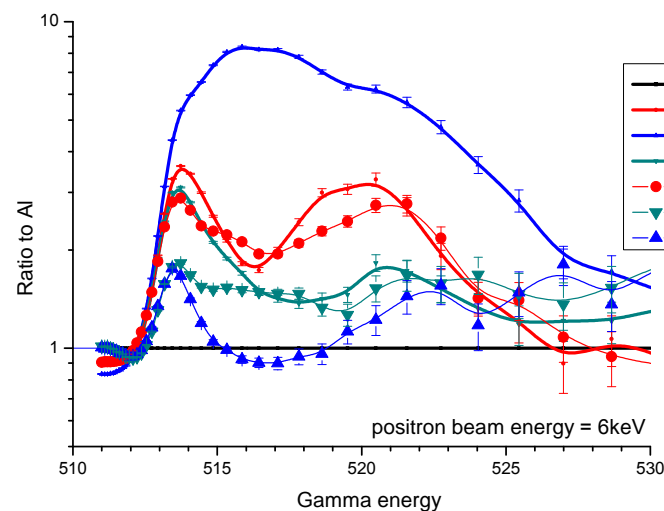


Figure 1: Coincident Doppler spectra of reference materials (thick lines) and layered samples with 100nm intermediate films (thin lines). All curves are normalized to the aluminium reference.

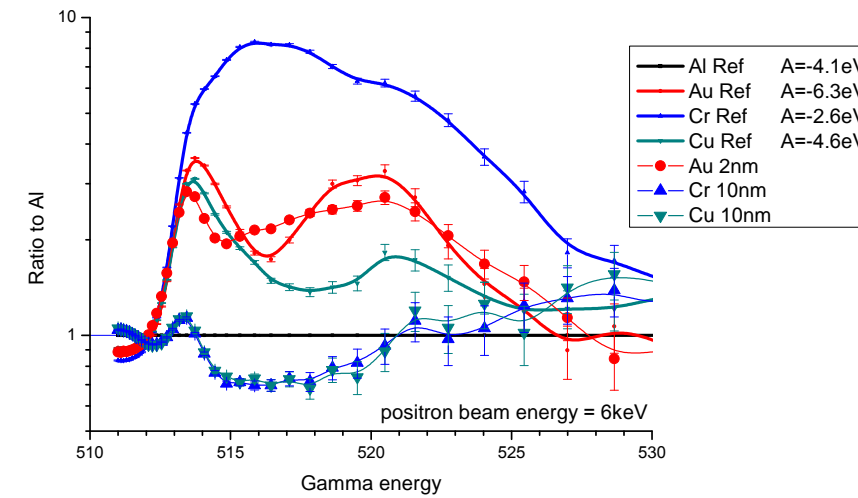


Figure 2: The same as fig. 1 with thin intermediate layers.

## CDB measurements

In the layered samples, it is of interest to establish whether the positron is trapped and annihilates in the intermediate layer or in the aluminium substrate. Therefore, reference data of the elements used have been recorded with annealed samples of high purity (> 99.99 %). The data obtained are normalized to the spectrum of the aluminium reference, which is shown as a baseline in the resulting spectrum (figs. 1 and 2). Due to this normalization, the element specific shapes of the references become visible and are shown as the thick lines in the graphs. All materials proved to be clearly distinguishable.

Figure 1 shows a set of samples with a thick intermediate layer of 100 nm of gold, copper and chrome, respectively. The positron energy was set to 6 keV so that the mean implantation depth of the positrons was 220 nm in a pure aluminium substrate and so the implantation profile overlap with the layer was maximized. As expected, the signature of gold and copper becomes clearly visible, as the largest fraction of the positrons is implanted in the layer, and the positron affinity ratio does not allow diffusion of positrons out of the layer. A different picture is seen at the chrome layer, which has a positron affinity of 1.5 eV higher than the substrate. This results in a diffusion process of the positrons out of the layer, so that practically no chrome signature can be detected.

Figure 2 shows samples with a very thin intermediate layer. Now, the signature of chrome vanishes totally, and only the influence of defects caused by the lattice mismatch between chrome and aluminium is visible. The same situation is visible for copper, which has nearly the same af-

finity as aluminium. However, for gold, with its high affinity, a layer of only 2 nm is clearly visible, although implantation calculations show that only 2.7 % of the positrons are implanted directly into the layer. This is explained by the diffusion of the positrons after the implantation, which leads to an effective trapping in the potential well formed by the gold layer.

## Unique method for highly sensitive measurements

This measurement on thin metallic layers is fundamental for the application of the CDB-technique in material sciences. Many experiments with positrons on binary metallic alloys have already been performed. However, it is still challenging to obtain quantitative results because there is little experimental data about the trapping by metallic clusters available. The measurements presented show the high suitability of layered systems to systematic studies, and confirm the influence of theoretically calculated positron affinities on the sensitivity of the measurement. In further measurements, the energy of the incident positron beam will be varied during the measurement, so that positron diffusion lengths become visible. Also a heatable sample holder will be mounted to induce growth of precipitations, which should be observed in the non-deformed, undisturbed volume of the metallic sample. In the light of these developments, CDBS using a monoenergetic positron beam has been established as a unique method for selective and highly sensitive measurements on embedded structures of appropriate positron affinity.

[1] C. Hugenschmidt et al., Phys. Rev. B, 77, 092105 (2008).

# Positron Age Momentum Correlation (AMOC) measurements on thin SiO<sub>2</sub> layers

B. Löwe<sup>1</sup>, W. Egger<sup>1</sup>, G. Kögel<sup>1</sup>, L. Ravelli<sup>1</sup>, P. Sperr<sup>1</sup>, C. Hugenschmidt<sup>2,3</sup>, G. Dollinger<sup>1</sup>

<sup>1</sup>Universität der Bundeswehr München, Institut für Angewandte Physik und Messtechnik (LRT 2), Neubiberg, Germany

<sup>2</sup>Technische Universität München, Forschungs-Neutronenquelle Heinz Maier-Leibnitz (FRM II), Garching, Germany

<sup>3</sup>Technische Universität München, Physik Department E21, Garching, Germany

In 2009, a new measurement technique was set up at the pulsed positron beam experiment PLEPS. The AMOC technique provides correlated information about the positron lifetime and the electron momentum in the sample. First measurements on differently manufactured thin SiO<sub>2</sub> layers were performed.

Positron Annihilation Lifetime Spectroscopy (PALS) is an established method of measuring the type and concentration of vacancy defects in solid states. Positrons that have been implanted into a solid are very sensitive to negatively charged vacancy defects and can become trapped in these potential wells. Due to the reduced electron density in these vacancies, the positrons exhibit a longer lifetime than in the volume before they annihilate with an electron into, in most cases, two gamma quanta, with an

energy of about 511 keV each. For usual lifetime measurements using PLEPS (Pulsed Low Energy Positron System), only one gamma quantum is detected. PALS measurements have been carried out in routine operation with PLEPS at FRM II since June 2008 [1].

In contrast to PALS, Doppler Broadening Spectroscopy (DBS) is based on the measurement of the energy of the annihilation radiation. Due to the momentum of the electron that annihilates with the positron the energies of the two gammas are shifted to lower and higher values, leading to the so-called Doppler Broadening of the 511 keV annihilation peak. To characterize the broadened peak, two parameters are commonly used: the S and the W parameter (fig. 1). The S parameter is a measure of annihilations with low momentum (valence) electrons, whereas the W parameter shows the annihilation rate with intermediate to high momentum (core) electrons and is therefore

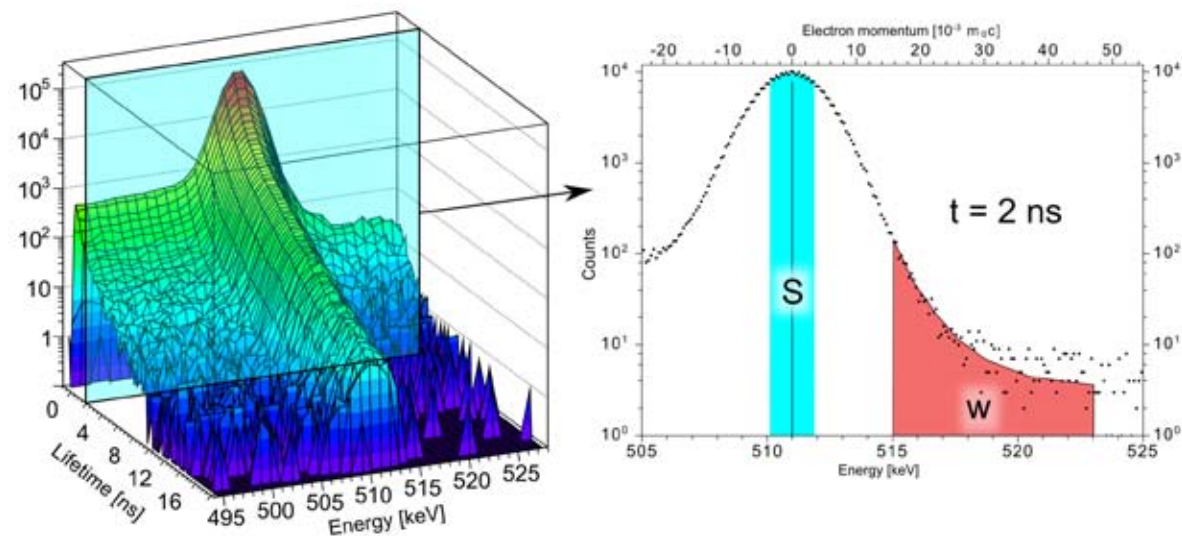


Figure 1: Left: AMOC spectrum of the vapour deposited SiO<sub>2</sub> layer. Right: Slice through the AMOC spectrum at 2 ns. The S and W parameter are calculated as the ratio of the integral of the respectively marked regions to the total peak integral.

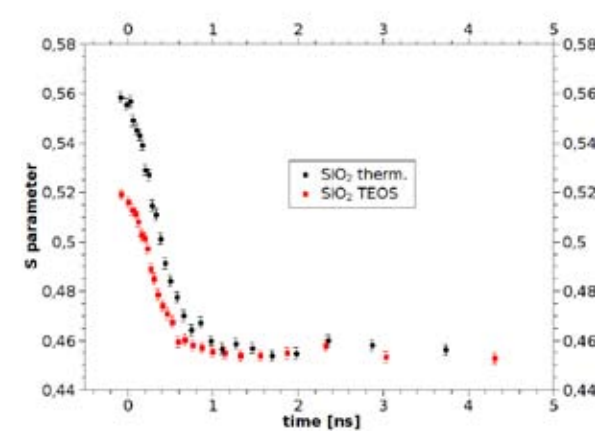


Figure 2a: S parameter as a function of the positron lifetime.

a measure for the chemical environment of the annihilation location. Transversal electron momentum components lead to a deviation from the 180° emission angle between the two emitted gammas that can be measured by angular correlation of annihilation radiation (ACAR).

In a 2D age-momentum correlation (AMOC) measurement, the lifetime of the positron and the energy of the annihilation radiation is registered for each annihilation event and a two dimensional AMOC spectrum is generated (fig. 1). This has the advantage that AMOC can reveal the chemical environment of a specific defect, which is hardly possible with separate PALS and DBS measurements. A 2D AMOC system has recently been installed at the PLEPS system.

The annihilation radiation is detected by two detectors, installed at two opposing ports at the sample chamber of PLEPS. The lifetime is obtained using BaF<sub>2</sub> scintillation detector by measuring the time difference between the implantation time, which is determined by the pulsing system, and the annihilation time. The second detector, a high purity germanium detector, measures the energy of the other gamma quantum of the same event. All events are stored on a PC for later off-line analysis.

With this setup, two differently manufactured 100 nm thin SiO<sub>2</sub> layers on a Si substrate were measured. The first sample (SiO<sub>2</sub>-therm.) has been thermally grown, whereas the second sample (SiO<sub>2</sub>-TEOS) was produced by chemical vapour deposition (CVD) of tetraethylorthosilicate (TEOS). The energy of the positrons was

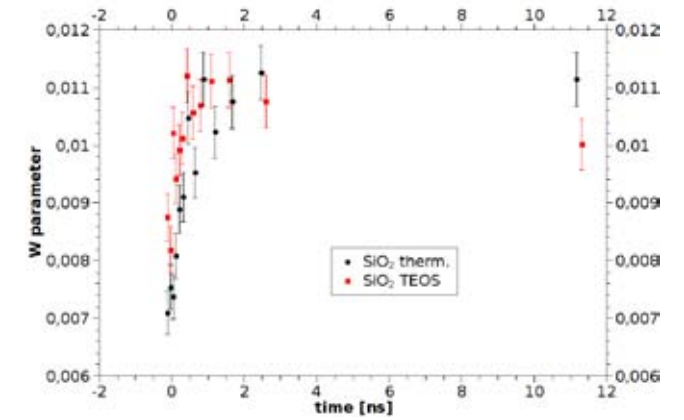


Figure 2b: W parameter as a function of the positron lifetime.

set to 2 keV to implant positrons into the oxide layer only. Figure 1 shows the AMOC spectrum of SiO<sub>2</sub>-TEOS and a slice through it at 2 ns. Figure 2a shows the S parameter as a function of the positron lifetime of both samples. The high fraction of annihilations with low momentum electrons (high S parameter) at short positron lifetimes is due to singlet positronium creation in the sample. Annihilations at lifetimes larger than 3 ns only arise from triplet positronium annihilation. Figure 2b shows the W parameter as a function of the lifetime. The difference in the W parameter at longer lifetimes is a strong indicator of different chemical environments at the annihilation location in both samples.

In summary, AMOC has been successfully implemented as a new special feature of PLEPS, available to users as an additional tool which allows enhanced identification of defects and its related chemical environment. To reduce measurement time and increase statistics it is planned to install detectors with greater efficiency.

In addition, a combination of a segmented germanium detector with a pixelated photomultiplier-scintillator is envisaged to run 4D-AMOC measurements, including angular correlation analysis. Thus, a complete 3D electron momentum reconstruction becomes possible in correlation with positron lifetime for each detected event.

[1] P. Sperr et al., Appl. Surf. Sci., 255, 35 (2008).

# Technical developments for instruments

K. Zeitelhack<sup>1</sup>, J. Peters<sup>1</sup>, G. Borchert<sup>1</sup>, J. Krüger<sup>1</sup>, J. Neuhaus<sup>1</sup>

<sup>1</sup>Technische Universität München, Forschungs-Neutronenquelle Heinz Maier-Leibnitz (FRM II), Garching, Germany

At the FRM II, central service groups support the technical development and the operation of the instruments in all kinds of areas. The detector and electronics group, the sample environment group, neutron optics as well as IT infrastructure and software development, which comprise 30 staff members in total. Major achievements include the completion of the large small angle scattering detector for the SANS-1 instrument, new equipment for sample environment for soft matter experiments, building <sup>3</sup>He-cells and the coating of super mirrors as well as more powerful software for instrument control and organisation.

## New detectors

The largest detector so far constructed at the FRM II is the 1 x 1 m<sup>2</sup> detector used for the small angle scattering instrument SANS-1. It consists of 128 individual 1 m long position sensitive pro-

portional counters (PSD) with 8 mm diameter. In 2009 they were qualified, assembled and tested in detail, the electronics included. The final commissioning at the instrument is foreseen for spring 2010. The individual detectors showed a high homogeneity in respect of the efficiency and position resolution. Figure 1 shows the resulting 2-dimensional position spectrum when the full size detector is illuminated with neutrons from a <sup>252</sup>Cf-source. Three 20 mm wide straight Cd-bars mounted in front of the detector are used to calibrate the position response of the 128 individual PSDs.

Based on the development program MILAND of the NMI3 consortium in the framework program 6 of the European Union, a new multi-wire detector for the instrument STRESS-SPEC is under development. The high spatial resolution of around 1 x 1 mm<sup>2</sup> is achieved via a single wire readout technique using special digital electronics developed at the FRM II. Several small size prototypes have been built in order to define all characteristic properties of the neutron detector. Designing and building the final detector will be the task for next year.

In a joint collaboration of six research groups, the FRM II is actively involved in the development of new detector technologies based on Gaseous Scintillation Proportional Counters (GSPC). Instead of using the electric charge produced in the neutron absorption in a <sup>3</sup>He-CF<sub>4</sub> gas, the scintil-

Figure 1: Two-dimensional position spectrum of the 1x1m<sup>2</sup> SANS-1 detector illuminated with neutrons from a <sup>252</sup>Cf-source. Three straight Cd-bars mounted in front of the detector were used to calibrate the position response of the 128 individual PSDs.

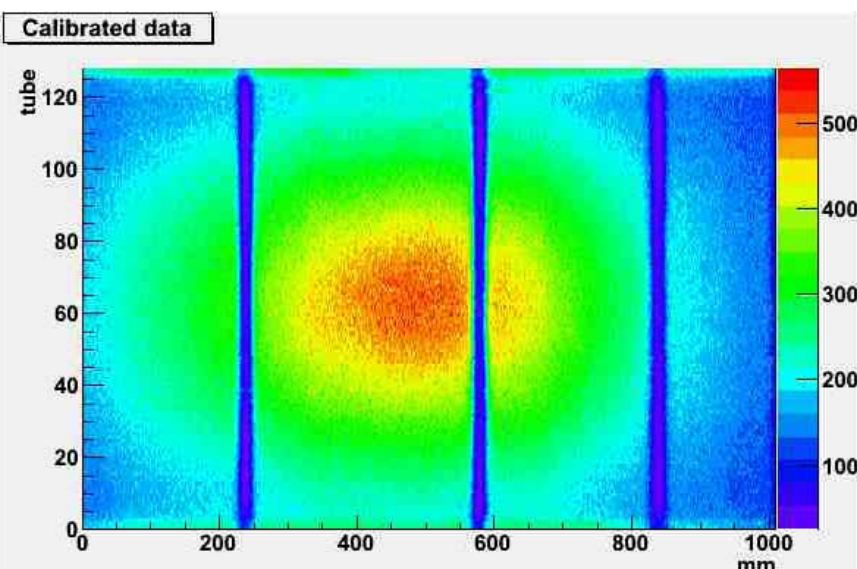


Figure 3: Liquid-cooling free cryostat (front) to be mounted in the high pressure machine (back).

lation light emitted in the amplification process will be used for detection. The major advantage anticipated from this new technique is the high light output which exceeds the photon yield of conventional scintillators by more than an order of magnitude, and also the very short duration, less than 100 ns, of the light pulses. This technology could enable the design of detectors with superior performance in view of its high counting rate capability, position resolution and low gamma-ray sensitivity. For the first tests, three identical small size detectors have been constructed at the FRM II to develop the readout electronics.

## Conditioning sample parameters

Of the 4 parameters, temperature, pressure, magnetic field and stress, routinely varied on

measured samples at the FRM II, temperature is still the most frequently requested. The number of top-loading liquid cooling free cryostats is still increasing and a larger one having an 80 mm diameter free space for the sample volume was taken into operation in 2009. The buy out of a small company near Garching, which developed these systems in collaboration with our own group, has led us to the decision to build new cryostats ourselves in the future. The base temperature of about 3 K is routinely extended down to 500 mK using <sup>3</sup>He-inserts. After a time-consuming optimisation of the cooling down time using a demixing <sup>3</sup>He-<sup>4</sup>He-chamber, low temperatures of 50 mK are now available for user experiments.

Varying several parameters simultaneously is even more challenging, especially to combine temperature with pressure. So far, pressure has been applied to a sample in a pressure cell at room temperature, which could subsequently be mounted in a cryostat to achieve low temperatures. With a newly designed setup, the pressure can even be changed at temperatures as low as 20 K during an experiment. A powerful 1.5 W cold head is attached to a pressure transmitting piston which is mounted inside the hydraulic press which loads up to 50 tonnes.

Several experiments requiring gas absorption equipment have been set up in 2009 in close collaboration with external users. Upon request, further equipment can be provided at short notice. The absorption of gas can even be achieved at the lowest temperatures.

Two inert gas filling boxes for sample cans have been installed in the neutron guide hall, as well as in the experimental hall. They will serve our users



Figure 2: Test detectors for developing Gaseous Scintillation Proportional Counters.

when handling oxygen sensitive sample material or improve thermal contacts by using He-gas inside the sample cans, for low temperature experiments. As these glove boxes are placed on wheels, the work can be done quite comfortably near the experimental area of the instrument.

#### Instrument control and software development

In collaboration with the sample environment group, mobile devices will be gathered with a common software interface, i.e. the sample environment devices will be joined to a software system which reduces the effort of integration to the different instruments. This long lasting idea, known as Taco-boxes, will be realised using newly available, rugged, computing hardware.

The widely used Taco-system for instrument control at the FRM II will be replaced by its successor Tango, developed at the ESRF in Grenoble. A major effort has been invested to programming the new communication interfaces and servers which will allow one to overcome the drawbacks

of the so far simplified communication between the numerous hardware devices installed at one instrument.

Besides the instrument control, much work has been done to rebuild the user office software. In a joint collaboration of 5 research facilities, the Digital User Office developed at the Paul Scherrer Institut in Switzerland served as a basis for the new integrated work flow software. It will be taken into operation in 2010.

#### Conditioning neutron beams

Building up new instruments in the guide hall always involves the neutron optics group in extending or modifying the neutron guide system. For the new reflectometer MARIA of the JCNS, the guide system has been extended from the velocity selector to the sample area. The option to use polarized neutrons on MARIA requires mounting and adjusting 4 guide sections, two polarising and alternatively, two non-polarising sections. For the new diffractometer for protein crystallography BIODIFF, the existing neutron guide NL1 had to be modified. An open section has been cut into the guide to incorporate the graphite monochromator of the new instrument.

Sometimes, repairing the existing system is even more challenging than building new components, especially if the work is pressed for time. During the first maintenance period in 2009, the o-ring gasket of the neutron windows of beam tube 1 showed a leak. All instruments of the neutron guide hall are fed with neutrons by this beam tube. In order to access the seals, the first 8,5 m of the six neutron guides had to be unmounted and the big shutter pulled out from the reactor wall. After changing the o-rings, all guides had to be reinstalled. This challenge was managed within only 13 working days in close collaboration with the mechanical work shop and the construction group.

To replace some of the guides in the neutron tunnel, super mirrors with an area of 20 m<sup>2</sup> and reflectivities up to  $m = 3$  were coated. A high quality having reflectivities above 90 % at  $m = 2$  and 80 % at  $m = 3.5$  were achieved routinely on glass substrates and silicon wafers. The quality control of the super mirrors is monitored using neutrons at the instrument TREFF. This test and



Figure 4: New mobile glove boxes available in the experimental areas.

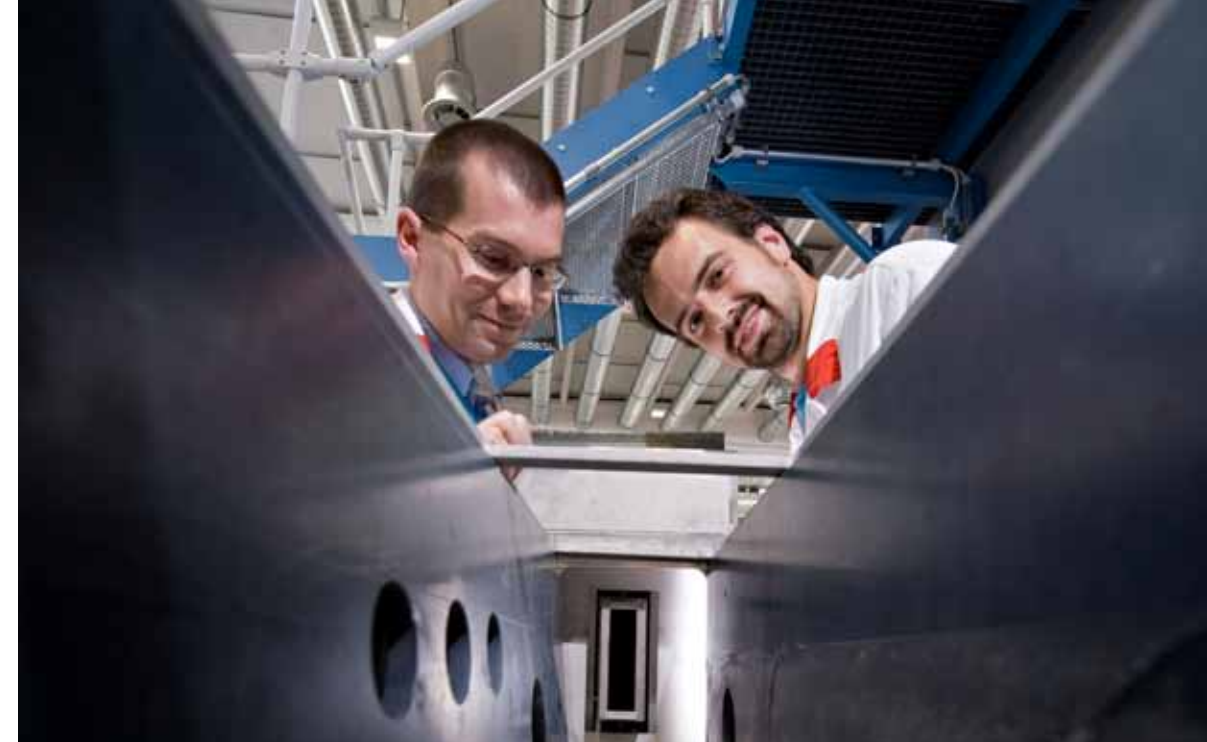


Figure 5: Installing neutron guides for MARIA.

development machine has got a new control cabin on top of to the new small angle scattering instrument SANS-1, together with an optimised moving detector now reaching scattering angles of more than 90 degrees.

Continuous development of <sup>3</sup>He-filter cells to produce polarized neutron beams or to analyze the polarisation has lead to a significant improvement in the operation time of these filter cells. To achieve a reasonable flipping ratio, i.e. to measure the difference of the scattering for different

polarization directions of the neutron beam, cells with a decay time of up to 270 hours have been used. A large variety of different experiments was performed using the <sup>3</sup>He-filter cells, including imaging (ANTARES), reflectometry (N-REX<sup>+</sup>) and structural research (HEiDi). To improve the service for refilling the filter cells, a new transportation device with better magnetic field homogeneity has been designed and fabricated.

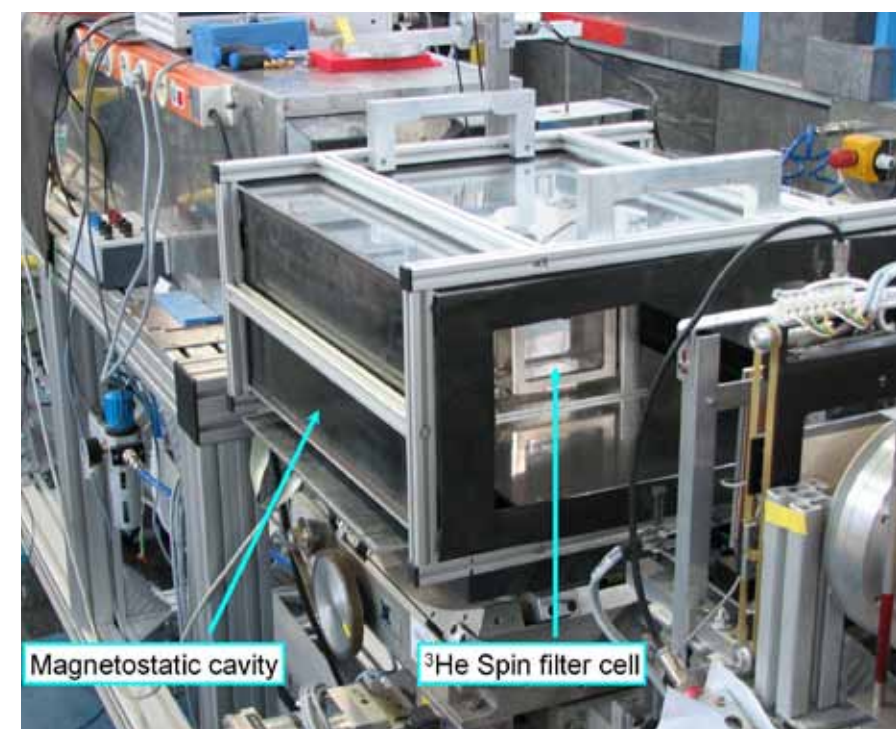


Figure 6: <sup>3</sup>He-filter cells on the instrument TREFF measuring the neutron beam polarization.

A commercial rechargeable lithium-ion battery is examined at the neutron powder diffractometer SPODI.

## Scientific Highlights



# 3

# A study of the denaturation of horse heart met-myoglobin by chemical agents using SANS

<sup>1</sup>M.-S. Appavou, <sup>2</sup>D. Richter

<sup>1</sup>Forschungszentrum Jülich GmbH, Jülich Centre for Neutron Science at FRM II, Garching, Germany

<sup>2</sup>Forschungszentrum Jülich GmbH, Institut für Festkörperforschung, Jülich, Germany

Within the framework of trying to understand the folding of proteins, we investigated the mainly helical structured myoglobin. Guanidinium hydrochloride at various concentrations was used as denaturing agent in order to trap some of the folding intermediates of this protein. Small angle neutron scattering (SANS) allows one to characterize these intermediates by applying polymer physics theory: by the extrapolated radius of gyration in the Guinier regime, the intermolecular interactions using the Zimm approximation and the Kratky representation of the scattered intensity.

## Understanding the folding of proteins

Proteins can be considered as heteropolymers composed of a sequence of amino acid residues which have different chemical properties. According to their position along the backbone and the presence of hydrogen bonds, they induce a specific folding related to the function of the pro-

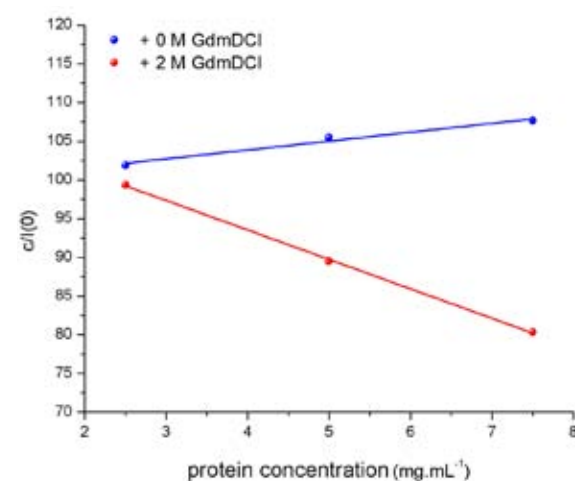


Figure 1: Zimm representation ( $c/I(0) = f(c)$ ) for myoglobin in the native (+ 0 M GdmDCI) and fully denaturated state (+ 2 M GdmDCI).

tein. From a medical point of view, it was shown that degenerative diseases such as Alzheimer's originate from a misfolding of some proteins which aggregate around some brain receptors. In our attempt to understand the folding of proteins, we have investigated the unfolding of a model protein: the horse heart myoglobin using SANS techniques and applying polymer physics theory.

## Trapping the intermediate states

Small angle neutron scattering experiments using the JCNS-KWS-2 diffractometer were performed at room temperature and at atmospheric pressure using a 4.5 Å wavelength and two detector distances : 2 m and 8 m. It is then possible to investigate a  $q$ -range from  $1.10^{-2}$  to  $0.32 \text{ \AA}^{-1}$ . A myoglobin solution in a deuterated phosphate buffer 100 mM pD 7.0 was prepared in a dilute regime (2.5 to 7.5 mg/mL) in order to extrapolate the radius of gyration at null concentration. We added an increasing concentration of deuterated guanidinium hydrochloride into these solutions as a denaturing agent in order to trap the intermediate folding state of the protein. The radius of gyration  $R_g$  and forward intensity  $I(0)$  were extracted from a fit of the scattering patterns in the Guinier regime using the Guinier approximation for the native myoglobin and the Debye approximation for the denatured myoglobin.

## Hydrophobic interactions exposed

From the Guinier regime investigation, we observed an increase in the radius of gyration extrapolated to null concentration, as long as chemical denaturing agent was added to the protein solution. We recovered a radius of gyration of  $13.5 \pm 1.0 \text{ \AA}$  in the native state, values which are in agreement with those found in

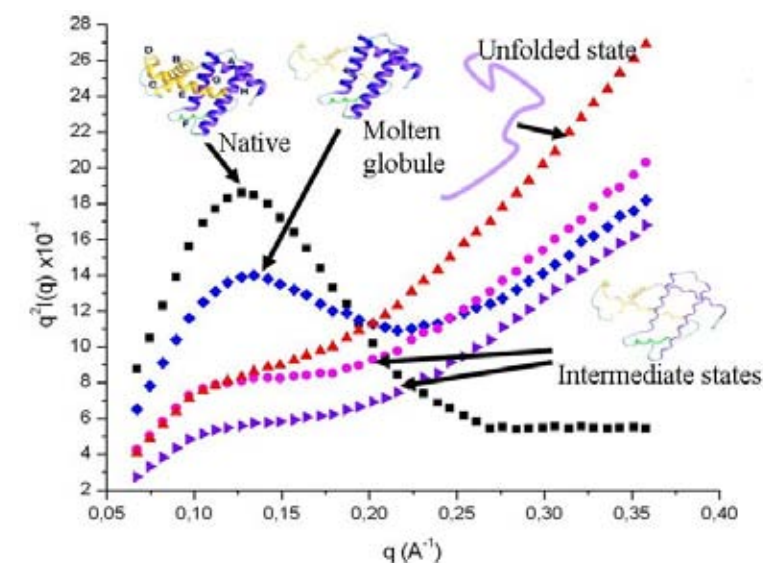


Figure 2: Kratky representation of the intensity signal for myoglobin in solution at 10 mg/mL at several concentrations of GdmDCI. Black square : 0 M GdmDCI, blue diamonds: 1.2 M GdmDCI, violet triangle: 1.5 M GdmDCI, pink full circle: 1.8 M GdmDCI, red triangle: 2 M GdmDCI.

the literature and by simulation. We obtained a radius of gyration of  $32.5 \pm 2.0 \text{ \AA}$  in the presence of 2 M GdmDCI corresponding to an unfolded myoglobin.

From the forward intensities and using the Zimm approximation, we were able to extract the second virial coefficient relating to intermolecular interactions. Zimm plots for myoglobin in the native and fully denaturated state are shown in figure 1. We observed repulsive interactions in the native state and GdmDCI inducing the unfolding of the protein leads to attractive interactions by exposing some hydrophobic residues usually buried in the protein. Proteins tend to congregate, leading to some aggregation phenomena for higher protein concentrations. Large  $q$ -range measurements allow us to glean information about the shape of the protein as a function of the denaturing agent concentration. Figure 2 shows the Kratky representation of the scattered intensity for each GdmDCI concentration condition. As presented in figure 2, the Kratky representation shows evidence of the effect of the guanidinium hydrochloride on myoglobine structure. It is possible to assign a protein intermediate folding state description to some typical polymer behaviour. Thus, from a bell-shaped spectrum characteristic of a native globular molecule, we can distinguish one kind of molten globule which starts to exhibit a Gaussian-like behaviour (plateau) until a fully unfolded protein behaving like a polymer in a good solvent (proportionality as a function of  $q$ ) is formed.

## Fully unfolded protein behaving like a polymer

We were able to trap some intermediate folding states of a model protein, myoglobin, using

a chemical denaturing agent and investigated them using small angle neutron scattering and applying polymer theory. In the low  $q$ -range (Guinier Regime), we have gained a value of radius of gyration in agreement with those in the literature. On increasing the denaturing agent concentration, we observed an increase of the  $R_g$  from  $13.5 \pm 1.0 \text{ \AA}$  in the native state to  $32.5 \pm 2.0 \text{ \AA}$  for the fully denaturated protein. From the forward intensities, information related to intermolecular interactions shows a change from repulsive, for the native protein, to attractive intermolecular interactions, for the denatured protein, as long as some GdmDCI was added. Indeed, some residues usually buried near the core of the protein are exposed and then tend to recover their initial environment by congregating with the other unfolded molecules. This leads to some aggregation phenomena for high protein concentration. In the larger  $q$ -range, the Kratky representation describes the different folding states of myoglobin as a compact globular molecule in its native state, a molten globule state with a larger radius of gyration and a behaviour somewhere between a native compact globular molecule and a Gaussian chain. The intermediate folding state was found at the mid-point denaturation and resembles a Gaussian chain with an even larger radius of gyration and starts to behave like a polymer like molecule. The early stage folding state seems to display the same behaviour as the intermediate folding state. The fully unfolded protein has a similar behaviour to a polymer in good solvent. This is essentially due to electrostatic interactions between the GdmDCI and the protein.

# Study of homogeneous lipid coatings on implant surface materials

R. Willumeit<sup>1</sup>, V. Haramus<sup>1</sup>, A. Schreyer<sup>1</sup>, J.-F. Moulin<sup>1,2</sup>

<sup>1</sup>GKSS-Forschungszentrum Geesthacht, Institut für Werkstofforschung, Geesthacht, Germany

<sup>2</sup>Technische Universität München, Forschungs-Neutronenquelle Heinz Maier-Leibnitz (FRM II), Garching, Germany

Titanium and its alloys are the preferred materials for medical implant applications. Phospholipid coatings of the titanium surfaces have been shown to improve biocompatibility. In previous studies at REFSANS, we elucidated the thickness and structure of lipid films prepared by casting from a chloroform/methanol solution. Here, we present the first analysis of a spin coated specimen which give a more homogeneous and better defined lipid coating, resulting in 5 to 10 lipid bilayers attached to the surface.

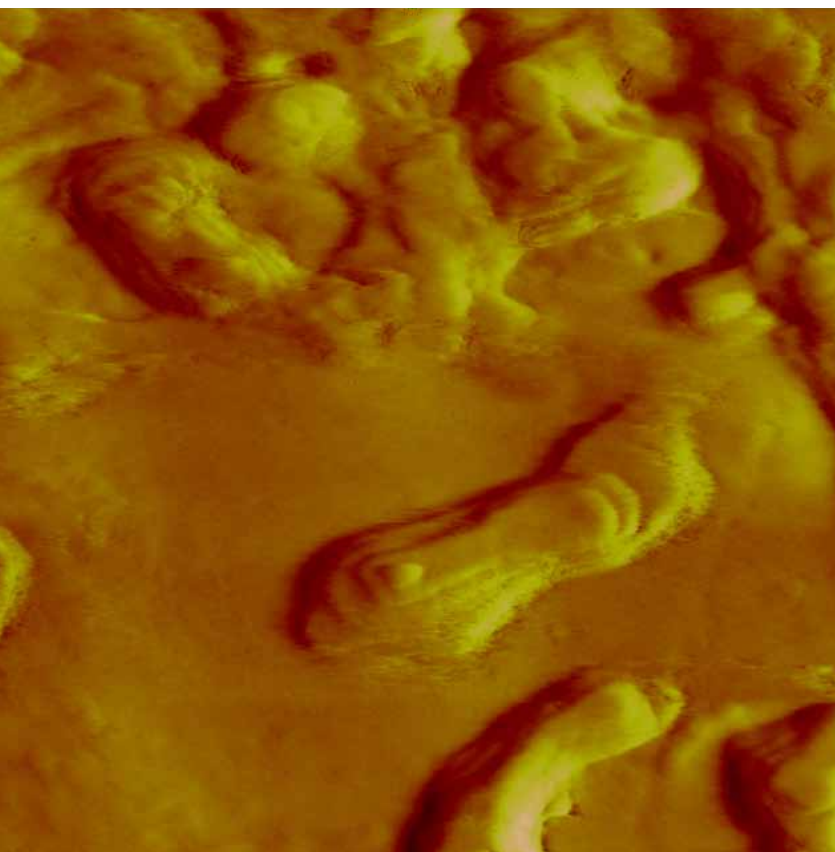


Figure 1: AFM image (5 x 5 micron) of a drop cast POPE sample showing a large phospholipid island.

## Metallic implants coated with cell membrane

Permanent implants such as metallic hip prostheses are widely used and successfully implemented in medicine. Due to modifications of the material properties, design and optimisation of a variety of surface parameters, the durability of these implants has been significantly improved. However, a lifetime of more than 20 years is hardly ever achieved.

Many attempts have been made to develop new implant surface modifications which may prolong the life span of an implant, or shorten the recovery time of a patient by quicker and more stable implant incorporation. Among them are attempts to cover the metallic implants with hydroxylapatite [1], or with peptide or proteins (adhesion sequences such as 'Arg-Asp-Gly' (RGD), collagen, growth factors; [2, 3, 4]), or to produce a nanostructured surface.

In our group, an alternative approach is proposed and discussed: the use of a cell biomembrane mimic. Cell membranes consist of approximately 60 % proteins and 40 % lipids. The importance of proteins is widely accepted, while the role of lipid layers is not fully acknowledged.

In several studies we showed as a proof of principle that even a simple model phospholipid membrane system can significantly influence the cell behaviour of metallic biomaterials. Several phospholipids were chosen, among them POPE (palmitoyl-oleoyl-phosphatidyl-ethanolamine). This phospholipid has been shown to be essential for cytokinesis [5], but further physiological functions are not known. It also shows interesting biophysical properties (such as the formation of an inverse hexagonal phase) and is found in

small amounts in erythrocyte membranes. Our lipid coatings are so far not covalently linked to the surface as the preparation is based on the self assembly of multilamellar lipid layers by evaporation of a solvent. To date, the only hint of the persistence of a lipid film on the surface, even after exposure to water or a growth medium derives from the modified cell reaction on these substrates. We have thus undertaken a scattering study of these substrates and their modifications. The first step of this study was to establish a coating protocol reproducibly leading to homogeneous layers of well-defined thickness and structure.

## Coating the samples

Titanium alloy ( $Ti_6Al_7Nb$ ) was sputter coated on the silicon substrates with a nominal layer thickness around 100 nm. Our previous experiments were performed on relatively small samples (ca. 20 x 40 mm<sup>2</sup>) and a special effort was made here to deliver larger substrates in order to both maximize the available signal in a scattering experiment and achieve the best possible homogeneity by use of spin coating. Our new sputtering setup allows the routine substrates of 100 x 50 mm<sup>2</sup>. The experiment described hereafter was performed on 50 x 50 mm<sup>2</sup> samples. Phospholipid thin films were then spin coated from 1-palmitoyl-2-oleoyl-sn-glycero-3-phospho-ethanolamine (POPE) solution in chloroform : methanol (80 : 20).

## Spin coating leads to more homogenous films

By neutron reflectometry (NR) we first assess the quality of our large Ti alloy layers. These measurements indicated that the mirrors were produced with as good a quality as the much smaller samples used in the preliminary study. The layer thickness was 100 nm with low roughness. (c.a. 0.5 nm). We then compared the spin coated and drop cast POPE overlayers. In the case of the drop cast samples, thick patches of POPE were observed by atomic force microscopy (AFM) (fig. 1) and NR displayed a Bragg peak around 0.15 Å<sup>-1</sup>. Reflectometry on the spin coated POPE overlayer showed the presence of a film of ca. 100 Å and no Bragg peak was observed for the spin coated layers (fig. 2).

The drop casting method leads to the formation of very irregular films showing material accumu-

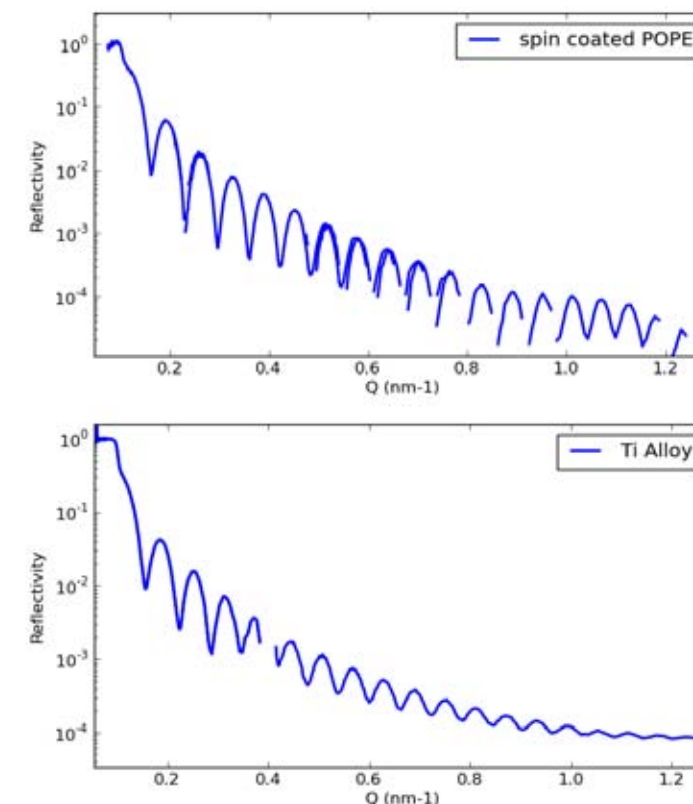


Figure 2 : Neutron reflectometry curves obtained for the Ti alloy substrate and the spin coated POPE.

lation patches of high thickness, which are responsible of the Bragg signal. In contrast with this technique, spin coating leads to much more homogeneous films of rather low thickness.

These samples with well controlled morphology will be used for further investigation of the cell growth behaviour.

- [1] J. S. Chen et al., J. Mater. Sci.: Mater. Med., 9, 297 (1998).
- [2] K. Emoto et al., J. Biol. Chem., 280 (45), 37901 (2005).
- [3] H. P. Jennissen et al., Mat.-wiss. u. Werkstofftech., 30, 838 (1999).
- [4] M. Otto et al., J. Mater. Sci.: Mater. Med., 15, 35 (2004).
- [5] S. Roessler et al., J. Mater. Sci.: Mater. Med., 12, 871 (2001).
- [6] R. Willumeit et al., J. Mater. Sci.: Mater. Med., 18, 367 (2007).

# Infiltration of a conducting polymer into a mesoporous TiO<sub>2</sub> network

G. Kaune<sup>1</sup>, M. Haese-Seiller<sup>2</sup>, R. Kampmann<sup>2</sup>, J.-F. Moulin<sup>2</sup>, P. Müller-Buschbaum<sup>1</sup>

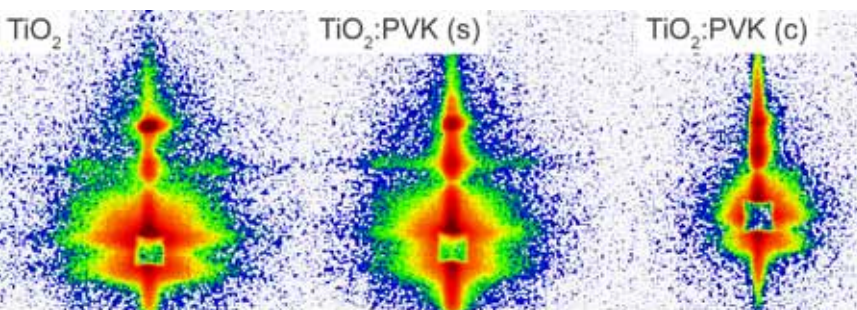
<sup>1</sup>Technische Universität München, Physik Department E13, Garching, Germany

<sup>2</sup>GKSS-Forschungszentrum Geesthacht, Institut für Werkstofforschung, Geesthacht, Germany

To construct an efficiently working hybrid solar cell, a mesoporous network of an inorganic semiconductor must be completely filled with a hole conducting material. We infiltrated the conductive polymer poly(N-vinylcarbazole) into a porous TiO<sub>2</sub> network and investigated the resulting composite film structure with grazing incidence small-angle neutron scattering at REFSANS. The data show a good penetration and high degree of pore filling when the polymer is solution cast into TiO<sub>2</sub>, and only low penetration when spin coating is applied.

In the past few years the application of nanostructured titanium dioxide (TiO<sub>2</sub>) in photovoltaic devices has become a topic of enormous interest. A typical TiO<sub>2</sub> solar cell consists of a mesoporous network, which is coated with a light absorbing dye and then filled with an organic semiconducting material [1]. Since charge generation occurs only at the interface between the two components, the interface between them must be maximized. Consequently, it is of utmost importance that the transport material completely penetrates the pore structure and exploits the whole volume.

To study the influence of the infiltration condi-

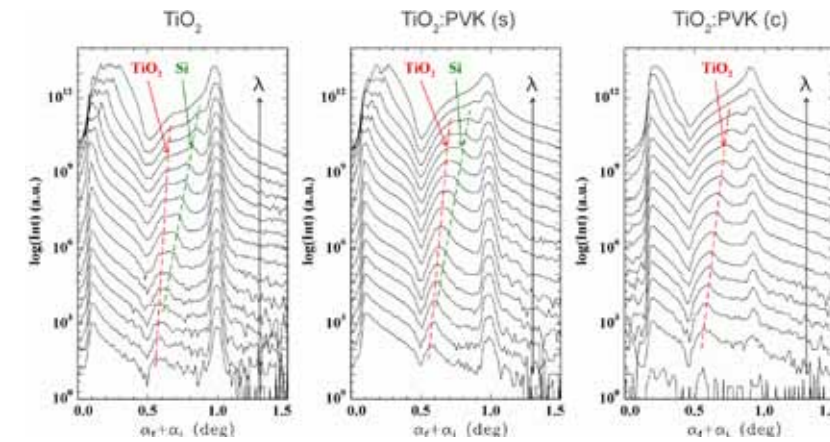


tions on the penetration process, we prepared TiO<sub>2</sub> thin films with a porous structure by the application of a sol-gel process [2] and infiltrated a conductive polymer, poly(N-vinylcarbazole) (PVK), into the voids by spin coating and solution casting. The structure of the resulting composite films was investigated using time-of-flight grazing incidence small-angle neutron scattering (TOF-GISANS) at the REFSANS instrument and compared with the structure of the bare TiO<sub>2</sub> matrix. By use of the TOF technique, where a whole spectrum of wavelengths is used and wavelength resolution achieved by time resolved measurement at the detector, it was possible to record scattering images at a number of different wavelengths without changing the experimental setup [3]. For the measurements, the neutron spectrum ranging from 2 to 19 Å was sliced into 22 channels, corresponding to 22 single images recorded for each sample.

Figure 1 shows a comparison of the scattering images of the unfilled TiO<sub>2</sub> network and the composite films. Between the intense transmitted beam and the specular reflected beam, all images show a Yoneda maximum originating from the scattering of the film. Since the Yoneda maximum is located at the position of the critical angle for specular reflection, from its experimentally determined value, the density of the material can be calculated. In the case of porous materials or composite films, this density is an average over all components. To extract the positions of the Yoneda maxima from the scattering

Figure 1: TOF-GISANS scattering images of the unfilled TiO<sub>2</sub> structure, the TiO<sub>2</sub>:PVK composite film prepared by spin coating (s) and the TiO<sub>2</sub>:PVK composite film prepared by solution casting. The images were recorded at a wavelength of 4.8 Å.

Figure 2: Horizontal cuts through the scattering images. From bottom to top the neutron wavelength increases. Between the transmitted beam (left, partially covered by a beam stop) and the specular reflected beam (right) the splitted Yoneda maxima are located.



images, horizontal cuts along the plane of reflection were taken (fig. 2). The cuts show a splitting of the Yoneda maxima into two components corresponding to the silicon substrate and the TiO<sub>2</sub> or composite film, respectively. By plotting the angular positions over the wavelength, the scattering length densities of the materials were determined and converted to porosity values (fig. 3). For the unfilled TiO<sub>2</sub> network, a high porosity of 85 % was found. After applying the PVK film by spin coating, the porosity was reduced, but was still found to be as high as 64 %, corresponding to only 25 % of the pores filled. This high porosity value suggests that the spin coated PVK film does not penetrate the TiO<sub>2</sub> network, but forms a compact layer on top of it. By the application of solution casting, a much better penetration resulting in a low porosity of only 28 % and 67 % filled pores was achieved. This difference results from the different process behaviour of spin coating and solution casting. In the spin coating process, the evaporation of the solvent is fast, and a polymer concentration gradient from the surface to the depth of the solution forms. Because time is sufficient for a relaxation of the gradient, the polymer concentration inside the pore structure remains low and only a little polymer is deposited. Under solution

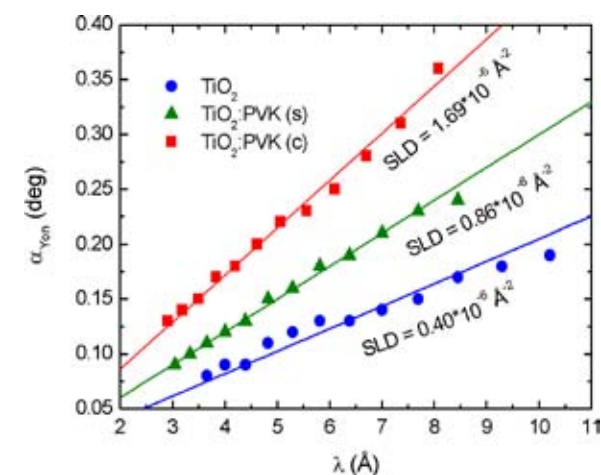


Figure 3: Plot of the observed Yoneda peak positions over the wavelength. From the slope results the scattering length density (SLD) of the material. For comparison, the SLD of TiO<sub>2</sub> and PVK are 2.61 · 10<sup>-6</sup> Å<sup>-2</sup> and 2.29 · 10<sup>-6</sup> Å<sup>-2</sup>, respectively.

casting conditions, the evaporation rate is considerably slower. Here, the concentration also relaxes and increases continuously inside the film, allowing deposition of a thick PVK film inside the pores [4].

In addition to the Yoneda maxima the scattering images also show lateral intensity maxima originating from the ordered pore structure of the TiO<sub>2</sub>. The peak position corresponds to the mean pore size, which is found to be around 50 nm. In the composite film prepared by solution casting the lateral maxima are vanished, since the pores are filled with PVK, which matches the scattering length density of TiO<sub>2</sub>. In contrast, in the spin coated film, the maxima are well pronounced. This again shows the differences in penetration and the high degree of pore filling achieved with solution casting.

In summary, we successfully applied TOF-GISANS to characterize the structure of TiO<sub>2</sub>:PVK composite films prepared by infiltrating the polymer into the porous TiO<sub>2</sub> matrix. The results found are of great interest for the application of the films in photovoltaics, and might be another step to improve the response of TiO<sub>2</sub> solar cells.

[1] U. Bach et al., Nature, 385, 583 (1998).

[2] G. Kaune et al., ACS Appl. Mater. Interfaces, 1, 2862 (2009).

[3] P. Müller-Buschbaum et al., Eur. Phys. J. ST, 167, 107 (2009).

[4] G. Kaune et al., J. Polym. Sci. Part. B, accepted for publication.

# Phospholipid membranes exhibit a flow-like transport mechanism

S. Busch<sup>1,2</sup>, C. Smuda<sup>3</sup>, L. C. Pardo<sup>4</sup>, T. Unruh<sup>1,2</sup>

<sup>1</sup>Technische Universität München, Physik Department E13, Garching, Germany

<sup>2</sup>Technische Universität München, Forschungs-Neutronenquelle Heinz Maier-Leibnitz (FRM II), Garching, Germany

<sup>3</sup>ETH Zürich, Institut für Pharmazeutische Wissenschaften, Zürich, Switzerland

<sup>4</sup>Universitat Politècnica de Catalunya, Grup de Caracterització de Materials, ETSEIB, Barcelona, Spain



Figure 1: Sebastian Busch and Dr. Tobias Unruh (r.) explaining the flow-like transport mechanism and the free volume model in front of the TOFTOF instrument.

The long-range motion of phospholipid molecules in a membrane is not only important for processes in a cell membrane, but also for the pharmaceutical and food industry where these molecules are used to stabilize emulsions and suspensions. Short- and long-time techniques have, so far, observed vastly different mobilities: Neutron scattering experiments have seen much faster motion on a picosecond time scale than macroscopic techniques. We show that our new high-precision quasielastic neutron scattering experiments, performed at the TOFTOF spectrometer at the FRM II [1], are compatible with recent molecular dynamic (MD) simulations which propose a flow-like motion of the phospholipid molecules at short times [2]. This offers an explanation for the different mobilities observed. With neutron scattering, one sees collective rearrangements of the molecules, whereas macroscopic techniques give access to the normally diffusive behaviour which is recovered at long time scales.

The cell membrane accommodates many important biological processes, for example, signaling processes between the cell and its environment. It is often necessary that proteins located in the membrane interact with one another – which requires that they be mobile within the membrane.

Several methods have been used to characterize the lateral mobility of phospholipids, working at very different time and length scales. On a macroscopic level, the long-range diffusion of the molecules was found to be rather slow, in stark contrast to the fast motion of molecules at the atomic scale, which has been measured using neutron scattering.

## Free volume model

To explain this discrepancy, the “free volume model” was developed which assigned the fast motion, seen by neutron scattering, to a rattling motion of a molecule the a cage of neighbouring molecules [2]. It was assumed that this motion did not contribute to the long-range motion at a macroscopic level, which was only due to rare escape events of the molecules from the cage. For some 20 years, this was the accepted theory of diffusion in phospholipid membranes. However, as these systems have been more closely studied using molecular dynamic simulations, it has become clear that these escape events were hardly ever observed in the simulations. Very recently, a completely new mechanism for short-time motion in the membranes has been suggested [3], assuming that the molecules do not perform normal diffusion at short time scales, but exhibit a flow-like motion. As this should happen on a time scale observable with neutron scattering, we performed experiments to check whether the data are compatible with

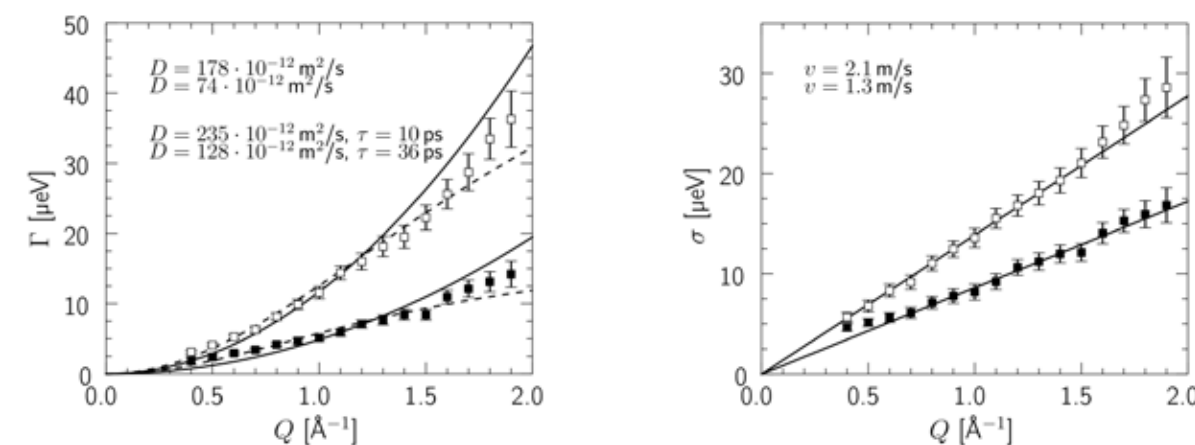


Figure 2: Left: The parameter  $\Gamma(Q)$  extracted from the diffusion model, shown for two temperatures as a function of  $Q$ . The lines are fits with a continuous diffusion model (drawn-out line) and a jump diffusion model (dashed line). For comparison: the “real” diffusion coefficient on a macroscopic scale is of the order of  $5 \cdot 10^{-12} \text{ m}^2/\text{s}$ . Right: The parameter  $\sigma(Q)$  extracted from the flow model, shown for the same temperatures as a function of  $Q$ .

this assumption.

## The motions of phospholipids observed by quasielastic neutron scattering

We studied the phospholipid dimyristoylphosphatidylcholine (DMPC) which was fully hydrated with  $\text{D}_2\text{O}$ . The experiments were performed at the time-of-flight neutron spectrometer TOFTOF at the FRM II. With this spectrometer, it is possible to observe motions on time scales between about 0.1 and 1000 ps, covering approximately the same range as the MD simulations.

The transfer of momentum  $Q$  and energy  $\hbar\omega$  between neutrons and sample was measured. The data could be described using a model assuming two localized motions which are attributed to the head- and tail-group of the phospholipid molecules, respectively, and a long-range motion of the whole molecule,

$$S(Q, \omega) = \int_0^\infty \left\{ X \cdot \prod_{i=1,2} \left( (1 - A_{0i}) \cdot e^{-\Gamma_i t} + A_{0i} \right) \right\} e^{-i\omega t} dt$$

with

$X = \exp[-\Gamma(Q)t]$  for diffusive long range motion

or

$X = \exp[-t^2/(2\sigma(Q)^2)]$  for flow motion.

These two possibilities were compared to the data. The diffusion model has to yield  $\Gamma \propto Q^2$ . That this is not obtained can be seen from figure 2. The flow model has to yield  $\sigma \propto Q$ , which is in good agreement with the extracted parameters, also shown in figure 2.

Apart from the  $Q$ -dependence of the parameters,

the flow model has additional support from its numerical values, whilst the extracted diffusion coefficients are more than an order of magnitude above the well-known macroscopic value. The flow velocities are in perfect agreement with the MD simulation [2].

## A coherent picture of the long-range motions in membranes evolves

Previously, the fundamental step of the diffusion process in phospholipid membranes was seen as the opening of a void which a molecule could slip into. The new picture, which is experimentally supported by our measurements, respects the fact that the molecules are not moving independently from one another. In contrast, the motion of one molecule causes all neighbouring molecules to move preferentially in the same direction.

This relatively fast collective motion of dynamically assembled patches of molecules causes a pressure increase in flow direction which, in turn, slows the motion down. A molecule participates in many of these thermally excited events when covering macroscopic distances, resulting in the cross over from flow-like motions at short times to diffusive motions at longer times.

[1] S. Busch et al., J. Am. Chem. Soc., 132 (10) (2010).

[2] E. Falck et al., J. Am. Chem. Soc., 130 (44) (2008).

[3] W. L. C. Vaz, P. F. F. Almeida, Biophys. J., 60, 1553 (1991).

# Globular protein under denaturing conditions

V. Lacroix<sup>1,2</sup>, M.-S. Appavou<sup>1</sup>, P. Cayot<sup>2</sup>, C. Loupiac<sup>2</sup>, D. Richter<sup>1,3</sup>

<sup>1</sup>Forschungszentrum Jülich GmbH, Jülich Centre for Neutron Science at FRM II, Garching, Germany

<sup>2</sup>Université de Bourgogne, Equipe EMMA, AGRO SUP Dijon, Dijon, France

<sup>3</sup>Forschungszentrum Jülich GmbH, Institut für Festkörperforschung, Jülich, Germany

The isolation of protein folding intermediates is, somehow crucial to understanding protein misfolding and protein aggregation, for example. The process of protein unfolding is driven by the balance between protein-protein, protein-water and water-water interactions. Pressure denaturation studies provide fundamental thermodynamic parameters for protein unfolding: the volume change  $\Delta V^\circ/V^\circ$ . Using SANS, we have observed whether the ligand of beta-lactoglobulin (BLG) can stabilize its structure upon chemical and pressure denaturing conditions.

Small angle neutron scattering experiments using the JCNS KWS 2 diffractometer (fig. 1) were per-



formed at room temperature and at atmospheric pressure using a 4,5 Å wavelength and two detector distances: 2 m and 8 m. It is then possible to investigate a q-range from  $1.10^{-2}$  to  $0.32 \text{ \AA}^{-1}$ . The samples chosen were beta-lactoglobulin solutions in a dilute regime (2 to 10 mg/mL) in order to extrapolate the radius of gyration at null concentration, with and without retinol as a ligand and with increasing guanidinium hydrochloride concentration as a chemical denaturing agent. Similar measurements were also performed on BLG dilute solution with and without retinol as a ligand, at atmospheric pressure before and after pressurization at 1500 bar.

To evaluate data in the Guinier regime, we used the following Debye approximation:

$$I(D,c)^{-1} = I(0,D,c)^{-1} [1 + 0.359(qR_g(D,c))^{2.206}] \quad (1)$$

In this equation, the values 0.359 and 2.206 allow the accuracy of this approximation to remain below 0.4 % for  $qR_g(D,c) < 3 [1]$ .

Initially, we focused on the chemical denaturation of beta-lactoglobulin without and with retinol in the Guinier regime. Figure 2 represents Debye

	Rg(0) without retinol (Å)	Rg(0) with retinol (Å)
P atmospheric	21.2 ± 0.2	24.3 ± 0.8
P 1500 bar	30.2 ± 1.5	27.3 ± 1.7
$\Delta V^\circ/V^\circ$ (%)	42.5 ± 0.1	12.4 ± 0.1

Table 1: Evolution of the radius of gyration extrapolated at null concentration of beta-lactoglobulin without and with retinol before and after pressurization.

Figure 1: The small angle neutron scattering facility KWS 2 (second from the right) at the FRM II.

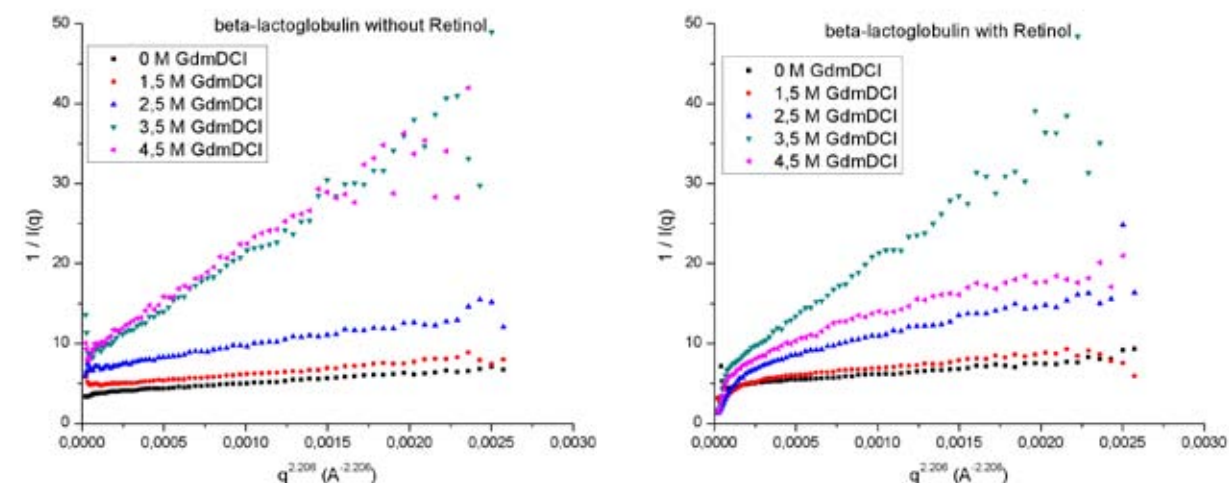


Figure 2: Debye representation of the scattering pattern for beta-lactoglobulin solution at 5 mg/mL at different GdmDCL concentration without (left) and with (right) retinol binding.

plots of the scattering pattern for BLG without and with retinol at different concentrations of guanidinium hydrochloride.

From the measurement for the retinol-free BLG in the Guinier regime, we found an increase in the radius of gyration extrapolated at null concentration from  $R_g(0) = 21.1 \pm 0.2 \text{ \AA}$  in the native state up to  $R_g(0) = 32.6 \pm 1.5 \text{ \AA}$  in the denatured state. However, we can observe a destabilization effect of the ligand binding on BLG with respect to GdmDCL addition according to the spectra related to the retinol-bound BLG. Some aggregation phenomena occur when we add the GdmDCL as concluded from the intensity increase observed towards low Q.

We have then investigated the pressure denaturation of beta-lactoglobulin without and with retinol in the Guinier regime. Table 1 presents the evolution of the radius of gyration extrapolated at null concentration of beta-lactoglobulin without and with retinol before and after pressurization.

Pressure induces the same increase in the null concentration extrapolated radius of gyration of the retinol-free BLG from  $R_g(0) = 21.1 \pm 0.2 \text{ \AA}$  in the native state up to  $R_g(0) = 30.2 \pm 1.5 \text{ \AA}$  in the denatured state. The volume of the ligand-free protein has increased by  $43.3 \pm 0.1\%$ .

A ligand bound to BLG induces a slight increase in the  $R_g(0)$  by 15.2 % without unfolding the protein. We can observe a smaller increase in the

radius of gyration from  $R_g(0) = 24.3 \pm 0.8 \text{ \AA}$  in the native state up to  $R_g(0) = 27.3 \pm 1.7 \text{ \AA}$  as long as the protein was pressurized at 1.5 kbar before being measured at atmospheric pressure. The volume of the ligand-bound protein has increased by  $12.4 \pm 0.1 \%$ .

Using the SANS technique, we investigated the stabilization effect of retinol binding on beta-lactoglobulin proteins. We have seen that the ligand does not protect the protein against chemical denaturation (by guanidinium hydrochloride) whereas it does decrease the effect of pressure. The difference between these two effects results from the fact that guanidinium hydrochloride, by competing with protein in the hydrogen bond network, involve secondary and tertiary structure modifications and unfolds the molecule from the surface of the protein. The pressure induces the penetration of water molecules into the hydrophobic core of the protein and thus unfolds the biomolecule from inside. Both unfolding processes lead to an increase in the radius of gyration by ~50 % in the case of the ligand-free beta-lactoglobulin. Former SANS measurements under pressure, performed by Loupiac et al [2], have shown an increase of the radius of gyration of about 7 %. Indeed, the pressure released after pressurization at 1,5 kbar has an effect on the structure of the beta-lactoglobulin.

[1] V. Receveur et al., FEBS Lett., 426, 57 (1998).

[2] C. Loupiac et al., Biochim Biophys. Acta, 1764, 211 (2006).

# Elastic properties of the interfacial membrane in fluctuating supercritical CO<sub>2</sub>-microemulsions

O. Holderer<sup>1</sup>, M. Klostermann<sup>2</sup>, M. Monkenbusch<sup>3</sup>, R. Strey<sup>2</sup>, D. Richter<sup>1,3</sup>, T. Sottmann<sup>2</sup>

<sup>1</sup>Forschungszentrum Jülich GmbH, Jülich Centre for Neutron Science at FRM II, Garching, Germany

<sup>2</sup>Universität zu Köln, Institut für Physikalische Chemie, Köln, Germany

<sup>3</sup>Forschungszentrum Jülich GmbH, Institut für Festkörperforschung, Jülich, Germany

Supercritical carbon dioxide (scCO<sub>2</sub>) has attracted much attention as an environmentally friendly solvent. Recently, bicontinuous microemulsions, containing water, supercritical carbon dioxide and a surfactant, have been formed with certain perfluoro-surfactants. The membrane fluctuations of a surfactant monolayer in such a bicontinuous microemulsion have been measured using neutron spin-echo (NSE) spectroscopy and allows us to determine the membrane rigidity to be  $0.4 k_B T$  in this novel type of bicontinuous microemulsions.

Over the last decades, supercritical fluids have attracted much attention as potential replacements for conventional organic solvents in the field of green chemistry. Of all these fluids, supercritical CO<sub>2</sub> ( $T_c = 31.1$  °C,  $p_c = 72.8$  bar) is seen as the most promising candidate since it is cheap, abundant, inflammable, non-toxic, bio- and food-compatible. To improve the solvent properties of scCO<sub>2</sub> especially for polar and/or high molecular weight solutes microscopic dispersions of water and CO<sub>2</sub> in the form of thermodynamically stable microemulsion have become the focus of attention of current research [1]. So far, studies on these novel microemulsion systems have concentrated on the phase behaviour and microstructure of water- and CO<sub>2</sub>-rich microemulsions, respectively [1-3]. Recently, and for the first time, we were able to formulate balanced supercritical CO<sub>2</sub> microemulsions containing equal volumes of water and CO<sub>2</sub> using technical grade polyethyleneglycolperfluoroalkylether surfactants [4]. The phase behaviour of such a microemulsion system H<sub>2</sub>O/NaCl-scCO<sub>2</sub>-Zonyl FSH/Zonyl FSN

100 is shown in figure 1 for various pressures in a range from  $p = 160$  to  $300$  bar as a function of the overall surfactant mass fraction  $\gamma$  and the temperature  $T$  [4]. The mass fraction  $\alpha$  of CO<sub>2</sub> has been adjusted to  $\alpha = 0.4$ .

The decay time  $\tau$  for thermally activated fluctuations of surfactant membrane patches is in the nanoseconds region and therefore inside the time window of neutron spin-echo (NSE) spectroscopy. The NSE experiments on scCO<sub>2</sub> microemulsions were performed at the J-NSE instrument at the FRM II with an amagnetic high pressure NSE-cell. It delivers the intermediate scattering function  $S(q, \tau)$ , the Fourier transform of the scattering function  $S(q, \tau)$ .

The fluctuation of membrane patches in “classical” microemulsions at ambient pressure has been described theoretically by Zilman and

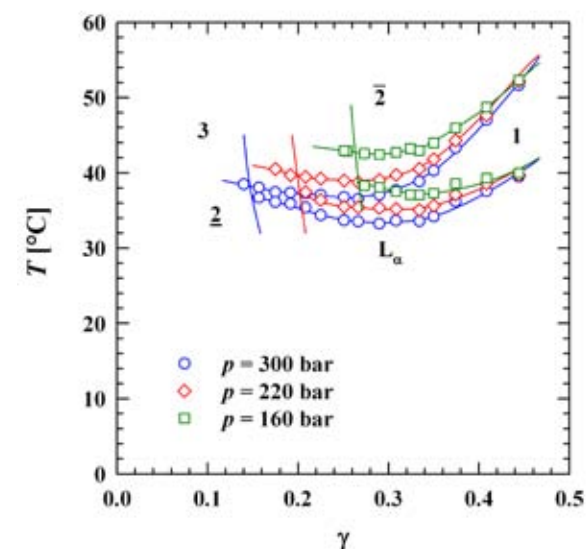


Figure 1: Phase diagram of the described microemulsion with supercritical carbon dioxide. The pressure varies from 160 to 300 bar

Granek [5], it relates the relaxation rate of the membrane to the bending rigidity  $\kappa$ . In an approximation, the intermediate scattering function is described by a stretched exponential function:

$$S(q, \tau) \approx S(q) \exp(-(\Gamma_q \tau)^\beta) \quad (1)$$

with the relaxation rate

$$\Gamma_q = 0.025 \gamma_{ZG} (k_B T / \kappa)^{1/2} k_B T / \eta q^3 \quad (2)$$

whereas  $\eta$  is the viscosity of the solvent that surrounds the surfactant membrane (in this case the average viscosity of water and CO<sub>2</sub>),  $\gamma_{ZG} \sim 1$  and  $\beta = 2/3$ . Figure 2 shows the intermediate scattering function  $S(q, \tau)$  of the D<sub>2</sub>O/NaCl-scCO<sub>2</sub>-Fluorosurfactant ( $\alpha = 0.40$ ,  $\delta = 0.50$ ) microemulsion near the optimum point at  $T = 35$  °C,  $\gamma = 0.26$  and a pressure of  $p = 220$  bar for four different  $q$ -values between  $q = 0.05$  and  $q = 0.15$  Å<sup>-1</sup> (corresponding to length scales in real space of  $d = 2\pi/q = 125 - 42$  Å). Thus, the fluctuation dynamics of the surfactant membrane patches is studied on a local scale, smaller than the membrane-membrane distance. Fitting the experimental data with the expression of equation 1 shows that the  $q^3$ -dependence of the relaxation rate, which is predicted for bicontinuous microemulsions according to equation 2, is also found for supercritical CO<sub>2</sub> microemulsions, as well as the typical stretching exponent  $\beta = 2/3$ .

A quantitative determination of the bending rigidity according to the Zilman-Granek theory implies numerical integrations of the expression for a fluctuating membrane patch instead of

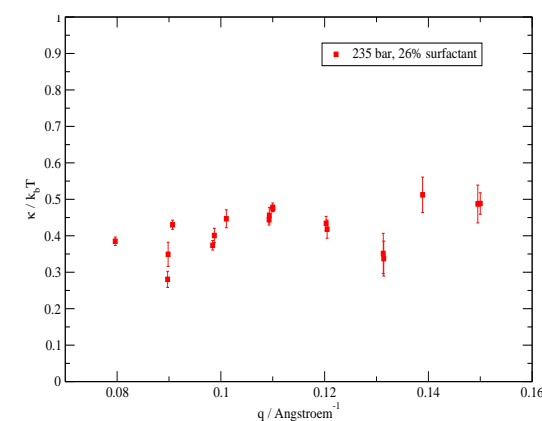


Figure 3: Bending rigidity as a function of  $q$  of a supercritical CO<sub>2</sub>-microemulsion at 220 bar obtained from the numerical evaluation of the Zilman-Granek theory.

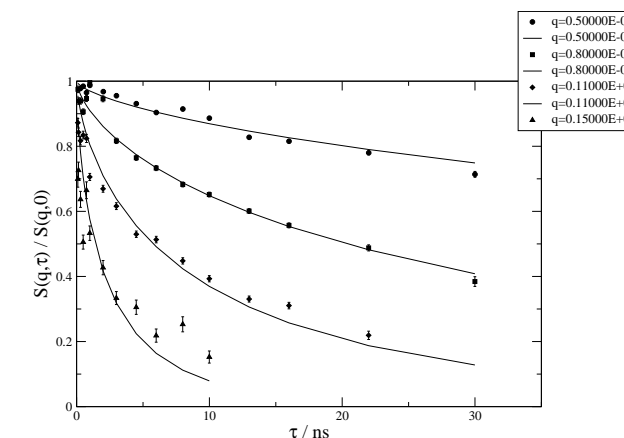


Figure 2: Intermediate scattering function of a supercritical CO<sub>2</sub> microemulsion at 220 bar and 35 °C measured at the J-NSE

equation 1, where the bending rigidity is the only free fitting parameter. This procedure provides  $\kappa$  without effects of renormalization, which is presented in figure 3 as a function of  $q$ .

In this experiment we were able to demonstrate that membrane fluctuations in bicontinuous supercritical CO<sub>2</sub> microemulsions can be measured using high pressure NSE. The relaxation rate obtained is about twice as high as in similar water-oil microemulsions. The bending rigidity thus determined yields a value of  $0.4 k_B T$ , smaller than in water-oil microemulsions ( $\kappa_{bare} \sim 1 k_B T$ ). Future studies on supercritical CO<sub>2</sub> microemulsions will be directed towards the investigation of the pressure dependence of the membrane fluctuations. Since the viscosity of the supercritical CO<sub>2</sub> domains can be varied at otherwise unchanged conditions, a deeper insight into the elastic properties of the membrane is expected.

[1] J. Eastoe et al., Langmuir, 22, 9832 (2006).

[2] K. Harrison et al., Langmuir, 10, 3536 (1994).

[3] M. Klostermann et al., Langmuir, in preparation.

[4] L. Kramer et al., Langmuir, in preparation.

[5] A. Zilman, R. Granek, Phys. Rev. Lett., 77, 4788 (1996).

# Nuclear spectroscopy of $^{200}\text{Hg}$ using cold neutron capture

C. Bernards<sup>1</sup>, J. Jolie<sup>1</sup>, R. Schulze<sup>1</sup>, N. Warr<sup>1</sup>, L. Canella<sup>2</sup>, P. Kudejova<sup>3</sup>

<sup>1</sup>Universität zu Köln, Institut für Kernphysik, Köln, Germany

<sup>2</sup>Technische Universität München, Institut für Radiochemie, Garching, Germany

<sup>3</sup>Technische Universität München, Forschungs-Neutronenquelle Heinz Maier-Leibnitz (FRM II), Garching, Germany

Neutron-capture reactions serve as a rather complete spectroscopic method to investigate the excited nuclear states. Here, we report on an experiment at the PGAA setup at the FRM II in Garching that was performed to investigate the structure of the nucleus  $^{200}\text{Hg}$ . The  $\gamma$ -rays following the reaction  $^{nat}\text{Hg}(n, \gamma)$  were observed using a pair spectrometer and a Compton-suppressed high-purity germanium detector. We analysed primary and secondary  $\gamma$ -rays to explore the inner structure of this nucleus and found new levels in  $^{200}\text{Hg}$ .

## $\gamma$ -rays elucidate the structure of the nucleus

Because there is no Coulomb interaction for neutrons, the cold neutrons available at the PGAA instrument ( $E_n = 1.8$  MeV) can populate capture states in nuclei with excitation energy  $E_x = S_n + E_n \approx S_n$ , with  $S_n$  the neutron binding energy, where  $S_n \sim 6 - 10$  MeV  $\gg E_n$ . The  $\gamma$ -decay spectrum following the neutron capture consists

of two components: the primary and secondary  $\gamma$ -rays, respectively. Their observation and analysis give hints as to the underlying structure of the nucleus [1].

For this work, we performed a measurement at the PGAA facility [2]. We used the cold neutron beam to induce neutron-capture reactions to investigate the nuclear structure of  $^{200}\text{Hg}$ . This nucleus is of particular interest, as it completes our research on the extended nuclear-structure supersymmetry in that mass region [3-8].

The setup we used at the PGAA station was similar to that in [9]. We ran the first HPGe detector (60 % efficiency = Det 1) as a so-called pair spectrometer and the second HPGe (36 % efficiency = Det 2) as a Compton-suppressed detector. The germanium crystal in Det 1 was surrounded cylindrically by eight NaI(Tl)/BGO segments. The opposed segments of the scintillator were used to detect annihilation  $\gamma$ -ray pairs of the primary  $\gamma$  radiation [10]. Figure 1 shows the experimental setup inside the PGAA bunker. Our target consisted of 13 mg  $^{nat}\text{HgS}$  powder sealed in a teflon bag. For energy calibration, we used a mixture of iron, urea, chloranil, and oxalic acid.

## New primary $\gamma$ -ray observed

Figure 2 shows a part of the  $^{200}\text{Hg}$  spectrum from 4.3 to 6.5 MeV, measured using the pair spectrometer. Peaks in the spectrum are the primary

Figure 1: Experimental setup in the PGAA bunker: The 60 % detector (Det 1) is located on the right, the 36 % detector (Det 2) on the left. The neutron beam comes from behind and the neutron capture takes place in the lead-shielded target chamber in the middle. The target ladder is mounted on top of the target chamber. Neutrons passing the target chamber are stopped in the neutron stopper on the left.

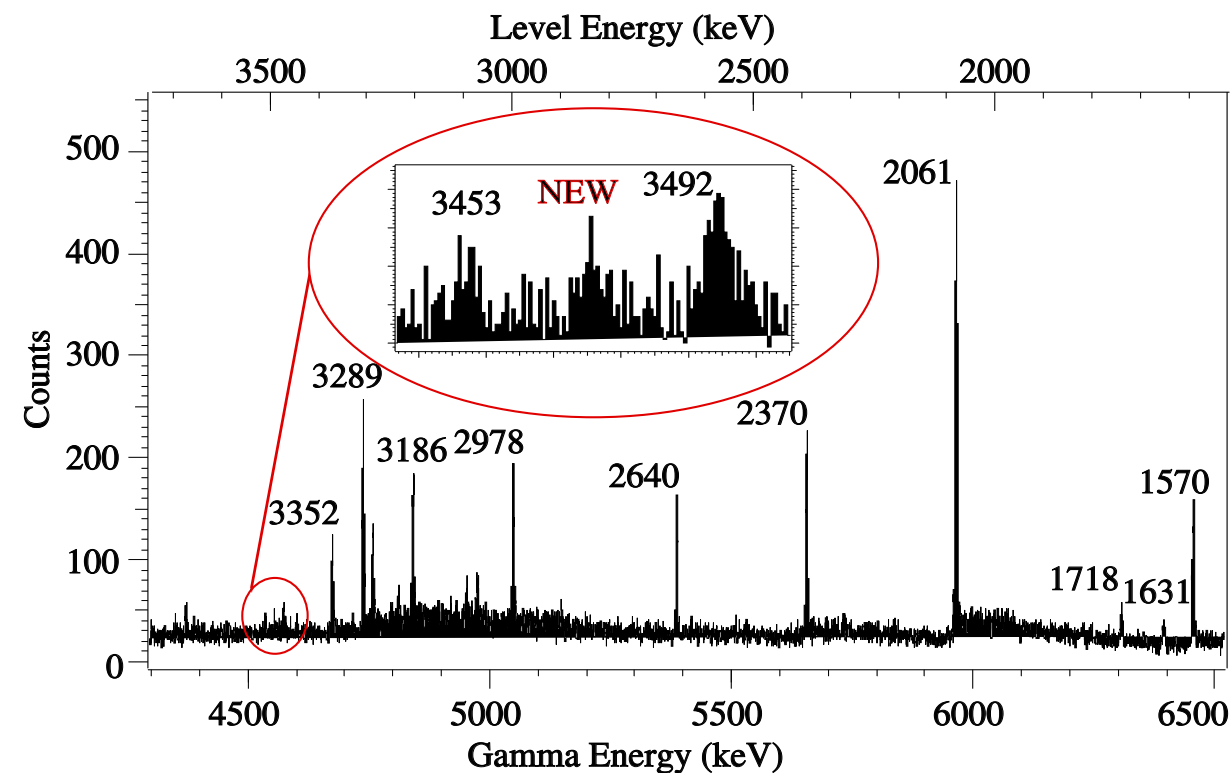


Figure 2: Primary  $\gamma$ -ray spectrum of  $^{200}\text{Hg}$  in the pair spectrometer. The most intensive primary  $\gamma$ -rays are labelled with their associated level energies:  $E_{\text{level}} = S_n - E_{\text{primary}}$ . A newly determined primary  $\gamma$ -ray is shown in the magnification.

ry  $\gamma$  rays directly populating different low-spin states in  $^{200}\text{Hg}$ . In figure 2, the given energies have already been corrected for the 1022 keV loss in energy due to the two escaping annihilation  $\gamma$ -rays from the HPGe crystal to the surrounding scintillators. In the energy range shown, we found one new primary  $\gamma$ -ray, leading to a new level. This  $\gamma$  transition is also shown in figure 2. We found more new primary  $\gamma$ -rays below 4.3 MeV. Although we used natural mercury sulfide as target material, the measured  $\gamma$ -rays originate from  $^{200}\text{Hg}$ , since the neutron-capture cross section for  $^{199}\text{Hg}(n, \gamma)$  is  $\sigma \approx 6300$  b, which is more than 99.9 % of the total  $^{nat}\text{Hg}$  neutron-capture cross section.

## Data set of $^{200}\text{Hg}$ completed

We investigated the structure of the nucleus  $^{200}\text{Hg}$  using a pair spectrometer. Although many different experiments have already been performed on  $^{200}\text{Hg}$  with an established set of data [11], the opportunity of directly analysing the primary  $\gamma$  radiation allowed us to complete this data set with new results. The analysis of  $\gamma$ -rays following cold-neutron capture is very interesting for nuclear-structure studies, since the capture state can populate all excited states, being

limited only by  $\gamma$  selection rules. In return, this limitation can determine the spins of the populated states, which is an important observable in nuclear-structure physics.

- [1] K. S. Krane, Introductory Nuclear Physics, John Wiley & Sons, New York, USA (1988).
- [2] P. Kudejova et al., J. Radioanal. Nucl. Chem., 278, 691 (2008).
- [3] P. Van Isacker et al., Phys. Rev. Lett., 54, 653 (1985).
- [4] A. Metz et al., Phys. Rev. Lett., 83, 1542 (1999).
- [5] C. Bernards et al., Phys. Rev. C, 79, 054307 (2009).
- [6] C. Bernards et al., submitted to Phys. Rev. C.
- [7] J. Barea et al., Phys. Rev. C, 79, 031304(R) (2009).
- [8] A. Frank et al., Symmetries in Atomic Nuclei - From Iso-spin to Supersymmetry, Springer, New York, USA (2009).
- [9] G. Meierhofer et al., Eur. Phys. J. A, 40, 61 (2009).
- [10] L. Genilloud et al., Nucl. Phys. A, 669, 407 (2000).
- [11] F. G. Kondev, S. Lalkovski, Nuclear Data Sheets, 108, 1471 (2007).

# Magnetic structure of a pnictide superconductor determined by single crystal neutron diffraction

Y. Xiao<sup>1</sup>, Y. Su<sup>2</sup>, M. Meven<sup>3</sup>, R. Mittal<sup>2</sup>, C. M. N. Kumar<sup>1</sup>, T. Chatterji<sup>4</sup>, S. Price<sup>2</sup>, J. Persson<sup>1</sup>, N. Kumar<sup>5</sup>, S. K. Dhar<sup>5</sup>, A. Thamizhavel<sup>5</sup>, T. Brueckel<sup>1,2,4</sup>

<sup>1</sup>Forschungszentrum Jülich, Institut für Festkörperforschung, Jülich, Germany

<sup>2</sup>Forschungszentrum Jülich, Jülich Centre for Neutron Science at FRM II, Garching, Germany

<sup>3</sup>Technische Universität München, Forschungs-Neutronenquelle Heinz Maier-Leibnitz (FRM II), Garching, Germany

<sup>4</sup>Forschungszentrum Jülich, Jülich Centre for Neutron Science at ILL, Grenoble, France

<sup>5</sup>Tata Institute of Fundamental Research, Department of Condensed Matter Physics and Material Sciences, Mumbai, India

Amongst various parent compounds of iron pnictide superconductors  $\text{EuFe}_2\text{As}_2$  stands out due to the presence of both the spin density wave of Fe and antiferromagnetic ordering of the localized  $\text{Eu}^{2+}$  moment. Single crystal neutron diffraction studies have been carried out to determine the magnetic structure of this compound and to investigate the coupling between two magnetic sublattices. The determination of magnetic structure of  $\text{EuFe}_2\text{As}_2$  parent compound is significant in understanding the relationship between superconductivity and magnetism in pnictide superconductors.

## Intimate relation between magnetism and superconductivity in iron pnictides

The recent discovery of pnictide superconductors has attracted extensive attention because it provides a new opportunity to investigate the mechanism of superconductivity [1]. All iron pnictides adopt a layered structure and the superconducting state is achieved either by electron or hole doping of the parent compounds [2]. Since magnetism and superconductivity appear to be intimately related in iron pnictides, it is therefore equally important to understand the magnetic properties, especially for those compounds that contain the magnetic lanthanide ions.  $\text{EuFe}_2\text{As}_2$  is a peculiar member of the iron arsenide  $\text{AFe}_2\text{As}_2$  family as the A site is occupied by  $\text{Eu}^{2+}$ , which is an S-state rare-earth ion possessing a  $4f^7$  structure with electron spin  $S = 7/2$ . However, the magnetic ordering and the details of magnetic structure of  $\text{EuFe}_2\text{As}_2$  have not been clarified so far. Here we report neutron diffraction studies on a high-quality  $\text{EuFe}_2\text{As}_2$  single crystal using the hot neutron source at FRM II.

The single crystals of  $\text{EuFe}_2\text{As}_2$  were grown by the high temperature solution growth method using a fourth element, Sn, as the solvent. A 50 mg single crystal with dimensions of about  $5 \times 5 \times 1 \text{ mm}^3$  was selected for the neutron diffraction experiment, which was performed using the hot-neutron four-circle diffractometer HEIDI at FRM II [3]. A Cu (220) monochromator was selected to produce a monochromatic neutron beam with wavelength  $0.868 \text{ \AA}$ . The diffraction data were collected using a  $^3\text{He}$  single detector at different temperatures from 300 K down to 2.5 K.

The crystal structure of  $\text{EuFe}_2\text{As}_2$  can be described within the framework of tetragonal symmetry at 300 K. Upon cooling down, the crystal structure distortion from tetragonal (S.G.  $I4/mmm$ ) to orthorhombic (S.G.  $Fmmm$ ) structure was revealed by the splitting of the tetragonal  $(220)_T$  reflection into the orthorhombic  $(400)_O$  and  $(040)_O$  reflections.

## Coupled structural and magnetic transitions

To clarify the magnetic structure of  $\text{EuFe}_2\text{As}_2$  at low temperature, extensive search of magnetic reflections was performed in the reciprocal space. In addition to the expected nuclear reflections, two sets of magnetic superstructure reflections can be clearly identified with two magnetic propagation wave vectors  $(1,0,1)$  and  $(0,0,1)$  respectively. The contour map of  $(103)_M$  and  $(401)_M$  reflections fully illustrated the intensity distribution, as shown in figures 1a and 1c. In figure 1b, the Q scan of  $(103)_M$  reflection can be fitted by a single Gaussian function with  $k = 0.991$ .

This strongly indicates that the  $(h0l)$  type reflections (with  $h$  and  $l$  equal to odd numbers) are

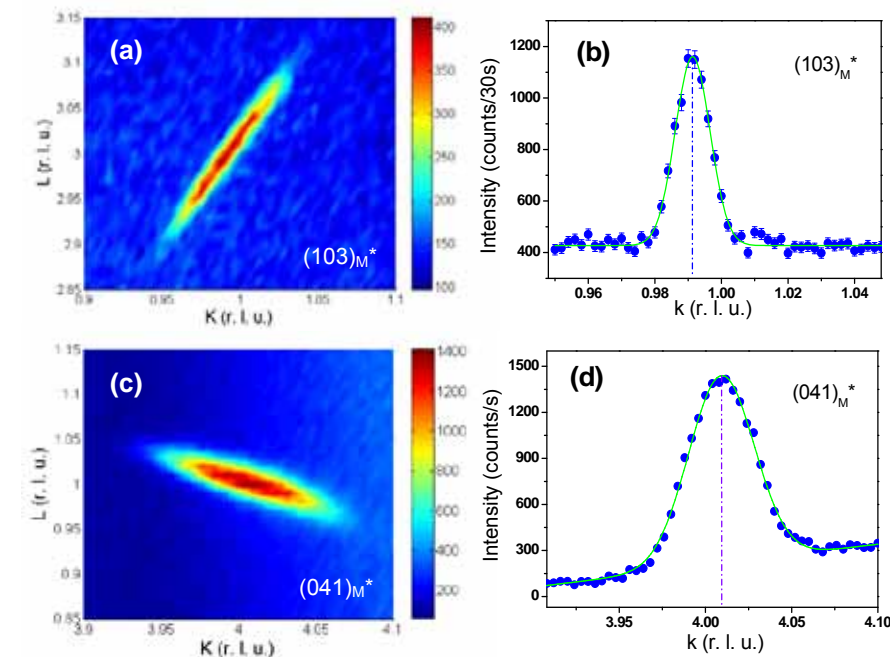


Figure 1: (a) (c) The contour map shows the Q dependence of the  $(103)_M$  and  $(041)_M$  magnetic reflections. (b) (d) Q scan of  $(103)_M$  and  $(041)_M$  magnetic reflections. The reflections are observed in k scan because of the existence of twinned domains.

associated with the  $(h00)$  domain and can thus be described with the propagation wave vector  $k = (1,0,1)$ , which is related to the antiferromagnetic order of  $\text{Fe}^{2+}$  moments. Consequently, the magnetic reflections with a propagation wave vector  $k = (0,0,1)$  (with  $h$  even and  $l$  odd) are due to the long range order of the localized  $\text{Eu}^{2+}$  moments. The moment direction of  $\text{Eu}^{2+}$  can be determined as along the  $a$  direction since the Q scan on  $(041)_M$  reflection (fig. 1d), gives a peak position of  $k = 4.01$ . By taking the twinned components into account properly, the refinement on both  $\text{Fe}^{2+}$  and  $\text{Eu}^{2+}$  magnetic sublattices was carried out and the magnetic structure of  $\text{EuFe}_2\text{As}_2$  is unambiguously determined as illustrated in figure 2a.

Figure 2b shows the temperature dependence of the  $(112)_M$  and  $(003)_M$  magnetic reflections attributed to the ordering of  $\text{Eu}^{2+}$  moments. The onset temperature of  $\text{Eu}^{2+}$  magnetic order is deduced to be 19 K. The magnetic ordering temperature of  $\text{Fe}^{2+}$  moment is estimated to be 190 K based on the temperature dependence of the  $(101)_M$  and  $(103)_M$  magnetic reflections (see fig. 2c). The tetragonal-orthorhombic structural phase transition also takes place at 190 K as revealed by the sharp change of full width at half maximum in the  $(040)_O$  nuclear reflection, which indicated the existence of the strong coupling between the structural and magnetic phase transitions in  $\text{EuFe}_2\text{As}_2$ .

In summary, with decreasing temperature, the

antiferromagnetic order of  $\text{Fe}^{2+}$  moments set in at 190 K with the propagation vector  $k = (1,0,1)$ . The tetragonal to orthorhombic structural transition occurs simultaneously with the antiferromagnetic order, which indicates the strong coupling between the lattice and Fe magnetic degree of freedom. Below 19 K, the  $\text{Eu}^{2+}$  moments order antiferromagnetically with the propagation vector  $k = (1,0,1)$  and are aligned along the  $a$  axis. Our studies also suggest a weak coupling between the  $\text{Fe}^{2+}$  and  $\text{Eu}^{2+}$  magnetic sublattice [4].

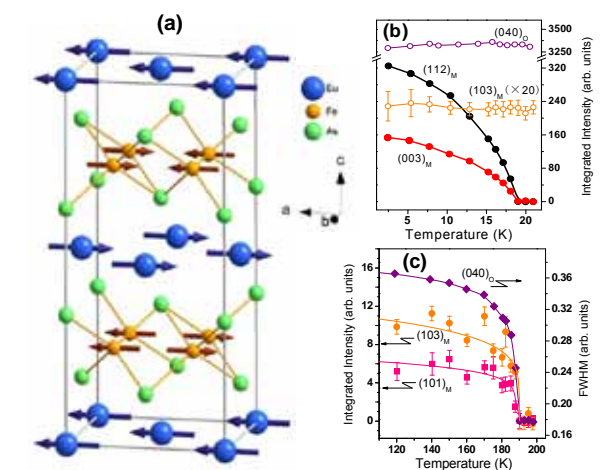


Figure 2: (a) Illustration of the magnetic structures of  $\text{EuFe}_2\text{As}_2$  at 2.5 K. (b)(c) Temperature dependence of integrated intensity of  $(040)_O$  nuclear reflection as well as the  $(112)_M$ ,  $(003)_M$ ,  $(103)_M$  and  $(101)_M$  magnetic reflections.

[1] Y. Kamihara et al., J. Am. Chem. Soc., 130, 3296 (2008).

[2] Z.-A. Ren, Z.-X. Zhao, Adv. Mater., 21, 4584 (2009).

[3] M. Meven et al., Neutron News, 18, 19 (2007).

[4] Y. Xiao et al., Phys. Rev. B, 80, 174424 (2009).

# In-operando neutron scattering studies of Li-ion batteries

A. Senyshyn<sup>1</sup>, M. J. Mühlbauer<sup>2</sup>, K. Nikolowski<sup>3</sup>, H. Ehrenberg<sup>3</sup>

<sup>1</sup>Technische Universität Darmstadt, FB Material- und Geowissenschaften, Darmstadt, Germany

<sup>2</sup>Technische Universität München, Physik Department E21, Garching, Germany

<sup>3</sup>Leibniz-Institut für Festkörper- und Werkstofforschung, Dresden, Germany

Despite its successful use in every day power applications lithium-ion battery technology, faces plenty of challenges regarding safety, lifetime, temperature range of stable operations and production costs per single battery, which make the motivation for further studies very strong. In the current contribution we report in-operando neutron scattering experiments (on charge/discharge) of “fresh” and “fatigued” commercial rechargeable batteries of the cylindrical 18650 type, performed at the high-resolution neutron powder diffractometer SPODI and the neutron tomography scanner ANTARES.

Cycling of the cells was controlled by a VMP3 potentiostat from Bio-Logic. The evolution of the crystal structures of battery constituents under different charge/discharge states is deduced from high-resolution neutron powder diffraction experiments performed at the structure powder diffractometer SPODI [1].

Data collection was carried out in quasi “equilibrium”, i.e. the desired charge level was kept constant for 2 hours and, thereby, allowed to relax. The data collection time per battery was ca. 3.5 hours. Data collection was performed at distinguished charging states of 3.40, 3.90, 3.95, 4.00, 4.05, 4.10, 4.15 and 4.20 V. The high-quality diffraction patterns obtained were analyzed using the Rietveld method, where an example of a Rietveld refinement, based on a neutron powder diffraction pattern collected for the “fresh” battery (charged to 4.05 V) is shown in figure 1. Clear signals corresponding to the cathode material  $\text{LiCoO}_2$  (row 1 of Bragg reflections in fig. 1), both copper (2) and aluminium (6) current collectors, steel housing (3), as well as the graphite anode (4,5), were observed.

## Visible fatigue of the graphite anode

During charging an intercalation of lithium into carbon was observed, which is reflected in the shift of the (002) reflections due to the expansion of c-axes corresponding to  $\text{LiC}_{12}$  and  $\text{LiC}_6$ , respectively (see fig. 2). Phases with lower lithium concentration, e.g.  $\text{LiC}_{18}$  and  $\text{LiC}_{x>25}$  are expected to occur in the range of 3.4-3.9 V, which was not considered in detail in the current study. Neutron powder diffraction patterns collected for both “fresh” and “fatigued” batteries have been found to be very similar. Nevertheless some differences concerning the processes in the anode occurred. For example from figure 2 it is evident that at 3.95 V the phase fraction of  $\text{LiC}_6$  for the “fresh” battery is obviously higher than that for the “fatigued” one. Furthermore this tendency continues up to higher charging states, e.g. 4.00 V, 4.05 V, whilst at higher voltages (4.10 V) the amount of  $\text{LiC}_6$  in both “fresh” and “fatigued” batteries becomes equal. At the same time, a much higher fraction of  $\text{LiC}_{12}$  remains untransformed to  $\text{LiC}_6$  in the “fatigued” Li-ion cell in

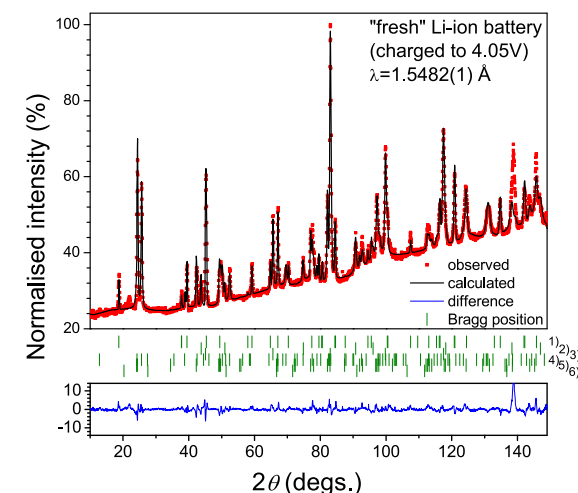


Figure 1: Rietveld refinement based on a diffraction pattern from a commercial 18650 Li-ion battery.

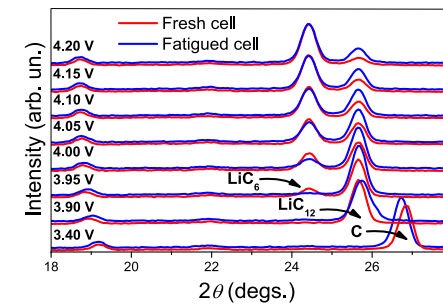


Figure 2: Enlarged sections of obtained neutron diffraction patterns from a commercial 18650 Li-ion battery (both “fresh” and “fatigued”) upon different applied charging states.

comparison to the “fresh” one. Both observations explicitly point to the fatigue of the graphite anode.

A closer inspection of the obtained diffraction data reveals a systematic broadening of the Bragg reflections for Li-intercalated carbon phases in the case of the “fatigued” battery, which might indicate a significant change of the microstructure. As this effect is already visible at low diffraction angles it can be related to a reduction in size of the carbon crystallites.

## Tomography: More lithium in the outer region

More detailed information concerning the Li-ion battery organization and its variations upon charging was obtained from neutron tomography (another non-destructive technique), whose working principle is very similar to that of X-ray and magnetic resonance imaging [3]. Radiography images were collected at the tomography scanner ANTARES [4] for different battery rotations around the cylinder axis with exposure time of 60 s, with an overall field of view  $100 \times 100 \text{ mm}^2$ . In combination with the high collimation ratio ( $L / D = 800$ ) a pixel resolution of about  $100 \mu\text{m}$  was reached. The 3D reconstruction was performed on the basis of a batch consisting of 600 single projections using a filtered back projection algorithm. Data visualization was undertaken using VGStudio Max from Volume Graphics [5].

The results of the 3D reconstruction are shown in figure 3a. As one can see the resolution of neutron tomography experiment was sufficient to resolve the steel can, gasket, safety vent and circuits inside a Li-ion battery (fig. 3b) as well as cathode/anode layers rolled up around the Cu current collector in the centre (fig. 3c). An enlarged view of figure 3c (fig. 3d) shows an absorption gradient from the centre (green color)

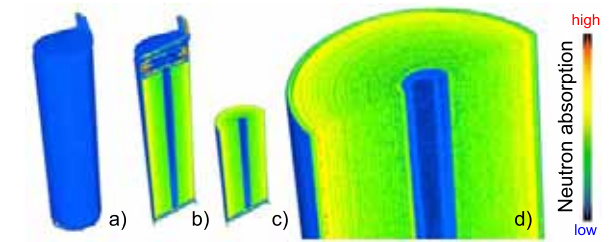


Figure 3: 3D model of commercial 18650 Li-ion battery reconstructed from neutron radiography a), its vertical cut b), its vertical and horizontal cut c) and its enlarged view d). Absorption levels are visualized by assignment to different colors.

towards the outer region (yellow color), which corresponds to an increase of absorption. As the natural isotope composition for Li is 7.5 % of  $^6\text{Li}$  and 92.5 % of  $^7\text{Li}$ , where  $^6\text{Li}$  has a very high absorption cross section, the observed absorption gradient can be attributed to the distribution of lithium inside the battery, i.e. more lithium is concentrated in the outer part of the battery.

Neutron tomography studies performed at different charging states (3.00, 4.00 and 4.20 V) resulted in a different contrast between cathode and anode layer boundaries, e.g. well resolved cathode and anode layer boundaries at 3.00 V were smeared out at 4.20 V. A derivative analysis of the observed tomography images requires more sophisticated analysis due to changes in the battery dimensions (ca.  $55 \mu\text{m}$  in diameter) upon charging/discharging from 3.0 V to 4.2 V. The smearing out of the cathode/anode layer boundaries at elevated charge levels reflects a more homogeneous Li distribution then in the discharged states, where all lithium is in the cathode and in the electrolyte. These studies unambiguously emphasize the need for neutron scattering for the investigations of serious challenges in Li-ion battery technology which still remain unanswered. A clearer understanding of these effects can be obtained from supplementary neutron scattering experiments at non-ambient conditions, allowing one to follow “live” degradation during operation.

[1] M. Hoelzel et al., Neutron News, 18, 23 (2007).

[2] T. Roisnel, J. Rodriguez-Carvajal, Mater. Sci. Forum, 118, 378 (2001).

[3] I. S. Anderson et al., Neutron Imaging and Applications: A Reference for the Imaging Community (Neutron Scattering Applications and Techniques), Springer, New York, USA (2009).

[4] <http://einrichtungen.physik.tu-muenchen.de/antares/>

[5] <http://www.volumegraphics.com/products/vgstudio-max/>

# Monoclinic and orthorhombic pyroxene-type $\text{CoGeO}_3$ : Magnetic properties and spin structure

G. J. Redhammer<sup>1</sup>, A. Senyshyn<sup>2</sup>, G. Roth<sup>3</sup>, G. Amthauer<sup>1</sup>

<sup>1</sup>Universität Salzburg, Fachbereich Materialforschung und Physik, Abteilung Mineralogie, Salzburg, Austria

<sup>2</sup>Technische Universität München, Forschungs-Neutronenquelle Heinz Maier-Leibnitz (FRM II), Garching, Germany

<sup>3</sup>RWTH Aachen, Institut für Kristallographie, Aachen, Germany

We report here on the magnetic ordering and determination of the commensurate magnetic spin structure of monoclinic and orthorhombic pyroxene-type  $\text{CoGeO}_3$  polymorphs from high resolution neutron diffraction data collected at the SPODI diffractometer. Both the  $C2/c$  and  $Pbca$  modification, show transitions to antiferromagnetically ordered spin states below 36 K and 33 K, respectively. The magnetic structures obtained are much more complicated than stated in the literature so far and may serve as models for other pyroxene type compounds.

The group of pyroxenes, which occur as impressive minerals in nature, have a rich crystal-chemistry and have therefore been the subject of great interest in the geosciences for a long time. Their structural topology, with quasi one-dimensional infinite chains of transition-metal bearing octahedral M1 sites and laterally attached 6-fold coordinated M2 sites (forming M1/ M2 site bands parallel to the crystallographic  $c$ -direction and inter-connected via infinite chains of  $\text{GeO}_4$  tet-

rahedra) and the recent discovery of multiferroic behaviour among some pyroxenes have also made this mineral group of more general interest for condensed matter research. This accounts especially for their magnetic properties at low temperatures. It is the concurring interplay between magnetic super-exchange within and between the M-site chains/ bands, which finally determines the overall bulk magnetic properties. A detailed knowledge of the magnetic spin structure is therefore of essential importance for understanding of the magnetic properties of these compounds. While in multiferroic  $\text{LiFeSi}_2\text{O}_8$  or in  $\text{LiFeGe}_2\text{O}_6$  [1] for example only the M1 site is occupied by a magnetic active transition-metal element ( $\text{Fe}^{3+}$ ), the title compounds have  $\text{Co}^{2+}$  in both the M1 and M2 sites, thus offering additional magnetic exchange pathways not studied the literature to date.

Synthetic polycrystalline samples in batches of 12 g were used for the powder diffraction experiments on the SPODI diffractometer. Between 3 K and 60 K data were acquired at wavelengths of  $\lambda = 1.5482 \text{ \AA}$  and  $2.537 \text{ \AA}$  down to  $d$ -values of

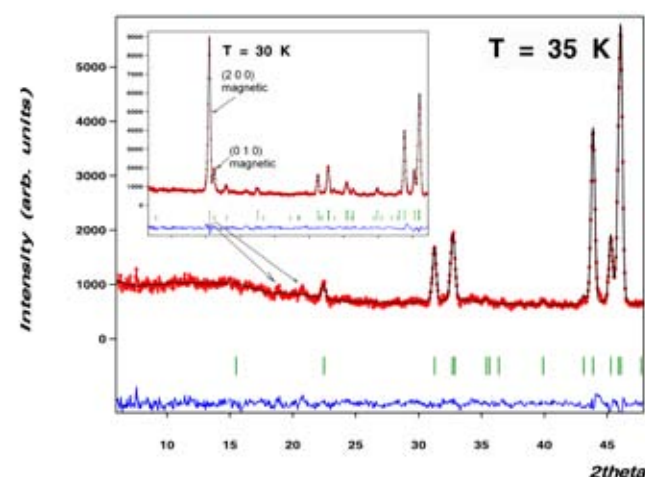


Figure 1: Low angle parts of the neutron diffraction pattern of  $Pbca \text{CoGeO}_3$  ( $\lambda = 2.537 \text{ \AA}$ ), collected at 35 K compared with the 30 K data. The presence of additional reflections, namely  $(2\ 0\ 0)$  and  $(0\ 1\ 0)$ , which are purely magnetic in nature, is evident.

$0.81 \text{ \AA}$  and  $1.33 \text{ \AA}$ , respectively. The high quality of the data allowed us to refine the nuclear structure and determine the magnetic spin structures of the two different  $\text{CoGeO}_3$  polymorphs and to elucidate the variation of the magnetic moments and secondary structural parameters (e.g. bond lengths and bonding angles) with temperature in great detail.

The onset of the three dimensional magnetic ordering in both compounds is clearly detectable through the appearance of additional Bragg-peaks at 35 K, which quickly gain intensity towards lower temperatures (see fig. 1).

In both modifications of  $\text{CoGeO}_3$ , the arrangement of magnetic spins is more complicated than has been stated in the literature to date. Until now only a simple magnetic structure with the magnetic moment-vectors on both the sites M1 and M2 parallel to a crystallographic axis has

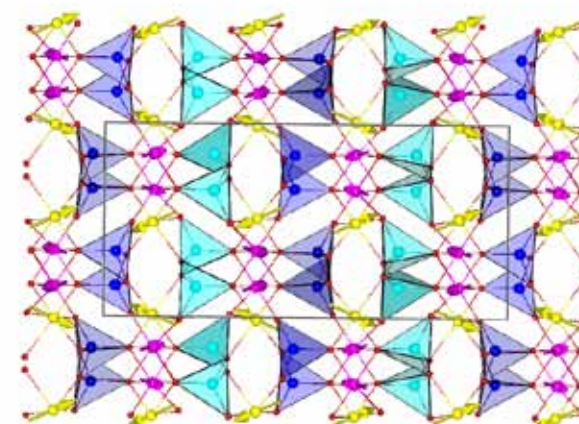


Figure 2: Diagram of the magnetic structure of orthorhombic  $\text{CoGeO}_3$ .

been proposed. The high resolution SPODI-data allowed us to clearly demonstrate that such a simple model is inadequate and no longer valid. In contrast, we have found that the magnetic moment vectors of  $\text{Co}^{2+}$  are aligned mainly in the  $a$ - $c$  plane of the structure (see fig. 2). Within the chains of octahedrally coordinated M1 sites, the  $\text{Co}^{2+}$  atoms are ferromagnetically (parallel) coupled. The coupling between neighbouring M1 chains, however, is antiferromagnetic (anti-parallel). At the M2 sites, the magnetic spins of  $\text{Co}^{2+}$  are parallel to each other within the same



Figure 3: SPODI in the experimental hall.

band of M1 and M2 sites, but are anti-parallel from band to band. The coupling of  $\text{Co}^{2+}$  atoms between M1 and M2 sites may be described as ferromagnetic, however, the spins at M1 and M2 do not have the same orientation, but are rotated away one another by  $54.5(5)^\circ$ . The magnetic structures of monoclinic and orthorhombic  $\text{CoGeO}_3$  obtained are qualitatively similar and differ mainly in the non-collinear arrangement of spins, especially at the M2 site in orthorhombic  $\text{CoGeO}_3$ . More details on this study can be found in [2].

[1] G. J. Redhammer et al., J. Solid State Chem., 182, 2374 (2009).

[2] G. J. Redhammer et al., Phys. Chem. Miner. (<http://dx.doi.org/10.1007/s00269-009-0335-x>) (2009).

# Structures, phase transitions and hydration of $\text{Ba}_4\text{Nb}_2\text{O}_9$ and $\text{Ba}_4\text{Ta}_2\text{O}_9$

C. D. Ling<sup>1,2</sup>, M. Avdeev<sup>2</sup>, M. Hoelzel<sup>3</sup>

<sup>1</sup>The University of Sydney, School of Chemistry, Sydney, Australia

<sup>2</sup>ANSTO, Bragg Institute, Menai, Australia

<sup>3</sup>Technische Universität Darmstadt, FB Material- und Geowissenschaften, Darmstadt, Germany

The high-temperature form of  $\text{Ba}_4\text{Nb}_2\text{O}_9$  is easily quenched to room temperature, whereupon it hydrates to form a stoichiometric phase  $\gamma\text{-Ba}_4\text{Nb}_2\text{O}_9 \cdot 1/3\text{H}_2\text{O}$ . This phase exhibits good protonic and oxide ionic conduction due to the presence of 2D layers containing  $\text{NbO}_4$  tetrahedra and discrete OH groups. The low-temperature form of  $\text{Ba}_4\text{Ta}_2\text{O}_9$  is isostructural with that of  $\text{Ba}_4\text{Nb}_2\text{O}_9$  and undergoes a reconstructive phase transition at a similar temperature; however, the high temperature forms are different. The tantalates hydrate to a greater extent than the niobates, but show slightly lower protonic and oxide ionic conduction.

## Potential use in fuel cells

Materials that exhibit “mixed” conductivity (e.g., oxide ions, protons, and electrons) have potential applications as fuel cells membranes, electrodes, batteries and sensors. A number of niobium and tantalum oxides have recently been shown to exhibit mixed conductivity associated with the uptake of protons at moderate temperatures (below  $\sim 600^\circ\text{C}$ ).

In this study, we investigated  $\text{Ba}_4\text{Nb}_2\text{O}_9$  and  $\text{Ba}_4\text{Ta}_2\text{O}_9$ . These ostensibly simple solid-state compounds were first synthesized in 1965 by Blasse. [1] The only other significant reports in the literature are by Leshchenko et al. [2-4] and Bezjak et al. [5, 6] who identified a complex sequence of structural phase transitions, but none of the structures was ever solved.

Both compounds appeared to undergo reconstructive phase transitions from low-temperature  $\alpha$  to high-temperature  $\gamma$  phases at  $\sim 1400\text{ K}$ . The  $\gamma$  phases in both cases are easily quenched to room temperature and, on re-heating, show a

series of subtle phase transitions before transforming to the  $\alpha$  phases at  $\sim 1200\text{ K}$ .

## Neutrons reveal oxygen positions

The structural transitions were investigated in an in situ high-temperature neutron powder diffraction (NPD) experiment on SPODI at FRMII. NPD has certain advantages over conventional X-ray powder diffraction (XRD) in this context: Neutrons can easily penetrate the thick walls of a furnace required to homogeneously heat a sample to above  $1400\text{ K}$ , through the transitions; and neutrons are far more sensitive to oxygen atoms in the presence of heavy metals such as Ba, Nb and Ta. Data were collected while slowly heating quenched samples of  $\gamma\text{-Ba}_4\text{Nb}_2\text{O}_9$  and  $\gamma\text{-Ba}_4\text{Ta}_2\text{O}_9$  from room temperature up to their reconstructive transitions to the  $\alpha$  phases at  $\sim 1200\text{ K}$  and then back to the  $\gamma$  phases above  $\sim 1400\text{ K}$ .

## Large voids in the structure

SPODI data were used to solve and Rietveld-refine the structures of the  $\alpha$  phases, both of which were found to adopt a geometrically frustrated structure of which  $\text{Sr}_4\text{Ru}_2\text{O}_9$  [7] is the archetype. The Rietveld fit and structure for  $\alpha\text{-Ba}_4\text{Nb}_2\text{O}_9$  are shown in figure 1. The structure contains isolated  $(\text{Nb,Ta})_2\text{O}_9$  face-sharing octahedral dimers, separated by very large voids. The structure of  $\gamma\text{-Ba}_4\text{Ta}_2\text{O}_9$  was also solved using SPODI data as a 6H-type perovskite, which is built of similar  $\text{Ta}_2\text{O}_9$  dimers.

Thermogravimetry (TGA) and impedance measurements [8, 9] indicate that all these phases absorb significant amounts of water (up to  $0.5\text{ H}_2\text{O}$  per formula unit) below  $\sim 600\text{ K}$ , becoming significant proton and oxide ion conductors. However, the locations of the mobile oxide ions

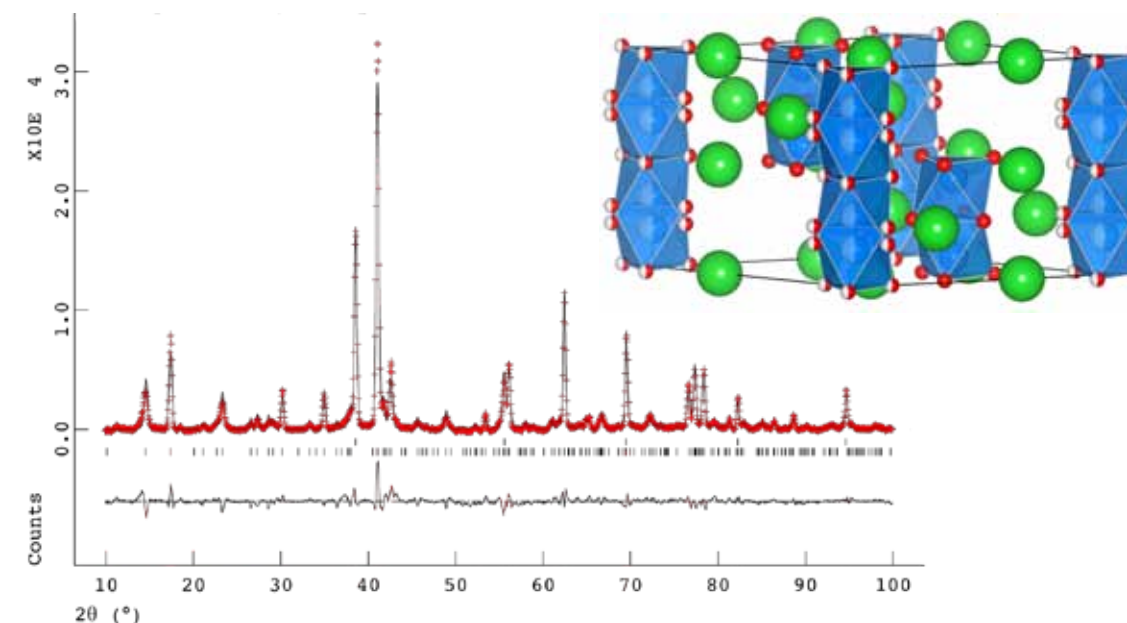


Figure 1: Diffractogram and structure of  $\alpha\text{-Ba}_4\text{Nb}_2\text{O}_9$ . Measured values are indicated by red crosses, the black line corresponds to the model calculation.

and protons from absorbed water within the structures have not yet been determined.

The most interesting case was  $\gamma\text{-Ba}_4\text{Nb}_2\text{O}_9$ , which was found to adopt an entirely new structure type. In addition to  $\text{Nb}_2\text{O}_9$  dimers, this structure contains  $\text{NbO}_4$  tetrahedra and discrete OH groups (see fig. 2). Its empirical formula can be written as  $\text{Ba}_6\text{Nb}_3\text{O}_{14}\text{H}$  or  $\gamma\text{-Ba}_4\text{Nb}_2\text{O}_9 \cdot 1/3\text{H}_2\text{O}$ . The existence of a stable hydrated phase of this stoichiometry was confirmed by TGA. This phase was found to be the best protonic and oxide ionic conductor investigated, presumably due to the presence of conductive 2D layers consisting of isolated  $\text{NbO}_4$  tetrahedra and discrete OH groups.

## Unique mechanisms for hydration

This study has resulted in the identification and characterisation of a series of promising new mixed conductors. A great deal of work remains to be done to fully understand the properties of these materials. The case of  $\gamma\text{-Ba}_4\text{Nb}_2\text{O}_9$  is particularly exciting, representing a new structure type and – potentially – a unique mechanism for hydration and ionic conduction. Hydration even appears to play a role in stabilizing  $\gamma\text{-Ba}_4\text{Nb}_2\text{O}_9$  at low temperatures, with the  $\gamma\text{-}\alpha$  transition on re-heating a quenched sample occurring at higher temperatures in humid atmospheres. The preliminary results described here were published in two papers. [8, 9]

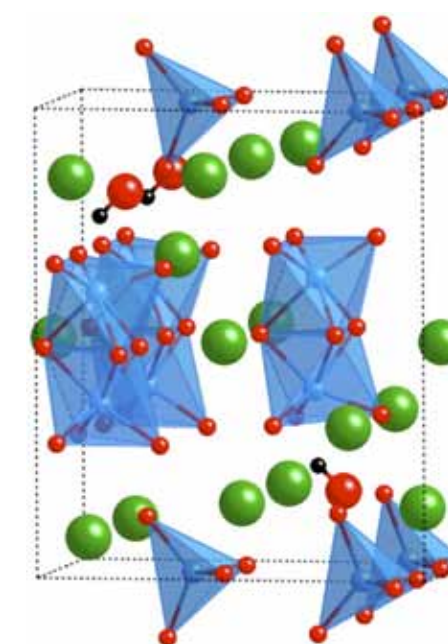


Figure 2: Structure of  $\gamma\text{-Ba}_4\text{Nb}_2\text{O}_9$ . Green atoms symbolize barium, red correspond to oxygen, blue symbolize niobium and hydrogen atoms are depicted in black.

- [1] G. Blasse, Eur. J. Inorg. Chem., 27, 993 (1965).
- [2] P. P. Leshchenko et al., Inorg. Mater., 21, 227 (1985).
- [3] P. P. Leshchenko et al., Vestn. Mosk. Univ. Ser. 2: Khim., 20, 148 (1979).
- [4] M. V. Paromova et al., Vestn. Mosk. Univ. Ser. 2: Khim., 17, 499 (1976).
- [5] J. Bezjak et al., J. Eur. Ceram. Soc., 28, 2771 (2008).
- [6] J. Bezjak et al., J. Am. Ceram. Soc., 92, 1806 (2009).
- [7] C. Dussarrat et al., Eur. J. Solid State Inorg. Chem., 32, 3 (1995).
- [8] C. D. Ling et al., Chem. Mater., in press (2010).
- [9] C. D. Ling et al., Chem. Mater., 21, 3853 (2009).

# Towards lead-free ferroelectrics: A neutron study under real operating conditions

M. Hinterstein<sup>1</sup>, M. Hoelzel<sup>1</sup>, H. Fuess<sup>1</sup>

<sup>1</sup>Technische Universität Darmstadt, FB Material- und Geowissenschaften, Darmstadt, Germany

The electrical field induced strain in 92%Bi<sub>0.5</sub>Na<sub>0.5</sub>TiO<sub>3</sub>-6%BaTiO<sub>3</sub>-2%KNN polycrystalline ceramic is shown to be the result of an electrical field induced phase transformation from pseudocubic tetragonal to rhombohedral symmetry. In combination with transmission electron diffraction, field induced domain formations could be linked to this phase transition. Superlattice reflections originating from oxygen octahedral tilting indicate a change from an a<sup>0</sup>a<sup>0</sup>c<sup>+</sup> tilt system to a<sup>-</sup>a<sup>-</sup>a<sup>-</sup>. A newly developed sample environment for neutron powder diffraction with applied electrical field was used to investigate the structural nature of the transformation.

Materials containing lead, such as Pb(ZrTi)O<sub>3</sub> (PZT), Pb(Mg<sub>1/3</sub>Nb<sub>2/3</sub>)O<sub>3</sub>-PbTiO<sub>3</sub>, and Pb(Zn<sub>1/3</sub>Nb<sub>2/3</sub>)O<sub>3</sub>-PbTiO<sub>3</sub> are currently used in industry. However, the toxicity of lead oxide and its high vapour pressure during processing have led to a demand for alternative lead-free environmentally friendly piezoelectric materials. Two promising lead free systems form the basis of our investigation. (Bi<sub>0.5</sub>Na<sub>0.5</sub>)TiO<sub>3</sub>-BaTiO<sub>3</sub> (BNT-BT) [1] on the one hand and K<sub>0.5</sub>Na<sub>0.5</sub>NbO<sub>3</sub> (KNN) [2] on the other. Rödel et al. [3-5] showed that the promising properties of BNT-BT can be improved by adding several percent of KNN. BNT-BT-KNN ceramics can deliver a giant recoverable strain (0.45 %), higher than that ever obtained with prominent ferroelectric PZT-ceramics and comparable to strains obtained in Pb-based antiferroelectrics [6]. Two structural modifications are reported in the literature for the parent system BNT: A tetragonal high temperature phase with space group P4bm exhibiting an a<sup>0</sup>a<sup>0</sup>c<sup>+</sup> tilt system of the oxygen octahedra [7] and a low tempera-

ture rhombohedral phase with space group R3c with an a<sup>-</sup>a<sup>-</sup>a<sup>-</sup> tilt system [8]. Recently, Kling et al. showed by transmission electron microscopy (TEM) that the application of an electrical field to a domain free material such as BNT-BT-KNN results in the formation of domain structures [9].

## New sample environment developed

The sample of the composition 0.92(Bi<sub>1/2</sub>Na<sub>1/2</sub>)TiO<sub>3</sub>-0.06BaTiO<sub>3</sub>-0.02(K<sub>1/2</sub>Na<sub>1/2</sub>)NbO<sub>3</sub> ((1-x-y)BNT-xBT-yKNN) was synthesised by conventional ceramic fabrication methods via calcination of Bi<sub>2</sub>O<sub>3</sub>, Na<sub>2</sub>CO<sub>3</sub>, K<sub>2</sub>CO<sub>3</sub>, BaCO<sub>3</sub>, TiO<sub>2</sub> and Nb<sub>2</sub>O<sub>5</sub> powders at 900 °C for 3 hours and sintering at 1150 °C for 3 hours.

Neutron powder diffraction measurements were carried out on the SPODI powder diffractometer at the neutron source FRM II at an incident wavelength of 1.548 Å. The polycrystalline sintered sample of cylindrical form had a height of 5.5 mm and a diameter of 10 mm. For electrical contacts, silver electrodes of a thickness of 40 nm and a diameter of 9 mm were sputtered onto the samples from both sides. The electrodes were fired at 350 °C.

For in situ neutron measurements with electrical field we developed a new sample environment. A cylindrical aluminium container with a wall thickness of 2 mm, 120 mm height and a diameter of 120 mm framed the sample environment. The sample environment is evacuated to around 1 mbar and then flooded with the electrically insulating gas SF<sub>6</sub> to a pressure of around 1.5 bar to assure electrical insulation and to avoid sparkovers. The electrical field is applied statically with a high voltage power supply FuG HCP 35-35000. For this setup the field vector is

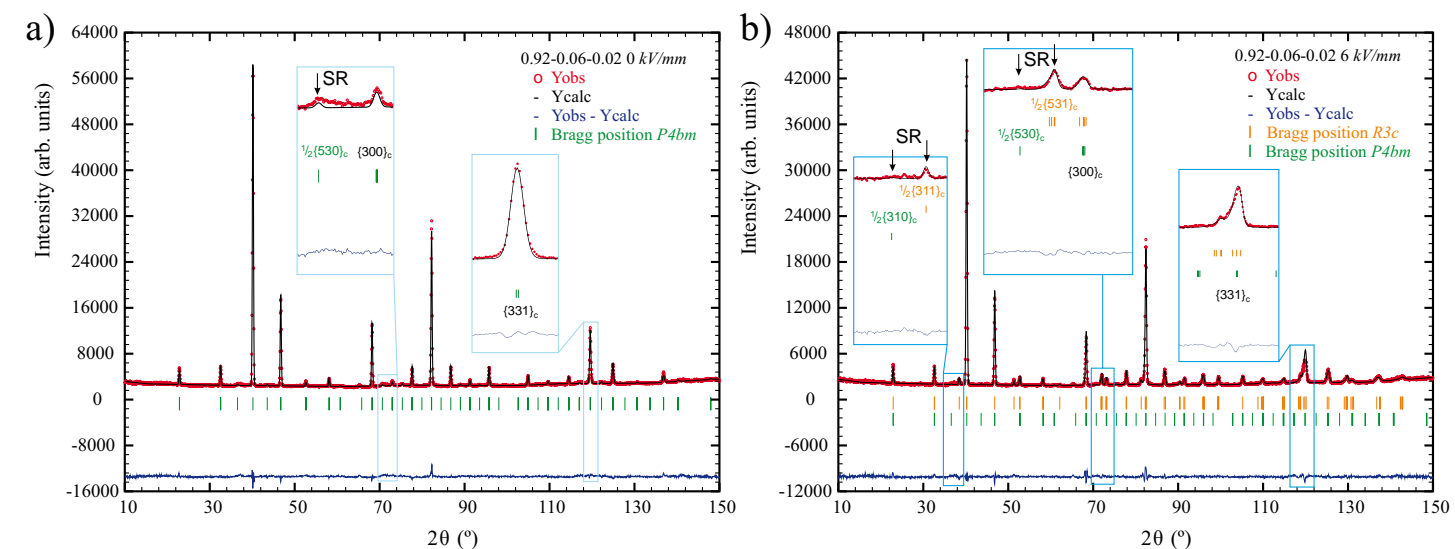


Fig. 1: Diffraction pattern of a) an unpoled sample and b) a sample at 6 kV/mm. The insets illustrate superlattice reflections.

perpendicular to the scattering plane, in contrast to all other existing in situ sample environments.

## Superlattice reflections

A measurement of the initial state of the sintered pellet exhibited a near cubic structure with weak tetragonal superlattice reflections of the type 1/2{00c}. The Rietveld refinement with space group P4bm exhibited a tetragonal distortion of 0.3 % and an octahedral tilting angle of  $\omega_T = 2.2^\circ$  (fig. 1a).

With the application of an electrical field new superstructure reflections of the type 1/2{00c} arise and the diffraction pattern shows reflection splitting, which could be assigned to rhombohedral symmetry. Figure 1b shows the two phase Rietveld refinement with space groups P4bm and R3c of the poled sample at 6 kV/mm. The two insets on the left show the most intense rhombohedral superstructure reflections that arise when an electrical field is applied and the inset on the right shows the rhombohedral split {331}c reflection. The refinement yields a rhombohedral distortion angle  $\alpha = 89.86^\circ$  and an octahedral tilting angle  $\omega_R = 5.37^\circ$ . The tetragonal phase did not change considerably and still exhibits pseudocubic structure with weak octahedral tilting.

## 20 % tetragonal, 80 % rhombohedral

A detailed analysis of the structural changes with applied electrical field is possible with the newly developed in situ neutron diffraction sample environment. The Rietveld refinement with the data yields a phase transition from 100 % tetragonal

to 20 % tetragonal and 80 % rhombohedral for 6 kV/mm. This field-induced phase transition is governed by the formation of rhombohedral superlattice reflections. Compared to the octahedral tilting angle of the initial state ( $\omega_T = 2.2^\circ$ ) the rhombohedral tilting is stronger ( $\omega_R = 5.37^\circ$ ). As Kling et al. have shown, the application of an electrical field to this material leads to domain formations [9]. The large field-induced strain [3] originates from the strong rhombohedral lattice distortion and is compensated for by octahedral tilting and domains. The large macroscopic strain and domain formations that occur when an electrical field is applied could be correlated with a field-induced phase transition from P4bm to R3c. This phase transition is accompanied by a change in the oxygen octahedral tilt system from a<sup>0</sup>a<sup>0</sup>c<sup>+</sup> to a<sup>-</sup>a<sup>-</sup>a<sup>-</sup>. The combination of in situ TEM with in situ neutron diffraction correlates giant recoverable strain [3] and the formation of domain walls [9] with structural changes.

- [1] T. Takenaka et al., Jap. J. Appl. Phys., 30 (9B), 2236 (1991).
- [2] L. E. Cross, Nature, 181, 178 (1958).
- [3] S.-T. Zhang et al., Appl. Phys. Lett., 91, 112906 (2007).
- [4] S.-T. Zhang et al., J. Appl. Phys., 103, 034107 (2008).
- [5] S.-T. Zhang et al., J. Appl. Phys., 103, 034108 (2008).
- [6] Y. J. Yu, R. N. Singh, J. Appl. Phys., 94, 7250 (2003).
- [7] G. O. Jones, P. A. Thomas, Acta Crystallogr. B, 58, 168 (2002).
- [8] G. O. Jones, P. A. Thomas, Acta Crystallogr. B, 56, 426 (2000).
- [9] J. Kling et al., J. Am. Ceram. Soc., submitted (2010).

# Long-range order in nanodomain FeCo alloys with ternary additions

R. Gilles<sup>1</sup>, M. Hofmann<sup>1</sup>, Y. Gao<sup>2</sup>, F. Johnson<sup>2</sup>, L. Iorio<sup>2</sup>, M. Larsen<sup>2</sup>, F. Liang<sup>1,3</sup>, M. Hoelzel<sup>4</sup>, B. Barbier<sup>5</sup>

<sup>1</sup>Technische Universität München, Forschungsneutronenquelle Heinz Maier-Leibnitz (FRM II), Garching, Germany

<sup>2</sup>GE Global Research, One Research Circle, Niskayuna, USA

<sup>3</sup>China Institute of Atomic Energy, Department of Nuclear Physics, Beijing, China

<sup>4</sup>Technische Universität Darmstadt, FB Material- und Geowissenschaften, Darmstadt, Germany

<sup>5</sup>Universität Bonn, Steinmann Institut für Geologie, Mineralogie, Paläontologie, Bonn, Germany

**T**ailoring FeCo alloys by the addition of the ternary elements Pt, Pd, Mn, Ir, and Re might improve the mechanical properties of these industrially important engineering materials. In the composition range 30-70 % Co, FeCo alloys undergo a continuous order-disorder phase transition at the equiatomic composition at the maximum temperature of 730 °C. The effect of temperature and composition on the degree of long-range order in six different alloys was investigated using neutron diffraction. The ordering is consistent with growth of the antiphase domains during the annealing process.

FeCo alloys are widely used as engineering materials due to their very high saturation magnetisation and Curie temperature. These alloys play an important role in applications that require soft magnetic materials, such as electrical generators and motors. Further examples are transformer cores, magnetically driven actuators, pole tips for high field magnets and solenoid valves. For many industrial applications, the challenge is to increase the tensile strength and the ductility of FeCo alloys while maintaining their magnetic performance. Methods used to meet this challenge include alloy design (e.g. addition of certain ternary metals such as Ni, V, Nb, Ta, Cr, Mo etc.), annealing and advanced deformation processing.

## Experimental procedure

Ingots of the alloys  $\text{Fe}_{70}\text{Co}_{30}$  and  $\text{Fe}_{67}\text{Co}_{30}\text{X}_3$ , with X = Mn, Re, Ir, Pd, Pt (atomic %) were prepared by vacuum induction melting, a subsequent heat treatment at 1000 °C for 48 hours and finally slowly cooling down to room temperature

in the furnace. All alloys were characterised by x-ray diffraction using Cu K $\alpha$  radiation. As Fe and Co have similar scattering factors for x-rays, no structural ordering of the alloying elements of the bcc type structure can be seen. The different neutron scattering lengths ( $b = 9.45$  fm for Fe and  $b = 2.49$  fm for Co), however, makes it possible to observe the structural order involving Fe and Co in a neutron diffraction measurement. Therefore measurements were made at the neutron facility FRM II. Full diffraction patterns were taken at ambient temperature and at  $T = 700$  °C at the high resolution powder diffractometer SPODI, whereas the high temperature measurements to follow the order-disorder phase transition were taken at the diffractometer STRESS-SPEC. The 2-dimensional area detector used in this work covers around  $15^\circ$  in  $2\theta$ . This makes it possible to follow the evolution of a superlattice reflection and a fundamental Bragg reflection in the temperature range 25 to 700 °C.

## Dark field TEM measurements

Full diffraction patterns were established at the instrument SPODI to determine the lattice constants and structural details of all the alloys. The superlattice peaks of all the alloys were broadened up to a few degrees, from which the domain sizes were evaluated. The FeCoPt sample was then taken as an example to show how the physical parameters are extracted from the measurements. The results are summarised in table 1.

The long-range order parameter S can be calculated using the relationship  $S = a \times [I(100) / I(200)]^2$  where a is a constant and I the integrated intensity of reflection (hkl). A fit of S using the equation  $S = c \times (1 - T/T_c)^\beta$  with c being a con-

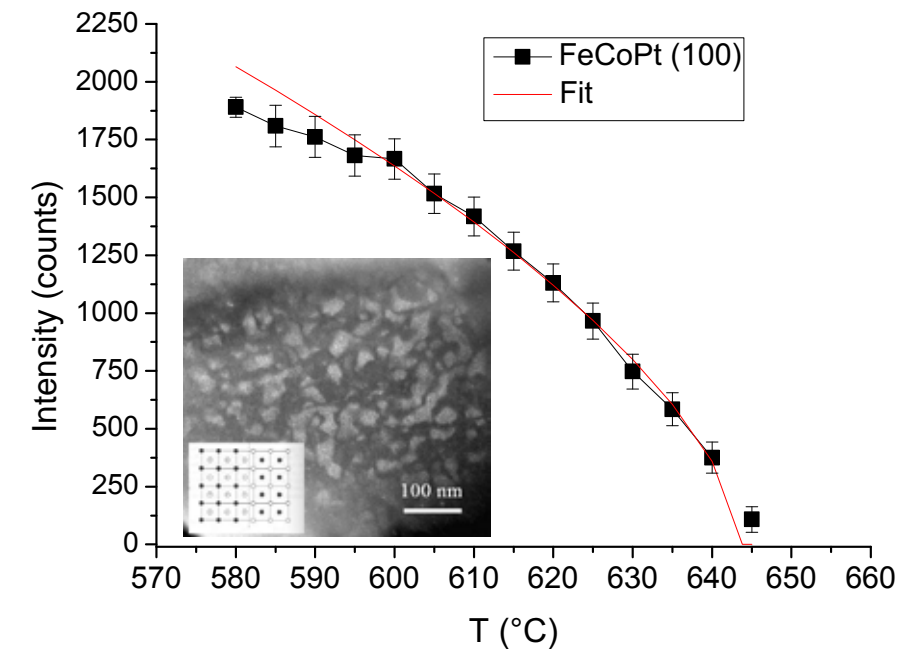


Figure 1: Determination of the  $T_c$  temperature and the parameter b from the intensity of (100) peak of the FeCoPt sample. The long-range order parameter S is fitted by  $S = c \times (1 - T/T_c)^\beta$ . Inset: Dark field TEM image of FeCoPt sample after annealing for 12 hours at 548 °C. Bright and dark regions in the image are ordered domains separated by antiphase boundaries.

stant and  $\beta$  as a critical exponent, determines the transition temperature  $T_c$  and a long-range order parameter S. In figure 1 the intensity of (100) is plotted against temperature for FeCoPt. The calculations reveal parameter  $\beta$  values of 0.31(5) which are close to those expected according theoretical calculations of the Ising model ( $T < T_c$ ,  $b = 0.312(5)$ ).

Several dark field TEM measurements were carried out to verify the assumption that the domain size extracted from the neutron diffraction results is a measure of the extent of the antiphase domain boundaries. Figure 2 shows a dark field TEM image of the FeCoPt sample annealed at 548 °C for 12 hours to create large ordered domains. The dark field image was generated from the  $g = \{001\}$  diffraction spot and shows a mixture of bright and dark areas of ordered regions within the grains of the microstructure.

Material	FeCo	FeCoMn	FeCoPt	FeCoPd	FeCoRe	FeCoIr
a [nm] at RT	0.28655(1)	0.28681(1)	0.28718(3)	0.28718(2)	0.28671(2)	0.28702(3)
$T_c$ [°C]	no (100) peak	586(5)	644(2)	604(3)	601(7)	603(1)
S value	no (100) peak	0.28(3)	0.40(2)	0.43(2)	texture!	0.13(2)
(000) Fe		0.84(3)	0.90(2)	0.91(2)		0.75(2)
( $\frac{1}{2}$ $\frac{1}{2}$ $\frac{1}{2}$ ) Co		0.44(3)	0.50(2)	0.51(2)		0.35(2)
Domain size at RT / 130 °C [nm]		3(1)	12(1)	7(1)	5(2)	7(2)

Table 1: Lattice constant a,  $T_c$  temperature, long-range order S, occupation of atoms, lattice shift, and domain size determination of different FeCoX alloys.

[1] R. Gilles et al., Metall. Mater. Trans. A., (2009).

# Anomalous structural behaviour and complex magnetic properties of Co-olivine, $\text{Co}_2\text{SiO}_4$

A. Sazonov<sup>1,2</sup>, M. Meven<sup>1</sup>, V. Hutanu<sup>1,2</sup>, G. Heger<sup>2</sup>

<sup>1</sup>Technische Universität München, Forschungs-Neutronenquelle Heinz Maier-Leibnitz (FRM II), Garching, Germany

<sup>2</sup>RWTH Aachen, Institut für Kristallographie, Aachen, Germany

Due to their geological importance many studies of the olivine-type oxides have been performed at high temperatures and pressures. However, there is a significant lack of information on the structural and magnetic properties of such materials at low temperatures.  $\text{Co}_2\text{SiO}_4$  crystallizes in the olivine structure with two crystallographically non-equivalent Co positions and shows complex antiferromagnetic ordering, including super-exchange interactions, below 50 K. We successfully performed detailed magnetic structure analysis based on polarized and non-polarized neutron and X-ray diffraction experiments on  $\text{Co}_2\text{SiO}_4$  and studied its anomalous thermal expansion.

The general chemical formula for olivine, one of the most common minerals on Earth, is  $\text{A}_2\text{BX}_4$ . The relatively large cations  $\text{A}^{2+}$  occupy the octahedral sites, whereas the small cations  $\text{B}^{4+}$  occupy the tetrahedral sites.  $\text{M}_2\text{SiO}_4$  (M-transi-

tion metal) olivines have an orthorhombic crystal structure (space group Pnma): M1 is located on a centre of symmetry and M2 on a mirror plane. At low temperatures, olivines are antiferromagnetically ordered with equal magnetic and crystallographic cells. The magnetic structure is quite complex and the magnetic moments and temperature dependence are different for the M1 and M2 sites.  $\text{Co}_2\text{SiO}_4$  was chosen as the focus for detailed magnetic studies.

## Anomalous thermal expansion of $\text{Co}_2\text{SiO}_4$

Accurate lattice parameters of  $\text{Co}_2\text{SiO}_4$  were obtained from both synchrotron X-ray (B2, HASYLAB/DESY, Germany) and neutron (D20, ILL, France) powder diffraction. To obtain a greater accuracy of both the nuclear and magnetic structure parameters, a  $\text{Co}_2\text{SiO}_4$  single crystal was studied on the four-circle diffractometer HEiDi.

The diffraction experiments indicate a small, but significant, anomaly in the anisotropic lattice expansion close to the magnetic phase transition

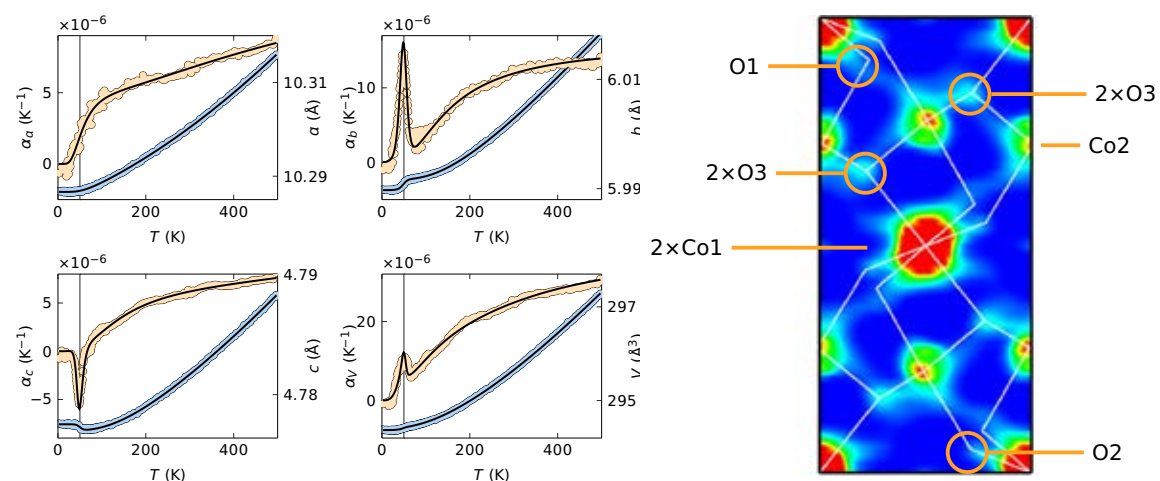


Figure 1: (left) Temperature dependencies of lattice parameters, cell volume and thermal expansion coefficients from powder neutron diffraction measurements of  $\text{Co}_2\text{SiO}_4$ . (right) Maximum-entropy reconstruction of the magnetization density distribution of  $\text{Co}_2\text{SiO}_4$  at 70 K (projection along the  $b$  axis).

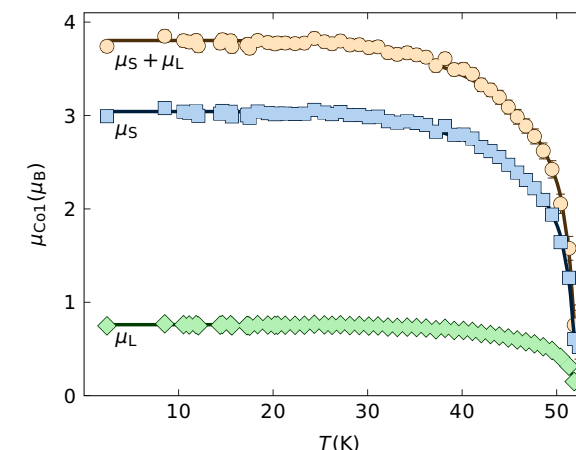
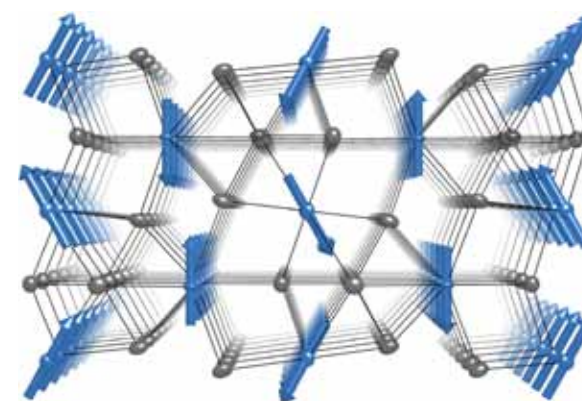


Figure 2: (left) Crystal and magnetic structures of  $\text{Co}_2\text{SiO}_4$ . (right) Temperature dependence of the Co1 spin, orbital and total magnetic moment for  $\text{Co}_2\text{SiO}_4$  according to the neutron diffraction measurements by applying the ratio  $\mu_L/\mu_S \approx 0.25$ .

at  $T_N \approx 50$  K. Below this temperature, the lattice parameter  $b$  is shortened abruptly, whereas  $c$  increases and  $a$  remains constant. The resulting unit cell volume shows anomalous contraction below 50 K (fig. 1, left). The orthorhombic space group symmetry Pnma is retained in the temperature range 2.5 K to 500 K.

In order to parameterize the cell parameters precisely, the measured molar specific heat data were fitted taking into account the Debye-Einstein lattice contribution, the magnetic part reflecting the antiferromagnetic phase transition and the Schottky contribution due to the spin-orbit splitting of the  $\text{Co}^{2+}$  ground state. The results show that the anomaly in the lattice parameters and the unit cell volume is caused by magnetostriction.

## Magnetic behaviour of $\text{Co}_2\text{SiO}_4$

Polarized neutron flipping ratio measurements above  $T_N$ , with an external magnetic field of 7 T along the  $b$  axis, were used to represent the magnetization density in the unit cell. The density maps reveal a non-negligible amount of magnetic moment on the oxygen positions, indicating a delocalization of magnetic moment from Co towards neighbouring O due to the superexchange interactions (fig. 1, right). The interactions  $\text{Co2-O-Co2}$  are much stronger than those between the Co1 ions and are probably responsible for the overall antiferromagnetic behaviour.

Non-polarized neutron diffraction measurements show that the ordered magnetic structure of orthorhombic  $\text{Co}_2\text{SiO}_4$  (fig. 2, left) is described as an antiferromagnetic arrangement of the  $\text{Co}^{2+}$  magnetic moments below  $T_N \approx 50$  K (fig.

2, right), with a magnetic propagation vector  $\mathbf{k} = (0; 0; 0)$ . Detailed symmetry analysis of the magnetic structure shows that it corresponds to the orthorhombic magnetic (Shubnikov) group Pnma. The magnetic anisotropy was studied by fitting the observed magnetic susceptibility  $\chi$  (T) curves above  $T_N$  to the Curie-Weiss law.

In order to follow the thermal evolution of the magnetic structure, the temperature dependence of the Co1 and Co2 magnetic moments obtained from neutron diffraction measurements was fitted in a modified molecular field model. The precise analysis of the neutron diffraction data also shows that canting angles of the magnetic structure of  $\text{Co}_2\text{SiO}_4$  are independent of temperature, which is in agreement with its strong magnetic anisotropy. An important orbital contribution to the total magnetic moment of  $\text{Co}^{2+}$  was found from polarized neutron diffraction studies, which indicate an orbital to spin magnetic moment ratio  $\mu_L/\mu_S \approx 0.25$  (fig. 2, right).

## Summary

$\text{Co}_2\text{SiO}_4$  crystallizes in the olivine structure with two crystallographically non-equivalent Co positions and shows complex antiferromagnetic ordering below 50 K. We successfully performed detailed atomic crystal and magnetic structure analysis based on polarized and non-polarized neutron and X-ray diffraction experiments on  $\text{Co}_2\text{SiO}_4$  and studied its anomalous thermal expansion. The details of this work have been published [1-3].

[1] A. Sazonov et al., J. Phys.: Conf. Ser., (to be published), (2010).

[2] A. Sazonov et al., Acta Crystallogr. B, 65 (6), 664 (2009).

[3] A. Sazonov et al., Acta Crystallogr. B, 64 (6), 661 (2008).

# Search for ferromagnetic quantum criticality using polarized neutron imaging

A. Neubauer<sup>1</sup>, M. Schulz<sup>1,2</sup>, C. Franz<sup>1</sup>, P. Böni<sup>1</sup>, C. Pfleiderer<sup>1</sup>

<sup>1</sup>Technische Universität München, Physik Department E21, Garching, Germany

<sup>2</sup>Technische Universität München, Forschungs-Neutronenquelle Heinz Maier-Leibnitz (FRM II), Garching, Germany

Quantum criticality is widely established as a road map to new forms of elementary excitations and electronic order. We showed in proof-of-principle studies that neutron depolarization tomography on ANTARES provides a new, powerful experimental tool in the search for heterogeneities near ferromagnetic quantum criticality under hydrostatic pressure and compositional tuning.

Quantum phase transitions are phase transitions that are driven by quantum fluctuations. In practice, this implies that quantum phase transitions occur at zero temperature as a function of non-thermal control parameters such as pressure, magnetic field, uniaxial stress or chemical composition [1]. Since the many-body wavefunction of systems at a quantum phase transition are exact, a cornucopia of unexpected novel electronic states may occur. Amongst the most prominent examples are superconductivity at the border of antiferromagnetism or deep inside ferromagnetic states [2], as well as various forms

of heterogeneities [1]. The latter are viewed as partial forms of magnetic or electronic order that share certain similarities with nematic or smectic order in liquid crystals. In turn, experimental methods, that allow one to track the evolution of heterogeneities across large sample volumes as a function of temperature and non-thermal control parameters are of great interest.

We have explored the use of neutron depolarization imaging in a comprehensive search for ferromagnetic quantum criticality. Neutron depolarization imaging has recently attracted interest as a method that allows to map out magnetic fields in complex solenoids or type 2 superconductors [3]. It is hence also suited as a method for addressing scientific challenges in ferromagnetic materials. As our non-thermal control parameters, we used hydrostatic pressure and compositional tuning. Ferromagnetic quantum phase transitions have thereby long attracted great interest as a particularly simple example of a quantum phase transition.

In order to establish the best experimental setup we first performed a series of studies in which we compared various types of polarizer and analyser, notably <sup>3</sup>He, solid state benders and a periscope. For a detailed account of the advantages of the various methods we refer to Ref. [4-6]. Subsequently we demonstrated the possibility of a tomographic reconstruction [7]. Further, in a study of the weak itinerant ferro-

Figure 1: (a) A single crystal of Fe<sub>2</sub>TiSn as mounted for the radiography experiments. (b) Depolarization radiography for various temperatures. The purple shading shows strong depolarization. A strong variation of the ferromagnetic properties is observed across the entire ingot.

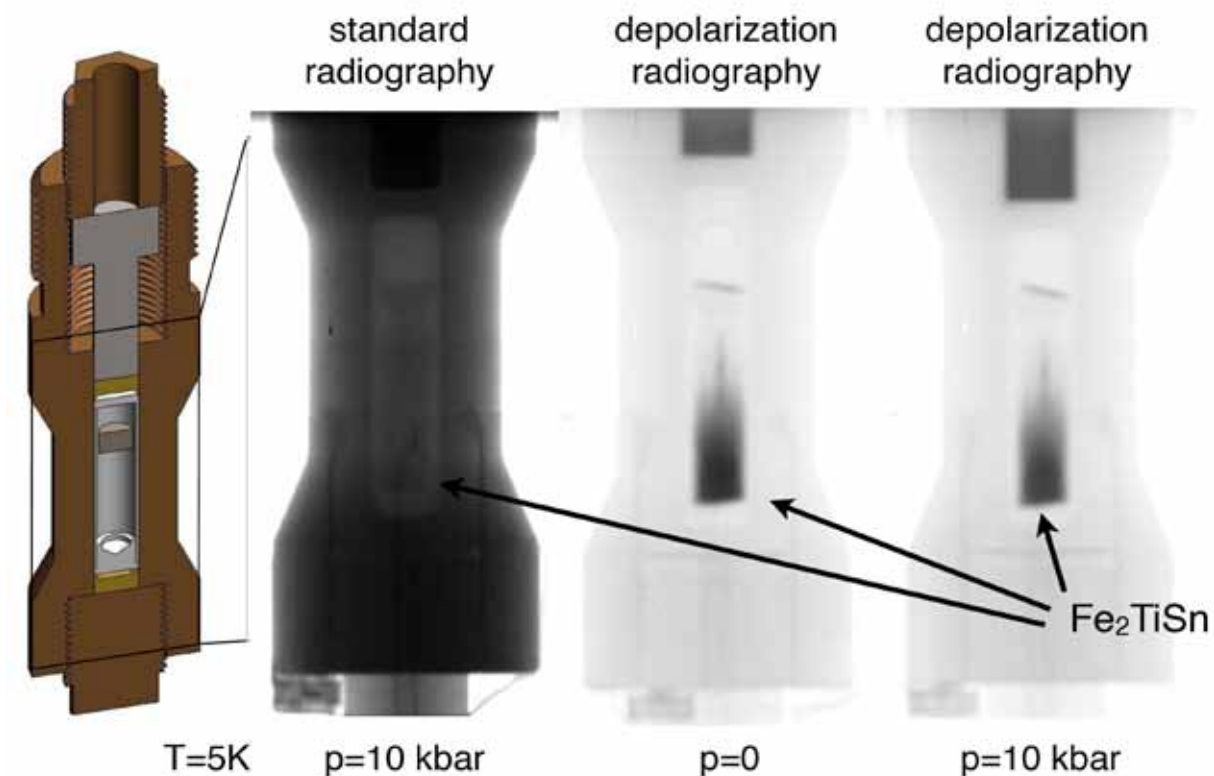
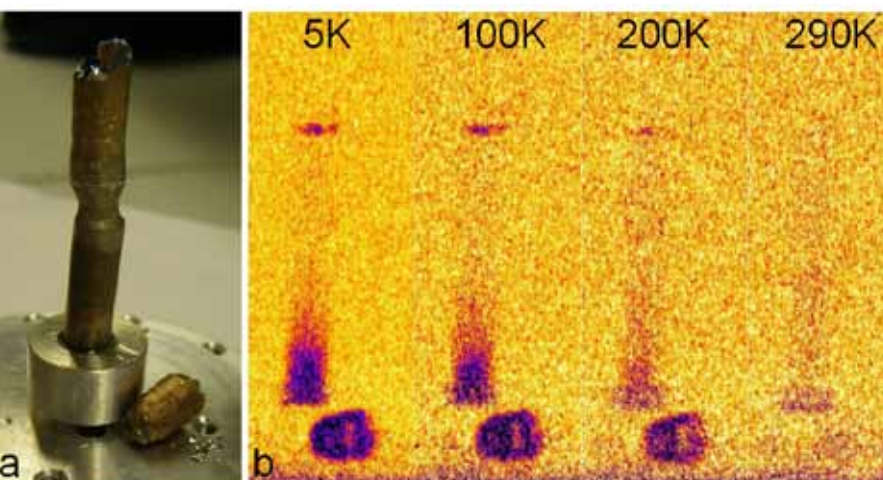


Figure 2: left: Schematic cut-away view of the clamp type pressure cell used in our studies of Fe<sub>2</sub>TiSn [8]. 2<sup>nd</sup> from left: Standard radiography of the central part of the pressure cell. Right: Depolarization radiography at ambient pressure and high pressure (10 kbar). The ferromagnetic properties are suppressed with increasing pressure. Note the lower position of the WC piston under pressure.

magnet Ni<sub>3</sub>Al we have demonstrated that neutron depolarization imaging is ideally suited to track the pressure dependence of ferromagnetic materials [8].

## Ferromagnetic properties suppressed

Recently, we applied neutron depolarization imaging to a wide range of ferromagnetic materials. An important example is the Heusler compound Fe<sub>2</sub>TiSn, which is believed to display weak ferromagnetism due to site disorder [9]. However, in single crystals of Fe<sub>2</sub>TiSn grown with optical float-zoning, we find a wide variety of magnetic properties ranging from ferromagnetism all the way to paramagnetism (fig. 1). Since the application of hydrostatic pressure tends to stabilize magnetic order in Heusler compounds [10], we also studied the pressure dependence of the ferromagnetism by means of neutron depolarization, as shown in figure 2. In our study we find, that the ferromagnetic properties are suppressed, consistent with the metallurgical complexity as the origin of the ferromagnetism. Closer inspection of the ferromagnetic regime using EDX finally revealed the presence of metallurgical segregation as the possible origin of the

ferromagnetism. Combining our imaging results with the growth conditions used in optical float-zoning promises important insights into how to improve the preparation of high purity single crystals [11,12].

Financial support through DFG Forschergruppe FOR 960 (Quantum Phase Transitions) and DFG Transregio TRR80 (From Electronic Correlations to Functionality) is gratefully acknowledged.

- [1] H. v. Löhneysen et al., Rev. Mod. Phys., 79, 001015 (2008).
- [2] C. Pfleiderer et al., Rev. Mod. Phys., 81, 1551 (2009).
- [3] N. Kardjilov, et al., Nat. Phys., 4, 399 (2008).
- [4] M. Schulz et al., Nucl. Instrum. Methods Phys. Res., Sect. A, 605, 43 (2009).
- [5] M. Schulz et al., J. Phys.: Conf. Ser., 200, 112009 (2010).
- [6] M. Schulz et al., J. Phys.: Conf. Ser. (2010).
- [7] M. Schulz et al., J. Phys.: Conf. Ser., 211, 012025 (2010).
- [8] A. Neubauer et al., to be published (2010).
- [9] A. Slebarski, et al., Phys. Rev. B, 62, 3296 (2000).
- [10] E. Sasioglu, et al., Phys. Rev. B, 71, 214412 (2005).
- [11] A. Neubauer, et al., to be published (2010).
- [12] W. Duncan et al., to be published (2010).

# Skyrmion lattices in metallic and semiconducting $B_2O$ transition metal compounds

T. Adams<sup>1</sup>, A. Bauer<sup>1</sup>, S. Mühlbauer<sup>1</sup>, A. Neubauer<sup>1</sup>, W. Münzer<sup>1</sup>, F. Jonietz<sup>1</sup>, C. Franz<sup>1</sup>, M. Schmidt<sup>3</sup>, R. Georgii<sup>1,2</sup>, P. Böni<sup>1</sup>, B. Pedersen<sup>2</sup>, A. Rosch<sup>4</sup>, C. Pfleiderer<sup>1</sup>

<sup>1</sup>Technische Universität München, Physik-Department E21, Garching, Germany

<sup>2</sup>Technische Universität München, Forschungs-Neutronenquelle Heinz Maier-Leibnitz (FRM II), Garching, Germany

<sup>3</sup>Max-Planck-Institut für Chemische Physik fester Stoffe, Dresden, Germany

<sup>4</sup>Universität zu Köln, Institut für Theoretische Physik, Köln, Germany

A comprehensive series of small angle neutron scattering measurements carried out at the cold diffractometer MIRA at FRM II showed that skyrmion lattices occur quite generally in metallic and semiconducting  $B_2O$  transition metal compounds. These studies establish magnetic order composed of topologically stable knots in the spin structure to be a general phenomenon.

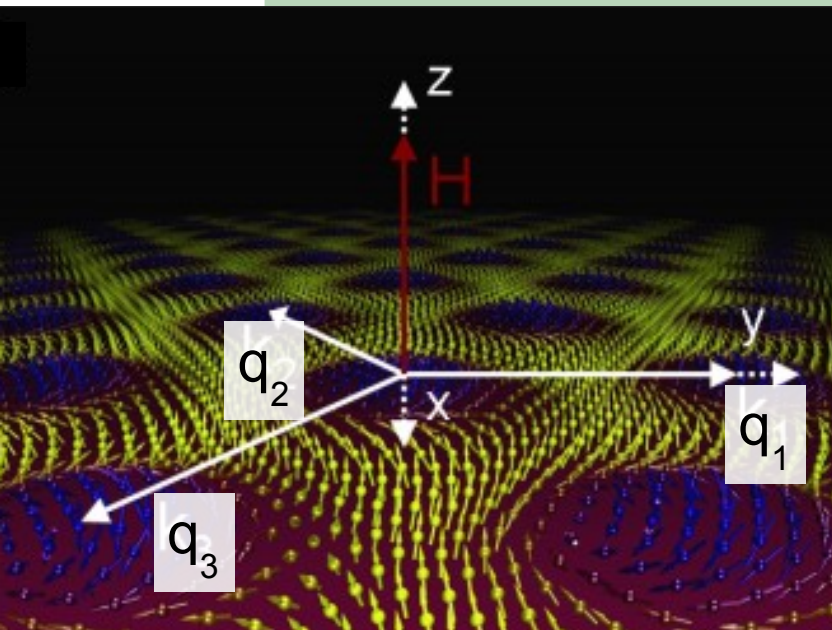


Figure 1: Top view of the skyrmion lattice in metallic and semi-conducting  $B_2O$  transition metal compounds. The skyrmion lattice represents a hexagonally closest packed arrangement of a type of vortex lines. The full spin structure is akin to a triple-Q structure with additional higher harmonic contributions (not indicated). It always stays strictly perpendicular to the applied magnetic field.

## Further materials with skyrmion lattices?

Recently, we identified a completely new type of magnetic order, a skyrmion lattice, in the cubic  $B_2O$  system MnSi [1, 2]. In the skyrmion lattice

the spins form a hexagonally closest packed arrangement of topologically stable knots parallel to an applied magnetic field (as shown in fig. 1). These knots are similar to a flux line lattice of vortices in a type II superconductor. The topological properties of this skyrmion lattice give rise to a new form of Hall effect: the topological Hall effect [2]. The observation of the skyrmion lattice in MnSi raises the possibility of further magnetic materials with skyrmion lattices as a more general phenomenon.

We have approached this question in two different ways: performing studies comprising single-crystal growth by optical float-zoning, measurements of the bulk properties and small angle neutron scattering at the cold diffractometer MIRA at FRM II.

## More complex forms of topological order

On the one hand, we performed comprehensive substitutional doping studies in the isostructural  $B_2O$  series  $Mn_{1-x}Fe_xSi$  and  $Mn_{1-x}Co_xSi$ . Here the Fe- and Co-doping of MnSi suppresses the helimagnetic transition temperature and introduces moderate site disorder. Nevertheless, we found, as before, that the skyrmion lattice forms in a small field at temperatures just below  $T_c$  and remains a stable feature of the magnetic phase diagram [3]. In addition our studies suggest the formation of more complex forms of topological order when approaching the quantum phase transition.

On the other hand we performed a detailed study of the helimagnetic order that stabilizes under substitutional Co doping of the paramagnetic insulator FeSi. Here, we find the formation of a skyrmion lattice in a doped semiconduc-

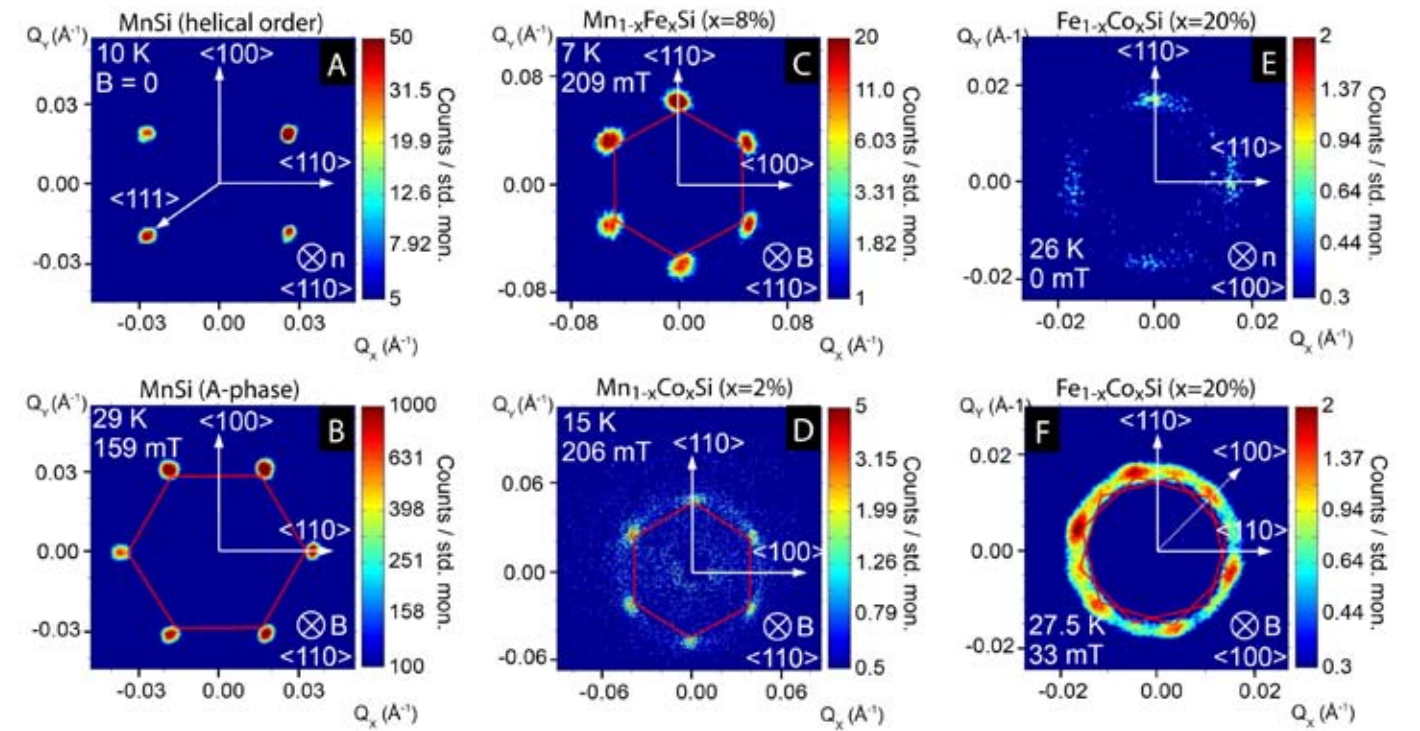


Figure 2: Typical scattering patterns as observed in our small angle neutron scattering studies of  $B_2O$  transition metal compounds at the cold diffractometer MIRA. (A) Normal helical order in MnSi, where the helical propagation vector is parallel to the  $\langle 111 \rangle$  cubic space diagonal. (B) Hexagonal scattering pattern for neutrons parallel to the skyrmion lattice in MnSi [1,2]. (C) Hexagonal scattering pattern parallel to the skyrmion lattice in  $Mn_{1-x}Fe_xSi$  ( $x = 8\%$ ) [3]. (D) Hexagonal scattering pattern parallel to the skyrmion lattice in  $Mn_{1-x}Co_xSi$  ( $x = 2\%$ ) [3]. (E) Zero-field cooled state in  $Fe_{1-x}Co_xSi$  ( $x = 20\%$ ) showing partial magnetic order (broad intensity maxima for  $\langle 110 \rangle$ ) [4]. (F) Two six-fold scattering patterns of the domain populations of the skyrmion lattice in  $Fe_{1-x}Co_xSi$  ( $x = 20\%$ ) for magnetic field parallel  $\langle 100 \rangle$  [4,5].

tor with strong site disorder [4]. Our study in  $Fe_{1-x}Co_xSi$  ( $x = 0.2$ ) revealed two additional features: First, the scattering pattern in the zero-field cooled state of  $Fe_{1-x}Co_xSi$  ( $x = 0.2$ ) is remarkably similar to partial order in MnSi under high pressure [4]. Second, the formation of skyrmion lattice domains occurs when the magnetic field is applied parallel to a 100 direction of the cubic crystal structure [5].

## A very general phenomenon

The existence of skyrmion lattices in anisotropic chiral magnets was first suggested theoretically by Bogdanov and Yablonski in 1989 using a mean-field description [6]. The theoretical description of the skyrmion lattice in MnSi [1, 2] showed that Gaussian fluctuations may stabilize skyrmion lattices in applied magnetic fields, even in cubic materials. Since the theoretical framework is very general, our experimental studies of metallic and semiconducting  $B_2O$  transition metal compounds establish the formation of skyrmion lattices as the first manifestations of a very gen-

eral phenomenon. In fact, they point to the existence of a much wider range of spin textures with non-trivial topology.

[1] S. Mühlbauer et al., Science, 323, 915 (2009).

[2] A. Neubauer et al., Phys. Rev. Lett., 102, 186602 (2009).

[3] C. Pfleiderer et al., J. Phys.: Cond. Matter, in press (2010).

[4] W. Münzer et al., Phys. Rev. B (Rapid Communications), 81, 041203 (2010).

[5] T. Adams et al., J. Phys.: Conf. Ser., in press (2010).

[6] A. N. Bogdanov, D. A. Yablonskii, JETP Lett., 68, 101 (1989).

# Spin-excitations of an optimally doped iron arsenide superconductor

D. S. Inosov<sup>1</sup>, J. T. Park<sup>1</sup>, P. Bourges<sup>2</sup>, D. L. Sun<sup>1</sup>, Y. Sidis<sup>2</sup>, A. Schneidewind<sup>3,4</sup>, K. Hradil<sup>5,4</sup>, D. Haug<sup>1</sup>, C. T. Lin<sup>1</sup>, B. Keimer<sup>1</sup>, V. Hinkov<sup>1</sup>

<sup>1</sup>Max-Planck-Institut für Festkörperforschung, Stuttgart, Germany

<sup>2</sup>Laboratoire Léon Brillouin, CEA-CNRS, CEA Saclay, Gif-sur-Yvette, France

<sup>3</sup>Technische Universität Dresden, Institut für Festkörperphysik, Dresden, Germany

<sup>4</sup>Technische Universität München, Forschungs-Neutronenquelle Heinz Maier-Leibnitz (FRM II), Garching, Germany

<sup>5</sup>Georg-August Universität Göttingen, Institut für Physikalische Chemie, Göttingen, Germany

To assess the strength of the magnetic pairing “glue” in the Fe-based superconductors, we have studied the spin excitations in optimally doped  $\text{BaFe}_{1.85}\text{Co}_{0.15}\text{As}_2$  ( $T_c = 25$  K) over a wide range of temperatures and energies using inelastic neutron scattering. In contrast to the cuprates, the spectrum follows the predictions of the theory of nearly antiferromagnetic metals without complications arising from a pseudogap or competing phases. Our data provide the foundation for the development of quantitative theories of magnetically mediated superconductivity in the iron arsenides.

Antiferromagnetic correlations persist throughout the phase diagram of iron arsenides, often coexisting with superconductivity deep within the superconducting dome. Besides, it was shown [1] that electron-phonon coupling is too weak to explain the relatively high superconducting transition temperatures observed in this class of materials. These observations have made spin

fluctuations the most likely mediator for the superconducting pairing. Similarly to the cuprates, iron-based superconductors also derive from antiferromagnetic parent compounds, but they remain metallic at all doping levels, rendering Fermi-liquid based approaches more promising than in the high- $T_c$  cuprates.

In both families of these unconventional superconductors, a redistribution of the magnetic spectral weight into a “resonance peak” heralds the onset of superconductivity. Such a resonant mode has recently been discovered both in hole-doped  $\text{Ba}_{1-x}\text{K}_x\text{Fe}_2\text{As}_2$  [2] and in electron-doped  $\text{BaFe}_{2-x}(\text{Ni}, \text{Co})_x\text{As}_2$  [3] near optimal doping.

In our recent work [4], we investigated the spin-excitation spectrum of an optimally doped single crystal of  $\text{BaFe}_{1.85}\text{Co}_{0.15}\text{As}_2$  ( $T_c = 25$  K) at temperatures up to  $T = 280$  K and energies up to  $\hbar\omega = 32$  meV. In figure 1, we compare the imaginary part of the dynamic spin susceptibility  $\chi''(Q_{\text{AFM}}, \omega)$  in the normal and superconducting states in absolute units. In the normal state we observe a broad gapless spectrum of commensurate magnetic excitations with a maximum around 20 meV at 60 K and a linear  $\omega$ -dependence for  $\omega \rightarrow 0$ . As temperature is increased to 280 K, the intensity is suppressed and the maximum of the spectrum is presumably shifted to higher energies, while the low-energy linearity is preserved. Such behaviour, with no signs of a pseudogap or incom-

Figure 1: Imaginary part of the spin susceptibility ( $Q_{\text{AFM}}, \omega$ ) in the superconducting ( $T = 4$  K) and the normal state ( $T = 60$  and 280 K). The data were obtained from the measured scattering function by correcting for the thermal population factor and were put on an absolute scale by comparing the magnetic scattering intensity to that of acoustic phonons and nuclear Bragg peaks after taking care of resolution corrections. The solid lines are guides to the eye. The dashed lines represent global fits of the formula described in the text.

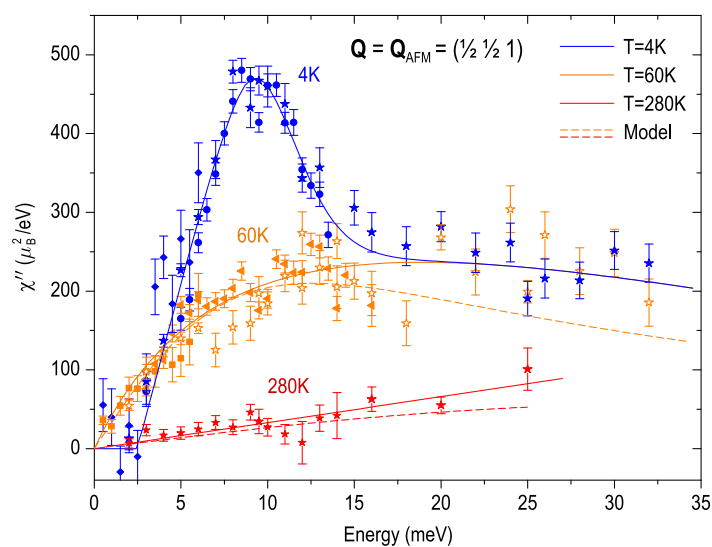
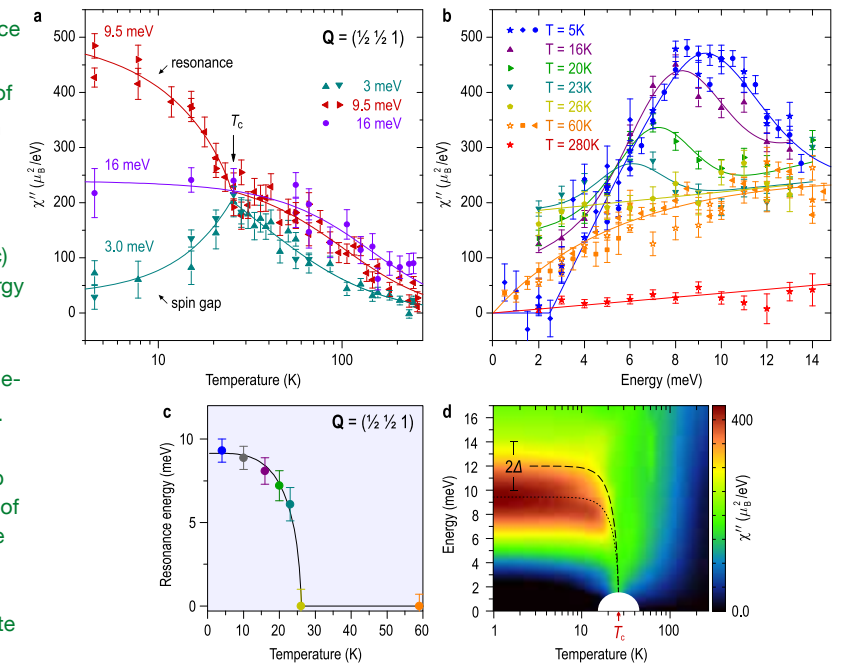


Figure 2: Energy and temperature dependence of  $\chi''(Q_{\text{AFM}}, \omega)$  and evolution of the resonance peak below  $T_c$ . a) Temperature dependence of  $\chi''(Q_{\text{AFM}}, \omega)$  at three different energies: within the spin gap (3 meV), at  $\hbar\omega_{\text{res}}$  (9.5 meV) and above  $2\Delta$  (16 meV). b) Energy scans at  $Q_{\text{AFM}}$  showing  $\chi''(Q, \omega)$  at different temperatures. The lines in a) and b) are guides to the eye. c) Temperature evolution of the resonance energy  $\hbar\omega_{\text{res}}$  defined by the maxima in panel b. The line has the same functional dependence as the superconducting gap  $\Delta$  obtained by angle-resolved photoemission, that is  $\omega_{\text{res}}(T) \propto \Delta(T)$ . d) Interpolation of the data in panels a and b showing  $\chi''(Q_{\text{AFM}}, \omega)$  in the  $\omega$ - $T$  plane for  $T$  up to 280 K. The vertical bar shows the interval of the reported  $2\Delta$  values. The dotted line is the same as the fit in c. The dashed line has the same functional dependence and tracks the average value of  $2\Delta(T)$  as a function of  $T$ . Note the logarithmic  $T$ -scale in panels a and d.



mensurate fluctuations, can be described within the theory of nearly antiferromagnetic metals [5]. The total spectral weight at 60 K, integrated over  $Q$  and  $\omega$  up to 35 meV, is  $\chi''_{60\text{K}} = 0.17\mu_B^2/\text{f.u.}$ , and is thus comparable to underdoped  $\text{YBa}_2\text{Cu}_3\text{O}_{6+x}$ . The total resonance intensity, however, is  $\chi''_{\text{res}} = \chi''_{4\text{K}} - \chi''_{60\text{K}} = 0.013\mu_B^2/\text{f.u.}$ , which is 3–5 times smaller than in  $\text{YBa}_2\text{Cu}_3\text{O}_{6+x}$ .

The spectrum in figure 1 consists of three energy intervals: The spin gap below  $\sim 3$  meV, the resonance region between  $\sim 3$  and  $\sim 15$  meV, and the region above  $\sim 15$  meV that is insensitive to superconductivity. Figure 2a illustrates the temperature evolution of  $\chi''(Q_{\text{AFM}}, \omega)$  within each interval up to 280 K. While at 16 meV the intensity evolves smoothly across  $T_c$ , there are pronounced anomalies at 3 and 9.5 meV due to the opening of the spin gap and the corresponding onset of the resonance, respectively. The resonance energy  $\hbar\omega_{\text{res}}$  decreases upon heating, following the same functional dependence as the superconducting gap  $\Delta$  (fig. 2b and 2c). The same data are summarized in figure 2d as a colour map of the  $\omega$ - $T$  plane. As indicated by the vertical “error bar”, the resonance maximum remains inside the  $2\Delta$  gap at all temperatures, while its tail might extend beyond. The interpolated spectrum of the low-temperature excitations is also presented in figure 3 as a function of wavevector and energy. Let us now consider the implications of our results for the physics of iron pnictides. Remarkably, the magnitude of  $\chi''(Q_{\text{AFM}}, \omega)$  in  $\text{BaFe}_{1.85}\text{Co}_{0.15}\text{As}_2$  is comparable to that in the cuprates. However, the

cuprate spectra exhibit poorly understood features such as a “spin pseudogap” and a broad peak reminiscent of the resonant mode in the normal state. In contrast, we have shown that the normal-state spin excitation spectrum of  $\text{BaFe}_{1.85}\text{Co}_{0.15}\text{As}_2$  is gapless and can be described by a simple formula for nearly antiferromagnetic metals discussed by T. Moriya in [5]. In the light of our results, random phase approximation and similar Fermi-liquid based approaches appear much better justified in arsenides than in high- $T_c$  cuprates.

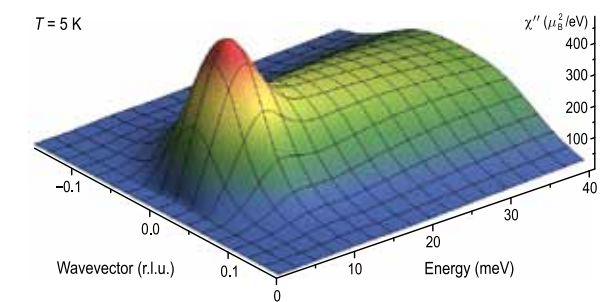


Figure 3: Presentation of  $\chi''(q, \omega)$  as a function of the wave-vector  $q = |Q - Q_{\text{AFM}}|$  and energy  $\omega$  in the superconducting state.

[1] L. Boeri et al., Phys. Rev. Lett., 101, 026403 (2008).

[2] A. D. Christianson et al., Nature, 456, 930 (2008).

[3] S. Li et al., Phys. Rev. B, 79, 174527 (2009) and M. D. Lumsden et al., Phys. Rev. Lett., 102, 107005 (2009).

[4] D. S. Inosov et al., Nat. Phys., 6, 178 (2010).

[5] T. Moriya, Spin Fluctuations in Itinerant Electron Magnetism, Springer, Berlin, Germany (1985).

# Parasitic small moment antiferromagnetism in the hidden order of URu<sub>2</sub>Si<sub>2</sub>

P. G. Niklowitz<sup>1,2</sup>, C. Pfleiderer<sup>1</sup>, T. Keller<sup>3,4</sup>, M. Vojta<sup>5</sup>, Y.-K. Huang<sup>6</sup>, J. A. Mydosh<sup>7</sup>

<sup>1</sup>Technische Universität München, Physik Department E21, Garching, Germany

<sup>2</sup>Royal Holloway, University of London, Department of Physics, Egham, United Kingdom

<sup>3</sup>Technische Universität München, Forschungs-Neutronenquelle Heinz Maier-Leibnitz (FRM II), Garching, Germany

<sup>4</sup>Max-Planck-Institut für Festkörperforschung, Stuttgart, Germany

<sup>5</sup>Universität zu Köln, Institut für Theoretische Physik, Köln, Germany

<sup>6</sup>University of Amsterdam, Van der Waals-Zeeman Institute, Amsterdam, The Netherlands

<sup>7</sup>Leiden University, Kamerlingh Onnes Laboratory, Leiden, The Netherlands

**W**e have used Larmor diffraction to establish quantitatively, that the small moment antiferromagnetism in the hidden order phase of the heavy-ferrion superconductor URu<sub>2</sub>Si<sub>2</sub> is parasitic. We also showed that the hidden order and the large moment antiferromagnetism, which emerges under pressure, must have a different symmetry. This makes an exotic origin of the hidden order, such as orbital currents, helicity order or multipolar order, most likely.

For over twenty years one of the most prominent unexplained properties of f-electron materials has been a phase transition of URu<sub>2</sub>Si<sub>2</sub> at T<sub>0</sub> ≈ 17.5 K into a state known as ‘hidden order’ (HO) [1-3]. The discovery of the HO was soon followed by the observation of a small, antifer-

romagnetic moment (SMAF), m<sub>s</sub> ≈ 0.03 μ<sub>B</sub> per U atom [9], long believed to be an intrinsic property of the HO. The discovery of large-moment antiferromagnetism (LMAF) with m<sub>s</sub> ≈ 0.4 μ<sub>B</sub> per U atom [5] under pressure, consequently prompted intense theoretical efforts to connect the LMAF with the SMAF and the HO. In particular, models have been proposed that are based on competing order parameters of the same symmetry and hence linearly coupled in a Landau theory; such models assume that the SMAF is intrinsic to the HO [6-9]. This is contrasted by proposals for the HO parameter such as incommensurate orbital currents [10], multipolar order [11], or helicity order [12], where HO and LMAF break different symmetries.

Prior to our study, some neutron scattering studies of the temperature-pressure phase diagram suggested that the HO-LMAF phase boundary ended in a critical end point [13, 14], while other studies concluded that it meets the boundaries of HO and LMAF in a bicritical point [15-18]. The lack of consistency is accompanied by considerable variations in the size and pressure dependence of the moment reported for the SMAF [19], whereas NMR and μ-SR studies suggested the SMAF to be parasitic [20, 21]. It was therefore long suspected that the conflicting results are due to a distribution of lattice distortions arising from defects. Notably, uniaxial stress studies showed that LMAF is stabilized if the c/a ratio η of the tetragonal crystal is increased by the small amount Δc/a ~ 5 × 10<sup>-4</sup> [22]. Hence, the SMAF may, in principle, result from a distribution of η across the sample, its magnitude being dependent on sample quality and experimental condi-

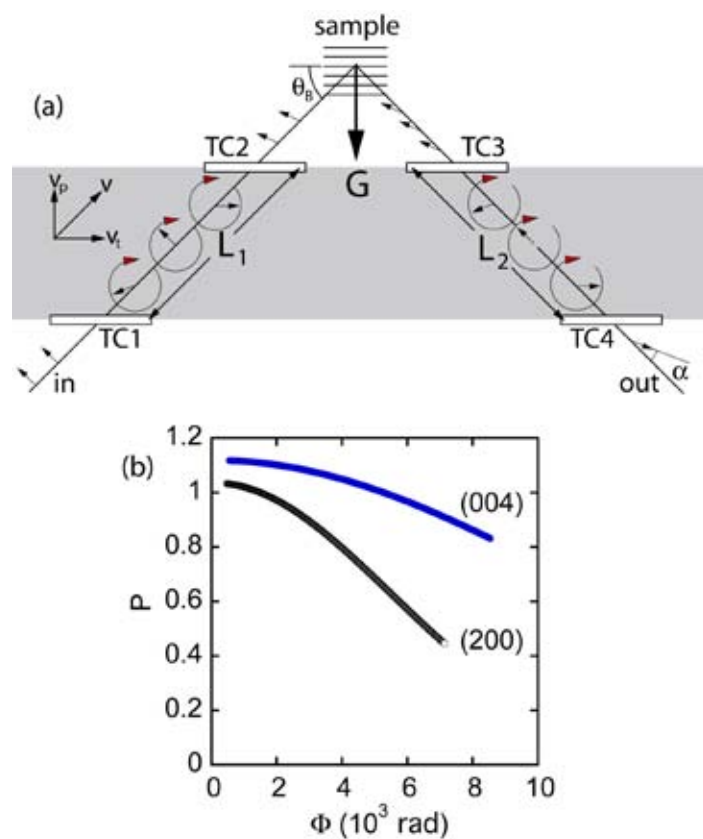


Figure 1: (a) Illustration of Larmor diffraction [24-26]; C1 through C4 are radio frequency spin flipper coils, G is the reciprocal lattice vector; θ<sub>b</sub> is the Bragg angle; AD is the polarization analyzer and detector. See text for details. (b) Typical variation of the polarization P as a function of the total Larmor phase Φ in URu<sub>2</sub>Si<sub>2</sub>.

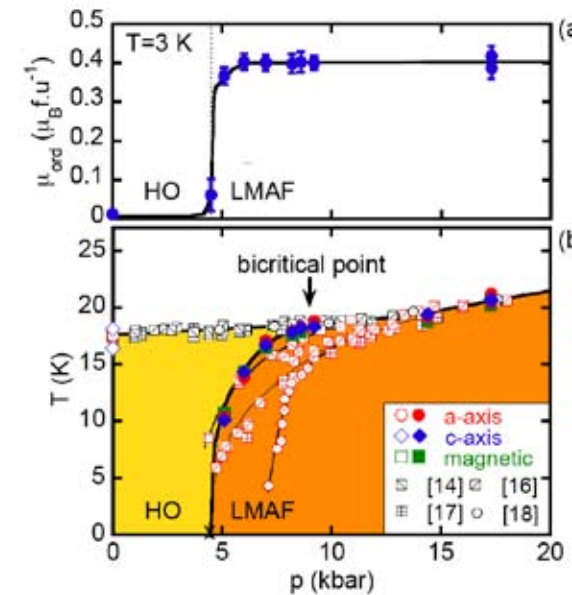


Figure 2: Key features and pressure versus temperature phase diagram of URu<sub>2</sub>Si<sub>2</sub>. (a) Pressure dependence of the low-temperature magnetic moment m<sub>s</sub>. (b) Phase diagram based on Larmor diffraction and conventional magnetic diffraction data. The onset of LMAF and HO in our data is marked by full and empty symbols, respectively (x marks a transition near base temperature). For better comparison data of T<sub>N</sub> and T<sub>0</sub> from Refs. [14, 16-18] are shown, where red symbols refer to T<sub>N</sub> and black symbols to T<sub>0</sub>.

tions.

For the first time, simultaneous measurements of the lattice constants, the distribution of the lattice constants and the antiferromagnetic moment of URu<sub>2</sub>Si<sub>2</sub> as a function of temperature, for pressures up to 18 kbar, employing Larmor and conventional diffraction [23]. Our measurements were carried out at the spectrometer TRISP at FRM II.

Larmor diffraction (LD) permits high-intensity measurements of lattice constants with an unprecedented high resolution of Δa/a ≈ 10<sup>-6</sup> [24-26]. In LD, the sample is illuminated by a polarised neutron beam (fig. 1a), (arrows indicate the polarisation). The radio frequency spin flipper coils, denoted as C1 through C4, continuously change the polarisation direction of the beam as a function of time. The coils C1 and C3 are set up such, that they generate a time dependence of the polarisation as if the polarisation precessed in the scattering plane at twice the radio frequency ω of the coils. The coils C2 and C4 are then tuned to terminate this time dependence of the polarisation; at any given location in the gray shaded regime, the beam polarisation therefore appears to precess, even though there is no applied magnetic field. The coils C1 through C4 are aligned parallel to the lattice planes, this way, changes in the lattice spacing sensitively affect the total time of travel t<sub>tot</sub> along L = L<sub>1</sub> + L<sub>2</sub> (t<sub>tot</sub> is determined purely by the velocity component v<sub>p</sub> of the neutrons parallel to G). Hence, the total phase of precession Φ along L<sub>1</sub> plus L<sub>2</sub> depends linearly on the lattice constant. Changes in the lattice constant affect the angle α and, thus, the

intensity recorded by the polarisation analyser and detector AD.

The distribution of lattice constants may be inferred from the change of polarization as a function of the Larmor frequency (fig. 1b). A quantitative analysis establishes that the distribution we observed experimentally accounts for the size of the SMAF in the same sample, which must be purely parasitic [23]. In addition, we find a rather abrupt transition from HO to LMAF, which extends from T = 0 up to a bicritical point (fig. 2). Our study demonstrates that the transition from HO to LMAF is intrinsically first order, i.e., the HO and LMAF must have different symmetry [23]. This supports exotic scenarios of the HO, such as incommensurate orbital currents, helicity order or multipolar order.

- [1] T. T. M. Palstra et al., Phys. Rev. Lett., 55, 2727 (1985).
- [2] M. B. Maple et al., Phys. Rev. Lett., 56, 185 (1986).
- [3] W. Schlabitz et al., Z. Phys. B, 62, 171 (1986).
- [4] C. Broholm et al., Phys. Rev. Lett., 58, 1467 (1987).
- [5] H. Amitsuka et al., Phys. Rev. Lett., 83, 5114 (1999).
- [6] L. P. Gor'kov, A. Sokol, Phys. Rev. Lett., 69, 2586 (1992).
- [7] D. F. Agterberg, M. B. Walker, Phys. Rev. B, 50, 563 (1994).
- [8] N. Shah et al., Phys. Rev. B, 61, 564 (2000).
- [9] V. P. Mineev, M. E. Zhitomirsky, Phys. Rev. B, 72, 014432 (2005).
- [10] P. Chandra et al., Nature, 417, 831 (2002).
- [11] A. Kiss, P. Fazekas, Phys. Rev. B, 71, 054415 (2005).
- [12] C. M. Varma, L. Zhu, Phys. Rev. Lett., 96, 036405 (2006).
- [13] F. Bourdarot et al., Physica B, 359, 986 (2005).
- [14] J. R. Jeffries et al., J. Phys.: Cond. Matter, 20, 095225 (2008).
- [15] G. Motoyama et al., Phys. Rev. Lett., 90, 166402 (2003).
- [16] S. Uemura et al., J. Phys. Soc. Japan, 74, 2667 (2005).
- [17] E. Hassinger et al., Phys. Rev. B, 77, 115117 (2008).
- [18] G. Motoyama et al., J. Phys. Soc. Japan, 77, 123710 (2008).
- [19] H. Amitsuka et al., J. Magn. Magn. Mater., 310, 214 (2007).
- [20] K. Matsuda et al., J. Phys.: Cond. Matter, 15, 2363 (2003).
- [21] A. Amato et al., J. Phys.: Cond. Matter, 16, 4403 (2004).
- [22] M. Yokoyama et al., Phys. Rev. B, 72, 214419 (2005).
- [23] P. G. Niklowitz et al., Phys. Rev. Lett., in press (2010); arXiv/0909.2071.
- [24] M. T. Rekveldt et al., Eur. Phys. Lett., 54, 342 (2001).
- [25] T. Keller et al., Appl. Phys. A (Suppl.), 74, 332 (2002).
- [26] C. Pfleiderer et al., Science, 316, 1871 (2007).

# Short-ranged spin correlations in the molecular magnet $\{\text{Mo}_{72}\text{Fe}_{30}\}$

Z. Fu<sup>1</sup>, P. Kögerler<sup>2</sup>, U. Rucker<sup>1</sup>, Y. Su<sup>3</sup>, R. Mittal<sup>3</sup>, T. Brueckel<sup>1</sup>

<sup>1</sup>Forschungszentrum Jülich GmbH, Institut für Festkörperforschung, Jülich, Germany

<sup>2</sup>RWTH Aachen, Institut für Anorganische Chemie, Aachen, Germany

<sup>3</sup>Forschungszentrum Jülich GmbH, Jülich Centre for Neutron Scattering at FRM II, Garching, Germany

The spin-frustrated molecular magnets have attracted intense interest. As a molecular analogue of Kagome lattice,  $\{\text{Mo}_{72}\text{Fe}_{30}\}$  is one of the largest molecular magnets synthesized to date representing a highly frustrated spin structure. In order to understand its magnetic ground state, we studied the spin correlations of  $\{\text{Mo}_{72}\text{Fe}_{30}\}$  by means of diffuse neutron scattering with polarization analysis at DNS. We have successfully interpreted the diffuse magnetic scattering obtained using a three-sublattice spin configuration, which has therefore proved to be a good model for the magnetic ground state of  $\{\text{Mo}_{72}\text{Fe}_{30}\}$ .

## Negligible molecular interactions

Spin-frustrated molecular magnets have attracted intense interest as they allow exotic magnetic ground states and unexpected spin dynamics. In this context, the polyoxomolybdate  $\{\text{Mo}_{72}\text{Fe}_{30}\}$  is of special interest because it represents a highly frustrated spin structure and possesses negligible intermolecular interactions. The  $\{\text{Mo}_{72}\text{Fe}_{30}\}$  molecule is shown in the insert of figure 3. 30  $\text{Fe}^{3+}$  ( $S = 5/2$ ) ions serve as magnetic centers and are antiferromagnetically coupled amongst nearest neighbors [1]. An approximate, diagonalizable effective Hamiltonian was adopted to explain the major low-temperature properties of  $\{\text{Mo}_{72}\text{Fe}_{30}\}$  [2]. The classical version of this effective Hamiltonian represents a frustrated ground state spin configuration called the “three-sublattice” model, where the 30 spins can be divided into three coplanar sublattices with angular spacing of  $120^\circ$  (see the insert in fig. 3). In order to understand the magnetic ground state of  $\{\text{Mo}_{72}\text{Fe}_{30}\}$ , the quantitative spin correlations of  $\{\text{Mo}_{72}\text{Fe}_{30}\}$

have been measured for the first time, by means of diffuse neutron scattering with polarization analysis.

The polarized neutron scattering measurements were carried out on the diffuse neutron scattering instrument DNS at various temperatures from 1.5 K to 100 K. The incident wavelength is 4.74 Å. Within the quasistatic approximation, the nuclear coherent, spin-incoherent and magnetic scattering cross sections have been separated simultaneously with the xyz-polarization method. The absolute scattering cross section is obtained by the calibration with a Vanadium standard.

## Strong geometrical spin frustration

Figure 1 shows the nuclear coherent, spin-incoherent and paramagnetic components of the total scattering from  $\{\text{Mo}_{72}\text{Fe}_{30}\}$  at 1.5 K. The nuclear coherent scattering shows a broad hump at high Q around  $1.80 \text{ \AA}^{-1}$ , which is due to the scattering from amorphous crystal water. The high intensity of nuclear coherent scattering below  $0.25 \text{ \AA}^{-1}$  originates from the background

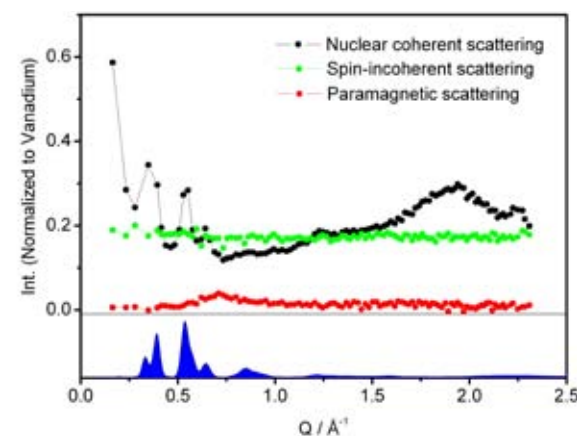


Figure 1: The nuclear coherent, spin-incoherent and paramagnetic contributions to the total scattering from  $\{\text{Mo}_{72}\text{Fe}_{30}\}$  at 1.5 K.

of the incident neutron beam. Several nuclear Bragg peaks are located within the Q range  $0.25 - 1.00 \text{ \AA}^{-1}$ , which are consistent with the powder diffraction simulation (blue area at the bottom of fig. 1). The magnetic contribution (red circles in fig. 1) is weak, leading to long counting time to obtain reasonable statistics.

Figure 2 presents the differential magnetic cross section,  $d\sigma/d\Omega$ , extracted from the total scattering cross section at 1.5, 2.5, 10, 20, 50, and 100 K. The scale of  $d\sigma/d\Omega$  in figure 2 corresponds to the experimental curve at 100 K. For clarity the data at other temperatures are displaced vertically by  $1.5 \text{ b sr}^{-1}$  per Fe atom. As expected, the magnetic scattering above 50 K agrees with the pure paramagnetic form factor (black line in fig. 2) of  $\{\text{Mo}_{72}\text{Fe}_{30}\}$  [2]. Below 20 K, a diffuse peak at  $Q \approx 0.70 \text{ \AA}^{-1}$  is seen to evolve and sharpen upon cooling, indicating the presence of short-ranged antiferromagnetic spin correlations. No long-ranged magnetic ordering can be seen down to 1.5 K owing to the strong geometrical spin frustration.

The magnetic scattering cross section in the quasi-static approximation can be described in terms of the Fourier transform of the spin pair-correlation function, [3],

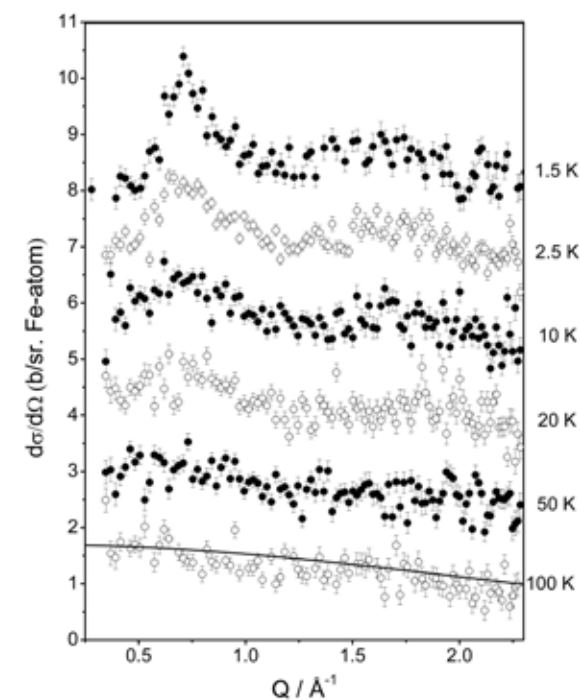


Figure 2: Temperature evaluation of the differential magnetic scattering cross section  $d\sigma/d\Omega$ . The solid line indicates the pure paramagnetic form factor of  $\text{Fe}^{3+}$ .

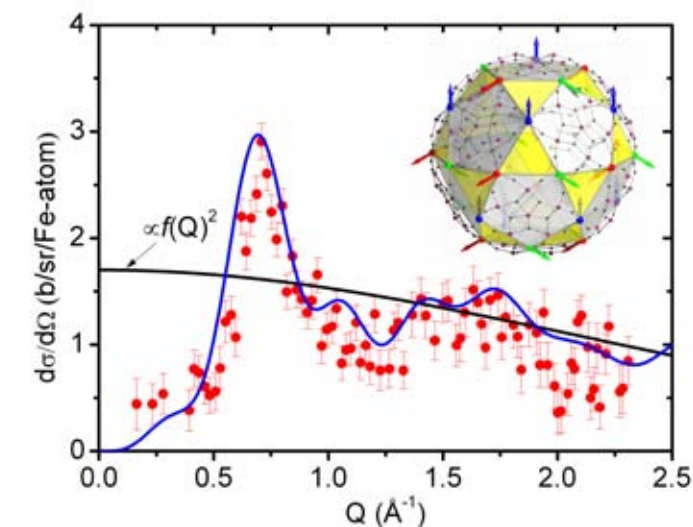


Figure 3: The magnetic diffuse scattering at 1.5 K (red circles) and the simulation (blue line); Insert: one  $\{\text{Mo}_{72}\text{Fe}_{30}\}$  molecule showing the three sublattice spin model.

$$\frac{d\sigma}{d\Omega}(Q) = \frac{2}{3}(\gamma r_0)^2 f^2(Q) \sum_r \langle S_0 \cdot S_r \rangle \frac{\sin Qr}{Qr} \quad (1)$$

where  $(\gamma r_0) = -0.54 \times 10^{-12} \text{ cm}$  is the magnetic scattering length,  $f(Q)$  is the magnetic scattering form factor,  $S_0$  and  $S_r$  are the atomic spin vectors at the origin and the position  $r$ . A simulation is carried out using equation (1) for the three-sublattice spin configuration of  $\{\text{Mo}_{72}\text{Fe}_{30}\}$ . The result of the simulation is compared with the measured profile of the magnetic diffuse scattering, as shown in figure 3. The simulation agrees well with the observed magnetic scattering.

## Three-sublattice model good approach

We have measured the short-ranged spin correlations from the spin-frustrated molecular magnet  $\{\text{Mo}_{72}\text{Fe}_{30}\}$  by means of diffuse neutron scattering with polarization analysis. The spin correlations collected at 1.5 K agree well with the simulation of the Fourier transform of the spin pair-correlation function using a three-sublattice spin configuration. We therefore believe that the three-sublattice model for the spin configuration could be a good approach to the magnetic ground state of  $\{\text{Mo}_{72}\text{Fe}_{30}\}$ .

[1] A. Müller, et al., ChemPhysChem., 2, 517 (2001).

[2] J. Schnack et al., Europhys. Lett., 56, 863 (2001).

[3] I. A. Blech, B. L. Averbach, Physics (N. Y.), 1, 31 (1964).

# Maxon position and linewidth at high pressures in superfluid helium

E. Blackburn<sup>1</sup>, T. Keller<sup>2,3</sup>

<sup>1</sup>University of Birmingham, School of Physics and Astronomy, Birmingham, United Kingdom

<sup>2</sup>Max-Planck-Institut für Festkörperforschung, Stuttgart, Germany

<sup>3</sup>Technische Universität München, Forschungs-Neutronenquelle Heinz Maier-Leibnitz (FRM II), Garching, Germany

The superfluid state of <sup>4</sup>He is characterized by the well-known phonon-maxon-roton dispersion curve. As the freezing pressure is approached, the maxon energy approaches twice the roton energy; previous studies implied that a crossover occurred. We present a detailed study, using TRISP, of the linewidth and relative position as a function of pressure, showing that this crossing is avoided. Instead, the maxon decays into the two roton bound state previously identified by Raman scattering.

At low enough temperatures, liquid helium becomes superfluid – the helium atoms form a macroscopic quantum state that persists down to absolute zero. The entire superfluid state can be described by a macroscopic wavefunction, and the characteristic excitations are large-scale collective modes, like phonons in solids. In fact, the dispersion relation, as shown in figure 1, shows that the parts particular to the superfluid (the sections labelled ‘maxon’ and ‘roton’) are continuations of the phonon spectrum in the liquid.

As the pressure of the superfluid is increased, the excitation spectrum shifts, the most noticeable change being a continuous drop in the energy of the roton. At a pressure of 25 bar, the superfluid solidifies, and the roton disappears, although the first order Bragg reflections from the static structure appear at the same momentum transfer value. Accompanying this shift in the roton energy, the peak in the excitation spectrum (the maxon) moves higher in energy.

The dispersion relation as a function of pressure has been mapped out by Gibbs and co-workers [1] up to a pressure of 20 bar. They found that, at 20 bar, the maxon energy increases as the roton

energy drops and, in fact, the maxon energy gets close to, and then appears to exceed twice the roton energy (2R). This is an unexpected observation, as Raman scattering studies [2] found evidence for a two-roton bound state (at zero momentum transfer), and so one would expect the maxon to decay into this bound state if its energy exceeded that of the two roton bound state.

## Precision down to microelectronvolts

To investigate this crossover region, we used the instrument TRISP, a cold three axis spectrometer with resonant spin echo capability. With this instrument, we can look at both the changes in energy transfer of the maxon as a function of pressure, and the associated energy linewidth. The narrower the energy linewidth, the longer the lifetime of the excitation. TRISP provides  $\mu\text{eV}$  resolution when looking at excitations, and so is perfect for this task, as the excitations in a superfluid are known to have long lifetimes, due to macroscopic wavefunction.

In general, with neutron scattering the energy

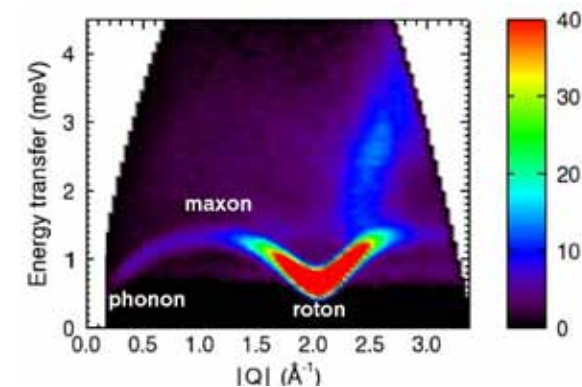


Figure 1: The excitation spectrum of superfluid helium at a temperature of 0.25 K and a pressure of 24.8 bar, as measured by neutron scattering on the DCS instrument at NCNR (NIST). The different parts of the spectrum are labelled. The roton is very intense due to its large density of states.

resolution cannot be divorced from the momentum transfer resolution, and is typically of the order of meV for inelastic excitations. However, TRISP uses the spin echo technique to circumvent this. In a spin echo measurement, the neutron spin is encoded with information about the energy transfer to the sample, and so the energy resolution can be improved independently of the momentum transfer resolution [3].

In the measurement, an ‘echo’ is obtained by changing the path length through which the neutrons can precess after being scattered by the sample. The change in path length is selected to cover a total phase change of  $2\pi$ . The echo can then be fitted to a cosine function, to obtain information about the polarization of the outgoing beam and changes in the relative phase for different environmental conditions. From these two pieces of information, the linewidth of the excitation and the relative energy transfer can be extracted, both to  $\mu\text{eV}$  precision.

The other experimental issue involves preparing the sample; to be superfluid, temperatures below 2.2 K are required and we used a <sup>3</sup>He cryostat capable of reaching 0.5 K. A custom sample cell was built. This had to be able to handle the requisite pressure, and had to have a capillary connection extending outside of the cryostat to a gas handling system, so that helium could be loaded into the cell and the pressure increased on demand.

## The maxon energy transfer

The upper panel of figure 2 shows the energy transfer of the maxon as a function of pressure. The actual measurement done on TRISP is very precise with respect to changes in position, but less so for the absolute value. As the pressure is increased, the change in energy transfer stops increasing and starts to decline. This decline prevents the maxon energy from becoming greater than two times the roton energy and our results indicate that, between 20 and 24 bar, the maxon energy remains slightly below twice the roton energy. This supports the idea that the maxon decays into the two-roton bound state.

## The maxon linewidth

The first surprising finding here is that the maxon is a very long-lived excitation deep in the superfluid state. As with the roton, the measurement of a linewidth of  $\sim 1 \mu\text{eV}$  is effectively at the resolu-

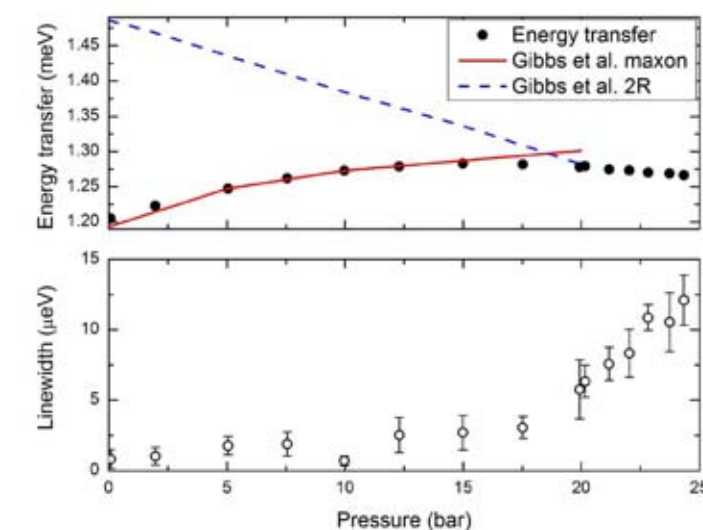


Figure 2: Energy transfer and linewidth of the maxon at 0.86 K, as measured on TRISP, compared to the values obtained by Gibbs et al. [1] for the maxon energy transfer and twice the roton energy (2R) up to 20 bar.

tion limit of the instrument.

However, as the pressure is increased (see the lower panel of figure 2), the linewidth does increase, and there is a clear change in slope starting at  $\sim 18$  bar. Looking at the change in the energy transfer, this switch occurs when the energy transfer of the maxon starts to decline. This decrease in the lifetime of the maxon fits well with the picture of the maxon decaying into the two-roton bound state. In fact, the linewidth just below the freezing pressure corresponds to a temperature of  $0.29 \pm 0.04$  K, and the binding energy of the two-roton bound state is  $0.27 \pm 0.04$  K at zero momentum transfer according to the Raman scattering experiments [2].

## Phonon experiments

As the pressure is increased in superfluid helium, the changes in the excitation spectrum are driven by the changes to the roton energy. The maxon part of the spectrum adapts to the requirements imposed by the position of the roton, and never surpasses twice the roton energy, decaying instead into the two-roton bound state. Similar experiments carried out on TRISP on the phonon part of the spectrum should help elucidate the nature of the crossover from phonon to maxon.

[1] M. R. Gibbs et al., J. Phys.: Cond. Matter, 11, 603 (1999).

[2] T. J. Greytak et al., Phys. Rev. Lett., 25, 1547 (1970).

[3] Neutron Spin Echo Spectroscopy, Eds: F. Mezei et al., (Lecture Notes in Physics 601), Springer, Berlin, Germany (2003).

# Magnon damping in spin-ladders

B. Náfrádi<sup>1</sup>, T. Keller<sup>1,2</sup>, H. Manaka<sup>3</sup>, A. Zheludev<sup>4,5</sup>, B. Keimer<sup>1</sup>

<sup>1</sup>Max-Planck-Institut für Festkörperforschung, Stuttgart, Germany

<sup>2</sup>Technische Universität München, Forschungs-Neutronenquelle Heinz Maier-Leibnitz (FRM II), Garching, Germany

<sup>3</sup>Kagoshima University, Graduate School of Science and Engineering, Kagoshima, Japan

<sup>4</sup>ETH Zürich und Paul Scherrer Institut, Laboratorium für Neutronenstreuung, Villigen, Switzerland

<sup>5</sup>ETH Zürich, Laboratorium für Festkörperphysik, Zürich, Switzerland

**A** knowledge of quasi-particle lifetimes and dispersion relations is crucial to an understanding of the ground-state properties of solids since these excitations govern the low-temperature behavior of strongly correlated systems. Here, we report on the determination of the low-temperature lifetime of spin wave excitations (magnons) in a quasi-one dimensional Haldane-gaped quantum spin ladder IPA-CuCl<sub>3</sub> by means of high energy resolution neutron resonant spin echo spectroscopy. Using this novel inelastic neutron technique, we have found two magnon modes at the antiferromagnetic zone centre separated by  $\Delta\omega = 50 \mu\text{eV}$  zero field splitting, exhibiting a line width of  $\Gamma_1 = 5 \mu\text{eV}$  and  $\Gamma_2 = 15 \mu\text{eV}$  respectively. These narrow magnon line widths cannot be measured by other commonly used inelastic neutron scattering techniques such as triple-axes spectrometers (TAS) since their resolution is limited to the meV range by beam intensity.

## Long lifetime at low temperatures

One-dimensional physics is unique due to unavoidable collisions among counter-propagating particles, regardless of their mutual interaction strength. In gapped quantum spin liquids, such as Haldane spin chains, the quasiparticles (magnons) persist in the limit  $T \rightarrow 0 \text{ K}$ , since mutual collisions are rare due to their exponentially small density. Interactions become important at elevated temperatures as a consequence of the increased density of the thermally excited magnons. This results in a reduction of magnon lifetimes and a thermally induced blue-shift of their energies.

An other remarkable feature of one dimensional gaped spin chains is that, when the  $T = 0 \text{ K}$  energy gap is used as the temperature scale, all experimental curves are identical to within system-dependent, but temperature-independent, scaling factors of the order of unity. This quasi-universal scaling behavior is the consequence of the shared one-dimensional topology of the spin chains. In the framework of the non-linear  $\sigma$  model (NL $\sigma$ M) [1], this quasi universality can be understood by combining all exchange interactions relevant for a particular material into one effective antiferromagnetic coupling constant  $J_{\text{eff}}$ , which will determine the low temperature behavior of the systems. According to NL $\sigma$ M, the zero temperature gap  $\Delta_0 = 0.41 J_{\text{eff}}$  and the temperature dependence of the magnon line width is described by the equation,

$$\Gamma(T) = 3 \sqrt{\frac{\Delta_0 k_b T}{2\pi v^2}} \exp\left(-\frac{\Delta_0}{k_b T}\right) \quad (1)$$

where  $v$  is the magnon velocity. According to this formula, an exponentially small magnon linewidth or, equivalently, an exponentially long magnon lifetime is expected at low temperatures. This prediction was partially confirmed by earlier inelastic neutron scattering experiments [2], since the magnon line width of IPA-CuCl<sub>3</sub> at temperatures lower than  $T = 10 \text{ K}$  was below experimental resolution limits. Due to the narrow magnon line width of IPA-CuCl<sub>3</sub>, it is an ideal system to test the low-temperature predictions of NL $\sigma$ M by TRISP, the neutron resonant spin echo spectrometer at the FRM II.

## Oscillating decay

IPA-CuCl<sub>3</sub> crystallizes in a triclinic space group

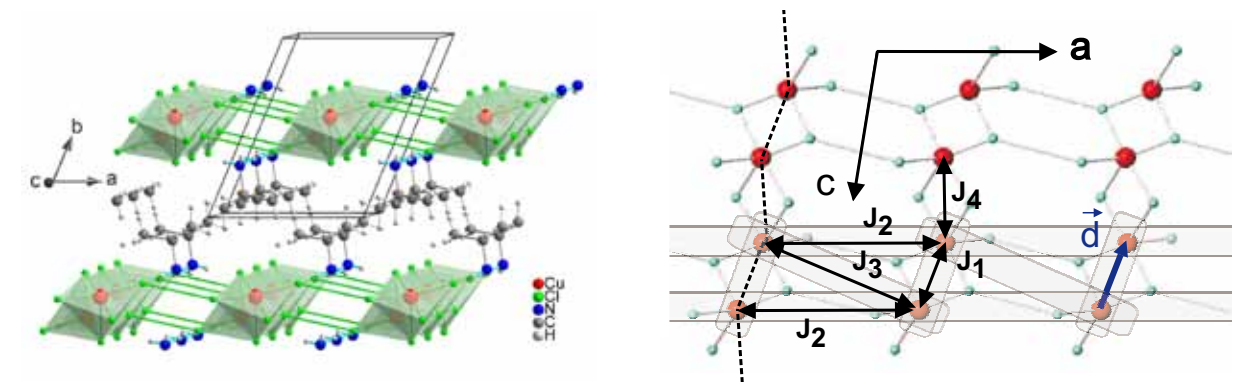


Figure 1: a) Crystal structure of IPA-CuCl<sub>3</sub>. Magnetic CuCl<sub>3</sub> and nonmagnetic polymeric IPA layers alternate along the b crystallographic direction. b) Single magnetic CuCl<sub>3</sub> plane viewed from the top. Characteristic spin-ladder running along a is showed in gray.

P1. The key features of the structure are shown in figure 1a. IPA forms layers in a-c plane preventing magnetic interactions along the b direction. The magnetic properties of IPA-CuCl<sub>3</sub> described by a single magnetic CuCl<sub>3</sub> layer in the a-c plane are shown in figure 1b. Cu<sup>2+</sup> ions that carry  $S = 1/2$  spins, form ladders that run along the crystallographic a axis, as described in detail in [3]. Exchange interactions along the ladder legs ( $J_1$  and  $J_2$  in fig. 1b) are antiferromagnetic. Pairs of spins on each ladder rung are correlated ferromagnetically due to the dominating  $J_1$  coupling. So, IPA-CuCl<sub>3</sub> is an archetypical composite Haldane spin-chain with a gap-energy  $\Delta_0 = 1.17 \text{ meV}$  at the antiferromagnetic zone center (0.5,0,0) at  $T = 0.5 \text{ K}$ . By measuring the neutron polarization as a function of spin echo time  $\tau_{\text{SE}}$ , we determined the Fourier transform of the scattering function of our sample. We found an oscillating decay (fig. 2) which is characteristic of a small separation of two magnon modes. Fitting the data with a fourier transform of two Lorentzian functions (green line in fig. 2), each describing a single magnon excitation, we have determined the splitting  $\Delta\omega = 47 \mu\text{eV}$  and the line widths  $\Gamma_1 = 5 \mu\text{eV}$  and  $\Gamma_2 = 15 \mu\text{eV}$ . The relative weight of the two magnon modes is 2:1, from which we infer that the broader mode corresponds to  $S^z = \pm 1$  triplets, while the narrower band is a  $S^z = 0$  triplet mode and the origin of the splitting is a single-ion anisotropy.

We thank Kathrin Buchner for technical assistance. B.N. acknowledges the financial support of the Swiss National Science Foundation.

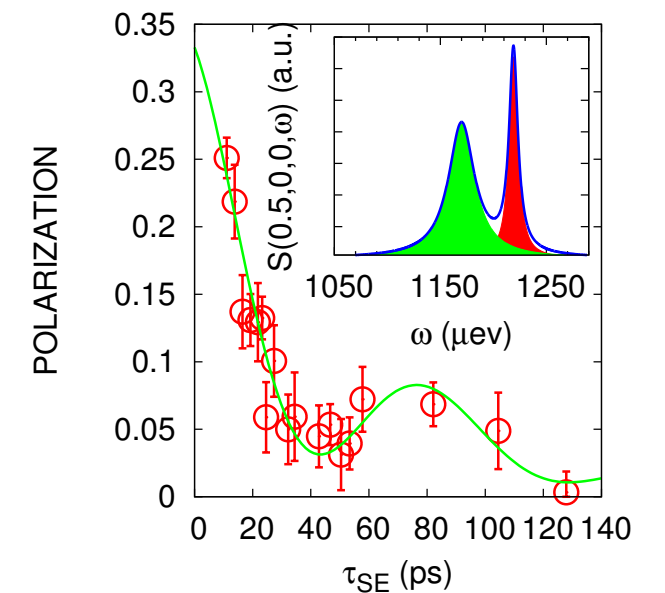


Figure 2: Neutron polarization ( $P$ ) as a function of spin echo time ( $\tau_{\text{se}}$ ) measured at  $T = 0.5 \text{ K}$  at the antiferromagnetic zone centre (0.5,0,0). The blue line is a fit assuming two magnon modes separated by a small zero field splitting. The inset shows the resulting neutron spectral function determined from the fit.

[1] T. Jolicoeur, O. Golinelly, Phys. Rev. B., 50, 9265 (1994).

[2] A. Zheludev et al., Phys. Rev. Lett., 100, 157204 (2008).

[3] T. Masuda et al., Phys. Rev. Lett., 96, 047210 (2006).

# Anisotropy of the superconducting gap in lead investigated by neutron spectroscopy

P. Aynajian<sup>1</sup>, N. Munnikes<sup>1</sup>, T. Keller<sup>1,2</sup>, L. Boeri<sup>1</sup>, B. Keimer<sup>1</sup>

<sup>1</sup>Max-Planck-Institut für Festkörperforschung, Stuttgart, Germany

<sup>2</sup>Technische Universität München, Forschungs-Neutronenquelle Heinz Maier-Leibnitz (FRM II), Garching, Germany

The anisotropy of the superconducting energy gap is a key source of information on the microscopic mechanism of superconductivity, but there has hitherto been no momentum-resolved method available that allowed the width of the energy gap in superconducting elements to be probed. Now, the gap anisotropy in superconducting lead was accurately determined by high-resolution neutron spectroscopy at TRISP [1, 2].

**Comparison of experimental and theoretical data**  
The momentum dependence of the energy gap  $\Delta(k)$  of elemental superconductors has been of long-standing interest. Variations of typically 10 % in  $\Delta(k)$  were inferred from experimental data and attributed to anisotropies of the Fermi surface, the phonon spectrum and/ or the electron-phonon coupling. However, the comparison of experimental and theoretical results has been severely limited by experimental difficulties such as uncontrolled momentum space averaging in tunneling spectroscopy and nonequilibrium effects in phonon imaging experiments. Angle-resolved photoemission spectroscopy, a direct, fully momentum resolved probe of the energy gap in high-temperature superconductors, is only applicable to materials with low-dimensional electronic structure and has therefore not contributed to research on elemental superconductors.

In principle, high-resolution phonon spectroscopy can serve as a similarly comprehensive probe of the superconducting gap anisotropy without restrictions on the dimensionality of the electronic structure. Since an acoustic phonon with wave vector  $q = k - k'$  and energy less than

$2\Delta(q) = \Delta(k) + \Delta(k')$  cannot decay into electron-hole pairs and is therefore not broadened by the electron-phonon interaction, the linewidth of such a phonon exhibits a discontinuity when its energy exceeds  $2\Delta(q)$ . The gap anisotropy can thus be inferred from a map of these discontinuities in different crystallographic directions. In practice, however, it is difficult to obtain the requisite energy resolution of a few  $\mu\text{eV}$ , comparable to the normal-state electron-phonon linewidth.

We have recently introduced a neutron spin-echo method that has sufficient energy resolution to detect superconductivity-induced linewidth anomalies in the phonon spectra of elemental lead and niobium [3], and found that, along specific crystallographic directions, the superconducting gap locks into the lowest-energy Kohn anomaly in the transverse acoustic phonon branches at low temperatures [4]. Here, we use this method to accurately determine the anisotropy of the superconducting gap in different high-symmetry directions. By combining the experimental results with those of ab-initio density functional calculations, we show that the newly discovered lock-in effect is likely to control the gap anisotropy over the entire Brillouin zone.

## High resolution neutron spectroscopy at TRISP

The experiments were performed on high-purity Pb single crystals with  $T_c = 7.2$  K. Figure 1 displays the linewidth of the lowest-energy transverse acoustic phonon branches in Pb along  $q = (100)$  and  $(110)$  at a temperature well below  $T_c$ , where the energy gap is saturated (blue symbols). As expected, sharp jumps reflecting the BCS density of states are apparent in the linewidth when the phonon energy exceeds  $2\Delta$ .

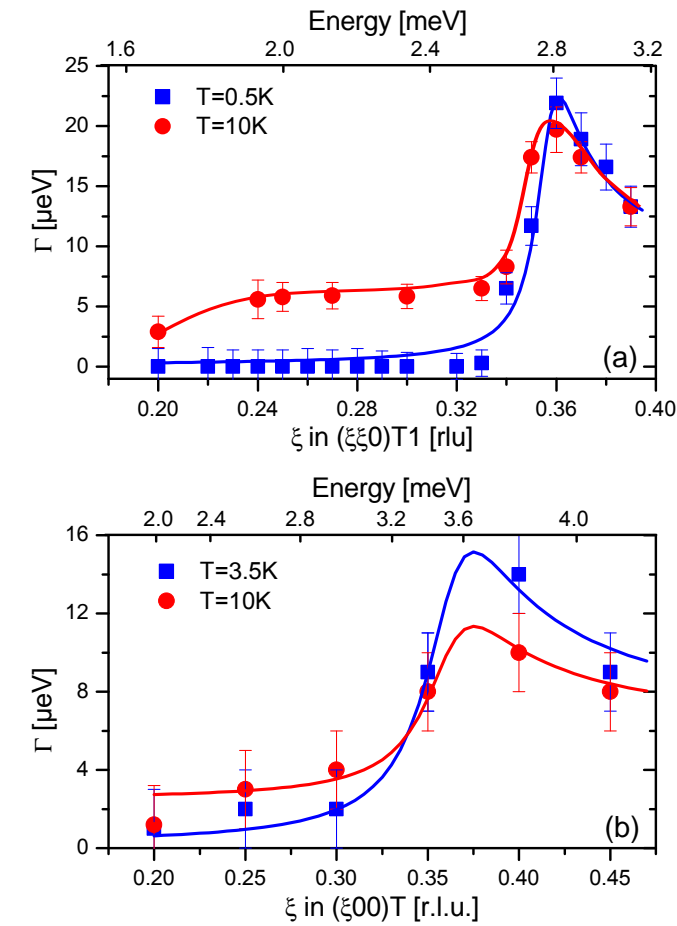


Figure 1: Linewidths of transverse acoustic phonons resulting from electron-phonon interaction in Pb in the vicinity of the superconducting gap. Data are shown along (a)  $q = (110)$  and (b)  $q = (100)$  above (red) and far below (blue) the transition temperature. (c) and (d) show cuts through the calculated Fermi surface of Pb, with arrows indicating decay channels responsible for the Kohn anomalies in the corresponding panels.

While  $2\Delta_{110} = 2.80 \pm 0.05$  meV is in agreement with the average gap value for Pb determined by tunneling spectroscopy,  $2\Delta_{100} = 3.49 \pm 0.05$  meV exceeds the average by 20 % (top scale in fig. 1).

The data shown in figure 1 also provide an important clue to the origin of the superconducting gap anisotropy. Specifically, sharp anomalies in the phonon linewidth are observed in both directions at  $T = 10$  K, well above the superconducting transition temperature, at the same energies at which the superconducting gap saturates at low temperatures. This effect was previously reported along a single crystallographic direction, and attributed to a lock-in of the gap to a Kohn anomaly resulting from Fermi surface nesting [4]. The arrows on the right side panels of figure 1 indicate the decay channels responsible for the Kohn anomalies in the  $(110)$  and  $(100)$  directions.

The coincident momentum dependence of both quantities now suggests that the superconducting gap anisotropy at low temperatures is con-

trolled by the location of Kohn anomalies in the acoustic phonon spectrum. The lock-in mechanism we have thus identified as the origin of the gap anisotropy in Pb involves the same ingredients as those discussed in earlier theoretical work, namely anisotropies of the Fermi surface and the phonon spectrum, but these are combined in a surprisingly simple manner.

[1] P. Aynajian, Dissertation, Stuttgart (2009).

[2] P. Aynajian et al., in preparation.

[3] T. Keller et al., Phys. Rev. Lett., 96, 225501 (2006).

[4] P. Aynajian et al., Science, 319, 1509 (2008).

# The life time of elementary excitations in superfluid $^4\text{He}$ studied by resonant spin-echo

B. Fåk<sup>1</sup>, K. Habicht<sup>2</sup>, T. Keller<sup>3,4</sup>

<sup>1</sup>Commissariat à l'Énergie Atomique, INAC, SPSMS, Grenoble, France

<sup>2</sup>Helmholtz-Zentrum Berlin für Materialien und Energie, Berlin, Germany

<sup>3</sup>Max-Planck-Institut für Festkörperforschung, Stuttgart, Germany

<sup>4</sup>Technische Universität München, Forschungs-Neutronenquelle Heinz Maier-Leibnitz (FRM II), Garching, Germany

We studied the decay mechanisms of elementary excitations in superfluid helium-4 using the zero-field resonant spin-echo spectrometer TRISP (fig. 1). Measurements of the life time as a function of wave vector and pressure clearly establish that the dominating decay mechanism of a phonon in superfluid  $^4\text{He}$  at low temperatures is due to decay into two low-energy phonons, wherever this decay process is kinematically allowed. The result confirms the theoretical work of Landau and Khalatnikov, and has applications for understanding the life time effects of bosonic excitations in general.

The properties of superfluid  $^4\text{He}$  at low temperatures can be understood from its low-lying excitations, predicted by Landau in 1941-47 [1]. The dispersion of these elementary excitations, or quasiparticles, are shown in figure 2. Excitations at low wave vectors  $Q$  in the linear region are

called phonons and those at higher  $Q$ 's around the local minimum of the dispersion curve near  $Q = 1.9 \text{ \AA}^{-1}$  are called rotons. A consequence of this dispersion is that low-energy thermally excited quasiparticles are scarce at low temperatures. This leads to the fact that phonons and rotons in superfluid  $^4\text{He}$  are long-lived even up to temperatures of the order of 1 Kelvin, since there are few thermally excited quasiparticles which they can decay into. This phenomena was explained by Landau and Khalatnikov (LK) as far back as in 1949 [2], well before the first roton was observed experimentally by neutron scattering in Stockholm in 1956 [3]. The LK theory for the temperature dependence of the roton life time was first experimentally confirmed in 1980 by Mezei [4] using his newly invented technique of neutron spin-echo.

Here, we are interested in the life time of the low- $Q$  phonons of superfluid  $^4\text{He}$ . A closer inspection of the phonon dispersion shows that

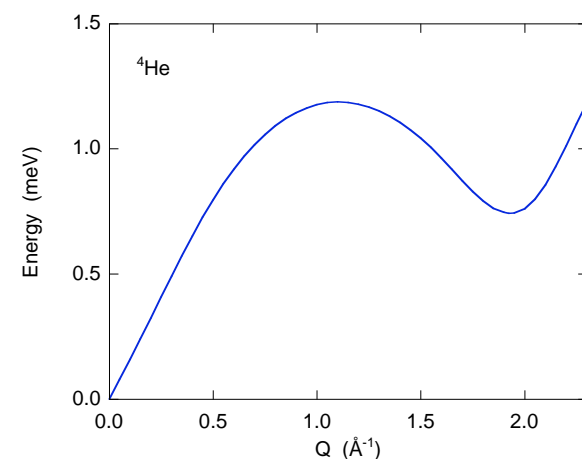


Figure 2 (above): Phonon-roton dispersion in superfluid helium-4 at zero pressure.

Figure 1 (left): TRISP at FRM II.

it has a tiny upward curvature at low  $Q$ -values. This phenomenon, called anomalous dispersion, implies that it is kinematically possible for a phonon to decay into two lower-energy phonons, even at zero temperature, a so-called three-particle (decay) process [5-6]. In superfluid  $^4\text{He}$ , phonons with wave vectors up to about  $0.4 \text{ \AA}^{-1}$  should therefore have a finite life time. This was observed experimentally in 1983 using (again) the spin-echo technique [7]. However, these measurements are much more difficult than measuring the temperature dependence of the roton life time, since one needs to measure the  $Q$ -dependence of the phonon life time in absolute units, which requires a perfect knowledge of the instrumental resolution as a function of wave vector and energy. One step forward was taken by Keller and collaborators [8], who used the zero-field resonant spin-echo method, which has the advantages that it can easily focus on dispersive excitations and that the instrumental resolution is essentially independent of wave vector. These measurements confirmed previous results, and clearly showed a shorter life time for wave vectors, where the anomalous dispersion is maximal. However, a perfect knowledge of the energy dependence of the instrumental resolution is still needed.

In the present work, we have also used the zero-field resonant spin-echo method but, in contrast to previous work, we performed the measurements at two pressures, 0 and 20 bars. The point is that at a pressure of 20 bar, three-particle processes are not allowed since the dispersion is no longer anomalous, which implies that the life time should be long and  $Q$ -independent.

The measurements were performed on TRISP in rocking-chair configuration and using a horizontally curved Heusler analyzer with a final wave vector of  $1.7 \text{ \AA}^{-1}$ . About  $30 \text{ cm}^3$  of high-purity helium was condensed into a cylindrical sample cell of inner diameter 26 mm made of thin-walled (0.3 mm) aluminium. The sample was kept below a temperature of 0.6 Kelvin in order to avoid scattering from thermally excited phonons, which would shorten the phonon life time.

The main results are shown in figure 3. At zero pressure, the phonon line width (the inverse of the life time) peaks in the region of anomalous

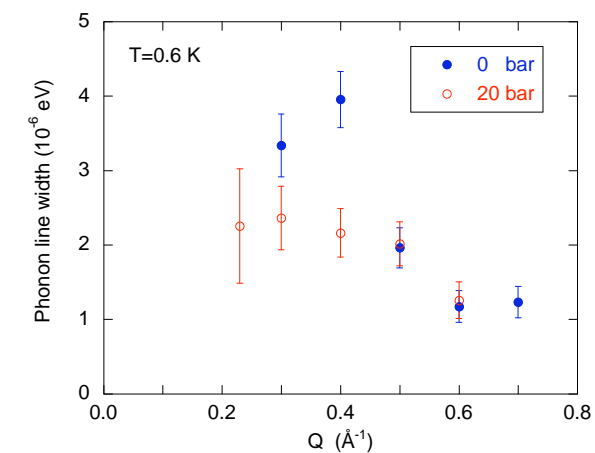


Figure 3: Phonon line width (inverse life time) of superfluid  $^4\text{He}$  at a temperature of 0.6 K as a function of wave vector  $Q$  for pressures of 0 and 20 bar.

dispersion  $Q = 0.3\text{-}0.4 \text{ \AA}^{-1}$ , in agreement with earlier measurements. However, at 20 bars, where the dispersion is not anomalous anywhere, this peak has disappeared and the life time is essentially independent of wave vector. This is a clear proof of that the shorter life time at zero pressure is due to three-particle (phonon-scattering) processes.

In conclusion, we have shown that the main decay mechanism of a phonon in superfluid  $^4\text{He}$  at low temperatures is due to decay into two other low-energy phonons, and that this decay mechanism disappears when the phonon dispersion becomes normal at high pressures. This is a beautiful confirmation of the Landau-Khalatnikov and Pitaevski theories on the life time of excitations in superfluid helium, in the year of Khalatnikov's 90's birthday. The result has direct implications for many areas in condensed matter where the elementary excitations are bosons.

[1] L. D. Landau, J. Phys. U.S.S.R., 5, 71 (1941); J. Phys. U.S.S.R., 11, 91 (1947).

[2] L. D. Landau, I. M. Khalatnikov, Zh. Eksp. Teor. Fiz., 19, 637 (1949); Zh. Eksp. Teor. Fiz., 19, 709 (1949).

[3] H. Palevsky et al., Phys. Rev., 108, 1346 (1957); Phys. Rev., 112, 11 (1958).

[4] F. Mezei, Phys. Rev. Lett., 44, 1601 (1980).

[5] L. P. Pitaevski, Sov. Phys. JETP, 36, 830 (1959).

[6] H. J. Maris, Rev. Mod. Phys., 49, 341 (1977).

[7] F. Mezei, W. G. Stirling, in „75<sup>th</sup> Jubilee Conference on Helium-4“, edited by J. G. M. Armitage (World Scientific, Singapore), p. 111 (1983).

[8] T. Keller et al., Europhys. Lett., 67, 773 (2004).

# Scission gamma-ray measurements at MEPHISTO

J. Klenke<sup>1</sup>

<sup>1</sup>Technische Universität München, Forschungs-Neutronenquelle Heinz Maier-Leibnitz (FRM II), Garching, Germany

The beamline MEPHISTO (a measurement facility for nuclear and particle physics with cold neutrons) hosted an experiment to search for asymmetry in the angular distribution of  $\gamma$ -rays in the induced fission process of  $^{235}\text{U}$ . The results are interpreted as the analog of the ROT effect recently described in induced ternary fission of  $^{235}\text{U}$ .

## MEPHISTO and fission of uranium

The MEPHISTO instrument is a white cold neutron beamline dedicated to experiments in the field of nuclear and particle physics. The experiments at MEPHISTO are long-term due to the fact that, for theories in this field small effects must often be measured with high precision. Such small effects give a better understanding of the current theories and provide data for any future theoretical refinement.

The experiment described at MEPHISTO dealt with the induced fission of uranium. A vivid description of fission is a separation of the excited nucleus (e.g. excited by a neutron) into two spheres connected for a short time by a small neck. The rupture of this neck forms two fission fragments with its famous “double-peak” distribution, dividing the fragments into a light and a heavy fragment.

Another possibility for fission is a double rup-

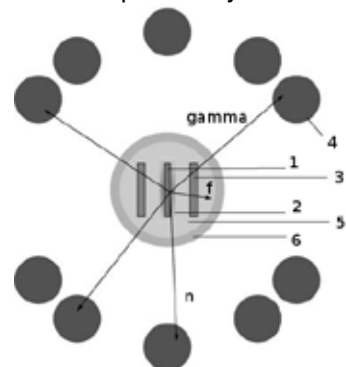


Figure 1: Layout of the experimental setup featuring gamma-ray detectors arranged at angles of  $\pm 35^\circ, \pm 57^\circ, \pm 90^\circ, \pm 123^\circ$  and  $\pm 145^\circ$  with respect to the axis along which fission fragments fly apart (horizontal). The polarisation is parallel/ antiparallel to the momentum of the incident neutron beam which is perpendicular to the drawing plane: (1)  $^{235}\text{U}$  target, (2) cross section of polarised cold neutrons, (3) detectors for fission fragments, (4) detectors for gamma-rays and fission neutrons, (5) isobutane at a pressure of 8 mbar, (6) steel walls of the fission chamber.

ture of the neck. This process (with a probability of 0.2 %) is a ternary fission with one light and one heavy fragment and a light charged particle. The mass of the fragments is also governed by a broad distribution, but 90 % of the light charged particles are  $\alpha$ -particles. The fission process is directly accompanied by  $\gamma$ -rays and particles from different possible fission channels. Additionally, the fragments produced are unstable nuclei emitting particle and  $\gamma$ -rays. The aim is to separate this information and explain the effects theoretically.

In 2007, a large international collaboration discovered a new phenomenon in the neutron induced ternary fission of  $^{235}\text{U}$  by polarised cold neutrons [1]. Roughly speaking, the distribution between the emission direction of the fragments and the light charged particle depends on the polarisation direction of the incident cold neutron. Their explanation can be summarized as follows: The incident polarised neutron excites the nucleus. This collective excitement is a rotation of the nucleus depending on the spin direction. The rupture of the nucleus produces fragments that travel to opposite sides, and the light charged particle, travelling perpendicular to the rupture axis. “During” the rupture, these particles are coupled by Coulomb forces. After a certain time they loose their coupling. The key in this explanation is the rotation of the excited nucleus. This rotation is very fast, but has already stopped after  $10^{-21}$  s with the rupture of the neck.

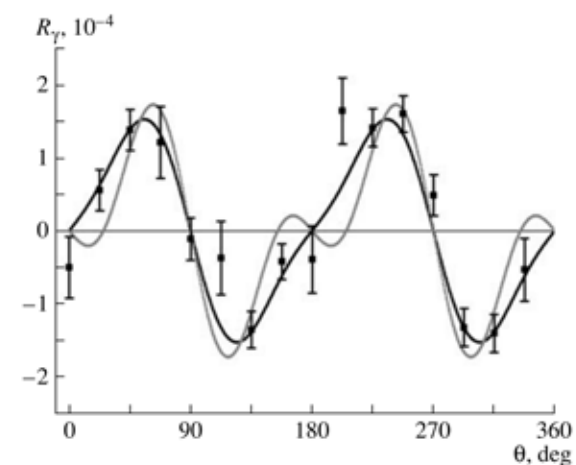


Figure 2: Angular dependence of the ROT asymmetry: (points) our experimental data; (black curve) approximation of the experimental data by formula 2, where  $N(\theta) = 1 + A_2 P_2(\cos \theta) + A_4 P_4(\cos \theta)$ ,  $A_2 = (-9.8 \pm 0.7) \cdot 10^{-2}$ ,  $A_4 = (1.8 \pm 0.5) \cdot 10^{-2}$  fixed at  $\delta\theta = 1 \cdot 10^{-3}$  (reduced  $\chi^2 = 1.02$ ); and (gray curve) approximation in which the parameters  $A_2$  and  $A_4$  were set to the values from [3] (reduced  $\chi^2 = 2.87$ ).

This short time is enough to explain the observed asymmetries. Due to the rotation of the nucleus, this effect has been named the “ROT” effect. The key is that the effect takes place in the small time window during fission and allows a separation of charged particles and  $\gamma$ -rays from the other processes.

## Asymmetry in scission gammas

The “ROT” effect above described is the motivation to search for similar asymmetries in  $\gamma$ -rays emitted during the time interval  $\Delta t = \pm 10^{-21}$  s around the neck rupture of  $^{236}\text{U}^*$ . The experiment [2] was set up as a coincidence experiment between the light fission fragment and the  $\gamma$ -rays in different angular directions. The setup is shown in figure 1.

The rotation of the polarised fissioning nucleus manifests itself in an asymmetry of coincidences of prompt fission gammas and fission fragments with respect to the direction of the polarisation of the incident neutron beam:

$$R = \frac{N_1(\theta) - N_2(\theta)}{N_1(\theta) + N_2(\theta)} \quad (1)$$

where  $N_i(\theta)$  is the counting rate for coincidences of  $\gamma$ -rays and fragments detected at an angle  $\theta$ . The  $i = 1, 2$  are the two spin directions of the beam. This asymmetry is very small (about  $10^{-4}$ ) and almost concealed by the irremovable background of  $\gamma$ -rays from excited fragments.

The measured asymmetry in this experiment  $R_\gamma(\theta)$  can be written as:

$$R_\gamma(\theta) = \delta\theta \frac{dN_{sc}(\theta)/d\theta}{N_{tot}(\theta)} \quad (2)$$

where  $\delta\theta$  is the angle of the shift,  $dN_{sc}(\theta)/d\theta$  the derivative of the angular distribution of scission gammas recorded at an angle  $\theta$  and  $N_{tot}(\theta)$  is the

counting rate for coincidences of prompt fission gammas. The absolute value of the asymmetry depends on many factors, e.g. the polarisation of the  $^{236}\text{U}^*$  nucleus and the anisotropy of the background of  $\gamma$ -rays from excited fission fragments. These influences suppress and overlay the asymmetry and, additionally, it is not clear if there is also a dependence on the energy of the  $\gamma$ -rays.

This experiment aimed to find an asymmetry in scission gammas. The results for the measured asymmetry are shown in figure 2. The values for  $R_\gamma(\theta)$  are averaged over the energy range of the gamma detectors.

## Larger dipole radiation

The observed asymmetry can be described by a linear combination of the  $P_2$  and  $P_4$  Legendre Polynom, describing a mixture of dipole and quadrupole radiation. In the figure the result is compared with the spontaneous fission of  $^{252}\text{Cf}$  from [3]. The  $^{252}\text{Cf}$  radiation should have a quadrupole character, see [3], but in this experiment a larger dipole radiation component was found. Possible other sources for asymmetric  $\gamma$ -rays cannot be completely excluded. Soft  $\gamma$ -rays from the excited nucleus before the fission takes place are a possibility, but the life time of these states is too long, according to the characteristic time of the rotation of the  $^{236}\text{U}^*$  nucleus. It can also not be excluded that electromagnetic radiation accompanying the separation of the nucleus into fragments in different reaction channels may be a source of asymmetries. Finally, excitations from fission fragments should show higher gamma energy than measured in this experiment [4].

## Further fission processes could refine the model

It is of interest to study the analogous process in the fission of  $^{233}\text{U}$  and  $^{239}\text{Pu}$ . A comparison would make it possible to refine the models of the fission process.

[1] F. Goennenwein et al., Phys. Lett. B, 652, 13 (2007).

[2] G. V. Danilyan et al., Phys. At. Nuc., 72 (11), 1812 (2009).

[3] Y. Kopach et al., Phys. Rev. Lett., 82 (2), 303 (1999).

[4] K. Pomorski et al., Z. Phys. A, 345, 311 (1993).

# Neutron capture cross sections of $^{74}\text{Ge}$ and $^{76}\text{Ge}$

G. Meierhofer<sup>1</sup>, P. Grabmayr<sup>1</sup>, J. Jochum<sup>1</sup>, P. Kudejova<sup>2</sup>, L. Canella<sup>3</sup>, J. Jolie<sup>4</sup>

<sup>1</sup>Universität Tübingen, Kepler Center for Astro and Particle Physics, Tübingen, Germany

<sup>2</sup>Technische Universität München, Forschungs-Neutronenquelle Heinz Maier-Leibnitz (FRM II), Garching, Germany

<sup>3</sup>Technische Universität München, Institut für Radiochemie, Garching, Germany

<sup>4</sup>Universität zu Köln, Institut für Kernphysik, Köln, Germany

New values for the thermal neutron capture cross section of  $^{74}\text{Ge}$  and  $^{76}\text{Ge}$  have been measured using neutron activation of  $\text{GeO}_2$  targets. The decay spectra were measured with HPGe detectors after activation of the targets using cold neutrons. The cross sections for the (n, $\gamma$ )-reaction of  $^{74}\text{Ge}$  and  $^{76}\text{Ge}$  were derived relative to the well-known neutron capture cross section of  $^{197}\text{Au}$ . The data obtained in our measurements are important for background prediction in the forthcoming GERDA (Germanium detector array) experiment searching for neutrinoless double beta decay in  $^{76}\text{Ge}$ .

The (n, $\gamma$ )-reaction of  $^{74}\text{Ge}$  and  $^{76}\text{Ge}$  is of interest in experiments that search for the neutrinoless double beta decay [1] using HPGe detectors. The HPGe detectors are made of germanium, isotopically enriched with  $^{76}\text{Ge}$  (86 %  $^{76}\text{Ge}$ , 14 %  $^{74}\text{Ge}$ ) [2]. Since neutrinoless double beta decay has a very long half-life, background reduction and rejection is the major experimental challenge. Neutron capture on  $^{74}\text{Ge}$  and  $^{76}\text{Ge}$  contributes to the background by prompt  $\gamma$ -radiation and the delayed decay of the activated nuclei. If a reliable evaluation of the anticipated background is to be achieved, the cross sections must be known accurately.

## Uncertainties significantly reduced

The cross sections for neutron capture on  $^{74}\text{Ge}$  and  $^{76}\text{Ge}$  have been measured at the PGAA instrument using the NAA method.  $\text{GeO}_2$  powder, pressed into pills of defined geometry, was irradiated with cold neutrons, together with a gold foil. The activated nuclei decay to the ground state or an isomeric state via prompt  $\gamma$ -emission.

In  $^{75}\text{Ge}$  and  $^{77}\text{Ge}$ , the isomeric states undergo isomeric transition (IT) or beta decay to arsenic. Additionally the respective ground states decay via beta decay (fig. 1).

Following the irradiation procedure, the delayed  $\gamma$ -rays emitted by the activated germanium and gold isotopes were measured using HPGe detectors. The cross sections of the germanium isotopes were then derived relative to the well-known cross section of gold, using peak areas and the emission probabilities of strong transitions.

Since the sample is activated and measured at the same position, the instrumental setup is suitable for the measurement of the rather short-lived isomeric states ( $t_{1/2} < 60$  s).

The cross sections for the (n, $\gamma$ )-reaction of  $^{76}\text{Ge}$  were obtained using  $\text{GeO}_2$ , isotopically enriched with  $^{76}\text{Ge}$ . The values derived from our measurement are  $\sigma_m = (115 \pm 16)$  mb for the cross section to the isomeric state and  $\sigma_t = (68.8 \pm 3.4)$  mb to

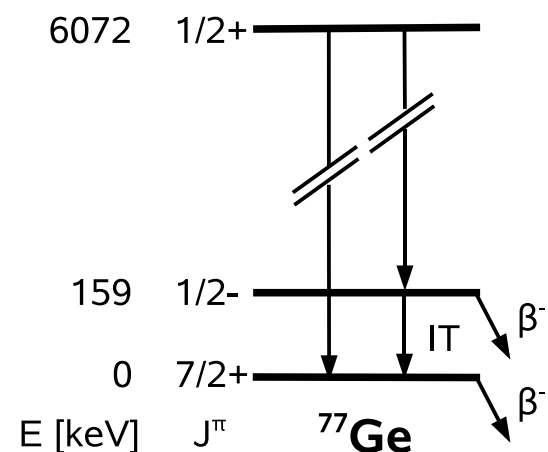


Figure 1: Decay scheme of  $^{77}\text{Ge}$

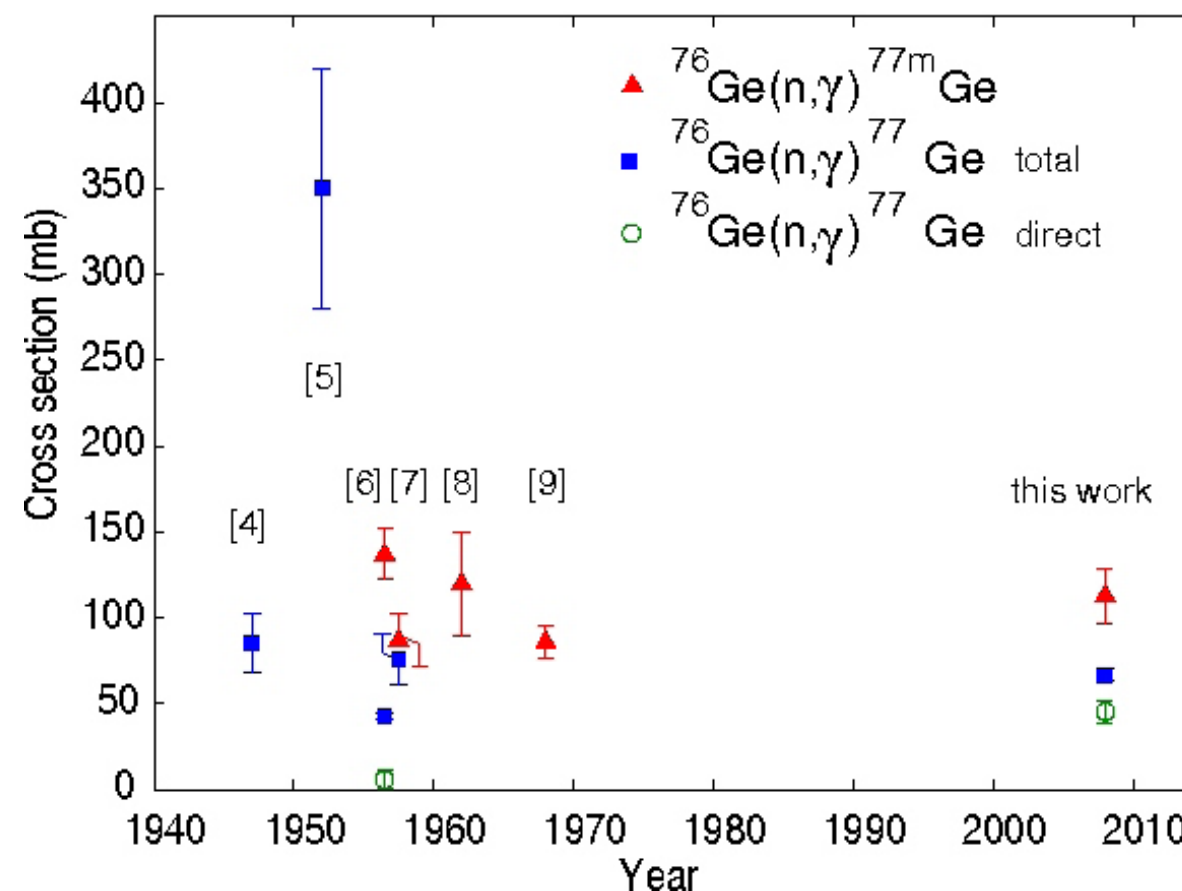


Figure 2: Neutron capture cross section for  $^{76}\text{Ge}(n,\gamma)^{77}\text{Ge}$  measured in our experiment compared with previous publications.

the ground state. Correcting  $\sigma_t$  for the feeding from the isomeric state by IT, the direct cross section obtained was  $\sigma_d = (46.9 \pm 4.7)$  mb [3]. The values measured in this work are compared with previous publications in figure 2. Due to the method used; (others: NaI-detectors with lower resolution than HPGe or  $\beta$ -particle detection with higher systematic uncertainties), the uncertainties of  $\sigma_t$  and  $\sigma_d$  were significantly reduced, whilst the uncertainty of  $\sigma_m$  could not be improved due to insufficient knowledge of the branching of the IT.

The cross sections for  $^{74}\text{Ge}(n,\gamma)^{75}\text{Ge}$  were measured using  $\text{GeO}_2$ , isotopically depleted in  $^{76}\text{Ge}$  (0.6 %  $^{76}\text{Ge}$ ). Depletion in  $^{76}\text{Ge}$  simplifies the analysis and leads to more precise results because the line at 264.4 keV of the decay of  $^{77}\text{Ge}$  would overlap with the most prominent one of  $^{75}\text{Ge}$  (264.6 keV). The preliminary value for the  $^{74}\text{Ge}(n,\gamma)^{75m}\text{Ge}$ -reaction is  $\sigma_m = (131.4 \pm 6.8)$  mb, to the ground state a cross section of  $\sigma_t = (499 \pm 53)$  mb was derived. The corresponding value corrected for feeding by IT is  $\sigma_d = (368 \pm 52)$  mb. (The preliminary results will appear in the proceedings for CNR09 Bordeaux

in EPJA).

## PGAA for fundamental physics

Our measurements delivered new values with lower uncertainties for the cross sections of the (n, $\gamma$ )-reactions of  $^{74}\text{Ge}$  and  $^{76}\text{Ge}$ . The prompt  $\gamma$ -rays after neutron capture on  $^{74}\text{Ge}$  and  $^{76}\text{Ge}$  were measured also. Together with the still analysed prompt spectra the cross section data will be used in Monte-Carlo simulations for the GERDA experiment. It was shown that the PGAA instrument is very useful for questions in fundamental physics, although it is for the most part dedicated to problems in applied physics.

[1] F. T. Avignone et al., Rev. Mod. Phys., 80, 481 (2008).

[2] GERDA, Proposal to the LNGS, (2004),

<http://www.mpi-hd.mpg.de/gerda>.

[3] G. Meierhofer et al., Eur. Phys. J. A, 40, 61 (2009).

[4] L. Seren et al., Phys. Rev., 72, 888 (1947).

[5] H. Pomerance, Phys. Rev., 88, 412 (1952).

[6] W. S. Lyon, J. S. Eldridge, Phys. Rev., 107, 1056 (1957).

[7] E. der Mateosian, M. Goldhaber, Phys. Rev., 108, 766 (1957).

[8] H. Weigmann, Z. Phys., 167, 549 (1962).

[9] W. Mannhart, H. Vonach, Z. Phys., 210, 13 (1968).

View into the reactor pool, while the silicon doping facility (left) is in operation.

# Reactor

# 4



# The operation of the neutron source in 2009

1. Neuhaus

<sup>1</sup>Technische Universität München, Forschungs-Neutronenquelle Heinz Maier-Leibnitz (FRM II), Garching, Germany

In 2009, the FRM II operated safely in five cycles (no. 18b, 19, 20, 21 and 22a). In total the neutron source was operational on 236 days. In the cycles no. 18b, 19 and 20, the fuel elements were used until the fuel irradiation level had reached 1200 MWd. The fuel element of cycle 21 had reached a level of 1099 MWd, when the cycle had to be stopped, ahead of schedule, because of the non-availability of the two water treatment trains. Cycle 22 was paused, as planned, before the Christmas holidays after reaching 724 MWd.

In total, the FRM II delivered 4720 MWd in 2009, which corresponds to a relative operational availability of 97.5 % which takes it to top position amongst national and international neutron sources.

## 1889 recurring checkups in one year

The high standard of safety and security at the neutron source could be maintained and even improved: 1889 recurring checkups, rounds of inspection by referees covering 18 different areas of interest, maintenance measures and in total 70 recommendations on amendments were carried out in 2009. Figure 1 shows work on the check valves in the reactor pool.

Another positive point is the availability of both cold and hot neutron source at the disposal of scientific users over the whole year.

## Neutron guide hall east to be converted soon

The new neutron guide hall east has not yet been converted for use under atomic law. However, the conversion is anticipated in the first quarter of 2010. As the technical infrastructure in the hall will be affected by amendments advice, its installation has not yet begun.

## Ultra cold neutron source: first components

The installation and operation of the future ultra cold neutron source (UCN) will be carried out within the ordinance concerning procedures according to the atomic energy act. The report to the permitting authorities was finished in 2009. The first components of the UCN have already been ordered (see fig. 2).

Five reportable incidents occurred in the year 2009. Four incidents were reported in the category N, one in the category E to the authority. All incidents were rated in the INES (International Nuclear Event Scale) to the level 0, i.e. below-scale events with no safety significance. There was also no effect on the safety of the personnel or the environment. Radioactivity was not released.

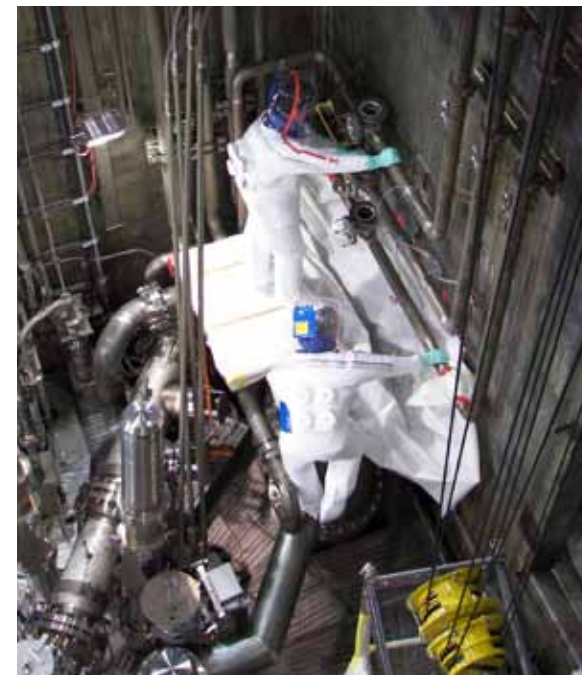


Figure 1: Work in the reactor pool during a maintenance break.

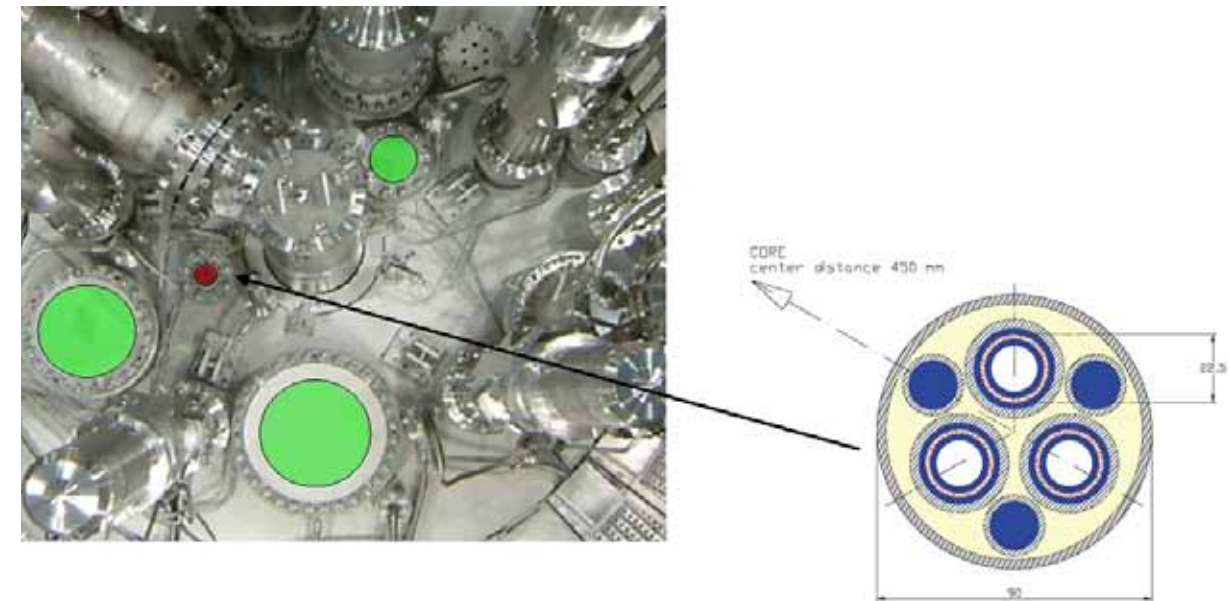


Figure 3: The position of the future molybdenum-99 thimble within the reactor pool.

## 50% of European requirements for Mo<sup>99</sup>

The positive outcome of the feasibility study for the production of molybdenum-99 at the FRM II was presented to the public in a press conference in June. Molybdenum-99 is the parent isotope for the isotope technetium-99m, which is used in radiology. This substance is required for the production of images known as scintigraphs which can be used to diagnose cancer and organ dysfunction. To produce a scintigraph, the radioisotope technetium-99m is bound to selected molecules. These then transport the radioisotope to a targeted location in the body, for example cancer metastases in the skeleton. There, the technetium-99m accumulates along

with the transporter molecules. It emits gamma rays which can then be detected using a special camera. In this way, the radioactive technetium-99m can be used to make undesired tissue or the structure of organs visible. Molybdenum-99 is generated through the fission of uranium by neutrons. An existing thimble located near the fuel element of the FRM II that releases neutrons will be converted in such a way that the targets to be irradiated will fit into it perfectly (see fig. 2). The cost of upgrading FRM II will come to a total of 5.4 million Euros, spread over a period of five years. When operational, the FRM II should produce approximately 50 % of the requirements in Europe.

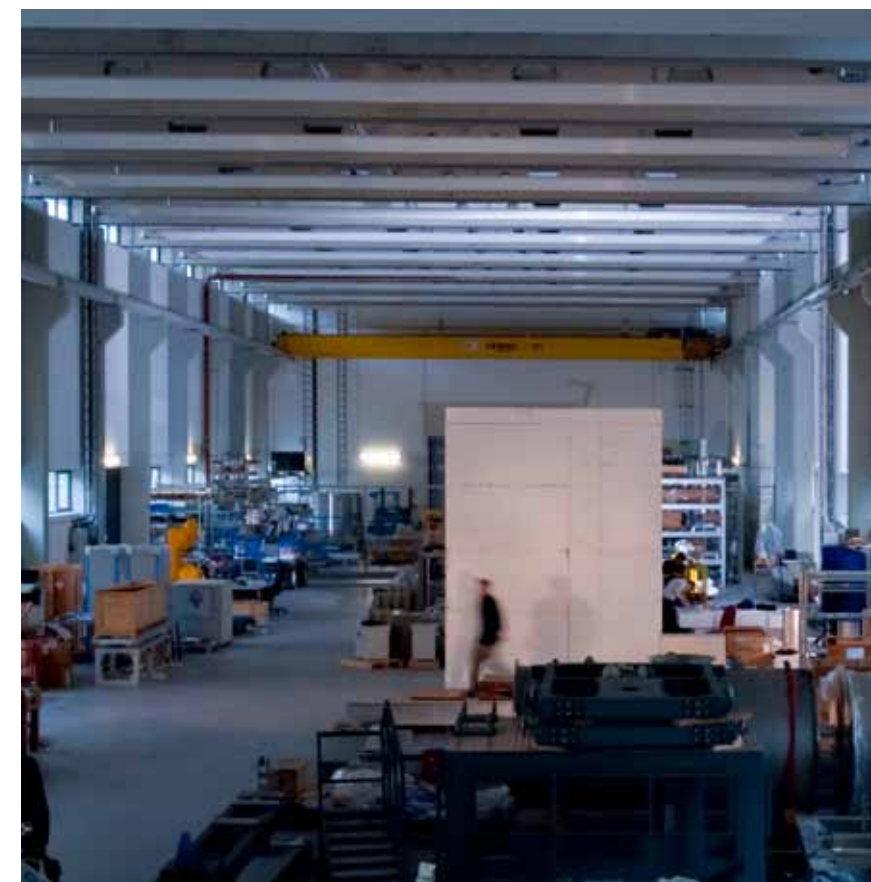


Figure 2: The cube in the neutron guide hall east houses one of the pre-experiments for the ultra cold neutron source, carried out by the excellence cluster universe. The new hall will be converted into a building subject to atomic law.

# Optimization of the Si content in UMo/Al(Si) fuel plates

R. Jungwirth<sup>1</sup>, W. Petry<sup>1</sup>, C. Jarousse<sup>2</sup>, H. Palancher<sup>3</sup>

<sup>1</sup>Technische Universität München, Forschungs-Neutronenquelle Heinz Maier-Leibnitz (FRM II), Garching, Germany

<sup>2</sup>Commissariat à l'Énergie Atomique, DEN, DEC, Saint Paul lez Durance, France

<sup>3</sup>AREVA-CERCA, Les Berauds, Romans, France

The Forschungs-Neutronenquelle Heinz Maier-Leibnitz (FRM II) together with colleagues from other research centres are making great efforts for a future replacement of its current highly enriched uranium (HEU) core by one using uranium of lower enrichment. Uranium-molybdenum (UMo) alloys with low Mo content dispersed in an aluminium matrix or as a monolithic foil are considered as the most promising candidates for such a high density fuel. Here we report on the effects of silicon addition to the aluminium matrix, a promising route to limit the undesired formation of interdiffusion layers at the interface between the UMo particles and the aluminium matrix.

Test fuel plates, made of UMo dispersed inside an Al matrix, suffer from billowing and exponential, so-called “break away” swelling during in-pile tests. The main reason for this behaviour appears to be the growth of an interdiffusion layer (IDL) between the UMo particles and the surrounding Al matrix. Over the last years, many different means to overcome this problem have been proposed [1]. We focused on the effect of silicon addition (2, 5 and 7 wt%) into the Al matrix, since protecting the UMo particles with a Si rich diffusion layer (SiRDL) appears to be one of the most promising routes to improve the in-pile performance of the UMo/Al nuclear fuels. We examined the behaviour of the SiRDL around the UMo particles under heavy ion irradiation. Irradiation of small fuel plate samples with heavy ions is one possibility to emulate out-of-pile some of the effects inside fuel plates during in-pile irradiation, avoiding strong activation of the samples. In particular the irradiation induced build-up of the IDL is well emulated [2].

## Irradiation at the tandem accelerator

Four miniplates of UMo (7 wt% Mo) dispersed in Al containing 0, 2, 5 and 7 wt% of Si were examined before and after irradiation with heavy ions. The Si samples containing the 5 and 7 wt% were prepared by blending very fine powders, while for those containing the 2 wt% Si, a commercially available pre-mixed powder was used. All miniplates were produced using the standard hot-rolling procedure by AREVA-CERCA. A part of the four mini-plates was irradiated at the tandem accelerator in Garching with an 80 MeV <sup>127</sup>I beam. The irradiation conditions were chosen identically for all samples, the equivalent of a high in-pile burn-up was reached. The irradiated surface of the samples has been examined by scanning electron microscopy (SEM) and energy dispersive X-ray spectroscopy (EDX).

## Characterization before irradiation

For the plates containing 2 wt% Si in general, no SiRDL was observed around the UMo particles. In the plates containing 5 wt% Si each UMo particle is at least partially covered by a SiRDL. Smaller particles reveal a thicker and more homogenous layer than larger particles. The biggest particles are frequently only partially covered by the SiRDL. The thickness of the layer varies from 0.4 µm to 1.2 µm. In the plates containing 7 wt% Si each particle is completely covered by the SiRDL. Also, for this Si content, the layer around the smaller particles is thicker than around the bigger particles. In general, the thickness of the SiRDL is not very homogenous, varying between 0.4 µm and 2 µm. Small Si precipitates have been found for all Si contents inside the Al matrix. It is self-evident that no SiRDL is present for the reference sample having no Si addition to the matrix.

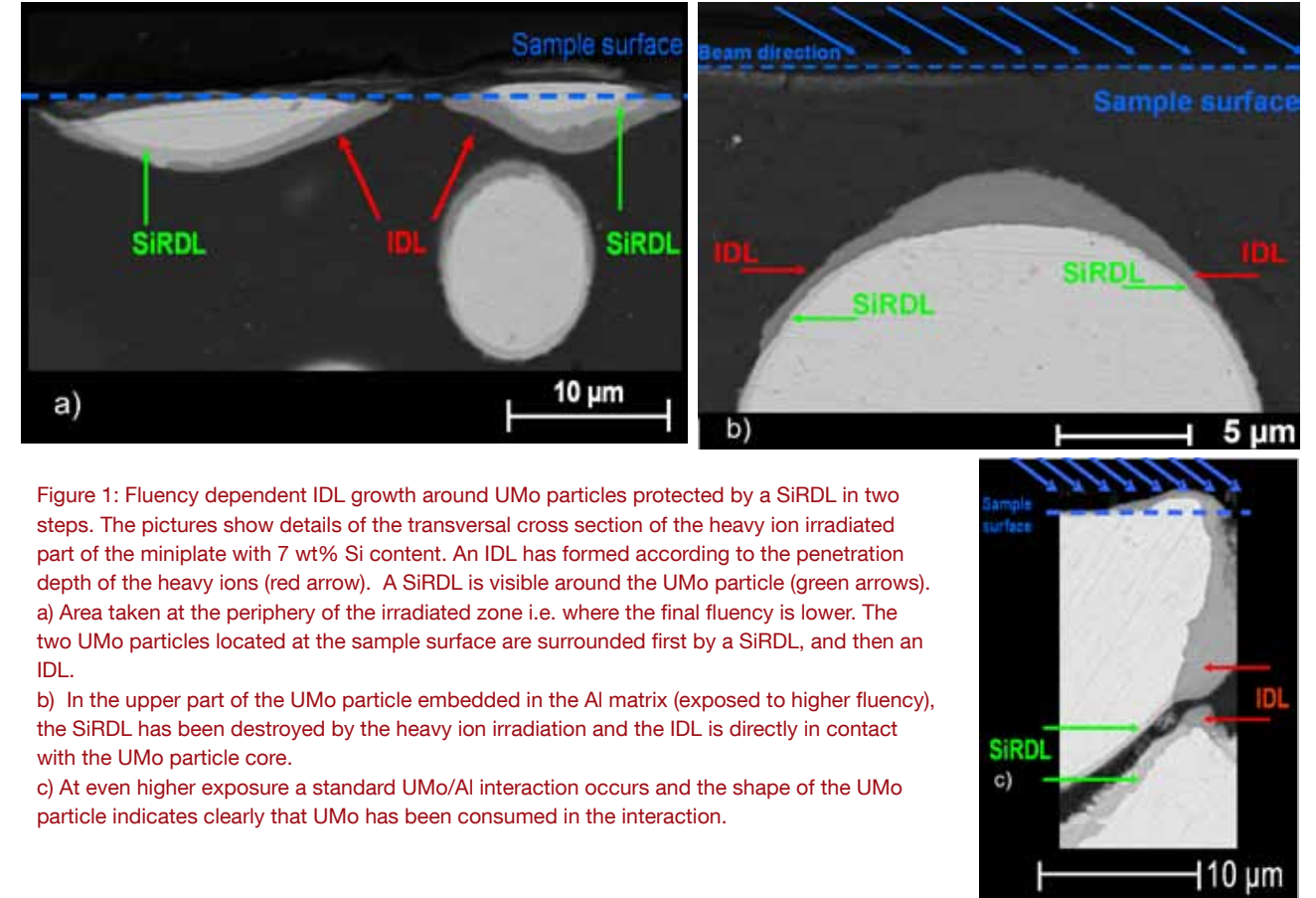


Figure 1: Fluency dependent IDL growth around UMo particles protected by a SiRDL in two steps. The pictures show details of the transversal cross section of the heavy ion irradiated part of the miniplate with 7 wt% Si content. An IDL has formed according to the penetration depth of the heavy ions (red arrow). A SiRDL is visible around the UMo particle (green arrows). a) Area taken at the periphery of the irradiated zone i.e. where the final fluency is lower. The two UMo particles located at the sample surface are surrounded first by a SiRDL, and then an IDL. b) In the upper part of the UMo particle embedded in the Al matrix (exposed to higher fluency), the SiRDL has been destroyed by the heavy ion irradiation and the IDL is directly in contact with the UMo particle core. c) At even higher exposure a standard UMo/Al interaction occurs and the shape of the UMo particle indicates clearly that UMo has been consumed in the interaction.

## Characterization after irradiation

The reference sample with no Si addition and the miniplate containing 2 wt% Si showed a thick (~5 µm) IDL around the UMo particles affected by the ion beam. For the Si sample containing 2 wt% a significant reduction in the size of the IDL was only observed at locations where a Si precipitate was found close to the UMo/Al interface.

In contrast, the samples containing 5 and 7 wt% Si allowed a detailed study of the dose-dependent behaviour of the SiRDL. Observation of transversal cross sections showed that the SiRDL had vanished in the zones exposed to the highest fluencies and a conventional IDL has formed. EDX measurements in the IDL prove the absence of measurable Si quantities, except for locations in the vicinity of a Si precipitate. It appears that the IDL formation process may be divided into two main steps, illustrated in figure 1. First an interaction occurs between the SiRDL and the Al matrix (cf. fig. 1a) until the SiRDL had disappeared (cf. fig. 1b). In this case, the IDL is often too thin to be probed with EDX. However it is likely that with the growth of the IDL, the Si concentration decreases. At this step, the UMo core of the particle is preserved from any interaction with Al. Thereafter, a conventional UMo/Al

interaction takes place, the IDL grows (cf. fig. 1c) and the UMo particle is now consumed.

## Important role of silicon

Our irradiation experiments suggest that the presence of the SiRDL around an UMo particle does not by itself prevent the growth of a conventional IDL (generally silicon free). The SiRDL is dose-dependent dissolved inside the IDL. When the SiRDL has been completely dissolved, a normal UMo/Al diffusion occurs. Only in the case of a Si precipitate in close contact to UMo, the resulting IDL is Si rich and the thickness of the IDL is significantly reduced.

This result underlines the important role played by Si precipitates located close to the UMo particle: they act as a Si source needed during in-pile irradiation, since it is shown here that the Si present inside the SiRDL will not be sufficient to stabilize the IDL. As a consequence, the AlSi alloy used as a matrix during upcoming in-pile tests should contain a high number of homogeneously dispersed small Si precipitates, rather than large Si precipitates [3].

[1] C. Jarousse et al., RRFM 09, Vienna, Austria (2009)

[2] N. Wieselmann et al., J. Nucl. Mater., 357, 191 (2006).

[3] R. Jungwirth et al., RERTR-2009, Beijing, China (2009).

# Lunar mission and batteries for locomotives - Neutrons for industry

H. Gerstenberg<sup>1</sup>, R. Gilles<sup>1</sup>, M. Hofmann<sup>1</sup>, M. Mühlbauer<sup>1</sup>, X. Li<sup>1</sup>, Y. Gao<sup>2</sup>, K. Seebach<sup>1</sup>, A. Voit<sup>1</sup>

<sup>1</sup>Technische Universität München, Forschungs-Neutronenquelle Heinz Maier-Leibnitz (FRM II), Garching, Germany

<sup>2</sup>GE Global Research, One Research Circle, Niskayuna, USA

Neutrons at the FRM II are utilised for both scientific research and industrial use. 30 percent of the beam time at the instruments is reserved for industry. In 2009, several projects were carried out, especially at the instruments ANTARES and STRESS-SPEC. However, the largest output of products for industry at the FRM II is gained without disturbing the beam time at these instruments: the silicon doping being an extra position next to the fuel element. In total 15.1 tons of silicon crystals were irradiated in 2009.

## Analysing battery cells for a hybrid locomotive

The US-company General Electric examines sodium metal-chloride batteries to be used in hybrid freight locomotives. 10,000 batteries will operate at 300 °C in a 200 ton diesel locomotive and will be charged when the locomotive brakes. This will cut down emissions from the locomotive, ideally by 10 %. At the FRM II, these NaCl-batteries were analysed non-destructively with

neutrons at the instruments STRESS-SPEC and ANTARES. If the structure and distribution of reagents in the interior of the battery are known, its life-time and efficiency can be influenced positively. Two battery cells were examined: one discharged, one half discharged. At STRESS-SPEC, the measurements showed that the concentration of the metal, which acts as a reactant when charging the battery, is higher on the edges than in the middle of the battery. Using radiography at ANTARES, the charging level of the sodium could be visualised. As these results are promising, GE plans to analyse a battery being charged using neutrons.

## Silicon doping

In total, 996 irradiations were performed by the irradiation service at the FRM II in 2009. This is an increase of 28 percent compared to the previous year. In particular, the silicon doping service has increased to a total of 784 irradiations: 15.1 tons of silicon were doped in 2009 for customers in Denmark, Japan, China and Germany. In total, since the beginning of silicon doping at the FRM II, 31.6 tons have already been doped in Garching.

## Production of molybdenum-99

Only five neutron sources worldwide produce the radioisotope molybdenum-99, the biggest supplier in Canada having been out of service since May 2009. Due to its half life of just 66 hours, it cannot be stored. As its daughter isotope, technetium-99m, is used in nuclear medicine to treatments for heart function and in cancer diagnoses, the lack of molybdenum-99 is considered life threatening by the medical profession.

At a press conference in June 2009, the feasibility

study of the FRM II and the Belgian company "Institut National des Radioéléments" was presented: The FRM II is able to produce sufficient molybdenum-99 to supply a great part of the European demand for this radioisotope. The installation of a new facility for the irradiation of uranium targets and, consequently, the production of the fission product molybdenum-99 in the reactor tank is estimated to cost 5.4 million Euros.

Thanks to the immediate financial support of the Bavarian government and the help of potential clients, the construction of the thimble is scheduled for the end of 2010.

## Trace analysis of high-purity graphite

According to the Nuclear Non Proliferation Treaty (NPT), trade in nuclear grade graphite, which is highly pure and can be used as a moderator in nuclear facilities, is strictly controlled worldwide. To determine ultra trace impurities in high-purity graphite, it is necessary to use sensitive and multi-element analytical techniques such as NAA. The neutron-capture cross section of graphite is increased by trace impurities (e.g. some rare earth elements Gd, Sm, Eu, Dy, and Er), which have very large neutron cross sections. Knowledge of the concentration of trace elements is of particular interest to manufacturers and users of high-purity graphite. Samples from a German company destined for export were analysed with NAA. More than 50 elements could be determined. The analysis showed, however, a high degree of purity and therefore the German company has to deal with the custom authorities before being allowed to ship the graphite abroad.

Other customers for neutron activation analysis in 2009 were from Israel, Spain, Australia, France, Norway and Great Britain.

## Mission to the moon

Rocks on the moon will be analysed to find out more about the geological age of the earth's neighbour. For this mission the irradiation group of the FRM II is creating in collaboration with the University Heidelberg and the Kayse-Thred-Institut, a neutron source to enable neutron activation analysis on-site. The source, which is equipped with a <sup>232</sup>Cf specimen - an emitter of fast neutrons by spontaneous fission - will be operated by a lunar robot on the moon.



Figure 2: The high volume irradiation facility at the FRM II reactor pool, which is used to identify the age of rock.

## The age of rocks

Irradiation of rock at the FRM II helps geologists to find out the age of their samples. The so-called fission track analysis was used 120 times in 2009 as a service for geologists and companies, who explore rock for oil or gas on site. The rocks contain apatite and muscovite, which both carry traces of uranium-238. The fission of <sup>238</sup>U leaves visible tracks: fission tracks. From the radioactive half-life of <sup>238</sup>U and the number of fission tracks per volume, the age of rock can be determined. At the FRM II, the fission of the <sup>235</sup>U in the rock is induced by irradiating the samples at the high volume irradiation facility. Thus, the exact amount of uranium in a rock can be established and the age of the rock determined successfully.

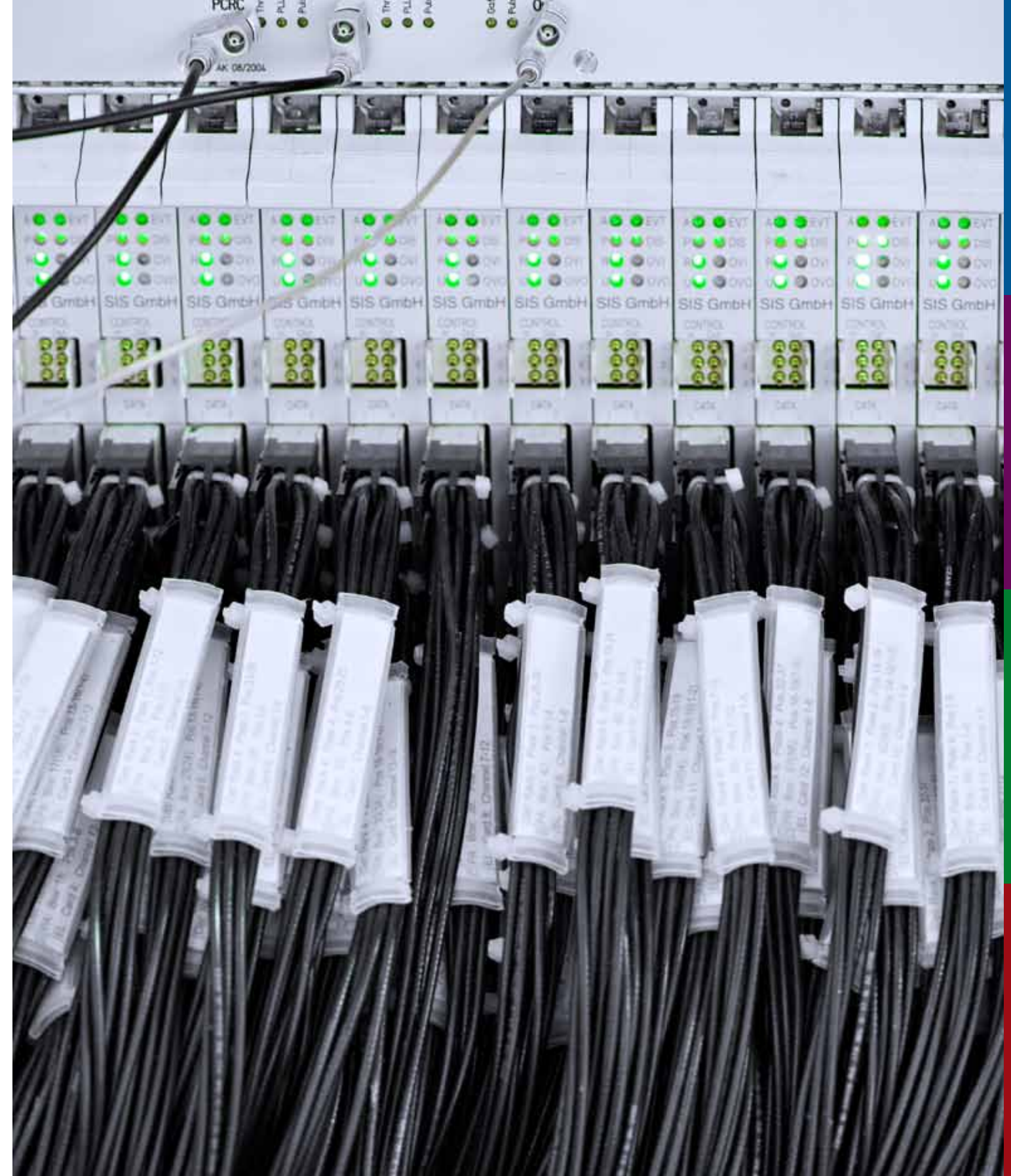
## Irradiation for an ultimate storage in Germany

The irradiation positions in the spent fuel elements is to be prepared for usage in 2010. The German Research Association (DFG) funds the RWTH Aachen university in order to build the irradiation facility at FRM II. It will be used to irradiate saline crystals with pure gamma radiation. This will contribute to the exploration of an ultimate storage for radioactive waste in German salt mines.



Figure 1: Michael Hofmann adjusting the battery cell for the hybrid locomotive at STRESS-SPEC.

Electronics for the data transfer of the neutron measurements at the time-of-flight spectrometer TOFTOF.



Facts and Figures

5

# Events: JCNS-workshops, LabCourse and Fortgeschrittenenpraktikum

T. Gutberlet<sup>1</sup>, R. Zorn<sup>2</sup>, R. Georgii<sup>3</sup>

<sup>1</sup>Forschungszentrum Jülich GmbH, Jülich Centre for Neutron Science at FRM II, Garching, Germany

<sup>2</sup>Forschungszentrum Jülich GmbH, Institut für Festkörperforschung, Jülich, Germany

<sup>3</sup>Technische Universität München, Forschungs-Neutronenquelle Heinz Maier-Leibnitz (FRM II), Garching, Germany

A large number of scientists joined the two workshops organised by JCNS at FRM II in 2009. Both events highlighted scientific areas of increasing interest. The main emphasis was on the use of neutrons, namely the investigation of thin films, multilayers and laterally patterned heterostructures by neutron reflectometry and neutron scattering in structure and dynamics in soft matter science.

## Workshop Off-Spec 2009



The JCNS workshop *Off-Spec 2009* was held on September 27<sup>th</sup>-29<sup>th</sup> at Feldafing in the south of Munich. The co-organiser was the KFKI Research Institute for Particle and Nuclear Physics (RMKI) of the Hungarian Academy of Sciences in Budapest. Representatives of all major facilities offering neutron or X-ray off-specular scattering instruments were amongst the more than 40 participants from Europe and the United States.

The lectures looked at the current available theoretical approaches. The audience listened attentively to Boris Toperverg (Universität Bochum), Laszlo Deak (KFKI), Frederic Ott (LLB) and Peter Müller-Buschbaum (TUM). Various talks demonstrated examples in soft matter, as well as

magnetism measuring off-specular and grazing incidence scattering. Also, some talks dealt with current existing software and programs such as that of Adrian Rühm (MPI). In addition, the running status and new instruments such as RefSANS or MARIA at FRM II were reviewed. Both the potential of off-specular and grazing incidence scattering and the increasing demand for application-oriented programs to simulate and fit the obtained data were shown at the meeting.

The participants discussed the various facets of the workshop's topic at length and were not interrupted by the delicious dinner at the famous Klostersgasthof Andechs. In order to strengthen the community, it was agreed that detailed information and programs would be offered over the internet.

## Workshop Trends and Perspectives in Neutron Scattering on Soft Matter

Only a few days later (October 5<sup>th</sup>-8<sup>th</sup>) the JCNS workshop *Trends and Perspectives in Neutron Scattering on Soft Matter* took place at Tutzing, on the famous Lake Starnberg. It attracted nearly 70 participants from Europe, Japan and the United States. With financial support from the European Network of Excellence *SoftComp* and



the Donostia International Physics Center, San Sebastian, an impressive list of 21 invited and 17 contributed lectures highlighted the usage of neutrons to elucidate dynamics in soft matter and biomacromolecular systems. The presentations dealt with the kinetics of structural transitions, ordering processes, structure and self-assembly, nano-composites, molecular dynamics simulations on biomolecules and soft matter systems as well as novel instrumentation. A large poster session gave additional opportunities to encourage conversation.

The beautiful environment and warm autumn sun encouraged the participants to engage in intense discussions. The German neutron source Forschungs-Neutronenquelle Heinz Maier-Leibnitz (FRM II) was the destination of the outing of the four-day meeting. Everybody enjoyed the tours of the reactor halls, guided by scientists of the JCNS on-site. Altogether, the workshop was very much appreciated. The participants expressed confidence that this event will further help to develop the use of neutrons in soft matter and enhance fruitful collaboration in this field of research. The meeting was so successful that a decision was made for a follow-up workshop, also organised by the JCNS, in 2012.

## LabCourse

On September 14<sup>th</sup>-18<sup>th</sup> the practical part of the 13<sup>th</sup> JCNS Laboratory Course – Neutron Scattering in cooperation with RWTH Aachen and



WWU Münster took place at the FRM II. After a week of theory at the Forschungszentrum Jülich, 56 students from Germany and mostly other European countries experienced hands-on experiments at the JCNS and FRM II instruments. The students very much enjoyed the intense and engaging atmosphere at FRM II and the direct

contact with the instrument scientists and PhD students acting as tutors during the course. A special highlight was the soccer game between students and scientists and the farewell party towards the end of the course. The 14<sup>th</sup> JCNS Laboratory Course is already scheduled for September 6<sup>th</sup>-17<sup>th</sup>, 2010.

## Fortgeschrittenenpraktikum

In summer and winter 2009, the practical training in neutron scattering for undergraduate students of the Technische Universität München was continued at the FRM II. The practical forms part of the *Fortgeschrittenenpraktikum* offered by the Physik Department. A total of 57 students in the fifth and sixth physics semester participated. After a half day introduction to the neutron source FRM II and the theory of neutron scattering, each student performed two different experiments at one of the eleven participating instruments (HEIDI, JNSE, KWS-2, MIRA, PANDA, PUMA, RESI, SPHERES, SPODI, Stress-Spec and TOFTOF). The experiments were adapted from standard user experiments typical for the physics investigated at these instruments. The experiments lasted a day each, including overnight measurements. During their stay, the students had the possibility of a guided tour of the reactor halls. In order to complete their practical, the students were asked to write a short report detailing the experimental results and present this in a short colloquium.

The response of the students to a short questionnaire was very enthusiastic. The main highlight for them was the possibility to carry out "real" user experiments themselves. They experienced this as a very sharp contrast to the demonstration experiments within the usual didactic teaching model.



# Statistics, meetings, access and much more: The user office of the FRM II and JCNS

T. Gutberlet<sup>1</sup> I. Lommatzsch<sup>2</sup>, U. Kurz<sup>2</sup>, B. Tonin<sup>2</sup>

<sup>1</sup>Forschungszentrum Jülich GmbH, Jülich Centre for Neutron Science at FRM II, Garching, Germany

<sup>2</sup>Technische Universität München, Forschungs-Neutronenquelle Heinz Maier-Leibnitz (FRM II), Garching, Germany

**F**acilitating access for scientists who visit in order to perform experiments at the FRM II is the main task of the joint User Office of the FRM II and JCNS. The remit of the user office is: Organising the various proposal rounds, proper access to the FRM II, the availability of information on the FRM II and JCNS via web pages and supervising the requests for accommodation which are handled by the FRM II visitors' service. The user office ensures that a visit to the FRM II runs smoothly.

Two thirds of the available beam time on the instruments at the FRM II is available for use by external scientists who submit proposals to the facilities. In 2009, the user office at the FRM II had to deal with a steady and continuous increase in proposals for beam time, with a total of 519 requests amounting to more than 4000 days of beam time. This high demand for beam time exceeded the beam time available at the instruments in operation by close to a factor 2 overall. In four independent proposal rounds

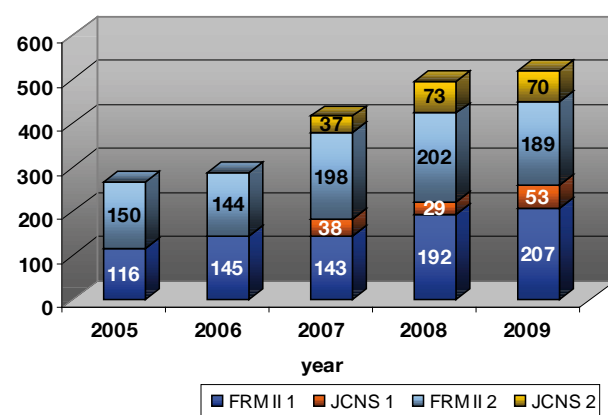


Figure 1: Proposals submitted to FRM II and JCNS

by the FRM II and JCNS, these proposals were reviewed by international scientific committees and beam time was allocated according to the scientific merit of the proposals submitted.

The increasing recognition of the scientific options at the FRM II and JCNS has led to the decision to bring the current deadline for proposal submission at the FRM II into line with that of the JCNS, starting in 2010.

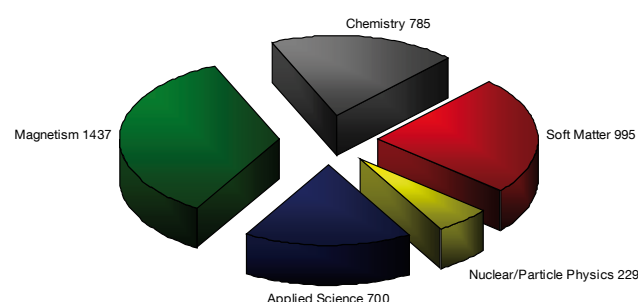


Figure 2: Beam time requested at FRM II and JCNS in 2009

## Users and financial support from the EU

Most users applying for beam time were from German universities and research centres, but about 40 % of the proposals were from Europe or further afield such as Japan, the USA or India. European users received special benefits from financial support by the European Commission within the FP7 NMI3 programme, in which the FRM II and JCNS participate. The programme started on 1<sup>st</sup> February, 2009, and offers access for European researchers over the next two years. Since the programme's inception, more than 100 scientists have already received financial support from NMI3, using nearly 300 days of beam time in 2009. This numbers far exceed the expected uptake for this European programme.

## 2<sup>nd</sup> User Meeting

A special highlight of the user service in 2009 was the 2<sup>nd</sup> FRM II User Meeting held on 25<sup>th</sup> May, 2009, in Garching. In a very friendly atmosphere at the Faculty of Physics of the Ludwig-Maximilians-Universität München, users gave talks on experiments recently performed at the FRM II. These were discussed by the audience in a full lecture hall and well received. The evening



poster session in the foyer of the Department of Physics of the Technische Universität München, with Bavarian finger food and beer, was a real summer special with lively scientific discussions and get-togethers by users and FRM II



staff members. More than 70 poster presentations gave an impressive and vivid overview of the broad range of scientific topics tackled with the instruments available at FRM II. Given the positive response of the users to this meeting, the FRM II looks forward to the 3<sup>rd</sup> User Meeting which is scheduled for 15<sup>th</sup> October, 2010: [www.frm2.tum.de/user-meeting-2010](http://www.frm2.tum.de/user-meeting-2010)

## FRM II news

The FRM II news launched in 2008 established itself in 2009. This electronic newsletter provides bi-annual information on the latest news and developments at the FRM II and JCNS. New instru-



mentation and projects are reviewed, as well as the scientific work of groups active at the FRM II and JCNS. Besides scientific topics, information on organisational issues and the operation of the FRM II reactor and facility is provided. The FRM II news can be downloaded from the user office web pages of the FRM II: [www.frm2.tum.de/user-office/downloads](http://www.frm2.tum.de/user-office/downloads)

## DUO 2.0

In order to update the Digital User Office for the growing demands of users and administration, the FRM II and JCNS started a European initiative to a DUO 2.0 in collaboration with major European neutron and synchrotron facilities. Based on the DUO software developed and used at the Paul Scherrer Institut in Switzerland, a consortium of PSI, BESSY, DESY, LLB, Soleil, MaxLab, JCNS and FRM II has been organised. This consortium has discussed and formulated the general concept for a new software package called DUO 2.0 and its realisation by the interested partners within the group. In 2009 the FRM II software division realised the core programming of the new package, which was presented and discussed at several meetings of the consortium. This new software package will now be used to create a full workflow of a digital user office at the FRM II which will be implemented at the user facilities of the other partners of the consortium and modified for their specific requirements. The novel DUO software will be a major step towards a general unified usage of digital user offices for many users in Germany and Europe in the future and will further help to simplify scientists' access to neutron and other scientific large-scale facilities such as the FRM II.

All pictures on this page: impressions of the 2<sup>nd</sup> User Meeting.

# Public relations and visitors' service: From cultural heritage to isotopes

A. Voit<sup>1</sup>, U. Kurz<sup>1</sup>, B. Tonin<sup>1</sup>

<sup>1</sup>Technische Universität München, Forschungs-Neutronenquelle Heinz Maier-Leibnitz (FRM II), Garching, Germany

The neutron source FRM II offers a kaleidoscope of topics for the national and international press. In addition to the hot topic of molybdenum-99, which can be produced in one of the FRM II's beam tubes, the results of several experiments were announced to the general public. Also, the interest of school classes, students and others in visiting the site increased in 2009.

## Visits by politicians

Several politicians visited the FRM II in 2009: In August, the district administrator Johanna Rumschöttel (SPD), was accompanied by Prof. Dr. Peter Paul Gantzer (SPD), vice-president of the Bavarian parliament. The SPD parliamentary candidate for "Landkreis München", Ingrid Lenz-Aktas, visited the neutron source in September. The Bavarian State Minister for Science, Research and Art, Dr. Wolfgang Heubisch (FDP), honoured the FRM II with a visit in November. He gave assurances of his financial and political support for the production of molybdenum-99 at

the neutron source, which is planned to start in 2014.

## Molybdenum and uranium

The production of molybdenum-99 has been one of the most popular topics in the media. The announcement of the positive outcome of a feasibility study for the medically important radioisotope production at the neutron source in Garching, was one of the public relations highlights of 2009. At a press conference, the directorate of the FRM II and the president of the Technische Universität München, Prof. Wolfgang A. Herrmann, communicated their plans to journalists, who spread the news within the national and international press (see fig. 1). There were more than a dozen contributions on radio and TV stations about the molybdenum-project and other research topics at the FRM II in 2009. Especially popular was a press release regarding the examination of an ancient Roman figurine at the instrument ANTARES: The news appeared in 17 articles in the print and online media.



Figure 1: The positive feasibility study for the production of molybdenum-99 was announced at a press conference at the Technische Universität München in June with (from left to right): Dr. Ingo Neuhaus, Prof. Dr. Winfried Petry, Prof. Dr. Wolfgang A. Herrmann, Dr. Ulrich Marsch, Prof. Dr. Andreas Bockisch and Henri Bonet.

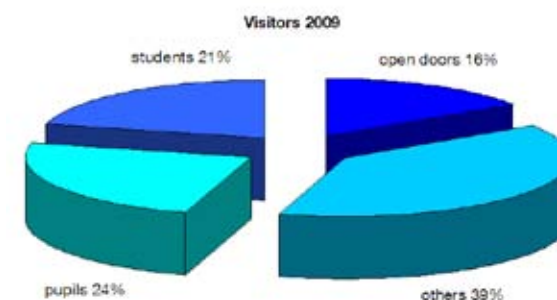


Figure 2: In total, 3139 visitors took the opportunity to get a look inside the neutron source FRM II.

Another important topic, in addition to several scientific press releases and the 5<sup>th</sup> anniversary of the start of the nuclear era at the FRM II, was the planned conversion of the FRM II fuel element from highly enriched uranium (93 % U235) to medium enriched uranium (40 % to 50 % U235). The FRM II announced that the conversion will be completed by 2016, as international laboratories have, so far, not produced a suitable fuel with higher density.

## Number of visitors increases

Exactly 3139 pupils, students and interested groups took the chance to visit the neutron source in 2009 (see fig. 2). This is an increase of four percent compared to the previous year and the highest number of visitors since 2005. The high interest of the public can only be met thanks to the indefatigable efforts of the employees of the FRM II, who guide the groups through the neutron source. On open day, October 24<sup>th</sup>, 487 people had the opportunity to attend one of the guided tours, which were quickly fully booked. Around 80 scientists, security service personnel and staff of the FRM II contributed to a successful day. The three talks at the TUM physics department, held by Winfried Petry, Jürgen Neuhaus and Christoph Hugenschmidt, were among the best attended lectures of the day.

The younger generation, i.e. students and school pupils, represents half the groups visiting during the year. Among the other visitors were many international groups such as the steering committee of the Institut Laue-Langevin in Grenoble and the Ministry of Industry and Energy Azerbaijan. Teachers (in total 41), as well as school classes, also visited the neutron source in Garching as part of their further training. For the first time, the FRM II participated in the "Girls' day" and the "Abitag" of the TUM, welcoming interested



Figure 3: The FRM II booth at the „Garchinger Herbsttage“ with Dr. Klaus Seebach (2<sup>nd</sup> from the right) and Dr. Jürgen Neuhaus (2<sup>nd</sup> from the left) was well visited

pupils in June and November. March proved to be the most frequented in 2009 with a total sum of 372 visitors.

## Booth at the tradeshow in Garching

To present the FRM II and its research activities to the local community, a booth at the "Garchinger Herbsttage", a local tradeshow, was organized in September: As figure 3 shows, many interested locals looked at the model of the fuel element, took one of the new image brochures or enjoyed the presentation on research highlights at the FRM II on the wide screen.

Made in Rome  
Serienproduktion in der Antike

Neutronen bringen  
Geheimnisse antiker  
Statuen ans Licht

München  
Neue Quelle in München  
Radioisotope für die Nuklearmedizin

Isotopes:  
l'Allemagne  
en voie de  
doubler  
le Canada

Tracking down water in aircraft

Umrüstung erst  
2016 möglich  
Reaktor wird weiterhin mit  
waffenfähigem Uran betrieben

Ärger um Garchinger Reaktor

US-Präsident soll zum  
FRM II Stellung nehmen

Störfall im Reaktor nur eine Übung  
Großaufgebot an Feuerwehr-Einsatzkräften gestern Abend auf dem Forschungscampus

Figure 4: Headlines in the national and international media about the FRM II in 2009.

1. **M. A. Abul Kashem, J. Perlich, A. Die-thert, W. Wang, M. Memesa, J. Gut-mann, E. Majkowa, I. Capek, S. V. Roth, W. Petry and P. Müller-Buschbaum**  
“Array of magnetic nanoparticles via par-ticle co-operated self-assembly in block copolymer thin films”,  
Macromolecules, 42, 6202, 2009.
2. **T. Adams, S. Mühlbauer, A. Neubauer, W. Münzer, F. Jonietz, R. Georgii, B. Peder-sen, P. Böni, A. Rosch and C. Pfeiderer**  
“Skyrmion lattice domains in  $\text{Fe}_{1-x}\text{Co}_x\text{Si}$ ”,  
J. Phys.: Conf. Ser., submitted, 2009.
3. **L. Balsanova, D. Mikhailova, A. Seny-shyn, D. Trots, H. Ehrenberg and W. Lottermoser**  
“Structure and properties of  $\alpha\text{-AgFe}_2(\text{MoO}_4)_3$ ”,  
Solid State Sci., 11, 1137, 2009.
4. **B. Bauer, B. Pedersen and P. Gille**  
“ $\text{Al}_4(\text{Cr, Fe})$ : single crystal growth by the Czochralski method and structural investi-gation with neutrons at FRM II”,  
Z. Kristallogr., 224, 109, 2009.
5. **P. Böni, W. Münzer and A. Ostermann**  
“Instrumentation with polarized neutrons”,  
Physica B, 404, 2620, 2009.
6. **K. Böning and W. Petry**  
“Test irradiations of full sized  $\text{U}_3\text{Si}_2$ -Al fuel plates up to very high fission densities”,  
J. Nucl. Mater., 383, 254, 2009.
7. **H. N. Bordallo, L. P. Aldridge, P. Fouquet, L. C. Pardo, T. Unruh, J. Wuttke and F. Yokaichiya**  
“Hindered water motions in hardened ce-ment pastes investigated over broad time and length scales”,  
ACS Appl. Mater. Interfaces, 1, 2154, 2009.
8. **H. Boysen, I. Kaiser-Bischoff, M. Lerch, S. Berendts, A. Börger, D. Trots, M. Hoelzel and A. Senyshyn**  
“Structures and properties of variously doped Mayenite investigated by neutron and synchrotron powder diffraction”,  
Z. Kristallogr. Suppl., 30, 323, 2009.
9. **M. Brodeck, F. Alvarez, A. Arbe, F. Juranyi, T. Unruh, O. Holderer, J. Col-menero and D. Richter**  
“Study of the dynamics of poly(ethylene oxide) by combining molecular dynamic simulations and neutron scattering experi-ments”,  
J. Chem. Phys., 130, 094908, 2009.
10. **T. Bücherl, F. M. Wagner and C. Lierse von Gostomski**  
“First steps towards real-time radiography at the NECTAR facility”,  
Nucl. Instrum. Methods Phys. Res., Sect. A, 605, 47, 2009.
11. **L. Canella, P. Kudejova, R. Schulze, A. Tuerler and J. Jolie**  
“PGAA, PGAI and NT with cold neutrons: Test measurement on a meteorite sample”,  
Appl. Radiat. Isot., 67, 2070, 2009.
12. **J. Chang, N. Christensen, C. Nieder-mayer, K. Lefmann, H. Ronnow, D. McMorrow, A. Schneidewind, P. Link, A. Hiess, M. Boehm, R. Mottl, S. Pailhès, N. Momono, M. Oda, M. Ido and J. Mesot**  
“Inelastic neutron-scattering measurement of a magnetic excitation gap in the high-temperature  $\text{La}_{1.855}\text{Sr}_{0.145}\text{CuO}_4$  super-conductor: evidence for a field-induced quantum phase transition”,  
Phys. Rev. Lett., 102, 177006, 2009.
13. **T. Chatterji, G. J. Schneider, L. van Eijck, B. Frick and D. Bhattacharya**  
“Direct evidence for the Nd magnetic or-dering in  $\text{NdMnO}_3$  from the hyperfine field splitting of Nd nuclear levels”,  
J. Phys.: Condens. Matter, 21, 126003, 2009.
14. **T. Chatterji and G. J. Schneider**  
“Low-energy nuclear spin excitations in  $\text{CoO}$ ”,  
Phys. Rev. B, 79, 212409, 2009.
15. **T. Chatterji and G. J. Schneider**  
“Anomalous hyperfine interaction in  $\text{CoF}_2$  investigated by high resolution neutron spectroscopy”,  
J. Phys.: Condens. Matter, 21, 436008, 2009.
16. **T. Chatterji, G. J. Schneider and J. Pers-son**  
“Low-energy nuclear spin excitations in  $\text{NdAl}_2$ ”,  
Phys. Rev. B, 79, 132408, 2009.
17. **S. Chi, A. Schneidewind, J. Zhao, L. W. Harriger, L. Li, Y. Luo, G. Cao, Z. Xu, M. Loewenhaupt and P. Dai**  
“Inelastic neutron scattering measure-ments of a three-dimensional spin reso-nance in the FeAs-based  $\text{BaFe}_{1.9}\text{Ni}_{0.1}\text{As}_2$  superconductor.”,  
Phys. Rev. Lett., 102, 107006, 2009.
18. **M. Deveaux, S. Amar-Youcef, A. Büden-bender, D. Doering, I. Fröhlich, C. Müntz, J. Stroth and F. Wagner**  
“Random telegraph signal in monolithic active pixel sensors”,  
IEEE, 2009.
19. **H. Ehrenberg, N. N. Bramnik, A. Seny-shyn and H. Fuess**  
“Crystal and magnetic structures of electrochemically delithiated  $\text{Li}_{1-x}\text{CoPO}_4$  phases”,  
Solid State Sci., 11, 18, 2009.
20. **G. Festa, C. Andreani, M. P. De Pascale, R. Senesi, G. Vitali, S. Porcinai, A. M. Giusti, R. Schulze, L. Canella, P. Kude-jova, M. Muehlbauer, B. Schillinger and A. C. Collaboration**  
“A non destructive stratigraphic and radio-graphic neutron study of Lorenzo Ghiber-ti’s reliefs from Paradise and North doors of Florence Baptistery”,  
J. Appl. Phys., 106, 074909, 2009.
21. **J. Francis, M. Turski and P. Withers**  
“Measured residual stress distributions for low and high heat input single weld beads deposited on to SA508 steel”,  
Mater. Sci. Technol., 25, 325, 2009.
22. **A. Frei, E. Gutmiedl, C. Morkel, A. Müller, S. Paul, M. Urban, H. Schober, S. Rols and T. Unruh**  
“Inelastic neutron scattering on solid deu-terium Part I: density of states”,  
Phys. Rev. B, submitted, 2009.
23. **M. Frontzek, F. Tang, P. Link, A. Schnei-dewind, J. Mignot, J. Hoffmann and M. Loewenhaupt**  
“A Generic Phase Diagram for  $\text{R}_2\text{PdSi}_3$  (R= Heavy Rare Earth)?”,  
J. Phys.: Conf. Ser., 2009.
24. **R. Garg, A. Senyshyn, H. Boysen and R. Ranjan**  
“Structure of the noncubic phase in the ferroelectric state of Pr-substituted Sr- $\text{TiO}_3$ ”,  
Phys. Rev. B, 79, 144122, 2009.
25. **S. Garny, V. Mares, H. Roos, F. M. Wag-ner and W. Rühm**  
“Measurement of neutron spectra and neutron doses at the Munich therapy beam with Bonner spheres”,  
Radiat. Meas., accepted, 2009.
26. **S. Garny, W. Rühm, F. M. Wagner and H. Paretzke**  
“Neutron therapy at the FRM II - calcula-tion of dose inside a Voxel phantom”,

- Transactions: Medical Physics and Biomedical Engineering, World Congress 2009, Sept. 7-12, Munich, Germany, 2009
27. **G. Gatta, M. Meven and G. Bromiley**  
“Effects of temperature on the crystal structure of epidote: a neutron single crystal diffraction study at 293 and 1070 K”, *Phys. Chem. Miner.*, accepted, 2009.
  28. **R. Gilles, M. Hofmann, Y. Gao, F. Johnson, L. Iorio, M. Larsen, F. Liang, M. Hoelzel and B. Barbier**  
“Probing the relationship of ordering in Nanodomain FeCo alloys with ternary additions using neutron diffraction”, *Metall. Mater. Trans. A*, accepted, 2009.
  29. **J. Guo, T. Bücherl, Y. Zuo, Z. Guo and G. Tang**  
“Comparison of the performance of different converters for neutron radiography and tomography using fission neutrons”, *Nucl. Instrum. Methods Phys. Res., Sect. A*, 605, 69, 2009.
  30. **L. W. Harriger, A. Schneidewind, S. Li, J. Zhao, Z. Li, W. Lu, X. Dong, F. Zhou, Z. Zhao, J. Hu and P. Dai**  
“Transition from Three-Dimensional Anisotropic Spin Excitations to Two-Dimensional Spin Excitations by Electron Doping the FeAs-Based  $\text{BaFe}_{1.96}\text{Ni}_{0.04}\text{As}_2$  Superconductor”, *Phys. Rev. Lett.*, 103, 087005, 2009.
  31. **M. Hofmann and R. Wimpory**  
“NET TG1: Residual stress analysis on a single bead weld on a steel plate using neutron diffraction at the new engineering instrument STRESS-SPEC”, *International Journal of Pressure Vessels and Piping*, 86, 122, 2009.
  32. **D. Holland-Moritz, S. Stüber, H. Hartmann, T. Unruh, T. Hansen and A. Meyer**  
“Structure and dynamics of liquid  $\text{Ni}_{36}\text{Zr}_{64}$  studied by neutron scattering”, *Phys. Rev. B*, 79, 064204, 2009.
  33. **I. Hurtado, U. Garbe, M. Bamberger and G. Arruebarrena**  
“Texture development in magnesium HPDC alloys”, *Scr. Mater.*, 2009.
  34. **V. Hutanu, M. Meven, M. Janoschek, P. Böni and G. Heger**  
“MuPAD: Test at the hot single-crystal diffractometer HEiDi at FRM II”, *Nucl. Instrum. Methods Phys. Res., Sect. A*, 612, 155, 2009.
  35. **V. Hutanu, M. Meven, E. Lelièvre-Berna and G. Heger**  
“POLI-HEiDi: The new polarised neutron diffractometer at the hot source (SR9) at the FRM II - Project status”, *Physica B*, 404, 2633, 2009.
  36. **D. S. Inosov, J. T. Park, P. Bourges, D. Sun, Y. Sidis, A. Schneidewind, K. Hradil, D. Haug, C. Lin, B. Keimer and V. Hinkov**  
“Normal-state spin dynamics and temperature-dependent spin resonance energy in an optimally doped iron arsenide superconductor”, *Nature Physics online*, 2009: <http://www.nature.com/nphys/journal/v6/n3/abs/nphys1483.html>
  37. **S. Ivanova, A. Senyshyn, E. Zhevcheva, K. Tenchev, V. Nikolov, R. Stoyanova and H. Fuess**  
“Effect of the synthesis route on the microstructure and the reducibility of  $\text{LaCoO}_3$ ”, *J. Alloys Compd.*, 480, 279, 2009.
  38. **R. Jungwirth, H. Breitzkreutz, W. Petry, A. Röhrmoser, W. Schmid, H. Palanchar, C. Jarousse**  
“Optimization of the Si content in UMo/AL(Si) fuel plates”, *Transactions: RERTR-2009*, Nov. 1-5, Beijing, China, 2009.
  39. **T. Jun, F. Hofmann, J. Belnoue, M. Hofmann and A. M. Korsunsky**  
“Triaxial residual strains in a railway rail measured by neutron diffraction”, *J. Strain Analysis*, 44, 563, 2009.
  40. **W. Kreuzpaintner, J. Moulin, D. Lott, R. Kampmann, M. Haese-Seiller, M. Störmer and A. Schreyer**  
“Time of flight grazing incidence small angle neutron scattering on Gd nanowires”, *Eur. Phys. J. E ST*, 167, 73, 2009.
  41. **A. Leenaers, S. van den Berghe, F. Charollais, P. Lemoine, C. Jarousse, A. Röhrmoser and W. Petry**  
“Microstructural analysis of ground U (Mo) fuel with and without Si in the matrix, irradiated to high burn-up”, *Transactions: RERTR-2009*, Nov. 1-5, Beijing, China, 2009.
  42. **X. Li, H. Gerstenberg and I. Neuhaus**  
“Silicon doping system at the research reactor FRM II”, *Appl. Radiat. Isot.*, 67, 1220, 2009.
  43. **C. D. Ling, M. Avdeev, R. Kutteh, V. V. Kharton, A. A. Yaremchenko, S. Filalkova, N. Sharma, R. B. Macquart, M. Hoelzel and M. Gutmann**  
“Structure, phase transitions, hydration, and ionic conductivity of  $\text{Ba}_4\text{Nb}_2\text{O}_9$ ”, *Chem. Mater.*, 21, 3853, 2009.
  44. **X. Lin, H. Gerstenberg, C. Lierse von Gostomski, R. Henkelmann, A. Türler and M. Rossbach**  
“Determination of  $k_0$ -values for the reactions  $^{94}\text{Zr}(n,\gamma)^{95}\text{Zr}$  and  $^{96}\text{Zr}(n,\gamma)^{97}\text{Zr}$ - $^{97\text{m}}\text{Nb}$  by irradiation in highly thermalized neutron flux”, *Appl. Radiat. Isot.*, 67, 2092, 2009.
  45. **I. Major, A. Vorobiev, A. Rühm, R. Maier, M. Major, M. Mezger, M. Nülle, H. Dosch, G. P. Felcher, P. Falus, T. Keller and R. Pynn**  
“A spin-echo resolved grazing incidence scattering setup for the neutron interrogation of buried nanostructures”, *Rev. Sci. Instrum.*, 80, 123903, 2009.
  46. **G. McGrady, P. Sirsch, N. Chatterton, A. Ostermann, C. Gatti, S. Altmannshofer, V. Herz, G. Eickerling and W. Schere**  
“Nature of the bonding in metal-silane sigma-complexes”, *Inorg. Chem.*, 48, 1588, 2009.
  47. **G. Meierhofer, P. Kudejova, L. Canella, P. Grabmayr, J. Jochum and J. Jolie**  
“Thermal neutron capture cross-section of  $^{76}\text{Ge}$ ”, *Eur. Phys. J. A*, 40, 61, 2009.
  48. **S. Meyer, E. Schweda, N. J. M. Meta, H. Boysen, M. Hoelzel and T. Bredow**  
“Neutron powder diffraction study and DFT calculations on the structure of  $\text{Zr}_{10}\text{Sc}_4\text{O}_{26}$ ”, *Z. Kristallogr.*, 224, 539, 2009.
  49. **R. Mole, J. A. Stride, T. Unruh and P. Wood**  
“Non-classical behaviour in an  $S = 5/2$  chain with next nearest neighbour interactions observed from the inelastic neutron scattering of  $\text{Mn}_2(\text{OD})_2(\text{C}_4\text{O}_4)$ ”, *J. Phys.: Condens. Matter*, 21, 076003, 2009.
  50. **S. Mühlbauer, B. Binz, F. Jonietz, C. Pfleiderer, A. Rosch, A. Neubauer, R. Georgii and P. Böni**  
“Skyrmion lattice in a chiral magnet”, *Science*, 323 (5916), 915, 2009.
  51. **P. Müller-Buschbaum, E. Metwalli, J. Moulin, V. Kudryashov, M. Haese-Seiller and R. Kampmann**  
“Time-of flight grazing incidence small angle neutron scattering - a novel scattering technique for the investigation of nanostructured polymer films”, *Eur. Phys. J. E ST*, 167, 107, 2009.
  52. **P. Niklowitz, C. Pfleiderer, S. Mühlbauer, P. Böni, T. Keller, P. Link, J. Wilson, M. Vojta and J. Mydosh**  
“New angles on the border of antiferromagnetism in  $\text{NiS}_2$  and  $\text{URu}_2\text{Si}_2$ ”, *Physica B*, 404, 2955, 2009.
  53. **M. Nülle**  
“Spin-echo resolved neutron scattering from self-organized polymer interfaces”, *PhD-Thesis*, 2009.
  54. **C. Ohms, R. Wimpory, D. Katsareas and A. Youtsos**  
“Residual stress assessment by neutron diffraction and finite element modelling on a single bead weld on a steel plate”,

- International Journal of Pressure Vessels and Piping, 86, 63, 2009.
55. **L. Orsingher, A. Fontana, J. R. Carini, G. Tripodo, T. Unruh and U. Buchenau**  
“Vibrational dynamics of densified vitreous GeO<sub>2</sub>”,  
J. Chem. Phys. accepted , 2009.
56. **H. Palancher, N. Wieschalla, P. Martin, R. Tucoulou, C. Sabathier, W. Petry, J. Berar, C. Valot and S. Dubois**  
“Uranium-molybden nuclear fuel plates behaviour under heavy ion irradiation: An x-ray diffraction analysis”,  
J. Nucl. Mater., 385, 449, 2009.
57. **S. Park, B. Pedersen, M. Meven and H. Krüger**  
“Cation dynamics in six-membered ring and chain lithosilicates”,  
Z. Kristallogr. Suppl., 29, 122, 2009.
58. **S. Parnell, E. Babcock, K. Nünighoff, M. Skoda, S. Boag, S. Masalovich, W. C. Chen, R. Georgii, J. Wild and C. Frost**  
“Study of spin-exchange optically pumped <sup>3</sup>He cells with high polarisation and long lifetimes”,  
Nucl. Instrum. Methods Phys. Res., Sect. A, 598, 774, 2009.
59. **J. I. Pérez-Landazábal, V. Recarte, V. Sánchez-Alarcos, J. A. Rodríguez-Velamazán, M. Jiménez-Ruiz, P. Link, E. Cesari and Y. Chumlyakov**  
“Lattice dynamics and external magnetic field effects in Ni-Fe-Ga alloys”,  
Phys. Rev. B, 80, 4301, 2009.
60. **J. Perlich, V. Koertgens, E. Metwalli, L. Schulz, R. Georgii and P. Müller-Buschbaum**  
“Solvent content in thin spin-coated polystyrene homopolymer films”,  
Macromolecules, 42, 337, 2009.
61. **W. Petry**  
“Nicht zu schaffen - Die für 2010 vereinbarte Umrüstung des Forschungsreaktors FRM II auf Brennelemente mit geringerer Urananreicherung muss bis mindestens 2016 verschoben werden”,  
Physik Journal, 8, 7, 2009.
62. **W. Petry**  
“Neutrons made in Garching”,  
Public Service Review Science and Technology, 3, 330, 2009.
63. **C. Pfleiderer, T. Adams, A. Bauer, W. Biberacher, B. Binz, F. Birkelbach, P. Böni, C. Franz, R. Georgii, M. Janoschek, M. Jonietz, R. Ritz, S. Mühlbauer, W. Münzer, A. Neubauer, B. Pedersen and A. Rosch**  
“Skyrmion lattices in metallic and semiconducting B<sub>2</sub>O transition metal compounds”,  
J. Phys.: Conf. Ser., 2009.
64. **C. Pfleiderer, A. Neubauer, S. Mühlbauer, F. Jonietz, M. Janoschek, S. Legel, R. Ritz, W. Münzer, C. Franz, P. Niklowitz, T. Keller, R. Georgii, P. Böni, B. Binz and A. Rosch**  
“Quantum order in the chiral magnet MnSi”,  
J. Phys.: Condens. Matter, 21, 164215, 2009.
65. **G. Pigozzi, D. Mukherji, R. Gilles, P. Jenicus and C. Siemers**  
“The measurement of internal strain in core-shell Ni<sub>3</sub>Si(Al)-SiO<sub>x</sub> nanoparticles”,  
Nanotechnology, 20, 245704, 2009.
66. **R. Ranjan, R. Garg, A. Senyshyn, M. Hedge, H. Ehrenberg and H. Boysen**  
“Magneto-structural study of a Cr-doped CaRuO<sub>3</sub>”,  
J. Phys.: Condens. Matter, 21, 326001, 2009.
67. **R. Ranjan, V. Kothai, R. Garg, A. Senyshyn, A. Agrawal, A. Senyshyn and H. Boysen**  
“Degenerate rhombohedral and orthorhombic states in Ca-substituted Na<sub>0.5</sub>Bi<sub>0.5</sub>TiO<sub>3</sub>”,  
Appl. Phys. Lett., 95, 042904, 2009.
68. **J. Rebelo-Kornmeier, M. Hofmann, U. Garbe, C. Randau, J. Repper, A. Ostermann, W. Tekouo, G. Seidl, R. Wimpory, R. Schneider and H. Brokmeier**  
“New developments at materials science diffractometer STRESS-SPEC at FRM II”,  
Adv. X-Ray Anal., 52, 209, 2009.
69. **G. J. Redhammer, A. Senyshyn, G. Tippelt, C. Pietzonka, G. Roth and G. Amthauer**  
“Magnetic and nuclear structure and thermal expansion of orthorhombic and monoclinic polymorphs of CoGeO<sub>3</sub> pyroxene”,  
Phys. Chem. Miner., 2009.
70. **J. Repper, T. Keller, M. Hofmann, C. Krempasky, W. Petry and E. Werner**  
“Neutron Larmor diffraction for the determination of absolute lattice spacing”,  
Adv. X-Ray Anal., 52, 201, 2009.
71. **J. Repper, M. Hofmann, C. Krempaszky, R. Wimpory, E. Werner and W. Petry**  
“Micro stress accumulation in multiphase superalloys”,  
Powder Diffr. J., 24, 65, 2009.
72. **M. R. Ripoll and J. Ocenasek**  
“Microstructure and texture evolution during the drawing of tungsten wires”,  
Engineering Fracture Mechanics, 76, 1485, 2009.
73. **A. Röhrmoser and W. Petry**  
“Fuel plate temperatures during operation of FRM II”,  
Transactions: RRFM 2009, March, 23-25, Vienna, Austria, 2009.
74. **O. Russina, M. Beiner, C. Pappas, V. Arrighi, M. Russina, T. Unruh, C. Mullan, C. Hardacre and A. Triolo**  
“Temperature dependence of the primary relaxation in 1-Hexyl-3-methylimidazolium bis((trifluoromethyl)sulfonyl)imide”,  
J. Phys. Chem. B, 113, 8469, 2009.
75. **A. Sarapulova, D. Mikhailova, A. Senyshyn and H. Ehrenberg**  
“Crystal structure and magnetic properties of Li,Cr-containing molybdates Li<sub>3</sub>Cr(MoO<sub>4</sub>)<sub>3</sub>, LiCr(MoO<sub>4</sub>)<sub>2</sub> and Li<sub>1.8</sub>Cr<sub>1.2</sub>(MoO<sub>4</sub>)<sub>3</sub>”,  
J. Solid State Chem., 182, 3262, 2009.
76. **A. Sazonov, V. Hutanu, M. Meven and G. Heger**  
“Orbital contribution to the magnetic moment in Co<sub>2</sub>SiO<sub>4</sub>”,  
Acta Crystallogr., Sect. A, 65, 68, 2009.
77. **A. Sazonov, M. Meven, V. Hutanu, G. Heger, T. Hansen and A. Gukasov**  
“Magnetic behaviour of synthetic Co<sub>2</sub>SiO<sub>4</sub>”,  
Acta Crystallogr., Sect. B, 65, 664, 2009.
78. **I. Schaaf, S. Cusenza, M. Bamberger, Y. Amran, K. Weiss, L. Meier, U. Wasmuth and M. Hofmann**  
“Phase transition kinetics in austempered ductile iron (ADI)”,  
International Foundry Research, 61, 14, 2009.
79. **T. Schaffran, M. Bergmann, I. Grunwald, R. Peschka-Süss, R. Schubert, F. M. Wagner and D. Gabel**  
“Tumoral hemorrhage induced by dodecaborate cluster lipids”,  
ChemMedChem., 2009.
80. **E. Schmid, F. M. Wagner, H. Romm, L. Walsh and H. Roos**  
“Dose-response relationship of dicentric chromosomes in human lymphocytes obtained for the fission neutron therapy facility MEDAPP at the research reactor FRM II”,  
Radiation and Environmental Biophysics 48, 67, 2009.
81. **E. Schmid, F. M. Wagner, H. Romm, L. Walsh and H. Roos**  
“RBE of the fission neutron therapy facility MEDAPP at the new research reactor FRM II determined by dicentrics in human lymphocytes”,  
Radiation and Environmental Biophysics, 2009.
82. **A. Schönleber, J. Angelkort, S. van Smaalen, L. Palatinus, A. Senyshyn and W. Morgenroth**  
“Phase transition, crystal structure, and magnetic order in VOCl”,  
Phys. Rev. B, 80, 064426, 2009.
83. **A. Senyshyn, D. Trots, J. Engel, L. Vasylechko, H. Ehrenberg, T. Hansen, M.**

- Berkowski and H. Fuess**  
“Anomalous thermal expansion in rare-earth gallium perovskites: a comprehensive powder diffraction study”,  
J. Phys.: Condens. Matter, 21, 145405, 2009.
84. **S. P. Singh, R. Ranjan, A. Senyshyn, D. Trots and H. Boysen**  
“Structural phase transition study of the morphotropic phase boundary compositions of  $\text{Na}_{0.5}\text{Bi}_{0.5}\text{TiO}_3\text{-PbTiO}_3$ ”,  
J. Phys.: Condens. Matter, 21, 375902, 2009.
85. **M. Skidmore, R. Ambrosi, D. Vernon, E. Calzada, G. Benedix, T. Bücherl and B. Schillinger**  
“Prompt gamma-ray activation analysis of Martian analogues at the Forschungs-Neutronenquelle Heinz Maier-Leibnitz neutron reactor and the verification of a Monte Carlo planetary radiation environment model”,  
Nucl. Instrum. Methods Phys. Res., Sect. A, 607, 421, 2009.
86. **C. Smuda, S. Busch, R. Schellenberg and T. Unruh**  
“Methyl group dynamics in polycrystalline and liquid ubiquinone Q0 studied by neutron scattering”,  
J. Phys. Chem. B, 113, 916, 2009.
87. **L. Sobczyk, M. Prager, W. Sawak-Dobrowolska, B. G., A. Pawlukojc, E. Grech, L. van Eijck, A. A. Iwanow, S. Rols, J. Wuttke and T. Unruh**  
“The structure and dynamics of methyl groups in diaminodurene (DAD)”,  
J. Chem. Phys., 130, 164519, 2009.
88. **A. Stadler, I. Digel, J. Embs, T. Unruh, M. Tehei, G. Zaccai, G. Büldt and G. Artmann**  
“From powder to solution: hydration dependence of human hemoglobin dynamics correlated to body temperature”,  
Biophys. J., 96, 5073, 2009.
89. **I. Strunz, R. Gilles, D. Mukherji, M. Hofmann, D. Genovese, J. Roesler, M. Hoelzel and V. Davydov**  
“SANS contrast dependence on difference in thermal expansions of phases in two-phase alloys”,  
J. Appl. Crystallogr. 42, 981, 2009.
90. **Y. Su, P. Link, A. Schneidewind, T. Wolf, P. Adelman, Y. Xiao, M. Meven, R. Mittal, M. Rotter, D. Johrendt, T. Brueckel and M. Loewenhaupt**  
“Antiferromagnetic ordering and structural phase transition in  $\text{Ba}_2\text{Fe}_2\text{As}_2$  with Sn incorporated from the growth flux”,  
Phys. Rev. B, 79, 064504, 2009.
91. **F. Tang, P. Link, M. Frontzek, J. Mignot, J. Hoffmann, W. Löser and M. Loewenhaupt**  
“Neutron diffraction study of magnetic structures in single crystal  $\text{Ho}_2\text{PdSi}_3$  in magnetic fields up to 5T”,  
J. Phys.: Conf. Ser., 2009.
92. **D. Trots, A. Senyshyn, L. Vasylechko, R. Niewa, T. Vad, V. Mikhailik and H. Kraus**  
“Crystal structure of  $\text{ZnWO}_4$  scintillator material in the range of 3-1423 K”,  
J. Phys.: Condens. Matter 21, 325402, 2009
93. **I. Troyanchuk, D. Karpinsky, A. Sazonov, V. Sikolenko, V. Efimov and A. Senyshyn**  
“Effect of iron doping on magnetic properties of  $\text{Sr}_{0.78}\text{Y}_{0.22}\text{CoO}_{2.625+\sigma}$ -layered perovskite”,  
J. Mater. Sci. 44, 5900, 2009.
94. **N. Tsyrlin, T. Pardini, R. Singh, F. Xiao, P. Link, A. Schneidewind, A. Hiess, C. Landee, M. Turnbull and M. Kenzelmann**  
“Quantum effects in a weakly-frustrated  $S=1/2$  two-dimensional Heisenberg antiferromagnet in an applied magnetic field”,  
Phys. Rev. Lett., 102, 197201, 2009.
95. **R. Valicu and P. Böni**  
“Focusing neutron beams to sub-millimeter size”,  
Phys. Proc., 2009.
96. **W. van Renterghem, A. Lennaers, S. van den Berghe, M. Anselmet, F. Charollais, P. Lemoine and W. Petry**  
“TEM Investigation of irradiated atomised and ground U(Mo) dispersion fuel, with or without Si added to the matrix”  
Transactions: RERTR-2009, Nov. 1-5, Beijing, China, 2009.
97. **L. Vasylechko, A. Senyshyn and U. Bismayer**  
“Chapter 242 Perovskite-Type Aluminates and Gallates”,  
Handbook on the Physics and Chemistry of Rare Earths, 39, 113, 2009.
98. **F. M. Wagner, B. Loeper, T. Bücherl, H. Breitzkreutz and W. Petry**  
“Use of fission radiation in life sciences and materials characterization”,  
Transactions: RRFM 2009, March, 23-25, Vienna, Austria, 2009.
99. **H. Wang, H. Ehrenberg, A. Senyshyn, R. Schierholz, J. Jaud and H. Fuess**  
“Structural investigation on the  $(1-x)\text{Pb}(\text{Mg}_{1/3}\text{Nb}_{2/3})\text{O}_{3-x}\text{PbTiO}_3$  ( $x=0; 0.21$ ) solid solution using powder diffraction”,  
Z. Kristallogr. Suppl., 30, 407, 2009.
100. **E. Welcomme, H. Palancher, C. Sabathier, P. Martin, J. Allenou, C. Valot F. Charollais, M. Anselmet, R. Jungwirth, W. Petry, L. Beck, C. Jarousse, R. Tucoulou and P. Lemoine**  
“Heavy ion irradiation of UMo7/Al fuel: methodological approach”,  
Transactions: RRFM 2009, March, 23-25, Vienna, Austria, 2009.
101. **R. Wimpory, C. Ohms, R. Schneider, A. Youtsos and M. Hofmann**  
“Statistical analysis of residual stress determination using neutron diffraction”,  
International Journal of Pressure Vessels and Piping, 86, 48, 2009.
102. **Y. Xiao, Y. Su, M. Meven, R. Mittal, C. Kumar, T. Chatterji, S. Price, J. Persson, N. Kumar, S. Dhar, A. Thamizhavel and T. Brueckel**  
“Magnetic structure of  $\text{EuFe}_2\text{As}_2$  determined by single crystal neutron diffraction”,  
Phys. Rev. B, 80, 174424, 2009.

# Committees

## Strategierat FRM II

### Chairman

Prof. Dr. Gernot Heger  
RWTH Aachen  
Institut für Kristallographie

### Members

MRin Dr. Ulrike Kirste  
Bayerisches Staatsministerium für  
Wissenschaft, Forschung und Kunst

Dr. Rainer Koepke  
Bundesministerium für Bildung und Forschung

Prof. Dr. Georg Büldt  
Forschungszentrum Jülich GmbH  
Institut für Biologische Informationsverarbeitung

Prof. Dr. Helmut Dosch  
Deutsches Elektronen-Synchrotron DESY  
Hamburg

Prof. Dr. Dieter Richter  
Forschungszentrum Jülich GmbH  
Institut für Festkörperphysik

Prof. Dr. Dirk Schwalm  
Max-Planck-Institut für Kernphysik  
Heidelberg

Prof. Dr. Helmut Schwarz  
Technische Universität Berlin  
Institut für Chemie

Prof. Dr. Dr. Michael Wannemacher  
Universität Heidelberg  
Radiologische Klinik und Poliklinik  
Abteilung Strahlentherapie

Prof. Dr. Ewald Werner  
Technische Universität München  
Lehrstuhl für Werkstoffkunde und -mechanik

Prof. Dr.-Ing. Heinz Voggenreiter  
German Aerospace Center (DLR) Köln  
Institute of Structure and Design

Prof. Dr. Markus Braden  
Universität zu Köln  
II. Physikalisches Institut

### Honorary Members

MDgt i.R. Jürgen Großkreutz  
Prof. Dr. Tasso Springer

### Guests

Prof. Dr. Dr. h.c. mult. Wolfgang A. Herrmann  
Präsident  
Technische Universität München

Dr.-Ing. Rainer Kuch  
Technische Universität München  
Beauftragter der Hochschulleitung

Prof. Dr. Winfried Petry  
Dr. Ingo Neuhaus  
Dr. Klaus Seebach  
Technische Universität München  
Forschungs-Neutronenquelle  
Heinz Maier-Leibnitz (FRM II)

### Secretary

Dr. Jürgen Neuhaus  
Technische Universität München  
Forschungs-Neutronenquelle  
Heinz Maier-Leibnitz (FRM II)

## Instrumentation advisory board (Subcommittee of the Strategierat)

### Chairman

Prof. Dr. Markus Braden  
Universität zu Köln  
II. Physikalisches Institut

### Members

Prof. Dr. Dirk Dubbers  
Universität Heidelberg  
Physikalisches Institut

Prof. Dr. Michael Gradzielski  
Technische Universität Berlin  
Institut für Chemie

Prof. Dr. Rainer Hock  
Universität Erlangen-Nürnberg  
Lehrstuhl für Kristallographie und Strukturphysik

Prof. Dr. Olaf Kühnholz  
Deutsches Elektronen-Synchrotron DESY  
Hamburg

Prof. Dr. Werner Kuhs  
Universität Göttingen  
GZG Abteilung Kristallographie

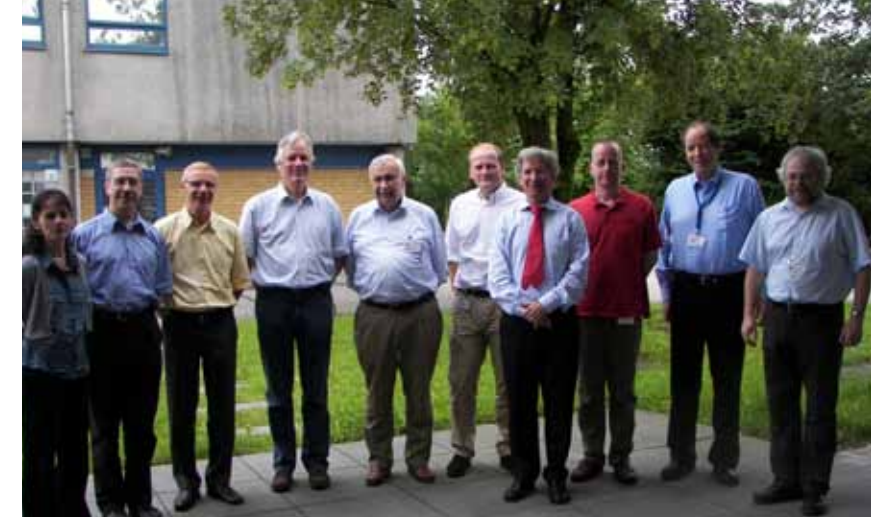
Prof. Dr. Martin Müller  
GKSS-Forschungszentrum Geesthacht

Prof. Dr. Stephan Paul  
Technische Universität München  
Physik Department E18

Prof. Dr. Wolfgang Scherer  
Universität Augsburg  
Lehrstuhl für Chemische Physik

Prof. Dr. Wolfgang Schmahl  
Deputy of the Chairman  
Ludwig-Maximilians-Universität München  
Fakultät für Geowissenschaften

Dr. habil. Dieter Schwahn  
Forschungszentrum Jülich GmbH  
Institut für Festkörperforschung



The instrumentation advisory board at a meeting in July 2009.

Prof. Dr. Andreas Türler  
Technische Universität München  
Institut für Radiochemie

Prof. Dr. Albrecht Wiedenmann  
Institut Laue-Langevin  
Grenoble

Prof. Dr. Regine Willumeit  
GKSS-Forschungszentrum Geesthacht

### Guests

Dr. Klaus Feldmann  
Forschungszentrum Jülich GmbH  
BEO-PFR

MRin Dr. Ulrike Kirste  
Bayerisches Staatsministerium für  
Wissenschaft, Forschung und Kunst

Prof. Dr. Gernot Heger  
RWTH Aachen  
Institut für Kristallographie

Prof. Dr. Winfried Petry  
Dr. Ingo Neuhaus  
Dr. Jürgen Neuhaus  
Dr. Klaus Seebach  
Technische Universität München  
Forschungs-Neutronenquelle  
Heinz Maier-Leibnitz (FRM II)

### Secretary

Dr. Peter Link  
Technische Universität München  
Forschungs-Neutronenquelle  
Heinz Maier-Leibnitz (FRM II),

Members of the scientific committee for the evaluation of beam time proposals with Dr. Peter Link (2nd from right) at the referees' meeting in March.



Committee for industrial and medical use  
(Subcommittee of the Strategierat)

Chairman

Prof. Dr.-Ing. Heinz Voggenreiter  
German Aerospace Center (DLR) Köln  
Institute of Structure and Design

Members

Automobile industry  
Dr.-Ing. Rainer Simon  
BMW AG München

Dr.-Ing. Maik Broda  
Ford Forschungszentrum Aachen

Aerospace industry  
Dr.-Ing. Rainer Rauh  
Airbus Deutschland Bremen

Chemistry and environment  
Dr. Jens Rieger  
BASF AG Ludwigshafen

Secretary

Dr. Ralph Gilles  
Technische Universität München  
Forschungs-Neutronenquelle  
Heinz Maier-Leibnitz (FRM II)

Scientific committee - Evaluation of beamtime proposals  
(Subcommittee of the Strategierat)

Chairman

Prof. Dr. Wolfgang Schmahl  
Ludwig-Maximilians-Universität München  
Fakultät für Geowissenschaften

Members

Prof. Dr. John Banhart  
Helmholtz-Zentrum Berlin für Materialien  
und Energie  
Institut Angewandte Materialforschung

Dr. Françoise Bourrée  
CEA Saclay  
Laboratoire Léon Brillouin

Dr. Olwyn Byron  
University of Glasgow  
Glasgow Biomedical Research Centre

PD Dr. Reiner Dahint  
Universität Heidelberg  
Angewandte Physikalische Chemie

Prof. Dr. Antonio Deriu  
Università degli Studi di Parma  
Dipartimenti di Fisica

Prof. Dr. Helmut Ehrenberg  
Leibniz-Institut für Festkörper-  
und Werkstoffforschung Dresden  
Institute for Complex Materials



The referees' meeting in March.

Dr. Björn Fåk  
CEA Grenoble  
INAC, SPSMS

Prof. Dr. Rupert Gebhard  
Archäologische Staatssammlung München  
Abteilung Vorgeschichte

Prof. Dr. Christoph Genzel  
Helmholtz-Zentrum Berlin für Materialien  
und Energie  
Institut Angewandte Materialforschung

Dr. Matz Haaks  
Universität Bonn  
Helmholtz-Institut für Strahlen- und Kernphysik

Dr. Klaus Habicht  
Helmholtz-Zentrum Berlin für Materialien  
und Energie  
Institut Methoden und Instrumente der  
Neutronenstreuung

Dr. Rudi Hackl  
Technische Universität München  
Walther-Meissner-Institut

Dr. Thomas C. Hansen  
Institut Laue-Langevin  
Grenoble

Dr. Nikolay Kardjilov  
Helmholtz-Zentrum Berlin für Materialien  
und Energie  
Institut Angewandte Materialforschung

Dr. Kim Lefmann  
Kobenhavns Universitet  
Niels Bohr Institute / Nanofysik

Dr. Eberhard Lehmann  
Paul Scherrer Institut  
Villigen

Dr. Bernd Leiss  
Universität Göttingen  
Geowissenschaftliches Zentrum

Dr. Stéphane Longeville  
CEA Saclay  
Laboratoire Léon Brillouin

Dr. Elena Mashkina  
Universität Erlangen-Nürnberg  
Lehrstuhl für Kristallographie und Strukturphysik

Prof. Dr. Michael Monkenbusch  
Forschungszentrum Jülich GmbH  
Institut für Festkörperforschung

Prof. Dr. Martin Müller  
GKSS-Forschungszentrum Geesthacht  
Institut für Werkstoffforschung

Prof. Dr. Juan-Manuel Pérez-Mato  
Universidad del País Vasco  
Departamento de Fisica de la Materia

Dr. Wim Pyckhout-Hintzen  
Forschungszentrum Jülich GmbH  
Institut für Festkörperforschung

Prof. Dr. Joachim Rädler  
Ludwig-Maximilians-Universität München  
Department für Physik



Another intense discussion on proposals. On the left: Martin Meven, secretary of the referee group Structure.

Prof. Dr. Klaus Rätzke  
Universität zu Kiel  
Institut für Materialwissenschaft/  
Materialverbunde

Dr. Dmitry Reznik  
CEA Saclay  
Laboratoire Léon Brillouin

Prof. Dr. Henrik Ronnow  
Ecole Polytechnique Fédérale de Lausanne  
Laboratory for Quantum Magnetism

Prof. Dr. Georg Roth  
RWTH Aachen  
Angewandte Kristallographie und Mineralogie

Dr. Juerg Schefer  
ETH Zürich and Paul Scherrer Institut Villigen  
Laboratory for Neutron Scattering

Dr. Henk Schut  
TU Delft  
Technische Natuurwetenschappen/RRR

Dr. Werner Schweika  
Forschungszentrum Jülich GmbH  
Institut für Festkörperforschung

Dr. Ivan Sidis  
CEA Saclay  
Laboratoire Léon Brillouin

Prof. Dr. Jean-Michel Sprael  
Université de la Méditerranée  
IUT, Dept. Génie Mécanique et Productique

Dr. Peter Staron  
GKSS-Forschungszentrum Geesthacht  
Institut für Werkstofforschung

Prof. Dr. Katharina Theis-Bröhl  
Hochschule Bremerhaven  
Process Engineering und Energy Technology

Prof. Dr. Helena Van Swygenhoven  
Paul Scherrer Institut  
Villigen

Prof. Dr. Ewald Werner  
Technische Universität München  
Lehrstuhl für Werkstoffkunde  
und Werkstoffmechanik

Dr. Michael Zawisky  
Atominstytut der Österreichischen Universitäten  
Wien

Prof. Dr. Oliver Zimmer  
Institut Laue-Langevin  
Grenoble

#### Scientific secretaries

Dr. Jürgen Neuhaus  
Dr. Ralph Gilles  
Dr. Wolfgang Häußler  
Dr. Michael Hofmann  
Dr. Christoph Hugenschmidt  
Dr. Peter Link  
Dr. Martin Meven  
Dr. Tobias Unruh  
Technische Universität München  
Forschungs-Neutronenquelle  
Heinz Maier-Leibnitz (FRM II)

#### TUM Advisory board

##### Chairman

Prof. Dr. Ewald Werner  
Technische Universität München  
Lehrstuhl für Werkstoffkunde  
und Werkstoffmechanik

##### Members

Prof. Dr. Peter Böni  
Technische Universität München  
Physik Department E21

Prof. Dr. Andreas Türler  
Technische Universität München  
Institut für Radiochemie

Prof. Dr. Markus Schwaiger  
represented by Prof. Dr. Senekowitsch-  
Schmidtke  
Technische Universität München  
Nuklearmedizinische Klinik und Poliklinik  
Klinikum Rechts der Isar

Prof. Dr. Bernhard Wolf  
Technische Universität München  
Heinz Nixdorf-Lehrstuhl für  
medizinische Elektronik

Prof. Dr. Arne Skerra  
Technische Universität München  
Lehrstuhl für Biologische Chemie

##### Guests

Prof. Dr. Winfried Petry  
Dr. Ingo Neuhaus  
Dr. Klaus Seebach  
Technische Universität München  
Forschungs-Neutronenquelle  
Heinz Maier-Leibnitz (FRM II)

#### Scientific steering committee

##### Chairman

Prof. Dr. Winfried Petry  
Technische Universität München  
Forschungs-Neutronenquelle  
Heinz Maier-Leibnitz (FRM II)

##### Members

Dr. Hans Boysen  
Ludwig-Maximilians-Universität München  
Fakultät für Geowissenschaften

Prof. Dr. Bernhard Keimer  
Max-Planck-Institut für Festkörperforschung  
Stuttgart

Prof. Dr. Dieter Richter  
Forschungszentrum Jülich GmbH  
Institut für Festkörperforschung



Referees at the evaluation of the instrument TOFTOF with Dr. Jürgen Neuhaus (left) and Dr. Tobias Unruh (right).

## Partner institutions



Georg-August-Universität Göttingen  
Institut für Physikalische Chemie  
Tammannstraße 6  
37077 Göttingen  
[www.uni-pc.gwdg.de/eckold/](http://www.uni-pc.gwdg.de/eckold/)

Geowissenschaftliches Zentrum  
Goldschmidstraße 1-3  
37077 Göttingen  
[www.gzg.uni-goettingen.de](http://www.gzg.uni-goettingen.de)



GKSS-Forschungszentrum Geesthacht GmbH  
Max-Planck-Straße 1  
21502 Geesthacht  
[www.gkss.de](http://www.gkss.de)



Helmholtz Zentrum Berlin  
für Materialien und Energie  
Hahn-Meitner-Platz 1  
14109 Berlin  
[www.helmholtz-berlin.de](http://www.helmholtz-berlin.de)



Jülich Centre for Neutron Science JCNS  
Forschungszentrum Jülich GmbH  
52425 Jülich  
Außenstation am FRM II: 85747 Garching  
[www.jcns.info](http://www.jcns.info)



Ludwig-Maximilians-Universität München  
Sektion Kristallographie  
Theresienstraße 41  
80333 München  
[www.lmu.de/kristallographie](http://www.lmu.de/kristallographie)

Sektion Physik  
Schellingstraße 4  
80799 München  
[www.softmatter.physik.uni-muenchen.de](http://www.softmatter.physik.uni-muenchen.de)



Max-Planck-Institut für Festkörperphysik  
Heisenbergstraße 1  
70569 Stuttgart  
[www.fkf.mpg.de](http://www.fkf.mpg.de)



RWTH Aachen  
Institut für Kristallographie  
Jägerstraße 17 - 19  
52066 Aachen  
[www.xtal.rwth-aachen.de](http://www.xtal.rwth-aachen.de)

Institut für Anorganische Chemie  
Landoltweg 1  
52074 Aachen  
[www.ac.rwth-aachen.de](http://www.ac.rwth-aachen.de)



Technische Universität Clausthal  
Institut für Werkstoffkunde und Werkstofftechnik  
Agricolastraße 6  
38678 Clausthal-Zellerfeld  
[www.iww.tu-clausthal.de](http://www.iww.tu-clausthal.de)



Technische Universität Darmstadt  
Fachbereich Material- und Geowissenschaften  
Petersenstraße 23  
64287 Darmstadt  
[www.tu-darmstadt.de/fb/matgeo/](http://www.tu-darmstadt.de/fb/matgeo/)



Technische Universität Dresden  
Institut für Festkörperphysik  
Zellescher Weg 16  
01069 Dresden  
[www.physik.tu-dresden.de/ifp](http://www.physik.tu-dresden.de/ifp)



Universität Augsburg  
Institut für Physik  
Lehrstuhl für Chemische  
Physik und Materialwissenschaften  
Universitätsstraße 1  
86159 Augsburg  
[www.physik.uni-augsburg.de/cpm/](http://www.physik.uni-augsburg.de/cpm/)



Universität der Bundeswehr München  
Institut für Angewandte Physik und Messtechnik  
Werner-Heisenberg-Weg 39  
85577 Neubiberg  
[www.unibw.de/lrt2/](http://www.unibw.de/lrt2/)



Universität zu Köln  
Institut für Kernphysik  
Zülpicher Straße 77  
50937 Köln  
[www.ikp.uni-koeln.de](http://www.ikp.uni-koeln.de)

II. Physikalisches Institut  
Zülpicher Straße 77  
50937 Köln  
[www.ph2.uni-koeln.de](http://www.ph2.uni-koeln.de)

# Staff



Teaching students in the JCNS lab course: Dr. Giovanna Simeoni at the instrument TOFTOF.



The Jülich centre for neutron science staff at the FRM II with head of the station, Dr. Alexander Ioffe (front, 6th from the right).

## Board of Directors

### Scientific director

Prof. Dr. Winfried Petry

### Technical director

Dr. Ingo Neuhaus

### Administrative director

Dr. Klaus Seebach

## Experiments

### Head

Prof. Dr. Winfried Petry

### Deputy

Dr. Jürgen Neuhaus

### Executive assistant

Dr. Peter Link

### Office

Elisabeth Jörg-Müller

Silvia Valentin-Hantschel

### Coordination

Dr. Jürgen Neuhaus

Uwe Reinecke

Harald Türck

### Instruments

Prof. Dr. Peter Böni (TUM, Physik Dep., E 21)

Kathrin Buchner (MPI Stuttgart)

Dr. Thomas Bücherl (TUM, Inst. f. Radiochemie)

Sebastian Busch

Elbio Calzada

Lea Canella

Dirk Etzdorf

Dr. Enrico Faulhaber (HZB)

Jörgen Franke (MPI Stuttgart)

Florian Gärtner

Dr. Weiman Gan (GKSS)

Dr. Robert Georgii

Dr. Ralph Gilles

Rolf Hähnel

Martin Haese-Seiller (GKSS)

Dr. Wolfgang Häußler

Dr. André Heinemann (GKSS)

Tobias Heller

Dr. Michael Hofmann

Dr. Markus Hölzel (TU Darmstadt)

Werner Hornauer

Dr. Klaudia Hradil (Universität Göttingen)

Dr. Christoph Hugenschmidt

Dr. Vladimir Hutanu (RWTH Aachen)

Norbert Jünke (Universität Göttingen)

Reinhard Kampmann (GKSS)

Dr. Thomas Keller (MPI Stuttgart)

Dr. Wilhelm Klein

Dr. Jens Klenke

Dr. Petra Kudejova

Dr. Peter Link

Dr. Birgit Loeper-Kabasakal

Andreas Mantwill (TUM, Physik Dep., E21)

Dr. Janos Major (MPI Stuttgart)

Dr. Martin Meven

Dr. Richard Mole

Dr. Jean-François Moulin (GKSS)

Dr. Sebastian Mühlbauer

Dr. Andreas Ostermann

Dr. Bjørn Pedersen

Philip Pikart

Dr. Christian Piochacz

Matthias Pomm (GKSS)

Dr. Joana Rebelo-Kornmeier (HZB)

Florin Repper

Julia Repper

Jandal Ringe

Dr. Adrian Rühm (MPI Stuttgart)

Dr. Andrew Sazonov

Dr. Burkhard Schillinger

Martin Schmiele

Dr. Astrid Schneidewind (HZB)

Prof. Dr. K. Schreckenbach (TUM, Physik Dep., E 21)

Michael Schulz

Reinhard Schwikowski

Dr. Anatoliy Senyshyn (TU Darmstadt)

Günther Seidl

Svatopluk Semecky

Prof. Dr. Torsten Soldner (TUM, Physik Dep., E 18)

Dr. Giovanna Simeoni

Stefan Söllradl (University of Bern)

Martin Stadlbauer

Rainer Stöpler (TUM, Physik Dep., E 18)

Dr. Tobias Unruh

Franz-Michael Wagner

Dr. Robert Wimpory (HZB)

Michael Wipp

Alexander Wolf

### Instruments – JCNS

Prof. Dr. Dieter Richter (Director JCNS)

Prof. Dr. Thomas Brückel (Director JCNS)

Dr. Alexander Ioffe (Head of Outstation at FRM II)

### Office

Franziska Michel

Dr. Marie-Sousai Appavou

Dr. Earl Babcock

Dr. Wouter Borghols

Dr. Peter Busch

Dr. Nicolas de Souza

Andreas Erven

Dr. Henrich Frielinghaus

Christine Gerstl

Thomas Glomann

Marco Gödel

Dr. Günter Goerigk

Dennis Gurzi

Dr. Thomas Gutberlet

Dr. Olaf Holderer

Michael Kerscher

Thomas Kohnke

Dr. Dennis Korolkov

Harald Kusche

Federik Lipfert

Dr. Stefan Mattauch

Dr. Ranjan Mittal

Andreas Nebel

Susanne Neueder

Klaus Nusser

Vladimir Ossovyi

Dr. Vitaliy Pipich

Stephen Price

Dr. Aurel Radulescu

Alfred Richter

Harald Schneider

Dr. Gerald J. Schneider

Dr. Tobias Schrader

Simon Staringer

Peter Stronciwilk

Dr. Yixi Su

Dr. Jörg Voigt

Dr. Joachim Wuttke

Andreas Zitzelsberger



The detector and electronics group with the new SANS-1 detector. Dr. Karl Zeitelhack, the head of the group, at the left.

#### Detectors and electronics

Dr. Karl Zeitelhack  
 Ilario Defendi  
 Christian Hesse  
 Max Panradl  
 Dr. Markus Petertill  
 Peter Wind

#### Sample environment

Dr. Jürgen Peters  
 Peter Biber  
 Michael-Marc Fiedler  
 Heinrich Kolb  
 Alexander Schmidt  
 Karl Georg Waldherr  
 Michael Wiesheu  
 Herbert Weiß  
 Jank Wenzlaff

#### Neutron optics

Prof. Dr. Gunther Borcher  
 Christian Breunig  
 Robert Iannucci  
 Eberhard Kahle  
 Dr. Sergey Masalovich  
 Andreas Ofner  
 Hermann Schölderle  
 Roxana Valicu

#### IT Services

Jens Krüger  
 Jörg Pulz  
 Harald Wenninger  
 Josef Ertl  
 Joao-Paulo Innocente  
 Nataliya Ivanova  
 Georg Kaspar



In the HELIOS-lab: members of the FRM II neutron optics.

Babette Oberholz  
 Andreas Steinberger  
 Manuel Stowasser

#### Apprentices at the IT Services

Andreas Erb  
 Florian Hänzel  
 Christoph Kick  
 Alexandra Kornhaas  
 Alexander Lenz  
 Benjamin Lindner  
 Andreas Preller  
 Christian Worf

#### Administration

##### Head

Dr. Klaus Seebach

##### Deputy

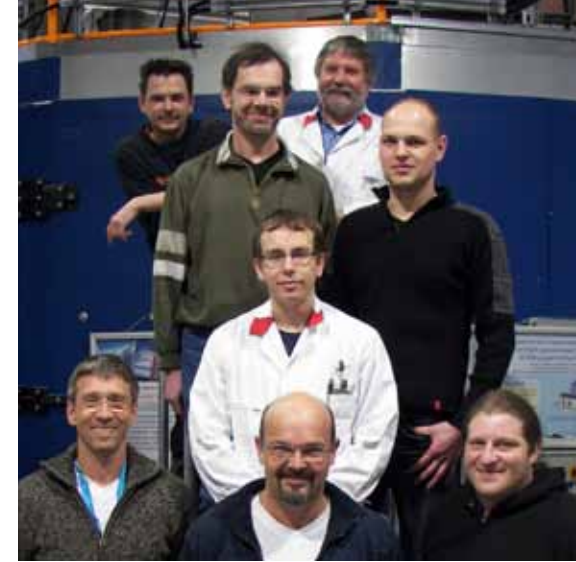
Reinhard Obermeier

##### Office

Christine Zeller

##### Staff

Reinhard Obermeier  
 Brigitte Gallenberger  
 Bernd Heck  
 Isabella Heinath  
 Alexandra Ippler  
 Katja Klaedtke  
 Beate Klein  
 Karin Lüttig  
 Sabine Osorio



The sample environment group in front of the instrument TOFTOF - at the left: the head Jürgen Peters.

Günter Wagner  
 Sabine Wünsch

#### Public relations

Andrea Voit

#### Visitors' service

Ulrike Kurz  
 Dott. Bianca Tonin-Schebesta

#### User office

Dr. Thomas Gutberlet (JCNS)  
 Dr. Ina Lommatzsch

#### Reactor operation

##### Head

Dr. Ingo Neuhaus

##### Deputy

Dr. Johann Meier  
 Dr. Anton Kastenmüller

##### Office

Marita Neuberger  
 Sylvia Rubsch

##### Management

Dr. Heiko Gerstenberg  
 (Irradiation and fuel cycles)  
 Dr. Johann Meier, Dr. Stefan Baldauf  
 (Reactor operation)  
 Roland Schätzlein



The administration of the FRM II with its head, Dr. Klaus Seebach (5th from the left) and deputy Reinhard Obermeier (2nd from the left).

(Electric and control technology)

Dr. Anton Kastenmüller  
 (Reactor enhancement)

#### Shift members

Friedrich Gründer  
 Attila Bancsov  
 Albin Benke  
 Manfred Danner  
 Christian Feil  
 Martin Flieher  
 Hubert Groß  
 Lutz Herdam  
 Florian Hofstetter  
 Konrad Höglauer  
 Thomas Kalk  
 Georg Kaltenecker  
 Ulrich Kappenberg  
 Frank Kewitz  
 Mark-Guido Krümpelmann  
 Johann Kund  
 Adolf Lochinger  
 Gerd Mauermann  
 Albert Meilinger  
 Markus Moser  
 Ludwig Rottenkolber  
 Gerhard Schlittenbauer

#### Technical services

Klaus Pfaff  
 Robert Binsch  
 Oliver Breu  
 Andreas Cziasto  
 Stefan Förg  
 Horst Gampfer  
 Wolfgang Glashauser  
 György Guld



Members of the electronic and control technology with their head Roland Schätzlein (left).

Simone Herrmann  
Christiane Wickfelder  
Albert Weber  
Michael Wöhner  
Christian Ziller  
Ismail Zöybek

**Sources**

Christian Müller  
Dietmar Päthe  
Andreas Wirtz

**Electronic and control technology**

Roland Schätzlein  
Günther Aigner  
Werner Buchner  
Franz Götz  
Andreas Düring  
Robert Krammer  
Karl-Heinz Mayr  
Üseyin Sarikaya  
Heribert Schwaighofer  
Johann Wildgruber

**Job safety**

Holger Bamberger  
Jean-Marie Favoli

**Irradiation**

Dr. Heiko Gerstenberg  
Alexander Draack  
Jean-Marie Favoli  
Wolfgang Fries  
Wolfgang Lange  
Dr. Xiaosong Li  
Volker Loder  
Jens Molch

Manfred Oberndorfer  
Alfred Richter  
Thomas Scheit  
Heike Schulz  
Franz-Michael Wagner  
Norbert Wiegner

**Reactor enhancement**

Dr. Anton Kastenmüller  
Wilhelm Bünten  
Florian Henkel  
Ralf Lorenz  
Britta Pollom  
Michael Schmitt  
Volker Zill

**Technical design**

Franz-Ludwig Tralmer  
Johan Fink  
Philipp Jüttner  
Suzan Küçük

**Workshops**

Christian Herzog  
Uwe Stiegel  
Alan Begic  
Michael Fuß  
Andreas Huber  
Andreas Scharl  
Robert Schlecht  
Josef Waronitza

**Radiation Protection**

Dr. Birgit Wierczinski  
Dubravka Bahmet  
Wolfgang Dollrieß  
Harry Hottmann

Vanessa Kindel  
Waltraut Kluge  
Daniela Lewin  
Bernhard Neugebauer  
Adelheid Schindler  
Michael Schmidt  
David Schrulle  
Katja Singler  
Daniela Strobl  
Hans-Jürgen Werth  
Susanne Wolff

**Chemical laboratory**

Christiana Auer  
Rita Bertsch  
Petra Müller  
Susanne Pohle  
Michaela Uhlmann

**Technical safety service**

Josef Wetzl  
Johann Aigner  
Nihad Hodzic  
Roland Maier  
Klemens Otto  
Johann Schreiner

**Reactor physics**

Dr. Anton Röhrmoser  
Harald Breitzkreutz  
Stefan Dirndorfer  
Rainer Jungwirth  
Wolfgang Schmid

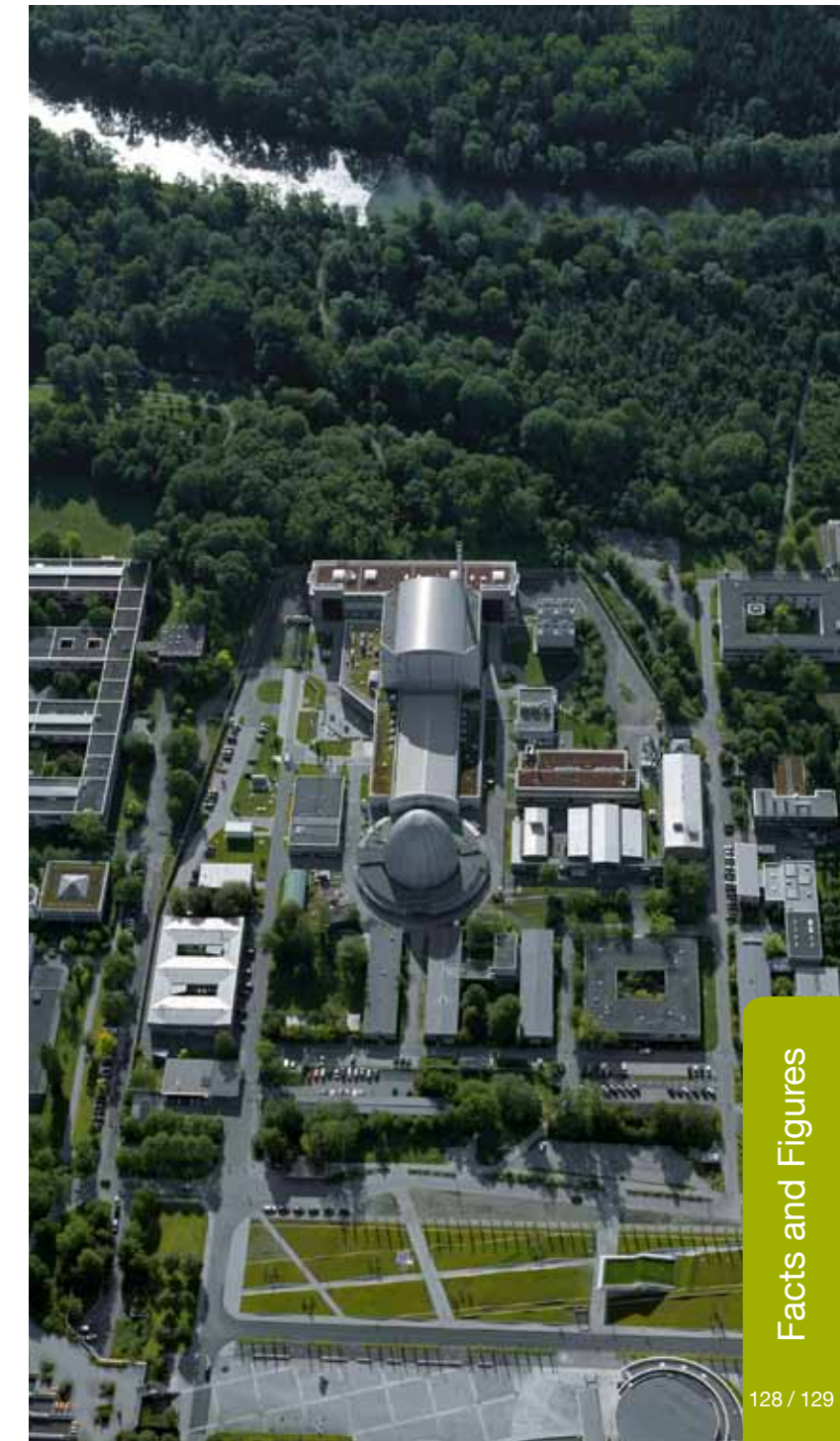
**Security department**

Ludger Stienen  
Johann Stephani



Christian Herzog (2nd from the left) and his workshops group.

The FRM II situated near the river Isar.



# Imprint

## Publisher:

Technische Universität München  
Forschungs-Neutronenquelle  
Heinz Maier-Leibnitz (FRM II)  
Lichtenbergstr. 1  
85747 Garching  
Germany

Phone: +49.89.289.14966  
Fax: +49.89.289.14995  
Web: [www.frm2.tum.de](http://www.frm2.tum.de)  
Email: [frm2@frm2.tum.de](mailto:frm2@frm2.tum.de)

## Editors:

Elisabeth Jörg-Müller  
Dr. Peter Link  
Dr. Ina Lommatzsch  
Dr. Jürgen Neuhaus  
Dr. Bjørn Pedersen  
Dr. Aurel Radulescu  
Andrea Voit

## Photographic credits:

Uli Benz, TUM:  
page 106

Astrid Eckert, Andreas Heddergott, TUM:  
pages 5, 6, 11, 15, 39, 41, 93, 95, 101

Wenzel Schürmann, TUM:  
title image, pages 9, 11, 16, 19, 48, 50, 54, 61,  
86, 103, 121, 124

Miriam Voss, TUM:  
page 11

Other images: editors, authors, TUM

## Design:

Benjamin Sanchez

## Typesetting:

Dr. Peter Link  
Dr. Ina Lommatzsch  
Andrea Voit